Delft University of Technology
Faculty of Civil Engineering and Geosciences
Department of Hydraulic Engineering

MSc. Thesis:

A combination of SWASH and Harberth to compute wave forces on moored ships

João P.H. Dobrochinski

Delft, October 2014

FINAL REPORT

MSc. Thesis Delft University of Technology

Title : A combination of SWASH and Harberth to compute wave forces on moored ships

Author : João P.H. Dobrochinski

Date : October 2014

Graduation committee:

Prof. ir. T. Vellinga	Delft University of Technology
ir. B. Wijdeven	Delft University of Technology
Dr. ir. M. Zijlema	Delft University of Technology
ir. J.C. van der Lem	Royal HaskoningDHV
ir. A.J. van der Hout	Deltares

This project was carried out at:

Royal HaskoningDHV
George Hintzenweg 85
3009 AM Rotterdam
The Netherlands

Royal HaskoningDHV
Enhancing Society Together

TU Delft Delft University of Technology

Preface

This thesis is part of the Master Programme in Hydraulic Engineering at Delft University of Technology. It marks the end of a two years phase of gaining knowledge and personal experiences in The Netherlands. This was an unique opportunity that will be always remembered.

I would like to thank Prof. Tiedo Vellinga for the guidance and motivation during the project; Bas Wijdeven, Cock van der Lem and Royal HaskoningDHV for giving the opportunity and all support; Marcel Zijlema for sharing his knowledge on wave modelling; and Arne van der Hout (Deltares) for the essential contribution to the project.

I would also like to acknowledge Wim van der Molen for the support during the project and remarks on this report; Martijn de Jong and Deltares for kindly providing the model test data used in the validation phase; Dirk Rijnsdorp and Pieter Smit for the contribution on the wave modelling; Alex van Deyzen for the daily assistance and for making these months more pleasant; and Lindino Benedet/CB&I Brazil for the support during my studies.

Finally I would like to thank all my friends, family and especially my lovely girlfriend Carolina Piccoli for staying by my side during these intense two years.

João P.H. Dobrochinski
October 2014

Summary

Moored vessels are subject to wave forces and moments at different frequencies, which induce motions of the body and can be transferred to the mooring lines and fenders. Under extreme forcing and vessel motions, dangerous line breaking accidents can occur or the ship movements can be simply too large to continue the on/off-loading process, causing downtime of the port. An accurate modelling of the waves in the harbour and the response of moored ships is of prime importance to determine the safety and workability of the berths.

In this project the combination of the wave model SWASH and the 3D diffraction model Harberth to compute waves forces acting on moored ships is investigated. The proposed approach using the SWASH wave model come as a possible alternative to the current practice of Royal HaskoningDHV, who experienced a sequence of numerical issues while simulating extreme incident waves with an operational Boussinesq-type model. The objectives of the study lead to the following research question: To which extent can the SWASH wave model and the Harberth model be combined in order to accurately compute wave forces acting on moored ships?

Each computational tool considered in the proposed approach (the wave model SWASH, the coupling procedure, and the diffraction model Harberth) can contribute to the (in)accuracy of the computed wave forces acting on a moored ship. A series of systematic tests with SWASH indicates that the dispersion errors are generally negligible, while amplitude errors remain small provided that: i) the number of vertical layers is sufficient (especially in relatively deep waters); ii) the horizontal resolution of the computational grid is sufficient; iii) important terms of the momentum equation are modelled with higher-order numerical schemes (especially for non-linear waves in relatively deep waters). The possible wave amplitude errors impact directly the predicted wave forces acting on the ship.

The coupling tool developed to combine the SWASH and Harberth models proved to be consistent for the simplified tested conditions. The first-order forces computed using SWASH and Harberth are generally well predicted, while larger deviations can occur for the second-order forces. These are partially related to the simplification of motions made by Harberth in the computation of second-order forces.

The proposed approach using the SWASH and Harberth models, combined with the developed coupling tool, is validated using model test data of waves and forces acting on a restrained ship. In general the performance is satisfactory, even for very energetic conditions, implying that the investigated modelling approach is a potential alternative for future applications.

Contents

Chapter 1

Introduction

The combination of the wave model SWASH and the 3D diffraction model Harberth is investigated in this MSc project, with the aim of computing wave forces acting on moored ships. The work had been done mainly at Royal HaskoningDHV office, in Rotterdam, between March and November 2014.

In the next sections of this introductory chapter background information and a description of the problem are provided. This is followed by the objectives of the study and the definition of the research approach.

Chapter 2 provides an overall review of relevant literature. The results of systematic tests are described in Chapter 3, including simulations of regular and bichromatic waves, and the associated wave forces acting on a ship. The link between the wave model and the model used to compute wave loads on a ship is firstly developed for these tests. In Chapter 4 the investigated approach is verified against results from physical scale model tests. The validation includes comparisons of measured and simulated waves and loads acting on a fixed ship. Partial conclusions are listed by the end of Chapter 2, 3 and 4. Final conclusions and considerations are provided in Chapter 5.

1.1 Background

Stationary vessels in irregular waves are subject to large, so-called first order, wave forces and moments which are linearly proportional to the wave height and have the same frequencies as the waves. They are also subject to small, so-called second order, mean and low frequency wave forces and moments which are proportional to the square of the wave height and have frequencies associated to the wave groups occurring in irregular waves.

In case of a free floating body, the exciting wave forces cause the body mass to accelerate. The moving body radiates waves away from the body, withdrawing energy and damping the motions on a rate proportional to the velocity of the movements. Further, restoring terms proportional to the body displacement force the ship back to its equilibrium position. When the ship is moored, the tension of the lines and reaction forces of fenders should be taken into account. The interaction of the different contributors is linked to the frequency of the exciting forces, leading to a frequency-dependent response of the system.

Due to the considerable contribution to the total forces and motions of ships, the first order waves forces and moments have been subject to investigation for several decades. It resulted in methods that are able to predict the processes with a reasonable degree of accuracy for many different vessel shapes. Even though relatively small in magnitude, the low frequency components of the second order wave forces in irregular waves can coincide with the natural frequencies of the horizontal motions of moored vessels. The damping of low frequency horizontal motions of moored bodies is generally very low, leading to large amplitude resonant behaviour of the system [Pinkster, 1980].

A moored ship experiences problems if motions become too large. This can be expected if the ship is moored in rough wave conditions, but also in apparently sheltered ports significant ship motions can occur if long waves with periods between 0.5 and 5 minutes (i.e., the so-called infragravity waves) penetrate the harbour and excite harbour seiches, resulting in a potential increase on moored vessels motions. Under extreme forcing and vessel motions, dangerous line breaking accidents can occur or the ship movements can be simply too large to continue the on/off-loading process, causing downtime of the port. Thus, accurate modelling of the waves in the harbour as well as the response of moored ships is of prime importance to determine the safety and workability of the berths.

Concerning deep water open berth situations, relatively simple simulating tools may be sufficient to predict the first and second order wave forces acting on floating bodies. These tools usually make use of linear frequency-domain wave models to compute the incident wave field and its interaction with the floating body. Some programs are extended to include variable bottom topography and additional boundaries such as reflective quay walls (usually one infinite wall or two semi-infinite walls meeting at a corner), widening their range of application. However, if the waves incident on the ship are closely associated to complex wave processes, the use of a more sophisticated approach is necessary. The referred complexity of the waves may be related to non-linear wave processes, wave breaking, wave diffraction, wave refraction on complicated bed topography, wave interaction with structures (dissipation, reflection, transmission), complicated port geometries, occurrence of harbour oscillations/seiches/standing waves, etc. Table 1.1 lists the numerical models usually applied for computations of wave forces acting on moored ships which are mentioned along this report:

TABLE 1.1: Different numerical models cited along the report.

Numerical model	**Characteristics**
SWASH	General-purpose numerical tool for simulating flow and transport phenomena in coastal waters, including non-linear wave transformations from deep water to a beach, port or harbour. The hydrodynamics are based on the Reynolds-averaged Navier-Stokes equations and mass balance equation.
Mike 21 BW / TRITON	Non-linear wave models often used in studies of wave disturbances in ports, harbours and coastal areas. Solve the time-domain formulations of Boussinesq type equations
Wavescat / DELFRAC	Linear 3-D boundary-integral equation models that compute first-order wave forces and the floating body response in regular waves. The steady second-order wave drift force and hydrodynamic coefficients are also calculated. Solve the linear free surface Green function in frequency-domain.
Harberth	Linear 3-D boundary-integral equation model that computes first and second-order wave forces on a floating body. Hydrodynamic coefficients are also calculated. Solves the linear free surface Green function in time-domain and integrates the pressures acting on the floating body. Applicable for complex wave fields near the ship (e.g. due to harbour oscillations, passing vessels, significant bottom level changes).

1.2 Problem formulation

The current practice adopted by Royal HaskoningDHV for studies of wave penetration in harbours and dynamic mooring analysis includes the use of the Boussinesq-type wave model MIKE 21 BW, the 3D panel model Harberth, and specific tools dedicated to dynamic mooring analysis (*DMA*).

The waves in the near vicinity of the project area are determined using the non-linear MIKE 21 BW (Boussinesq) model, taking into account the influence of the harbour geometry, bathymetry, and characteristics of the harbour boundaries to compute the inhomogeneous and multidirectional wave field at the berth. This wave model is capable to reproduce the non-linear wave profile, infragravity waves and other non-linear wave-wave interactions. The presence of the 3D shape of the ship, however, cannot be directly incorporated in the wave model. Instead, time-dependent results of the numerical wave model at the position of the hull of the ship are used as boundary conditions to the Harberth panel model in order to determine the scattering

of the incident waves by the presence of the ship. The computation of this scattering is performed by the program Harberth with a linear wave model, which is also applied to compute the interaction of the moving body and the hydrodynamic field. The outcomes of Harberth are hydrodynamic coefficients and wave exciting forces and moments acting on the ship.

This information can be applied in *DMA* software to assess the dynamic behaviour of the moored ship by taking into account the external forces (i.e. waves, winds, currents), characteristics of the mooring lines and fenders, and viscous damping. Finally, the computed body motions and mooring loads are compared with the limits for loading/unloading operations and safe mooring requirements, resulting in the expected downtime of the port due to the considered environmental conditions. The general modelling procedure is summarized below:

Ocean waves
↓
Wave propagation without the ship
Surface elevations, pressures and fluxes in the harbour
↓
Definition of velocity and pressure profile
Undisturbed wave characters at the hull
↓
Wave diffraction around the ship (Harberth model)
Wave forces on the ship
↓
Interactions of the ship and mooring system
(DMA software)
Ship motions and mooring forces

An advantage of using Boussinesq equations to solve the wave propagation problem is that the vertical dimension is eliminated by expanding the velocity potential in a polynomial in terms of kd (local wave number times local water depth). So both high-frequency and low-frequency non-linearities are preserved within 2D equations. However, numerical issues are usually associated to operational Boussinesq-type wave models, such as the reduction of cross-terms in the model equations to reduce instabilities, user defined sponge and porosity layers to determine wave energy absorption/reflection/transmission at boundaries, and other general numerical instabilities. For example, Van der Wel (2011) reported unrealistic eddies with high velocity magnitude generated by Mike 21 BW on simulations of wave penetration in a harbour. Royal HaskoningDHV had also experienced such model instabilities in the past, especially in simulations of extreme offshore wave conditions that are relevant in the assessment of mooring issues. Besides undesirable impacts on the outcomes of the study, such instabilities can directly impact project schedules.

A sequence of undesired experiences with the Boussinesq-type model motivated Royal HaskoningDHV to investigate the feasibility of using the wave model SWASH in harbour penetration studies. A general description of SWASH is provided in section 2.1. In principle the SWASH model is capable to resolve in a robust way the relevant processes involved in wave penetration studies, being very likely competitive with the extended Boussinesq-type wave models in terms of robustness and the computational resource required to provide reliable model outcomes in challenging wave and flow conditions. Thus, the SWASH model can be seen as an attractive alternative to the operational Boussinesq-type wave models [User manual SWASH, 2014].

For linking SWASH and the 3D boundary-integral model Harberth, the computed wave pressures and particle velocities need to be interpolated to pre-defined locations along the hull of the floating body. Harberth can perform these transformations using Mike 21 BW model results, creating time series of pressures and flow velocities at the required points [Mike21-Harberth User Manual, 2007]. A similar tool to convert SWASH model results into Harberth input files is not available, so the model cannot be easily incorporated to the DMA modelling chain.

The aim of this project is to combine the numerical wave model SWASH and the 3D diffraction model Harberth in order to calculate forces and moments acting on a ship exposed to a complex wave field. Besides developing a program to interpolate SWASH model results into Harberth model input file format, there are more fundamental targets: i) to investigate the influence of numerical definitions considered in the wave modelling on the computation of forces on ships (e.g. number of vertical layers, horizontal grid resolution); ii) perform an analytical investigation of the background of the approach, identifying the components that govern the accuracy of the results; iii) to verify the results obtained with SWASH and Harberth against computations with other tools and data measured in model tests.

The analysis of the dynamic behaviour of the moored ship will not be covered in this MSc project.

1.3 Research question and objectives

Based on the settings described in the previous sections, the following research question is defined:

To which extent can the SWASH wave model and the Harberth model be combined in order to accurately compute wave forces acting on moored ships?

To answer the research question, the objectives listed below must be accomplished:

- Analyse the overall approach identifying the contribution of the different steps and associated assumptions/simplifications to the accuracy of the calculations;
- Develop a coupling tool to combine the wave model SWASH and the 3D diffraction model Harberth in order to compute wave forces acting on floating bodies;
- Investigate the influence of SWASH model definitions in the predictions of forces acting on moored ships;
- Validate the combination SWASH/Harberth for the computation of the wave fields and resulting forces acting on a moored ship.

1.4 Research approach

Regarding the combination of the wave model SWASH and the panel model Harberth, three possible sources of inaccuracy to the overall approach are indicated:

1. the wave modelling with SWASH;
2. the coupling tool used to combine SWASH and Harberth;
3. the computation of wave forces with Harberth model.

An evaluation of the influence of each contributor to the overall approach is the core of this project. In view of that, the project is divided in the general steps listed below:

- Review of theory and numerical tools
  - Description of the SWASH model
  - Analytical description of the Harberth model
- Model preparation
  - Wave model set up (SWASH simulations)
  - Development of coupling tool to use SWASH results as input to Harberth
  - Sensitivity analysis
- Validation
  - Verification of the results of the wave model against the measured datasets
  - Extension of coupling tool to handle 3D SWASH results
  - Comparison of modelled and measured forces acting on the ship

The flowchart presented in Figure 1.1 gives an overview of the project. In the following subsections more detailed information is provided for the individual items.

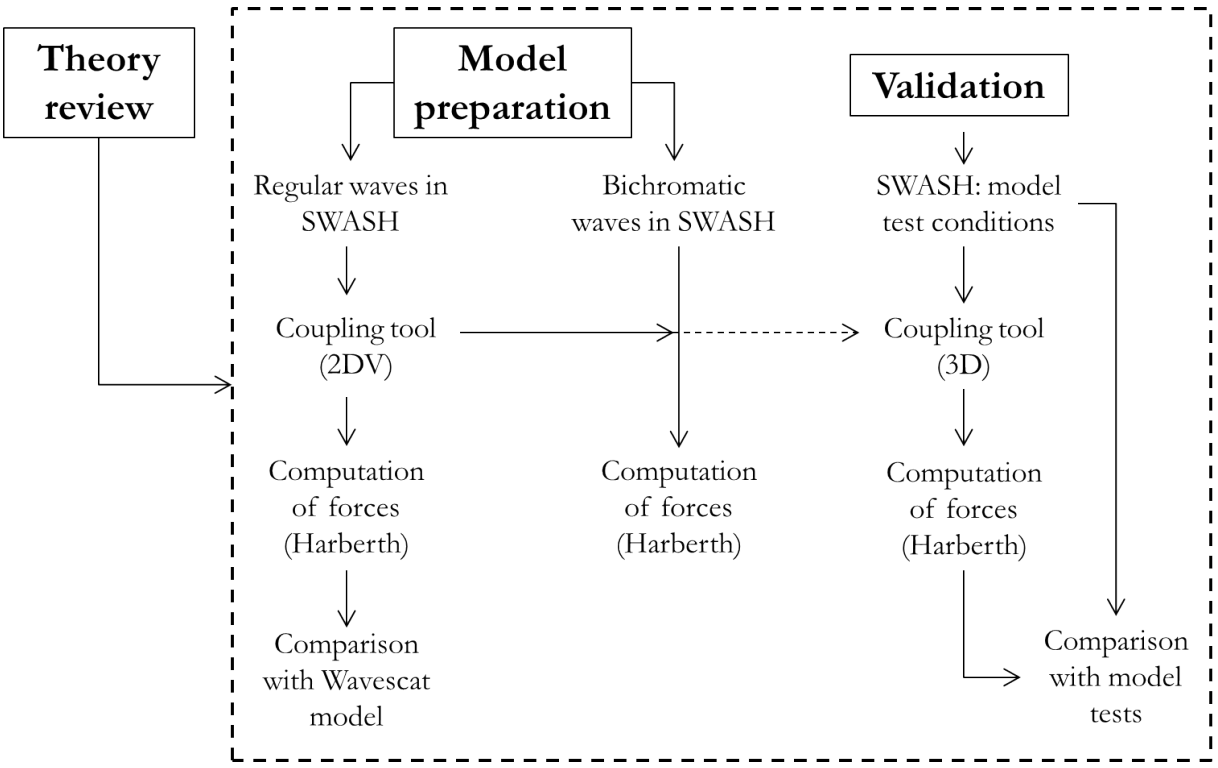

FIGURE 1.1: Research approach overview.

1.4.1 Literature/theory review

In order to attain the overall objectives of the study, an understanding of the relevant physical processes, modelling tasks and the commonly adopted practices is required. Special attention is given to comprehend and describe the functioning of the Harberth model, including its procedures to compute the forces, as well as the assumptions and limitations incorporated in the analysis.

1.4.2 Model preparation

A general validation of SWASH for different wave and flow situations is provided in literature. These references indicate that accuracy is related to model definitions (e.g., computational grid resolution, number of layers, boundary conditions and numerical methods employed) and characteristics of the modelled wave/flow conditions (e.g., relative water depth kd, degree of non-linearity). SWASH model settings can be directly related to the required computation

time for the simulations, therefore a trade-off between accuracy and computation efficiency is of interest, specially for engineering applications.

A series of systematic tests considering regular and bichromatic waves and different model settings is done with SWASH. The results of these tests provide insight on the relations between the modelled wave conditions, numerical model definitions, and the expected accuracy of the results.

A program referred as coupling tool is developed to read the SWASH model outputs and write Harberth input files. The proposed modelling chain (SWASH + coupling tool + Harberth) is then applied to compute forces acting on a moored ship for the different wave model definitions.

Firstly systematic tests with regular waves are considered. For these tests more elementary results are expected, leading to an insightful analysis of the performance of the wave model and the influence of assumptions and simplifications incorporated in the coupling procedure. The computed first- and second-order wave loads are compared with each other and with results obtained with other independent tools. These assessments give insight on the sensitivity of the computed forces to certain definitions, such as, for instance, the determination of the vertical profile of wave quantities when different number of layers are considered in the SWASH model.

A second set of tests considers bichromatic wave conditions. The accuracy of the wave simulations with different wave model definitions are verified against the analytical solutions. Accordingly, the coupling tool is applied so the simulated wave information is provided to Harberth model. The forces and moments acting on a moored ship due to the bichromatic waves are analysed distinguishing first- and second-order contributions and different oscillating frequencies. These results are interpreted but the consistency against other numerical tools is not assessed.

1.4.3 Validation

Besides comparing test results with other modelling tools, the overall approach including the SWASH model, the coupling tool and Harberth, is also verified against results of model tests.

The model tests were carried out in 2003 at the directional wave basin Vinjé of WL|Delft Hydraulics (Deltares) using a scale of 1:100 and a modelled uniform water depth of 20m (prototype scale). Different wave conditions and exposure of the ship were considered (i.e. ship in open water and into a simple rectangular open basin). The measured datasets include time series of water surface elevation at different locations of the basin and wave forces acting on a restrained ship in six degrees of freedom.

The characteristics of the basin are mimicked in a SWASH model and its results are verified against wave measurements on different locations. Once consistent, wave results are applied to

compute the forces acting on the moored vessel. This requires the extension of the coupling tool to handle 3-dimensional SWASH results in large output files. Finally, forces computed with the modelling chain including SWASH and Harberth are compared with the measured forces for different test cases.

Although different sources of inaccuracy may be involved in the comparisons between the results of the numerical models and the model tests, up to a certain extent the findings attained in the previous phases of the project can be used to interpret the validation outcomes. After all, the validation phase gives insight in the possibility of using the adopted computation approach in practical engineering applications.

Chapter 2

Review of theory and numerical tools

In this chapter general aspects regarding waves in coastal areas and the response of ships on waves are covered. Special attention is given to the theory implemented on the numerical tools applied in this study, including the wave model SWASH and the diffraction models Harberth and Wavescat, which are used to compute wave forces acting on moored ships.

2.1 Wave modelling

Sorting the various waves by their frequencies gives an overview of the wave types that can be encountered in oceanic and coastal waters (Figure 2.1). Wave periods vary from seconds up to 24 hours. In this study the frequency range between wind generated waves (periods longer than 1 second) and infragravity waves (periods between 30 and 300 seconds) is of interest.

Irregular sea and swell waves with small differences in wave frequency are known to propagate in groups of higher and groups of lower waves due to the modulation of wave height. Non-linear interactions of the incident modulated short waves generate longer waves with the frequency of the wave groups. These long waves are referred as bound infragravity waves, which are phase locked (*bound*) and in anti-phase with the wave groups. Their amplitude mainly depends on local conditions (i.e., water depth) and characteristics of the short wave spectrum (i.e. total wave energy and how it is distributed along frequencies and directions).

Free infragravity waves are generated when the bound infragravity waves are released (e.g., after short wave breaking in the surfzone and due to depth changes) and by the variation of the wave breaking point due to wave grouping (surfbeat mechanism). Other mechanisms can also induce the generation of free waves on the infragravity frequency range, such as varying

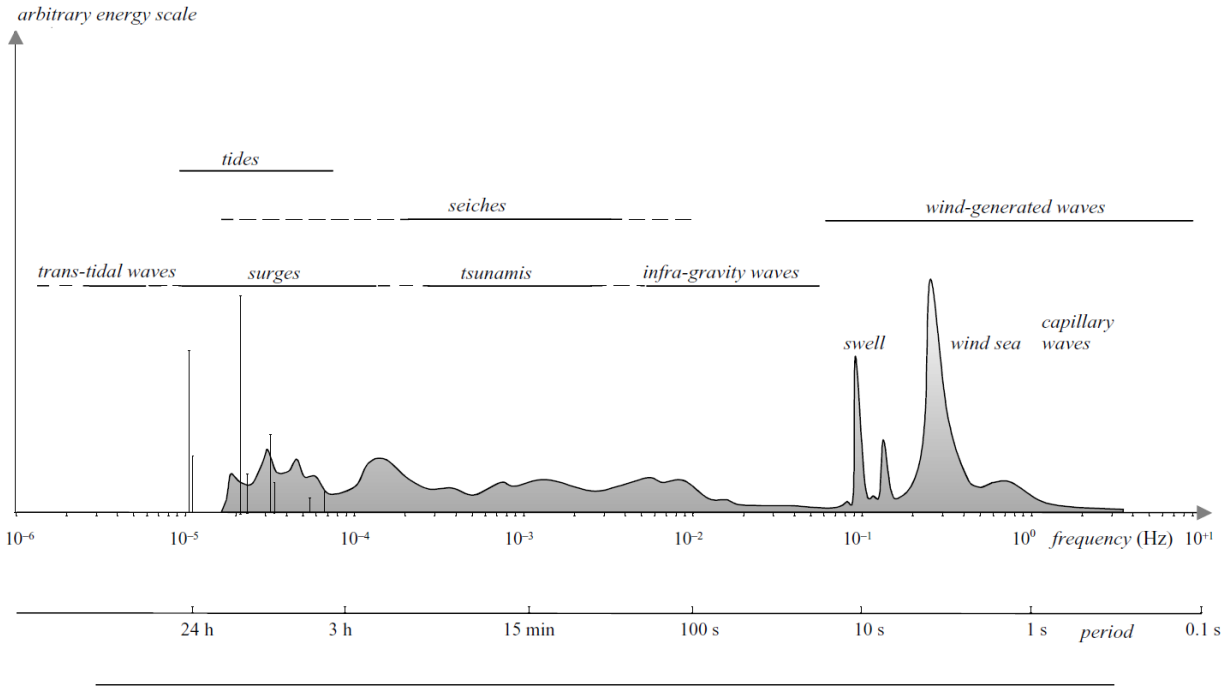

FIGURE 2.1: Frequencies and periods of the vertical motions of the ocean surface (from HOLTHUIJSEN, 2007).

wind set-up in shallow coastal waters, local atmospheric pressure changes, internal waves and tsunamis. In coastal areas free waves travel with the long wave celerity ($\sqrt{gd}$) and can reflect at the shoreline. The reflected free infragravity waves may either propagate towards deeper water (leaky waves) or remain trapped to the nearshore by refraction (edge waves). The characteristics of free infragravity waves have large dependency on local surroundings, i.e. shelf and shoreline topography.

Even with relatively small amplitudes, infragravity waves can influence considerably the behaviour of moored ships because they can induce sloshing-type modes in the basin and the associated frequencies overlap the range of natural frequencies of the moored ship. Thus, a proper assessment of the generation and nearshore transformation of infragravity waves in the surroundings of harbours is of utmost importance to the design of the mooring facilities and determine practical aspects of port operations. Here the objectives of coastal and port engineering come together: it should be possible to use the same theories for the prediction of harbour oscillations due to wave-group forcing as for the computation of infragravity waves near a beach.

Three types of numerical models are usually applied on simulations of infragravity wave generation and propagation: Surf beat models; Boussinesq models and non-hydrostatic models. Surf beat models compute infragravity waves by combining a phase-averaged wave driver model, which provides the wave forcing at the scale of the wave groups, and a shallow water model that accounts for the generation and nearshore transformation of the infragravity waves. Boussinesq and non-hydrostatic models are phase resolving, accounting for the relevant nearshore processes

(e.g. shoaling, refraction, diffraction, reflection, triad interactions and wave breaking), and therefore give a potentially accurate but computationally expensive approach.

2.1.1 SWASH model

Over the past decade, strong efforts have been made at Delft University to advance the state of wave modelling for coastal engineering applications. Within other achievements, these efforts resulted in the newly developed non-hydrostatic model SWASH (with the acronym standing for *Simulating WAves till SHore*). SWASH is intended to be used for simulating the transformation of surface gravity waves and shallow water flows in coastal regions up to the shore in an efficient and robust way [Zijlema et al., 2011]. A more detailed description of SWASH model is provided in Appendix A.

Even with only 2 or 3 vertical layers the model can accurately predict the evolution of short waves propagating in intermediate and shallow waters. The variations in total and incoming infragravity wave heights are also represented by SWASH, accordingly reproducing the phenomena associated with the evolution of those waves in the nearshore (i.e., shoaling of bound infragravity waves, shoreline reflections, phase lag between the wave envelope and the incoming infragravity waves, nonlinear interactions and the occurrence of infragravity wave breaking) [Rijnsdorp et al., 2014].

Zijlema et al. (2011) present a series of verifications of the SWASH model for generic wave and flow features which are expected to be encountered in most nearshore-related applications, including well-controlled laboratory conditions and cases for which analytical solutions are provided. The model with three non-equidistant vertical layers exhibits accurate wave dispersion up to $kd \approx 16$ when linear progressive waves are involved. Using two equidistant layers, accurate propagation of progressive waves is retained for $kd \leq 7.7$, which includes typical values in most nearshore applications [SWASH User Manual, 2014].

2.2 Interaction of waves and ships

The dynamics of rigid bodies due to fluid motions is governed by the combined actions of different external forces and moments (e.g. wave forces, wind forces, current forces, fender and mooring lines forces) and the inertia of the bodies themselves. Notice that the focus of this project is on the determination of wave forces acting on ships moored at areas subject to complex wave processes.

The motions of a ship, just as for any other rigid body, can be split into three mutually perpendicular translations of the center of gravity, G, and three rotations around G. Figure 2.2 presents

the definitions of the basic ship motions and the body-bound coordinate system $G(x_b; y_b; z_b)$ with the origin is the center of gravity of the body. The positive x direction is towards the bow, the positive y direction is towards the portside, and z is positive upward. The signs of the rotations are right handed.

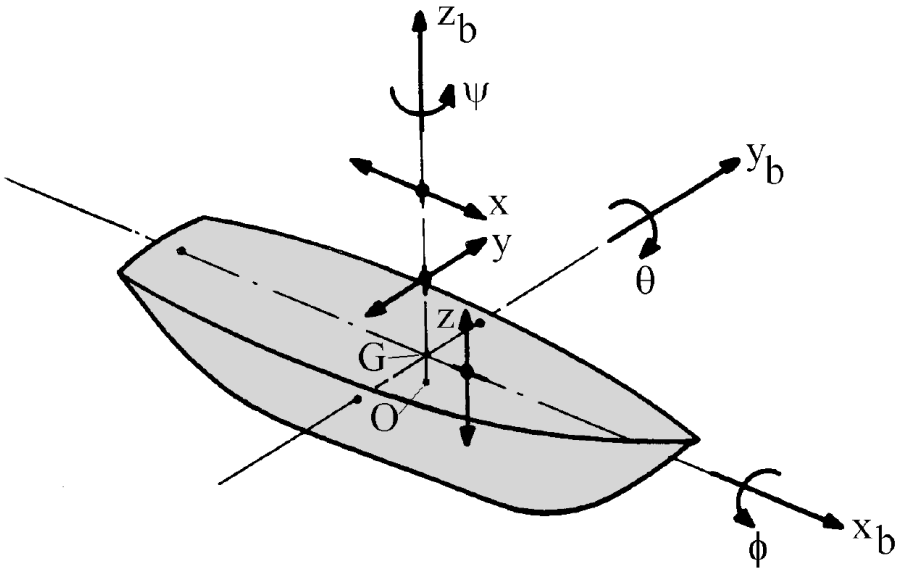

FIGURE 2.2: Body–bound coordinate system $G(x_b; y_b; z_b)$. (From JOURNÉE AND MASSIE, 2001).

To define the motions of a body in the earth fixed (EF) coordinate system, both its position and its orientation needs to be known. This can be described in a 6 component vector, which is illustrated in Figure 2.2. The first three components determine the movements of the centre of gravity of the body:

- Component 1 (surge) is positive from stern to bow (x);
- Component 2 (sway) is positive from starboard to portside (y);
- Component 3 (heave) is positive from keel towards deck (z).

Three rotation angles are used to specify the movements around the centre of gravity of the body. The order in which the rotations are applied is:

- Component 4 (roll) is a rotation around the surge axis (ϕ). Starboard down is positive;
- Component 5 (pitch) is a rotation around the sway axis (θ). Bow down is positive;
- Component 6 (yaw) is a rotation around the heave axis (Ψ). Bow to portside is positive.

The rigid body's equation of motions follow from Newton's second law. The vector equations for the translations of and the rotations about the center of gravity are respectively given by:

$$\vec{F} = \frac{d}{dt}\,(m\vec{U}) \qquad and \qquad \vec{M} = \frac{d}{dt}\,(\vec{H}) \tag{2.1}$$

in which:

$\vec{F}$ = resulting external force acting in the center of gravity (N)
m = mass of the rigid body (kg)
$\vec{U}$= instantaneous velocity of the center of gravity (m/s)
$\vec{M}$= resulting external moment acting about the center of gravity (Nm)
$\vec{H}$= instantaneous angular momentum about the center of gravity (Nms)
t = time (s)

If the system is linear, the forces acting on a body subject to waves can be computed based on the superposition of: 1) the forces resulting from movement of the rigid body in still water (hydromechanic forces and moments); and 2) the forces on the restrained body in waves (wave exciting forces and moments). This is an important assumption usually applied in the calculation of the loads on floating bodies. Accordingly, the motions of the body in six degrees of freedom can be expressed in matrix form as:

$$\begin{gathered}\frac{d}{dt}(\rho\nabla\cdot\dot{\vec{X}}) \;=\; \rho\nabla\cdot\ddot{\vec{X}} \;=\; \mathbf{M}\cdot\ddot{\vec{X}} \\ \mathbf{M}\cdot\ddot{\vec{X}} \;=\; \vec{F_h} + \vec{F_w}\end{gathered} \tag{2.2}$$

in which:

$\vec{X}$ = vector of body motions
ρ = density of water (kg/m^3)
∇ = volume of displacement of the body (m^3)
$\mathbf{M}$ = inertia matrix (kg);
$\vec{F_h}$ = hydromechanic forces and moments (N and Nm)
$\vec{F_w}$ = exciting wave forces and moments (N and Nm)

The motions of the floating body induces hydrodynamic reactions that generate a time-dependent pressure field around the body. The integration of the pressures in the required direction provides the hydrodynamic forces or moments (F_h). These loads can be expressed in terms of frequency-dependent potential mass and damping coefficients, computed with relatively simple frequency-domain computer programs based on potential theory.

Loads in-phase with the body acceleration give the potential mass (or inertia) coefficients. This coefficient has the dimension of mass, being the so-called the hydrodynamic mass or added mass. The hydrodynamic reaction in this case resembles a standing wave system and does not

dissipate energy from the motions. Loads in-phase with the body velocity provide the wave (or potential) damping coefficients. This hydrodynamic reaction corresponds to progressive waves propagating radially from the body, withdrawing energy and damping the motions. In a linear system the so-called wave damping is proportional to the velocity of the moving body.

A motion mode can cause a force in that same direction (e.g. heave motion causing a force in the direction of the z-axis), but also in different directions. This introduces what is called coupling between motions or between the hydromechanic forces and moments. The coupling of ships motions can be split into symmetric components about the vertical-longitudinal plane of symmetry (surge, heave and pitch) and anti-symmetric components (sway, roll and yaw). Symmetric and anti-symmetric motions do not have any effect on each other. Although, they can be coupled when external elements are influencing the motions (e.g. effects of anchor lines).

Boundary-integral 3D diffraction models (e.g. Wavescat and Harberth) can handle the radiation problem by computing potential flow resulting from body motions on different modes. The hydromechanic forces (F_h) are computed by integrating the pressures of the radiation problem along the 3D hull of the vessel. Similarly, the wave exciting forces (F_w) result from the integration of the total wave pressures along the hull. A detailed description of these forces as considered in Harberth and Wavescat models is given in the subsections 2.2.1 and 2.2.2.

An additional hydromechanic load is the restoring *spring* term, in-phase with the displacement of the body. This term is not directly related to the hydrodynamic reactions due to motions, but is an effect of the body out of its equilibrium position. The *stiffness* coefficient is obtained from A_w (area of the waterline) and S_w (first order moment of the waterline), both related to the geometry of the floating body. It is also possible to obtain the stiffness coefficients from static experiments. For free floating bodies the restoring term applies only for heave, roll and pitch motions.

By replacing the hydromechanic forces (F_h in Equation 2.2) by the above mentioned coefficients, the equation of motion in six degrees of freedom in the frequency-domain is obtained:

$$(\mathbf{M}+\mathbf{a})\vec{\ddot{X}} \;+\; \mathbf{b}\vec{\dot{X}} \;+\; \mathbf{C}\vec{X} \;=\; \vec{F_w} \tag{2.3}$$

in which:
$\mathbf{a}$ = matrix of frequency-dependent potential mass coefficient (kg);
$\mathbf{b}$ = matrix of frequency-dependent potential damping coefficient (kg/s);
$\mathbf{C}$ = matrix of hydrostatic restoring coefficient (kg/s^2).

In time-domain, the motions on a given time are influenced by the motions before this interval. The reaction force due to the accelerating body is also expressed in terms of an added mass coefficient, while the 'memory' is included in simulations with the so-called retardation functions.

These coefficients can be calculated using time-domain computer programs based on potential theory (i.e. direct approach), or alternatively using the frequency-dependent added mass and damping coefficients. The equation of motions in time domain is discussed in more detail on Section 2.2.1.2.

Viscous effects such as skin friction and vortices around the corners of the hull can introduce additional damping to the body motions. Viscous damping coefficient cannot be calculated with a potential flow model, therefore when relevant a viscous damping coefficient is prescribed explicitly. Specially for sway, heave, pitch and yaw motions of ships, viscous effects are sufficiently small relative to the potential damping and can be neglected. However, for surge and particularly roll the potential damping is generally small, so the contribution of viscous effects can be relevant to the overall damping of these motion modes.

With the mass matrix of the ship defined, as well as the hydromechanic (F_h) and wave exciting forces (F_w), the equation of motions of the ship can be integrated on time. Other forces such as the effect of a mooring system, fenders, winds and currents can be included in those computations as external source terms. The results of the integration are time records of ship motions and forces in mooring lines and fenders. These outcomes can be compared to the allowable motions and forces for an economic loading and safe mooring. Finally, the expected downtime of the port with respect to wave action on moored ships can be determined.

2.2.1 Harberth model

Harberth is a time-domain boundary-integral diffraction model developed at Delft University of Technology [Van der Molen, 2006]. The model calculates the scattering of the incident wave field by the presence of the ship using as input time-dependent undisturbed wave characteristics at the position of the hull. Harberth also deals with the hydrodynamic reactions due to motions of the ship in the different modes. From the results of these computations hydrodynamic coefficients, retardation functions and wave forces acting on the ship over time are derived. Eventually these results can be applied in a dynamic mooring analysis (DMA), so the complex interaction between wave forcing, harbour layout and the dynamic response of moored vessels is resolved.

A modelling approach consisting of a Boussinesq-type wave model and the time-domain panel model to calculate the wave forces on a moored ship has been verified and validated for various cases, including comparison with model test experiments, prototype measurements and computations with a frequency-domain panel model. The results of these comparisons indicate that the time-domain methods applied in Harberth are able to deal with non-linear input signals of incident waves for the computation of the scattering of waves around the floating body [Van der Molen, 2006; Van der Molen & Wenneker, 2008].

2.2.1.1 Linear potential theory

The incident waves provided as input to Harberth simulations are usually computed with non-linear wave models able to reproduce the relevant physical processes involved in wave penetration in harbours (e.g. Boussines-type models and SWASH model). The hull of the floating body, however, is not included in the non-linear wave model. The interactions between the body and the surrounding fluid are computed by Harberth based on linear potential theory[1], which is in most cases adequate for predicting the hydrodynamic interaction between a floating structure and waves in a protected region where mild slope waves are to be expected.

In linear potential theory all but the linear terms of the free surface condition, the kinematic boundary condition on the body and the Bernoulli equation are neglected. A general statement on when these assumptions are not valid anymore is not clearly defined, although three requisites concerning the use of linear potential theory might be considered for judging the applicability for an specific situation:

1. [wave height/water depth] and [wave height/wave length] are small, i.e. the shape of the wave is close to a sine wave and not too non-linear;
2. wave height is small compared with the body dimensions, i.e. there are no effects of bow slamming, green water on deck, etc.
3. viscous or turbulence effects are small, i.e. drag and additional damping due to these effects can be neglected.

The first requisite is met as long as the parameter ($kA/\tanh kd \ll 1$), where A is some measure of wave amplitude, k is the wave number, and d is the water depth. This parameter is proportional to the Stokes ratio, which is further discussed in Chapter 3, and gives the largest ratio between a linear and a non-linear term in the free surface boundary condition. When the ratio is small, neglecting the non-linear terms is justified. In deep water $\tanh kd = 1$, so the non-linearity relates only to the wave steepness, while in shallow water the condition becomes more restrictive (Bingham, 2000).

Assuming that the water motions due to the scattering of incident waves around the hull of the body are relatively small perturbations on the incident waves, the non-linearities on the scattered waves can be neglected. If the body motions are sufficiently small, which is usually the case in harbours, the radiated waves are also small. In this case, both the scattering and radiation problems can be treated using the linear potential theory. Otherwise, alternative tools

[1]The derivative of the potential Φ in a given direction is the velocity component in that direction, while the time derivative of the velocity potential is the dynamic pressure.

should be considered, such as fully nonlinear panel models, CFD models or RANS models, which are much more computationally extensive and more difficult to set up.

If the body motion remains small, the potential around a floating body (Φ) can be approximated with the superposition of the potentials due to the undisturbed incoming wave ϕ^I, the potential due to the scattering of the incoming wave around the restrained body ϕ^S, and the radiation potentials due to hydrodynamic reactions induced by the six body motions ϕ^j:

$$\Phi(x, y, z; t) = \phi^I + \phi^S + \sum_{j=1}^{6} \phi^j \tag{2.4}$$

in which:

ϕ^I = incident undisturbed wave potential

ϕ^S = scattered wave potential (diffraction of the incident waves about the restrained body)

ϕ^j = radiation potentials due to the moving body in the j-mode

The incident wave potential ϕ^I is calculated with a non-linear method capable to resolve waves on variable bottom topography and the effects of different boundary conditions (in this case the SWASH wave model). All relevant wave processes are properly handled in those simulations, such as wave refraction, diffraction, reflection, transmission through structures, dissipation due to breaking and bottom friction. Further, the occurrence of bound harmonics in the incident waves have a great influence on the behaviour of the ship and therefore should be accurately determined by the non-linear wave model. The ship's hull, however, is disregarded in the incident wave computations.

The scattered waves due to the diffraction of the incident wave field by the ship (ϕ^S) and the radiated waves due to the ship movements (ϕ^j) are computed separately using the 3D panel-based time-domain diffraction model Harberth, which applies the linear potential theory.

The linear potential model considers a body floating in a fluid assumed to be incompressible, inviscid, homogeneous, irrotational and without any effects of surface tension. The model domain $\mathcal{D}$ is bounded by the body surface $\mathcal{H}$, the fluid surface $\mathcal{F}$ and the horizontal sea floor $\mathcal{B}$. Γ is the intersection between the body and the fluid surface. The coordinate system is a right-handed system with the origin at the still water level and the z-axis is positive upwards (figure 2.3). The body is able to make any arbitrary motion $\vec{X}$ with six degrees of freedom, albeit motions are assumed to be small, so that linear approximations are valid [Van der Molen & Wenneker, 2008].

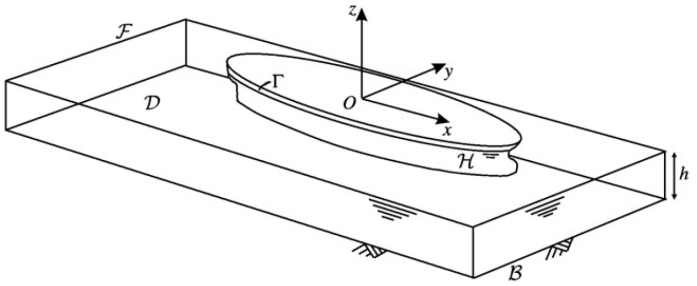

FIGURE 2.3: Definition sketch of the floating body in the computational domain (from VAN DER MOLEN & WENNEKER, 2008).

The simulated velocity potentials (ϕ^S and ϕ^j) share a number of requirements and boundary conditions in the fluid:

$$\nabla^2\phi = \frac{\partial^2\phi}{\partial x^2} + \frac{\partial^2\phi}{\partial y^2} + \frac{\partial^2\phi}{\partial z^2} = 0 \quad \text{(Continuity condition or Laplace equation)}$$

$$\frac{\partial\phi}{\partial z} = 0 \quad \text{for: } z = -h \quad \text{(Sea bed boundary condition)}$$

$$\left.\begin{array}{l} \frac{\partial^2\phi}{\partial t^2} + g\frac{\partial\zeta}{\partial t} = 0 \\ \frac{\partial\phi}{\partial z} = \frac{\partial\zeta}{\partial t} \end{array}\right\} \frac{\partial^2\phi}{\partial t^2} + g\frac{\partial\phi}{\partial z} = 0 \quad \text{for: } z = 0 \quad \text{(Free surface boundary condition)} \tag{2.5}$$

$$\lim_{R\to\infty} \phi = 0 \qquad \text{(with } R \text{ the horizontal distance from the body)}$$

The condition at the sea bed is a no-leak condition. The linearised free-surface condition follows from the assumptions that the pressure at the surface is constant and that water particles do not pass through the free surface. The wetted surface of the body is treated differently in the solution of the diffraction and radiation problem.

The diffraction problem is computed for the restrained ship by prescribing normal velocities along the submerged hull (i.e. sources and sinks). The normal velocities in the scattered wave oppose the normal velocities in the incident wave, so that the boundary condition on the hull $\vec{V} \cdot \vec{n} = 0$ is fulfilled, where $\vec{n}$ is the outward vector normal to the surface. VAN DER MOLEN (2006) has shown the ability of the diffraction model to treat non-linear incident waves as input conditions on the hull of the ship. The following boundary condition is specified for the diffraction model (the subscript n denotes the derivative of the potential in the direction normal to the panel, which is the velocity normal to the panel):

$$\phi_n^S = -\phi_n^I \quad \text{(along the submerged hull)} \tag{2.6}$$

The approach adopted in the treatment of the radiation problem (ϕ^j) is linear, so the forces associated to the hydrodynamic reaction are linearly related to the history of ship movements. Accordingly, the retardation functions and hydrodynamic coefficients can be derived beforehand by determining the hydrodynamic reaction due to the body making an impulsive movement in the j-mode in initially still water (at $t = 0$). After $t = 0$ the body is again fixed to its position, only the fluid surface has been disturbed.

The radiation potential ϕ^j is divided into an impulsive part and a time-varying part due to the disturbance of the free surface:

$$\phi^j(x, y, z; t) \;=\; \psi^j(x, y, z) \cdot V(t) \;+\; \chi^j(x, y, z; t) \cdot \Delta x \tag{2.7}$$

Taking an impulsive movement of $\Delta x = 1$ during $\Delta t \to 0$, the velocity $V(0) = \infty$ and $V(t > 0) = 0$. So the equation for the radiation potential becomes:

$$\phi^j(x, y, z; t) \;=\; \psi^j(x, y, z) \cdot \delta(t) \;+\; \chi^j(x, y, z; t) \tag{2.8}$$

in which:
ψ^j = impulsive potential
χ^j = time-varying potential
δ = Dirac delta function: $\delta(0) = \infty$; $\delta(t) = 0$; $\int_{-\infty}^{\infty} \delta(t)dt = 1$

The boundary conditions applied for the decomposed potentials are similar to the conditions listed in 2.5: the Laplace and free surface boundary conditions apply for χ^j, and the two potentials χ^j and ψ^j tend to zero far away from the body. The additional considerations are included:

$$\psi^j = 0 \qquad \text{for: } z = 0$$

$$\frac{\partial \psi^j}{\partial n} = \begin{cases} n^j & \text{along the body surface } (\mathcal{H}) \\ 0 & \text{on the bottom} \end{cases} \tag{2.9}$$

$$\frac{\partial \chi^j}{\partial n} = 0 \quad \text{along the body and bottom surfaces}$$

The boundary condition at the surface of the rigid body ($\mathcal{H}$) is taken such that the velocity of a water particle is equal to the velocity of the watertight body point itself (n^j).

Reflections of scattered and radiated waves against other structures such as a nearby quay wall can be incorporated in the Harberth panel model by including additional no-leak boundary conditions (i.e. velocities normal to the quay wall are equal to zero). Although, in this case the

incident waves are not prescribed along the structure because reflections against the quay are already included in the wave model.

To solve the potentials ϕ^S and ϕ^j (the last decomposed into ψ^j and χ^j) a continuous distribution of single sources is considered along the body surface. The mean wetted surface of the body is divided into N panels where the sources are assumed to be constant. The normal velocity requirement can be met only at one point for each panel. In Harberth this point is the centroid of the panel, referred as collocation point.

Substitution of the potential and the boundary condition in Green's theorem leads to integral equations for the two potentials. The volume problem is converted into a surface problem, from which the solutions are derived considering the boundary conditions. For the determination of the potentials ψ^j and χ^j the more efficient direct method is used. For the diffraction problem the indirect source potential formulation is used, which is a common technique in potential theory with the advantage that the velocities in the fluid are more easily obtained.

The problem is schematized such that the potential at a point (x, y, z) on the mean wetted body surface is function of an impulsive source in a point $(\hat{x}, \hat{y}, \hat{z})$ also in the wetted surface. The time-domain Green's function or influence function provides the relation between the impulsive source at $(\hat{x}, \hat{y}, \hat{z})$ and the potential at (x, y, z), satisfying the Laplace equation and boundary conditions. The other impulsive sources $(\hat{x}, \hat{y}, \hat{z})$ along the hull are also in the domain of dependence of (x, y, z), so the same applies.

The discretized equation is transformed into a set of simultaneous linear equations relating the $N \times N$ Green functions, the N source strengths, and the N normal velocity components, which are given as boundary condition along the hull based on the arbitrary time series of incident waves. The set of equations is solved in time providing the unknown source strengths, so then the potential ϕ^S can be determined.

The fluid forces and moments exerted on the body relative to body-fixed axes system $G(x'_b; y'_b; z'_b)$ follows from the direct integration of the pressure (p) over the submerged surface of the body S:

$$\begin{aligned} \vec{F} &= -\int_S \int p \cdot \vec{N} \cdot dS \\ \vec{M} &= -\int_S \int p \cdot (\vec{r} \times \vec{N}) \cdot dS \end{aligned} \tag{2.10}$$

in which:
p = total water pressure: $p = p^{(0)} + \varepsilon p^{(1)} + \varepsilon^2 p^{(2)} + \ldots$;
S = instantaneous wetted surface of the hull, with a constant part 'S_0' up to the waterline and an oscillating part 's' betweeen the static waterline and the wave profile along the body;

$\vec{r}$ = position vector of surface dS_0 on the Body-bound axes system;
$\vec{N}$ = instantaneous normal vector to the surface element dS relative to the body-fixed $G(x_b'; y_b'; z_b')$ coordinate system (with origin at the center of gravity but all times parallel to the axis of the Earth-fixed system).

The orientation of the surface elements of the hull of the body relative to the body-bound coordinate system $G(x_b; y_b; z_b)$ are denoted by the outward pointing normal vector $\vec{n}$. Relative to the body-fixed coordinate system $G(x_b'; y_b'; z_b')$, the normal vector of a surface element becomes:

$$\vec{N} \;=\; \vec{N}^{(0)} \;+\; \varepsilon\vec{N}^{(1)} \;+\; \varepsilon^2\vec{N}^{(2)} \tag{2.11}$$

where:

$\vec{N}^{(0)} = \vec{n}$
$\vec{N}^{(1)} = \vec{\alpha}^{(1)} \times \vec{n}$
$\vec{N}^{(2)} = \vec{\alpha}^{(2)} \times \vec{n}$
$\vec{\alpha}$ = the angular motion vector with components 4, 5 and 6 (roll, pitch and yaw)

The equation for forces (first line of equation 2.10) can be written with the expanded terms. The same applies for the moments, though they are omitted here for brevity.

$$\begin{aligned}\vec{F} = &-\int_{S_0}\int (p^{(0)} + \varepsilon p^{(1)} + \varepsilon^2 p^{(2)}) \quad (\vec{n} + \varepsilon\vec{N}^{(1)} + \varepsilon^2\vec{N}^{(2)})\; dS_0 + \\ &-\int_{s}\int (p^{(0)} + \varepsilon p^{(1)} + \varepsilon^2 p^{(2)}) \quad (\vec{n} + \varepsilon\vec{N}^{(1)} + \varepsilon^2\vec{N}^{(2)})\; ds \\ = \;& \vec{F}^{(0)} \;+\; \varepsilon\vec{F}^{(1)} \;+\; \varepsilon^2\vec{F}^{(2)} \;+\; \mathcal{O}(\varepsilon^3)\end{aligned} \tag{2.12}$$

The hydrostatic force $\vec{F}^{(0)}$ follows from integration of the hydrostatic pressure $p^{(0)}$ over the mean wetted surface S_0. The first and second order forces ($\vec{F}^{(1)}$ and $\vec{F}^{(2)}$, respectively) are treated separately in the next subsections with emphases to the exciting wave forces.

2.2.1.2 First-order wave forces and moments

The total first order oscillatory fluid force $\vec{F}^{(1)}$ relative to the body-bound coordinate system $G(x_b; y_b; z_b)$, including the wave exciting force and the hydrodynamic reaction force, follows from:

$$\vec{F}^{(1)} \;=\; -\int_{S_0}\int (\; p^{(1)} \cdot \vec{n} \;+\; p^{(0)} \cdot \vec{N}^{(1)} \;)\; dS_0 \tag{2.13}$$

The first order pressure $p^{(1)}$ is defined as:

$$\begin{aligned} p^{(1)} &= -\rho \frac{\partial \Phi^{(1)}}{\partial t} - \rho g X_3^{(1)} \\ &= -\rho \left(\frac{\partial \phi^I}{\partial t} + \frac{\partial \phi^S}{\partial t} + \frac{\partial \phi^j}{\partial t} \right) - \rho g X_3^{(1)} \end{aligned} \tag{2.14}$$

The integration of the pressure due to the radiated potentials ϕ^j (decomposed into ψ^j and χ^j) gives the added mass coefficients (determined from ψ) and the impulse response functions (from $\partial\chi/\partial t$). The last term of equation 2.14 gives the hydrostatic restoring forces after first order vertical motions $X_3^{(1)}$, and the second term inside the integral of equation 2.13 take into account the influence of the first order angular motions on the direction of the hydrostatic forces. These are required for the dynamic simulation of the ship motions.

The first order wave exciting forces and moments, which do not have a component relative to body motions and therefore act on the restrained body, are obtained by linearly superposing the Froude-Krylov force and the diffraction force. The Froude-Krylov force is given by the integration of the undisturbed wave pressures over the mean submerged hull. Undisturbed wave pressures are calculated with the wave model and provided as input to Harberth computation. The diffraction force is given by the integration of the pressures in the scattered wave (ϕ_t^S) over the submerged hull (ϕ^S is determined with the linear potential model described in Section 2.2.1.1):

$$\begin{aligned} \vec{F_w}^{(1)} &= \int_{S_0} \int \left(p^I - \rho \frac{\partial \phi^S}{\partial t} \right) \vec{n} \, dS_0 \\ \vec{M_w}^{(1)} &= \int_{S_0} \int \left(p^I - \rho \frac{\partial \phi^S}{\partial t} \right) (\vec{r} \times \vec{n}) \, dS_0 \end{aligned} \tag{2.15}$$

The second order force due to second order wave potential is already included in these forces, because a non-linear wave model is used for the incident waves.

For low frequencies (long waves), the contribution of the diffraction terms to the first order forces is generally small and the total first order forces tends to the Froude-Krilov forces. The relative contribution of diffraction forces becomes larger at higher frequencies for which the wave length becomes short relative to the ship size.

The first order motions of the ship in the six degrees of freedom are obtained by integrating the equation of motion in time. These results are subsequently applied on the computation of second order forces (see subsection 2.2.1.3). The inertia and the linear contributions of the hydrodynamic forces due to the moving body are collected in the left-hand side, and the first

order wave forces calculated for the restrained body are in the right-hand side:

$$(\mathbf{M}+\mathbf{A})\ddot{\vec{X}}(t) \;+\; \mathbf{B}\dot{\vec{X}}(t) \;+\; \mathbf{C}\vec{X}(t) \;+\; \int_0^\infty \mathbf{K}(\tau)\dot{\vec{X}}(t-\tau)d\tau \;=\; \vec{F}(t) \tag{2.16}$$

where $\mathbf{M}$ is the inertia matrix and $\vec{X}$ is the vector of body motions. $\mathbf{A}$, $\mathbf{B}$ and $\mathbf{C}$ are the matrices for the added mass, (linearized) viscous damping and hydrostatic restoring coefficient, respectively. $\mathbf{K}$ contains the impulse response functions, which are calculated based on ϕ^j together with the matrix of added mass $\mathbf{A}$. The external force in this case is the first order wave force ($\vec{F_w}^{(1)}$ = Froude-Krylov force + diffraction force), which was calculated for the restrained body and therefore does not have a component relative to the body motions.

2.2.1.3 Second-order wave forces and moments

Besides first order wave loads at the frequencies of the primary waves and with zero time-averaged and resulting components, mainly anchored and moored floating structures also experience the effects of second order wave forces. These include the so-called mean wave drift force, oscillations at higher frequencies (about two times the frequency of the primary waves) and low-frequency oscillating wave loads (low-frequency wave drift forces) associated to wave groups in irregular wave fields. The later oscillations can induce low-frequency surge motions in moored vessels with the period of the wave groups (in the order of 100 seconds). As mentioned previously for the infragravity waves, exciting forces on this frequency range can potentially convert into mooring problems because they overlap the frequencies of resonance of the ship and mooring system and hydrodynamic damping of motions is relatively low for those frequencies.

The terms associated to the second order forces and moments are calculated simultaneously with the determination of the diffraction force, being products of first order quantities obtained from the calculated incident, scattered and radiated waves, and the ship motions.

As described in the previous subsection, the first order wave forces are calculated considering the body restrained and disregarding the water surface elevation. The second order wave forces are given by the integration of all products of pressure p and normal vector $\vec{N}$ (Equation 2.12) that result in second order contributions over the constant wetted surface 'S_0', and by integration of first order pressures over the oscillating surface 's' (Pinkster, 1980):

$$\vec{F_w}^{(2)} \;=\; (\mathbf{I}) \;+\; (\mathbf{II}) \;+\; (\mathbf{III}) \;+\; (\mathbf{IV}) \tag{2.17}$$

Where the individual contributions refer to:

(I) Relative wave elevation: corresponds to the integral of the first order pressures over the oscillating surface s and is solved by writing the area of the surface element as $ds = dX_3 \cdot d\ell$,

considering that at the water line $-\rho\Phi_t^{(1)} = \rho g\zeta^{(1)}$, and finally substituting the last expression into $p^{(1)} = -\rho g X_3^{(1)} - \rho\Phi_t^{(1)}$. Where $\zeta^{(1)}$ is the water surface elevation due to the incident, the scattered and the radiated wave.

This results in the following term, including the water surface elevation and first order vertical body motions on the pressure integration:

$$-\int_s\int (p^{(1)}\cdot\vec{n})\,ds \quad = \quad -\frac{1}{2}\rho g\int_\ell (\zeta^{(1)} - X_{3,WL}^{(1)})^2\cdot\vec{n}\cdot d\ell \tag{2.18}$$

II) Pressure drop due to first order velocity (second order pressure): the second order pressure at the mean position of the body element follows from Bernoulli's equation, considering the body carrying first and second order motions about its mean position. This pressure contribution is integrated over the mean submerged hull of the vessel.

$$-\int_{S_0}\int (p^{(2)}\cdot\vec{n})\,dS_0 \;=\; -\int_{S_0}\int \left(-\frac{1}{2}\rho\left|\nabla\Phi^{(1)}\right|^2 - \rho\Phi_t^{(2)} - \rho(\vec{X}^{(1)}\cdot\nabla\Phi_t^{(1)}) - \rho g X_3^{(2)}\right)\vec{n}\,dS_0 \tag{2.19}$$

The last term on the right hand side part of the equation 2.19 contains the hydrostatic reaction forces due to second order motions and is ignored here since the computation focus on the wave exciting forces and moments. As mentioned previously, the forces associated to the hydrodynamic reactions induced by ship motions are expressed in terms of added mass and damping forces (or retardation functions).

The second term on the right hand side integral contains the contribution of the second order potentials due to the combined incident, scattered and radiated wave. $\phi^{I(2)}$ is ignored here because the wave model is non-linear and the influence of the second order waves is incorporated on the first order forces. The second order radiated potential ($\phi^{j(2)}$) is excluded from the computation of wave forces and may be accounted for on the definition of the hydrodynamic reaction coefficients, although in Harberth the radiated potential is computed with a linear model and therefore this second order contribution is neglected. The same applies for the second order scattered potential ($\phi^{S(2)}$): the contribution is assumed to be small enough so that it can be neglected and the linear potential model suffices.

The last but one term on the equation is treated separately (see item "III" below). Finally, the following expression is obtained after these considerations:

$$-\int_{S_0}\int (p^{(2)}\cdot\vec{n})\,dS_0 \;=\; -\int_{S_0}\int -\frac{1}{2}\rho\left|\nabla\Phi^{(1)}\right|^2\vec{n}\,dS_0 \tag{2.20}$$

The modulus of the divergence of the total potential ($\nabla\Phi$) give the velocity magnitude due to the incident, scattered and radiated waves. The velocity components along the hull associated to the incident waves are calculated by the wave model and provided as input to Harberth computations.

III) Product of gradient of 1st order pressures and 1st order motion: This term follows from the integration of the second order pressure (see previous item "II").

$$-\rho \int\limits_{S_0} \int \left(\vec{X}^{(1)} \cdot \nabla \frac{\partial \Phi}{\partial t} \right) \vec{n} \, dS_0 \tag{2.21}$$

IV) Products of 1st order angular motions and 1st order inertia forces: A second order force contribution relative to the body-fixed coordinate system arises by taking into account the (first order) rotations of the body. Since angular displacements are the same for all surface elements, the interaction between first order pressures and first order rotations can be written as:

$$-\int\limits_{S_0} \int p^{(1)} \cdot \vec{N}^{(1)} \cdot dS_0 \quad = \quad \vec{\alpha}^{(1)} \times -\int\limits_{S_0} \int p^{(1)} \cdot \vec{n} \cdot dS_0 \tag{2.22}$$

The integral on the right hand side corresponds to the first order fluid forces acting on the body and with respect to the body-bound coordinate system. It includes the hydrostatic restoring force, the wave exciting force and the hydrodynamic reaction force. The gravity force acting on the body is incorporated on this term, resulting on the total first order forces ($\vec{F}^{(1)}$). According to Newton's second law:

$$\vec{F}^{(1)} = M \cdot \ddot{\vec{X}}^{(1)} \tag{2.23}$$

The fourth term (IV) of the second order forces can be written as:

$$-\int\limits_{S_0} \int p^{(1)} \cdot \vec{N}^{(1)} \cdot dS_0 \quad = \quad \vec{\alpha}^{(1)} \times \left(M \cdot \ddot{\vec{X}}^{(1)} \right) \tag{2.24}$$

The derivation of the second order moment is analogous to that followed for the force, but including the arm $\vec{r}$, which is the distance vector on the body-bound coordinate system with origin at the centre of gravity of the body. The final expressions for the second order forces and

moments are:

$$\begin{aligned}
\vec{F_w}^{(2)} =& -\frac{1}{2}\rho g \int_s \left(\zeta^{(1)} - X^{(1)}_{3,WL}\right)^2 \vec{n}\, d\ell + \\
& - \int_{S_0}\int -\frac{1}{2}\rho \left|\nabla\Phi^{(1)}\right|^2 \vec{n}\, dS_0 \; - \; \rho \int_{S_0}\int \left(\vec{X}^{(1)} \cdot \nabla \frac{\partial \Phi}{\partial t}\right) \vec{n}\, dS_0 + \\
& + \; \vec{\alpha}^{(1)} \times \left(M \cdot \ddot{\vec{X}}^{(1)}\right)
\end{aligned} \tag{2.25}$$

$$\begin{aligned}
\vec{M_w}^{(2)} =& -\frac{1}{2}\rho g \int_s \left(\zeta^{(1)} - X^{(1)}_{3,WL}\right)^2 (\vec{r}\times\vec{n})\, d\ell + \\
& - \int_{S_0}\int -\frac{1}{2}\rho \left|\nabla\Phi^{(1)}\right|^2 (\vec{r}\times\vec{n})\, dS_0 \; - \; \rho \int_{S_0}\int \left(\vec{X}^{(1)} \cdot \nabla \frac{\partial \Phi}{\partial t}\right) (\vec{r}\times\vec{n})\, dS_0 + \\
& + \; \vec{\alpha}^{(1)} \times \left(M \cdot \ddot{\vec{\alpha}}^{(1)}\right)
\end{aligned}$$

The velocity potential Φ include the contributions of the incident, the scattered and the radiated wave. On the calculations of second order forces by Harberth, however, only heave, roll and pitch motions are considered. Horizontal motions do not have a restoring component and are not considered to prevent the ship to drift away. Large motions near the natural roll period may lead to inaccuracies, especially if viscous damping is not taken into consideration. Despite part of the motion modes are omitted, the influence of these assumptions is generally not so significant. This is demonstrated by Van der Molen (2006) in comparisons between results of Harberth and the frequency-domain 3D panel diffraction program DELFRAC (Pinkster, 1995), which does include all the motion modes.

The use of first-order wave forces to compute the (first-order) ship motions is supported by the hypothesis that second-order motions are of second order and small in relation to first-order motions. Due to large dynamic magnification of the motions resulting from small damping for low frequency motions, this assumption is in some cases strictly speaking incorrect (Pinkster, 1980). This is specially the case for horizontal low-frequency motions influenced by a mooring system. Heave, roll and pitch motions, however, are generally dominated by first-order contributions.

Additional external force terms representing mooring lines and fenders are omitted by Harberth, though usually the mooring system has limited influence on vertical motions. Nevertheless, Harberth model is mostly applied on calculations involving ships moored to fixed structures such as jetties and quay walls. On these situations body motions are generally not exceptional (i.e. around limits for loading/unloading operations and safe mooring).

2.2.1.4 Numerical issues

A numerical problem associated with the calculation of the diffraction and radiated potentials is the occurrence of so-called irregular frequencies. These correspond to the eigenfrequencies of the fictitious flow problem interior to the body and are known to have detrimental effects on computations with boundary-integral methods. An effective method to reduce the effects of irregular frequencies is to "close" the body by discretizing the free surface interior to the body (i.e. adding a so-called "lid" on the free surface inside the body). This solution is usually applied in frequency-domain panel models, but the numerical implementation in time-domain models as Harberth is more awkward.

Alternatively, by increasing the number of panels the irregular frequencies are not removed but tend be restricted to a narrower band of frequencies. It can be assumed that when the number of panels is sufficiently large and also the time step sufficiently small, the effects of irregular frequencies are reduced. Additionally, for normal hull shapes and without forward speed the irregular frequencies are well outside the range of frequencies of interest for mooring studies.

The occurrence of high-frequency instabilities is another phenomenon related to the discretization of the hull. These instabilities take place if the panels that intersect with the free surface are not vertical, so only small deviations of these angles are acceptable. Apart from the mesh of the hull and other structures, the most important parameters for time-domain computations are the computation time step and the cut-off period of the convolution integrals applied in the scattering and radiation problems (Green function and Retardation periods) [MIKE21-HARBERTH USER MANUAL, 2007].

2.2.2 Wavescat model

A wave field at the sea normally consists of irregular multi-directional waves, however it is often convenient to consider it as a sum of regular wave components. The program Wavescat (CSIR, 2011) is a frequency-domain model that computes wave forces and ship motions associated to regular linear waves. As result the model provides amplitudes and phase differences of harmonic components of forces and motions with respect to the exciting regular waves. The frequency of the individual harmonic components is the same as the frequency of the associated regular wave. These model outcomes are the so-called transfer functions relating the incident wave amplitude and frequency to a response amplitude operator (RAO) and response phase operator (RPO). The total wave force or the total ship motion in time can be obtained by superposition of the contributions of all relevant frequencies and directions.

Wavescat is a boundary-integral equation model based on the frequency-domain free surface Green function. Similarly to the Harberth model described on section 2.2.1, the submerged

hull of the ship and the surfaces of other structures are described by a large number of flat quadrilateral or triangular panels on which the velocity potential is assumed constant. The fluid flow around the floating body is also described by means of velocity potential Φ:

$$\Phi = \overline{\Phi} + \left(\phi^I + \phi^S + i\omega \sum_{j=1}^{6} \chi^j X^j \right) e^{i\omega t} \tag{2.26}$$

where $\overline{\Phi}$ is the effect of the steady potential due to currents or sailing speed; ϕ^I is the incident wave potential based on the linear wave theory as a regular wave with unit amplitude and a given direction; ϕ^S is the scattered wave potential due to the scattering of waves around the floating body and possibly other structures. The radiation potentials are written as the product of potentials χ^j and the body motions $\vec{X}$ in six degrees of freedom.

The model is linear, which means that the computed first-order wave force and the response are proportional to the regular wave amplitude. Although, the steady second-order wave drift force is calculated as well. This mean wave drift force in a regular wave can be used for computations of added resistance of ships sailing in waves and as input for computation of low-frequency body motions due to slowly-varying wave drift forces.

The model Wavescat has been verified against model test measurements and results of numerical calculations obtained with both the frequency-domain panel model DELFRAC (Pinkster, 1995) and the linear time-domain panel model Harberth. The comparisons show that the computed added mass and damping coefficients, motions and drift forces generally agree well with the other computations as well as with the model test data (CSIR, 2011).

2.3 Conclusions

The main conclusions from this chapter are listed below:

- Low frequency excitations with periods in the order of 30 to 300 seconds overlap the resonant frequencies of the moored ships and therefore are especially important regarding the dynamics of the ship and mooring system. Excitation loads on those frequencies are likely associated with wave grouping and, especially in coastal waters, with bound and free infragravity waves.
- The SWASH model takes into account in a robust way all the relevant physical processes involved in short wave propagation and infragravity wave generation in intermediate and shallow waters. The computation times required by SWASH are comparable with the ones associated with operational Boussinesq-type of models for similar applications, although

the latter models are renown to become unstable especially when extreme wave conditions are intended to be simulated. It makes SWASH an attractive tool to be applied on wave penetration studies in harbours when complex wave transformation through intermediate and shallow waters is involved.

- Different numerical tools, with their own assumptions and advantages, are available to assess wave forces acting on moored ships. The problem becomes more difficult to be solved when complex wave processes are involved in the wave penetration and when the resulting wave field is inhomogeneous in the mooring area (which is likely the case in harbour basins). In such cases the outputs of the higher order wave models (e.g. Boussinesq wave models and potentially SWASH model) can be directly applied into the Harberth model in order to compute wave forces acting on the ships. The combination is specially attractive since Harberth inputs and computations are in time-domain, so transformations are not required.

- The Harberth model uses a linear approach and superposes the effects of the incident undisturbed waves, the scattering of waves by the presence of the hull of the ship, and waves radiated from the ship when it is moving. The incident waves are computed with an external tool (e.g., a complex non-linear wave model), which is able to deal with all relevant wave processes but does not take into account the presence of the ship. Incident waves are provided to Harberth as input time series along the hull of the ship and the wave-body interactions (i.e. scattering and radiation) are calculated with a linear potential model in time-domain. This model is expected to be inaccurate when: i) non-linearities on the scattered and radiated waves are relevant (i.e., the scattered and radiated waves are large relative to the water depth and the wave length), ii) the waves height is large relative to the body dimensions (i.e., waterplane area changes considerably on time, effects of bow slamming, green water on deck), and iii) turbulent/viscous effects are considerable. Under such conditions inaccuracies will be incorporated on the results.

- Harberth computes the first-order forces by integrating the first order pressures over the restrained submerged hull (notice that the pressures related to the incident waves are of higher order). The second-order forces are computed considering ship motions induced by the first-order forces. This is a reasonable approximation if the second-order forces are a relatively small correction to the first-order forces, so the ship motions cannot be too large.

- Only free floating heave, roll and pitch motions are considered by Harberth in the computation of second-order forces. The effects of this simplification are not expected to be very significant because in the (fixed) mooring locations ship motions are not expected to be exceptional. Further, the two main components of the second-order forces are only indirectly influenced by the motions, i.e. component I: relative wave height ($X_3^{(1)}$ only

depends on heave, roll and pitch), and component II: second-order pressure due to first-order velocity (the contribution of the radiated potentials $\sum_{j=1}^{6} \phi^j$ to the total potential Φ is incomplete). The other two terms are directly influenced by this simplification, whose effects are expected to increase with the amplitude of ship motions.

- The wave exciting forces are generally the main contribution for the assessment of the dynamic behaviour of a moored ship, including the determination of port downtime due to ship motions and safe mooring issues. However, the forces themselves do not say much about their effects because these are also linked to the mooring structures (arrangement of mooring lines/fenders and the associated stiffness), inertia of the body, potential and viscous damping of motions, etc. These interactions are usually taken into consideration by solving the equation of motions in time-domain. A number of commercial computer packages are able to deal with that.

Chapter 3

Model preparation

A general assessment of the applicability of SWASH considering different model settings and forcing conditions is covered in this chapter. The variation of model settings include horizontal and vertical resolution of the computational grid, and numerical methods applied in the simulations. Additionally, the tests involve regular waves with different wave heights and wave periods, and bichromatic conditions with different primary waves and group characteristics. The simulations are performed in 2DV mode considering a flat bottom. Results obtained with SWASH are compared with analytical solutions.

A computational tool is developed to convert the SWASH model outputs into the input files required for Harberth model simulations. With this tool, the wave quantities predicted by SWASH can be applied in the computation of wave forces and moments acting on a ship. The computed forces are explored in order to verify the consistency and assess the accuracy of the coupling, highlighting possible limits of application of the computational approach combining SWASH, the developed coupling tool and Harberth model.

The tests considering regular wave simulations are treated in Section 3.1. The coupling tool is developed and described in this section (Subsection 3.1.2). The tests with bichromatic waves are presented in Section 3.2.

3.1 Regular waves

The tests with regular waves in SWASH consider a flat bottom 20 meters below the still water level. The results of the regular wave simulations with SWASH were analysed regarding different aspects that may be relevant for practical application on studies of wave penetration on harbours. Further, a program was developed to generate the input files for the Harberth model

based on SWASH output, so that it was possible to evaluate the forces acting on moored ships resulting from the modelled wave conditions.

3.1.1 Wave modelling

Waves are dispersive when travelling in deep and intermediate waters, meaning that the phase speed and wave length are a function of the wave period. The kd number (with k the wave number - $2\pi/L$ - and d the water depth) is a measure of the water depth relative to the wave length. A lower kd value indicates wave propagation in shallower conditions. The vertical variation of wave quantities, such as wave pressure and orbital velocity amplitudes, is directly related to the kd number, being this vertical distribution more homogeneous for lower kd's. Furthermore, this is an important parameter in short wave modelling. Models like SWASH and Boussinesq models are generally less accurate in the simulation of wave conditions with large kd numbers (deep water).

Another relevant aspect in wave modelling is the degree of non-linearity of the wave conditions. This characteristic may be important in SWASH since the implemented boundary conditions are linear and disregard higher harmonics in the generation of the input boundary signal. The relative contribution of non-linear terms associated to the wave propagation is larger for steeper waves (larger $amplitude/wavelength$ or ka), in shallower waters (lower kd) and when waves are bigger relative to the water depth. Non-linear terms make the wave form to be asymmetric about both the horizontal and vertical axis. The non-linear wave profile can be obtained by adding higher order harmonics as a correction to the basic linear harmonic. This is done, for instance, by the theories of Stokes.

The first correction in the Stokes theory is an 'extra' harmonic with half the wave length and wave period of the linear wave, thus propagating with the same phase speed as the primary wave. This correction term is written with the wave steepness raised to the second power, i.e. a second-order correction. The combination of the linear wave and the first correction is the second-order Stokes wave. The Stokes expansion can be continued by including additional harmonics, although rapidly the expressions become very complicated.

The degree of non-linearity of a regular wave condition can be evaluated comparing the free-surface amplitude of the second-order Stokes correction to the primary wave amplitude (Stokes ratio):

$$\frac{a_{2^{nd}order}}{a_{1^{st}order}} \;=\; \mathcal{S} \;=\; ka\,\frac{3-\tanh^2 kh}{4\,\tanh^3 kh} \tag{3.1}$$

It is highlighted that the theory of Stokes does not perform well in very shallow water (water depth of the order of the wave height or less). This is not the case in the present tests, so the

ratio $\mathcal{S}$ can be applied to estimate the degree of non-linearity. An overview of Stokes ratios for different wave conditions on 20m water depth is given in Figure 3.1.

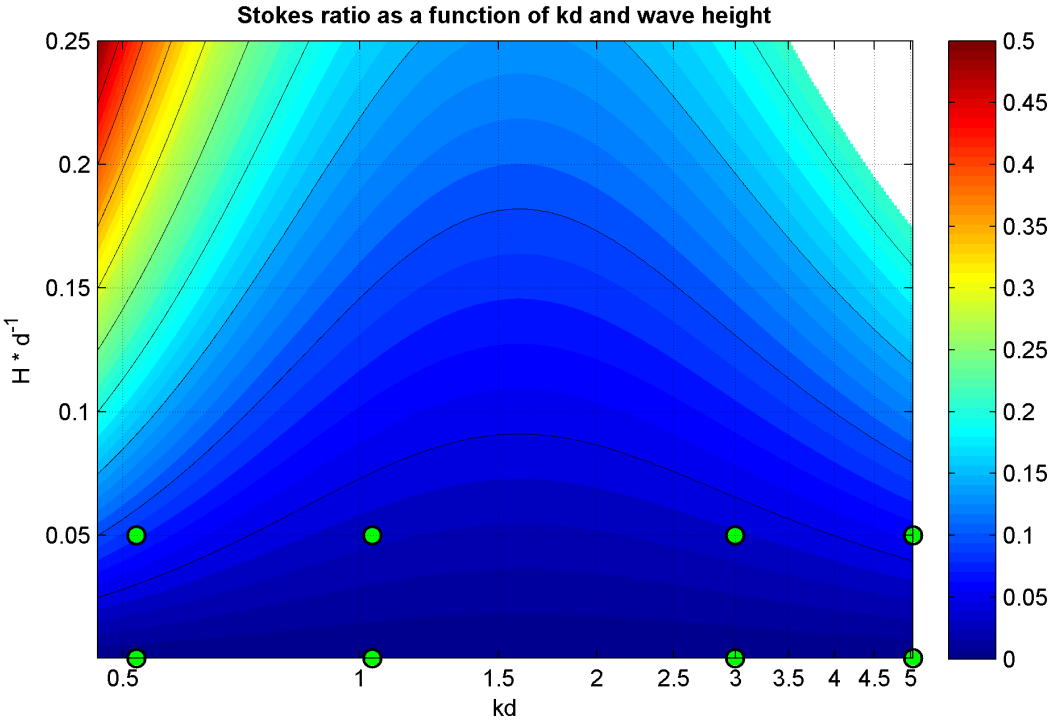

FIGURE 3.1: Stokes ratio as a function of kd and wave height. Green dots indicate the simulated conditions. Wave steepness exceeds 0.14 on the upper-right corner of the figure, leading to breaking of regular waves.

A total of 192 tests considering regular waves, horizontal bottom (20m water depth) and different model settings were simulated in SWASH (version 2.00A). The model settings variations are summarized below:

- Wave period (4): 18s; 10s; 5.2s; 4s (kd = 0.5, 1, 3 and 5, respectively).
- Wave height (2): 0.01m; 1m.
- Horizontal resolution [grid points/λ] (4): 100; 40; 20; 10.
- Vertical resolution [number of vertical layers] (3): 20; 3; 2.
- Numerical schemes applied for the advection terms in momentum equation: Default set[1], Adapted set.

The computational domain is $2DH$ domain, with grid points along one dimension in the horizontal plane and sigma layers. Hereafter this domain is also referred as a *line domain*. The

[1]The default numerical schemes applied in the integration of the advection terms in the momentum balance equations are related to other model definitions, so the 'Default set' is not always the same in SWASH.

wave conditions listed in Table 3.1 were simulated in SWASH considering different horizontal and vertical grid resolutions. The horizontal dimension of the domains are related to the wave lengths (λ): total domain length of 15λ, where 10λ used in the analysis and 5λ acting as a sponge layer at the end of the domain to prevent wave reflection. The duration of the simulations of each wave condition equals 15 wave periods. The computation time steps for the explicit time integration depend on the horizontal resolution of the computational grid and in these tests correspond to Courant numbers between 0.2 and 0.5 (for a definition of the Courant number and CFL stability condition in SWASH, see Appendix A).

TABLE 3.1: Regular wave conditions simulated in SWASH. Water depth (d) = 20m.

H[m]	**T[s]**	**L$_{wave}$[m]**	**kd**	**Stokes ratio ($\mathcal{S}$)**
0.01	18	242	0.5	8.3e-4
1	18	242	0.5	8.3e-2
0.01	10	121	1	3.3e-4
1	10	121	1	3.3e-2
0.01	5.2	42	3	3.8e-4
1	5.2	42	3	3.8e-2
0.01	4	25	5	6.3e-4
1	4	25	5	6.3e-2

Two sets of numerical schemes were selected for the discretization of advection terms in the momentum equations. The numerical schemes associated to the different terms are presented in Table 3.2. More detail about these choices is provided in Appendix A and in the SWASH USER MANUAL (2014).

TABLE 3.2: Discretization of advection terms in the momentum equations. BDF: 2^{nd} order Backward Difference Scheme; CDS: 2^{nd} order Central Differences Scheme; UPW: 1^{st} order Upwind Scheme.

Term	**Default set**	**Adapted set**
$u\frac{\delta u}{\delta x}$ (H. Adv. of H-momentum)	BDF	BDF
$w\frac{\delta u}{\delta z}$ (V. Adv. of H-momentum)	UPW	CDS
$u\frac{\delta w}{\delta x}$ (H. Adv. of V-momentum)	Ignored	BDF
$w\frac{\delta w}{\delta z}$ (V. Adv. of V-momentum)	Ignored	UPW

The required computational effort can be estimated by calculating the number of computation points in time and space. This number increases linearly with the number of vertical layers and is inversely related to the grid spacing and time step. The computational time step is proportional to the grid spacing, since it is adjusted during the simulation to keep the Courant

number sufficiently low. Therefore, in a line domain the computational effort is inversely related to the horizontal spacing to the power two. In spatial (area) domains this relation is to the power three. Thus, the horizontal resolution of the computational domain is clearly a critical definition with respect to the required computational time of practical applications.

Figure 3.2 presents the estimated number of computational points associated to a line domain (2DV) with three vertical layers. These are expressed as computational points per kilometre and per minute simulation, so it can be made a direct link to practical applications (i.e. simulations of wave penetration in harbours). The grid spacing in this case depends both on the horizontal resolution (number of grid points per wave length) and on the associated wave period and wave length. The differences in this comparison would necessarily increase for 3D domains used in practical applications, as the computational effort in those cases is related to the third power with the horizontal grid spacing.

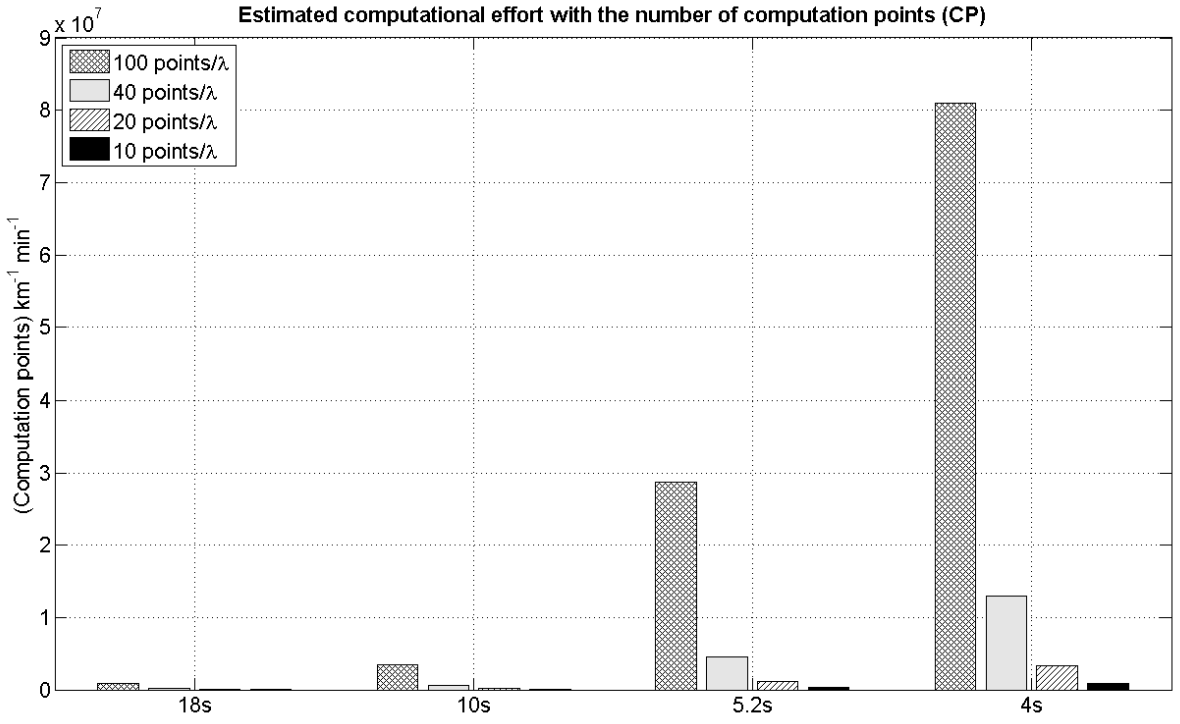

FIGURE 3.2: Estimated computational effort to simulate propagation of waves of different length in a line domain.

Because in practice the same computational grid is used to simulate longer and shorter waves, it is clear from Figure 3.2 that the required computation time will be dictated by how well the shorter wave of interest is represented on the grid. The number of vertical layers will also be relevant since an increment in the number of vertical layers leads to a proportional increase in the number of computational points.

It is often convenient to have an optimized model with simulations requiring feasible computation times. On the other hand, model results should be sufficiently accurate for the given application. The horizontal and vertical resolution considered in SWASH simulations are related to the accuracy of the results based on the 192 tests with regular waves.

A Matlab routine was developed to import and pre-process the output files of SWASH into Matlab workspace. This procedure is described in Appendix B. Results associated to the simulations considering the different kd, 20 vertical layers, 100 grid points per wave length and wave height of 0.01m are shown in Appendix C. Three different errors were calculated from the results of the 192 simulations considering regular waves:

1. wave celerity (dispersion) error relative to linear wave theory[2];
2. amplitude error after one wave length from the forcing boundary (at $x = \lambda$) relative to the forced amplitude;
3. amplitude error per wave length calculated between $x = \lambda$ and $x = 10\lambda$ and relative to the forced amplitude.

Figure 3.3 gives a schematic overview of the quantified errors. The upper panel shows the instantaneous water surface elevation along the domain. The forcing boundary is situated on the left side and the sponge layer on the right side. The lower plot indicates the steady wave height along the domain, which ideally would be homogeneous between the forcing boundary (left side) and the beginning of the dissipative sponge layer on the right side.

The plots showing the quantified errors associated to the different simulations are contained in Appendix D. In the next paragraphs each of the three computed errors is treated in detail.

1) Wave celerity error

The computation of the dispersion error is illustrated on the upper plot of Figure 3.3: the phase speed is computed along the domain and during the simulation by determining the wave phase displacement (Δx) during a time step ($\Delta t \approx 0.2s$). The calculated speed is compared with the analytical phase speed derived from the dispersion relation. These results are given in Appendix D.1.

The relative dispersion/celerity error for the simulations with different wave height and sets of numerical schemes are generally low (smaller than 1%). Errors larger than 1% are found only when low horizontal resolution is considered (i.e. 10 grid points per wave length). Even though these errors are relatively small, they can lead to greater deviances when large model domains are considered. However, for general applications of SWASH to studies of wave penetration into harbours the observed errors can be considered low and generally not relevant.

[2]Dispersion relation is the same for the second-order theory as for the first-order theory.

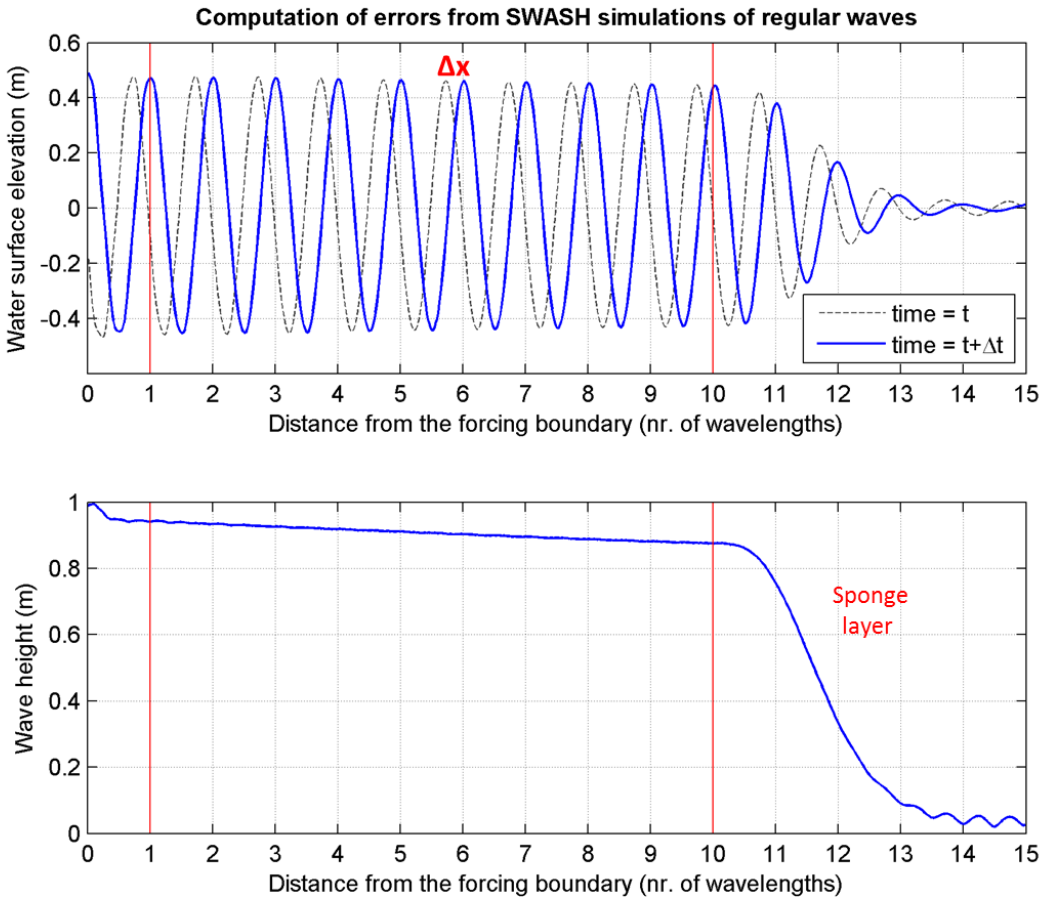

FIGURE 3.3: Schematic view of the computed errors from SWASH simulations of regular waves

2) Wave amplitude error near the incoming boundary

This error quantifies a relatively abrupt drop in wave amplitude in the vicinity of the incoming boundary ($0 \leq x \leq 1\lambda$). It can be visualized on the lower plot of Figure 3.3 near the incoming model boundary on the left hand side. For each individual simulation (192 tests) this drop is quantified and made relative to the imposed wave amplitude. Figures with these results are given in Appendix D.2.

The amplitude errors in the vicinity of the incoming boundary are more prominent for larger kd numbers (say $kd > 3$), for which the vertical profile of wave quantities is more curved. This unwanted behaviour under high kd conditions is likely caused by inaccuracies in the imposed velocities at the boundary, making necessary the use of more vertical layers to proper represent the vertical profile. As for the dispersion errors, the horizontal grid resolution and the considered sets of numerical schemes do not substantially affect the observed errors. Neither does the degree of non-linearity of the waves, so the fact that waves are imposed in SWASH based on the linear wave theory cannot solely explain its occurrence. The maximum relative amplitude error is in

the order of 15% for $kd = 5$, $H = 1m$ and two layers. This deviation is considerable and should be accounted whenever wave conditions with large associated kd numbers are relevant ($kd \geq 3$).

An alternative to minimize these errors is to increase the vertical resolution of the computational grid. However, for the bigger (weakly non-linear) wave conditions and the larger kd values, errors in the order of 5% occur even when 20 vertical layers are considered. Even though in coastal areas those waves are rather short and generally not relevant, the presented results indicate a limitation of SWASH with respect to the imposed velocity profiles of relatively short waves. While this problem is not addressed in the SWASH source code, the consequence of this limitation can be minimized by assessing the wave height in the vicinity of the forcing boundary in a preliminary simulation, and imposing a compensated wave height to the subsequent simulations.

3) Wave amplitude error per wave length along the domain

The third error considered in this analysis is an estimate of the decay in wave amplitude between $x = \lambda$ and $x = 10\lambda$ (see bottom plot of Figure 3.3). The tests do not consider dissipation due to bottom friction effects, so ideally the wave height would remain homogeneous along the domain (except for $x > 10\lambda$ where a dissipative sponge layer is placed to prevent wave reflection from the outgoing boundary). Any gradual decay of wave height within the analysed region is due to numerical effects. As for the amplitude errors adjacent to the forcing boundary, the amplitude errors per wave length are made relative to the imposed wave amplitude, so that results from the different simulations are directly comparable. These results are given in Appendix D.3.

The magnitude of this error is influenced by all variables considered in the tests. The largest contribution is the forced wave height, followed by the kd value. For small linear waves the gradual decay of wave height due to numerical diffusion is negligible for all considered tests, while it can increase dramatically for more energetic waves. The vertical and horizontal grid resolution have relatively small influence on this error. The use of the *Adapted set* of numerical schemes to the advection terms in the momentum equations (Table 3.2) improve considerably the results, specially for the larger kd numbers. These improved results are more influenced by the horizontal resolution of the computational grid, showing larger amplitude errors when only 10 grid points per wave length are taken.

For the tests with wave height of *1m* ($H/d = 0.05$) and horizontal grid resolution of 20 points/λ, errors can be in the order of 1.5% per wave length for $kd = 5$ and when the *Default set* of schemes is used. Considering the same wave condition and settings but only 10 grid points/λ, the errors are up to 2.5% per wave length. When the *Adapted set* of numerical schemes is considered, relative amplitude errors reduce considerably to approx. 0.25% per wave length for H=1m, *kd=5* and horizontal resolution larger than 20 grid points/λ. With less horizontal grid resolution (10 grid points/λ), the numerical dissipation increases, though the errors remain smaller relative to the *Default schemes*.

The differences between the results associated with the two sets of numerical schemes is mainly related to the treatment of the vertical advection of horizontal momentum ($w\delta u/\delta z$). If the *Default set* of schemes is considered this term is discretized using a first-order Upwind scheme, which can be inaccurate and diffusive when large the gradients of horizontal velocity along the vertical are involved. The accuracy is additionally deteriorated with large Δz, since the truncation error is of first-order with the vertical grid spacing. The *Adapted set* of numerical schemes considers the second-order Central Differences scheme for the vertical advection of horizontal momentum, which is fairly more accurate and thus less diffusive. The total numerical diffusion in this case is considerably reduced and does not relate directly to the vertical resolution, indicating the contribution of other terms (e.g. horizontal derivatives).

The amplitude errors per wave length are not linearly related to the wave height, so increased relative errors are expected for wave heights larger than *1m*. These deviations are specially relevant for waves with high *kd* number, not only because the error is larger for those waves, but also due to the cumulative effect along the simulation domain. Because those waves are relatively shorter, more 'wave lengths' are travelled thought a given domain.

It must be noticed that generally *kd* reduces as the wave propagates towards the shore and the water depth decreases, thus the relative error per wave length is also expected to diminish. Furthermore, $kd \geq 3$ is already rather large for practical applications involving wave penetration in harbours. However, both the nearly linear amplitude error adjacent to the boundary and the gradual non-linear amplitude error per wave length should be kept in mind. The presented results indicate that accuracy is not only a function of *kd* values, but also the horizontal and vertical resolution, degree of non-linearity of the waves (wave height) and selected numerical schemes.

A qualitative summary of the results of the 192 tests with regular waves run in SWASH is provided in Tables 3.3 and 3.4, for the linear and (weakly) non-linear conditions, respectively. These results refer to the SWASH simulations with both 3 and 2 vertical layers. The scoring presented on the tables should be regarded as a general summary of the findings described in this section, taking into account that the three individual errors treated here may be more or less relevant depending on the specific application of the model.

From Table 3.3, Table 3.4 and Appendix D, it is concluded that when dealing with linear waves both the *Default* and *Adapted* sets of numerical schemes give accurate results with respect to wave dispersion and numerical diffusion. In any case, amplitude errors may occur close the incoming boundary specially for large *kd* numbers (say $kd \geq 3$).

TABLE 3.3: Qualitative summary of SWASH performance with 3 or 2 layers and linear wave conditions. ↓kd = (kd ≤ 1); ↑kd = (kd ≥ 3). "++" = very good; "+" = good; "-" = bad; "- -" = very bad.

Schemes	**Horiz. resolution**	**Dispersion**		**Amplitude (boundary)**		**Amplitude /λ**		**Score**
		↓ kd	↑ kd	↓ kd	↑ kd	↓ kd	↑ kd	
Default set	100	++	++	++	-	++	++	**+9**
	40	++	++	++	-	++	++	**+9**
	20	++	++	++	-	++	++	**+9**
	10	+	+	++	-	++	++	**+7**
Adapted set	100	++	++	++	-	++	++	**+9**
	40	++	++	++	-	++	++	**+9**
	20	++	++	++	-	++	++	**+9**
	10	+	+	++	-	++	++	**+7**

TABLE 3.4: Qualitative summary of SWASH performance with 3 or 2 layers and non-linear wave conditions. ↓kd = (kd ≤ 1); ↑kd = (kd ≥ 3). "++" = very good; "+" = good; "-" = bad; "- -" = very bad.

Schemes	**Horiz. resolution**	**Dispersion**		**Amplitude (boundary)**		**Amplitude /λ**		**Score**
		↓ kd	↑ kd	↓ kd	↑ kd	↓ kd	↑ kd	
Default set	100	++	++	++	-	++	- -	**+5**
	40	++	++	++	-	++	- -	**+5**
	20	++	++	++	-	+	- -	**+4**
	10	+	+	++	-	-	- -	**0**
Adapted set	100	++	++	++	-	++	++	**+9**
	40	++	++	++	-	++	++	**+9**
	20	++	++	++	-	+	+	**+7**
	10	+	+	++	-	-	- -	**0**

Most usually a non-linear wave model like SWASH is applied for non-linear wave conditions. In this case, the results of the tests indicate that the *Adapted set* is more accurate leading to a considerable reduction of the numerical diffusion associated to waves with larger *kd* numbers. Regarding the horizontal resolution it is recommended to consider more than 10 grid points per wave length.

Aside from the errors described above, another issue related to the type of boundary condition was identified in the results. Waves are imposed in SWASH by prescribing a velocity magnitude in each vertical layer along the boundary. These velocities follow from the linear wave theory, so the imposed wave profile is always symmetric (i.e. linear sinusoidal wave). If the forced condition

is non-linear, spurious higher harmonics are introduced at the boundary as a compensation to the asymmetrical profile. These "corrective" harmonics are free and propagate with their own celerity from dispersion relation.

If the primary wave field correspond to relatively short waves (large kd numbers), the spurious higher harmonics are too short and generally die out after a few wave lengths due to the effect of numerical diffusion or the cutting frequency associated to the number of layers. Although, for longer waves (low kd numbers) the frequency of the higher harmonics is lower so the spurious waves generated at the boundary may remain along the domain. This can be minimized by imposing a higher order velocity signal at the boundary, including the super harmonics on the imposed signal. However, this option is not implemented on the version 2.00A of SWASH (only the second order low frequency correction is treated), so if required the higher order velocity signals including super harmonics must be calculated beforehand and provided as input to the SWASH simulations.

3.1.2 Coupling tool between SWASH and Harberth models

Wave forces acting on a ship can be computed using the results of a wave model as input to the program Harberth (Section 2.2.1). Beside files containing the input settings to be used by Harberth in the computation of forces, the model also requires a mesh file representing the ship's hull with a large number of quadrilateral flat panels, and two input files with wave information, named *panelwave.dat* and *wlenwave.dat*. The file *panelwave.dat* carries the time-dependent wave quantities at the (x, y, z) positions of the centroid of the panels (i.e. collocation points). The wave quantities are the dynamic pressure [kPa] without the contribution of hydrostatic pressures, U [m/s], V [m/s] and W [m/s], with the velocity components associated to the body-bound coordinate system (U positive to the bow, V positive to port side and W positive upwards). The file *wlenwave.dat* contains the water surface elevations at the midpoints of the segments on the waterline contour.

A Matlab code was developed to read the output files of SWASH, process the results, allocate the wave quantities at the required (x, y, z) points, and write Harberth input files. SWASH uses a staggered grid, so when model results are exported without any interpolation (i.e. *GROUP* results in SWASH) it must be certified that the variables are associated to the correct spatial coordinates. The general pre-processing procedure of SWASH results is given in Appendix B. Figure 3.4 provides and overview of the information flow and coupling processes.

In order to generate the input files to Harberth simulation, the *2DV* results of SWASH for the considered regular waves are extended from a line (*x-axis*) into a 2D area in space by replicating the line results in y-direction (perpendicular to the line domain). To change the incoming wave direction, the computation grid and vectorial quantities (U and V) are rotated, preserving

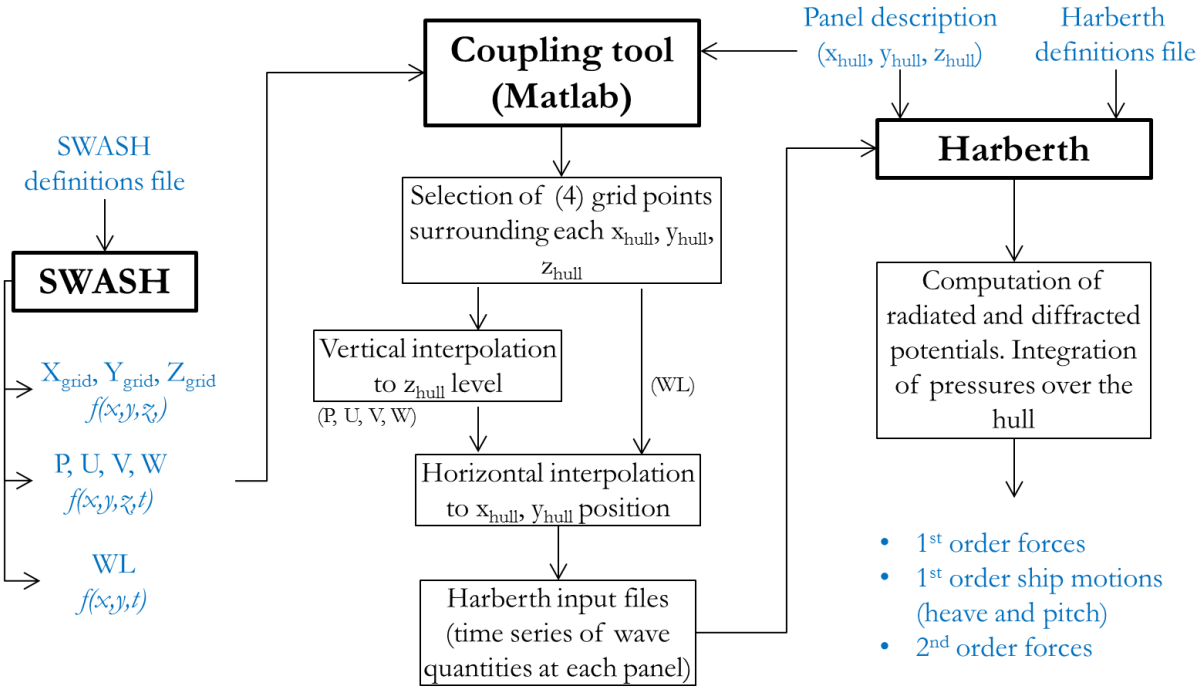

FIGURE 3.4: Flowchart with information (blue) and processes (black) relations within the coupling procedure.

body-bound coordinate system. The considered wave directions in the simulations with regular waves are 180°, 225° and 270° (Figure 3.5).

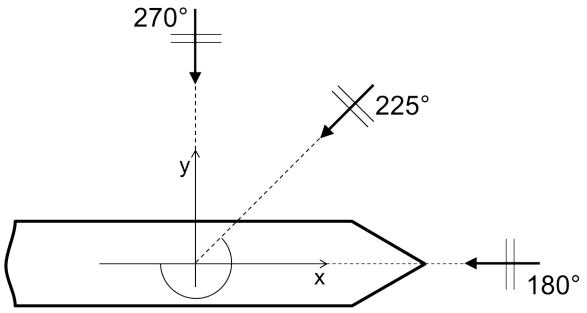

FIGURE 3.5: Wave direction relative to the body-bound coordinate system.

The interpolation of the SWASH model results to the collocation points $(x_{hull}, y_{hull}, z_{hull})$ is divided in three steps aiming to speed up the procedure (3-dimensional interpolation of the model results to the N collocation points for every time step requires too much time). First the four wave model grid points surrounding each collocation point are identified. The depth-dependent wave quantities at these points are then interpolated to the level of the collocation point z_{hull}. Finally, the information at the four surrounding points and at the same vertical

level as the collocation point is interpolated on the horizontal plane to the x,y position of the collocation point.

Large gradients of pressure and velocity components may occur along the vertical axis. The vertical interpolation of wave quantities is relatively trivial when a large number of vertical layers is considered in SWASH. However, especially when a few vertical layers are considered, information along the vertical is scarce to define the quantities in the collocation point level (z_{hull}). The wave pressure and the vertical velocity component are provided by SWASH at the edge of the layers, so these results can be linearly interpolated along the vertical axis to determine the input value at the required level. The horizontal velocity components are given in the middle of the vertical layer. Two different approximations are considered for the definition of these quantities at the required vertical level:

1. the horizontal velocity components are homogeneous in each layer (same approximation is adopted in SWASH computations);
2. the horizontal velocity components vary linearly, with the slope on each layer determined based on the model results (description provided below).

The second approximation considers a linear rate of change of horizontal flow velocity across each vertical layer. The slope of this line is defined as the average between the slopes at the upper and lower interfaces of the grid cell. At the internal interfaces the slopes are determined directly from the velocities computed by SWASH (i.e. dU/dz). At the bottom it is assumed that $dU/dz = 0$, and at the surface it is determined considering the rate of change along the lower layer interfaces:

$$\left(\frac{dU}{dz}\right)_s = \left(\frac{dU}{dz}\right)_{s-1} + (z_s - z_{s-1}) \cdot \frac{\left(\frac{dU}{dz}\right)_{s-1} - \left(\frac{dU}{dz}\right)_{s-2}}{z_{s-1} - z_{s-2}} \tag{3.2}$$

With both approaches the horizontal velocity in the middle level of the computational cell is the same as given by SWASH. The sloping method can be used only when 2 or more vertical layers are considered in SWASH, otherwise the vertical variations are neglected in the wave modelling and can be reasonably disregarded here. The pressures simulated in SWASH are considered to be placed on the interface between the vertical layers, so the *BOX-layout* should be used in SWASH for the non-hydrostatic pressures (detailed information about SWASH is given in Appendix A). Examples of results from the two interpolation approaches are given in figures 3.6 and 3.7.

The figures indicate that the number of layers must be increased if more curved vertical profiles are of interest (larger kd values). For low kd values the profile is well represented even with two layers.

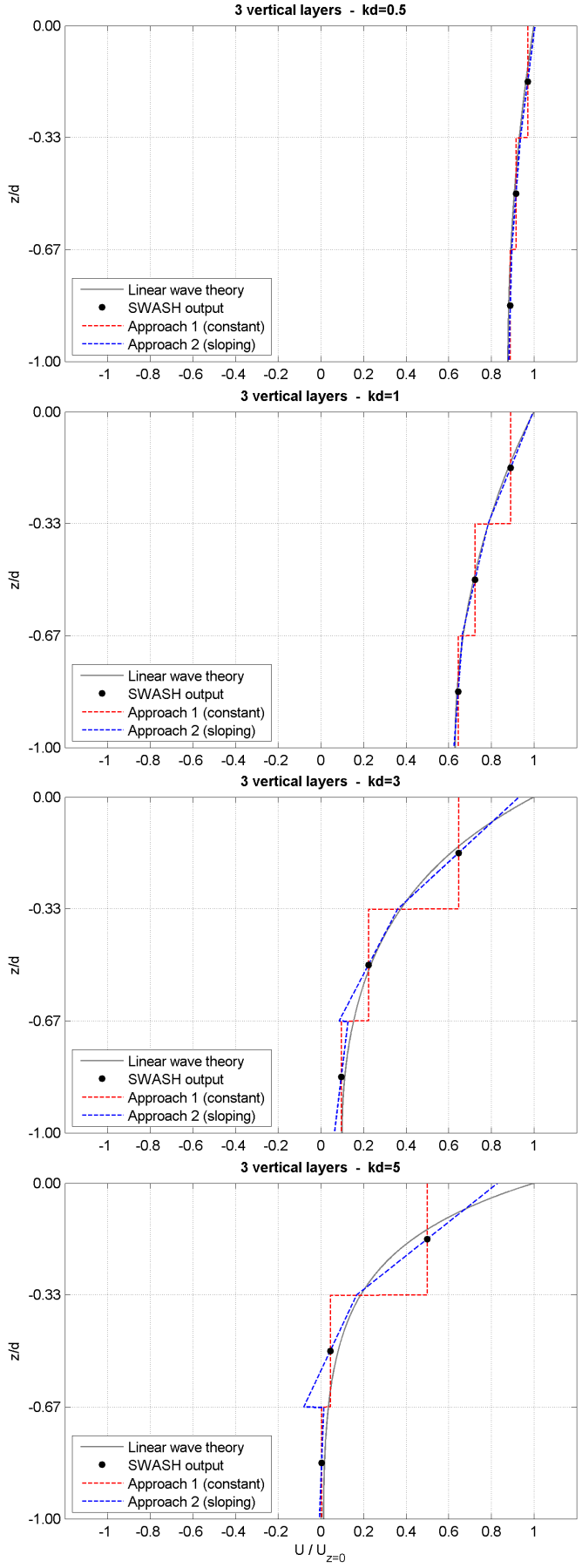

FIGURE 3.6: Schematic examples of vertical interpolation (3 layers).

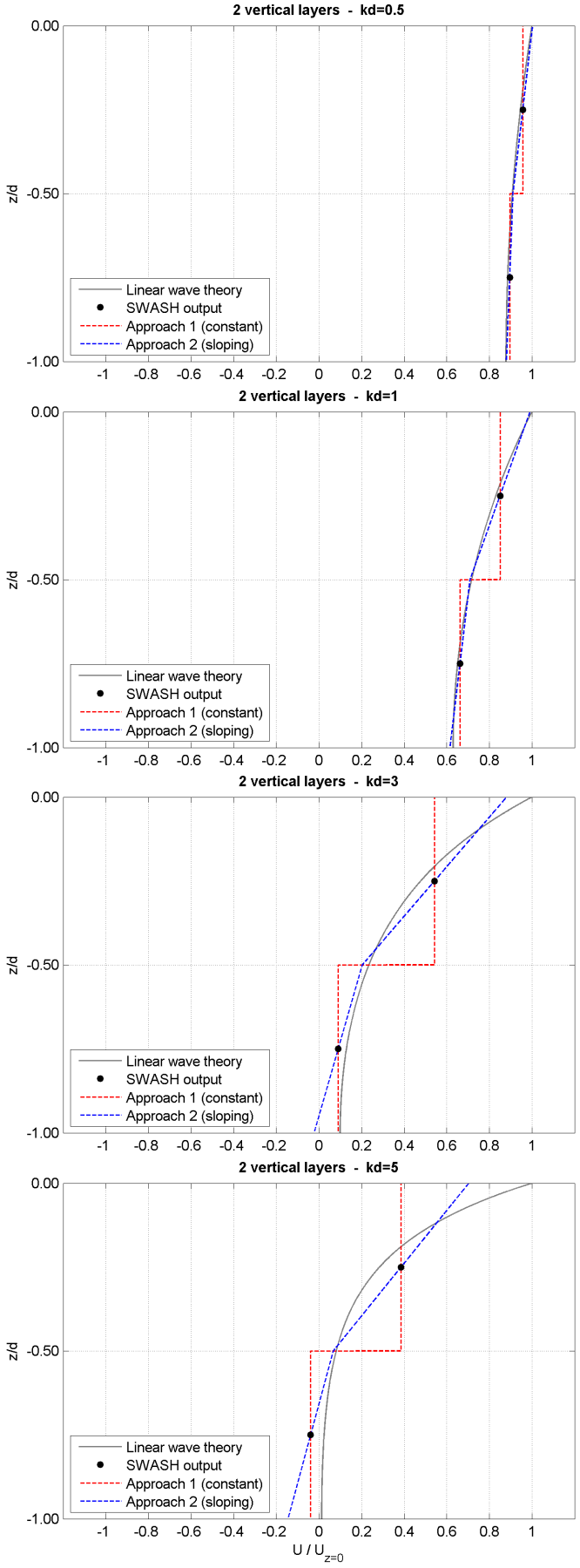

FIGURE 3.7: Schematic examples of vertical interpolation (2 layers).

For the sloping approach the velocity variation along each layer is represented by one single line, which crosses the output point in the middle of the layer. Especially for large kd values (more curved profiles), a greater variation of the slope takes place along the vertical. In this case the approximated profiles can be discontinuous at the layers interface.

The wave information surrounding the collocation point at the required vertical level is used to determine the input value to Harberth simulation. Generally the horizontal grid spacing considered in SWASH is much finer than the resolution of the panels describing the hull of the vessel, and because a relatively large number of grid points per wave length is required to properly model the waves only relatively small differences are expected between neighbouring grid points. Therefore the horizontal interpolation to the collocation point (x_{hull}, y_{hull}) is not so critical. For efficiency of the program this interpolation is approximated with a weighted average based on the inverse of the distance squared:

$$Q_{cp,i} = \frac{\sum_{i=1}^{4} (Q_i \cdot Weight_i)}{\sum_{i=1}^{4} Weight_i} \qquad \text{with} \qquad Weight_i = \frac{1}{(S_{cp,i})^2} \tag{3.3}$$

Where Q stand for the wave quantities (i.e., wave pressure, velocity components and water surface elevation); $S_{cp,i}$ is the distance between the collocation point (cp) and each surrounding grid point (i). Notice that only horizontal interpolation is required for the definition of water levels along the waterline contour of the mesh, so the overall procedure is simplified for this variable.

Results obtained with the above described interpolation procedure implemented in the coupling tool are consistent with results of 3D interpolation functions. With the alternative approach, however, only 1D and 2D interpolation are required, reducing considerably the calculation time. The wave information defined at the required locations along the hull of the ship is finally used to build the input files *panelwave.dat* and *wlenwave.dat* in the proper format recognized by the Harberth model.

3.1.3 Computation of forces acting on a ship: regular waves

Forces and moments acting on a ship are calculated using the results of the SWASH simulations of regular waves. The ship considered in these computations is a 125,000m^3 LNG carrier. The dimensions of the ship are given in Table 3.5 and the mesh describing the hull in Figure 3.8. The main definitions for the Harberth simulations are given on Table 3.6.

The outputs from Harberth simulations are time series of wave forces and moments acting on the ship. The different contributions to the total forces/moments are provided separately (i.e.

TABLE 3.5: Dimensions of the 125,000m^3 LNG carrier.

Designation	Symbol	Unit	Magnitude
Length between perpendiculars	L_{pp}	m	273
Breadth	B	m	42
Draft	d	m	11.5
Displacement volume	Δ	m^3	98,740
Centre of gravity above keel	$\overline{KG}$	m	13.7
Transverse radius of gyration	k_{xx}	m	14.7
Longitudinal radius of gyration	k_{yy}	m	65.52

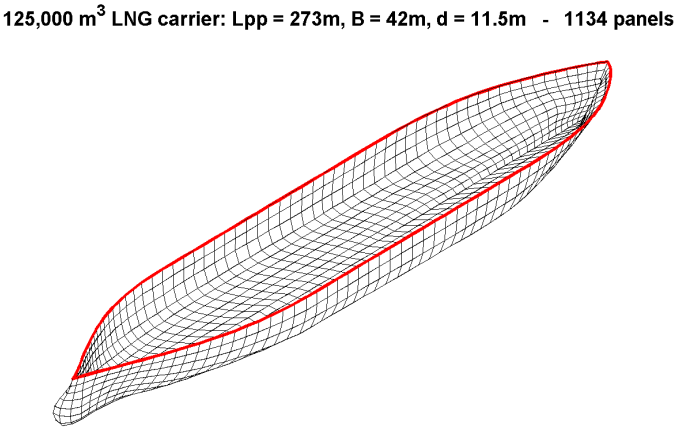

FIGURE 3.8: Panel description of the 125,000m^3 LNG carrier (1134 panels and 126 water line segments).

TABLE 3.6: Harberth definitions for the simulations with regular wave input.

Parameter	Value
Water depth	20m
Include quay wall	No
Simulation time	400s
Nr. of frequencies in hydrodynamic data file	30
Lowest frequency in hydrodynamic data file	0.05 rad/s
Frequency step in hydrodynamic data file	0.05 rad/s
Calculate retardation functions	Yes
Calculation time step	0.5s
Green function period	180s
Retardation period	180s
Calculate drift forces	Yes

Froude-Krylov forces, diffraction forces, and the four contributions to the second-order forces). On regular waves, the variation of the forces and moments becomes cyclic after some time of simulation, so the amplitude of the variation can be determined. The phase lag between the water level oscillations at the position of the centre of gravity of the ship and the forces and moments can be computed based on the time series.

The forces and moments computed with Harberth are compared with transfer functions obtained for the same vessel and wave directions, but using the frequency-domain 3D panel model *Wavescat*. In Wavescat model also the incident waves are treated as linear, so possible non-linearities in the waves are neglected in the computations (general information about Wavescat model is given on Section 2.2.2). As an additional verification against Wavescat model results, Harberth input files are created based on the linear wave theory.

The response of a floating body is small when the waves are very short relative to the body size. A proper representation of those short waves along the hull of the ship would require a large number of panels, increasing considerably computation time but not necessarily improving the accuracy of overall results, since the associated transfer functions are negligible. So in practice the panel description on the horizontal and vertical planes is optimized targeting the relevant frequencies, while a misrepresentation of (relatively) very short waves is usually acceptable.

First-order forces and moments on regular waves

As a first verification of the coupling procedure, Harberth input files are created using results of SWASH simulations with 20 vertical layers and 100 grid points per wave length. The regular wave conditions are presented in Table 3.1, wave directions are 180°, 225° and 270° relative to the ship axis. Besides the conditions simulated in SWASH with wave height of 0.01m and 1m (linear and weakly non-linear waves), Harberth input files are also built based on linear wave theory. This is an additional verification of the conceptual procedure by using a simplified approach (i.e., vertical and horizontal interpolation of model results is not required in this case). For brevity the comparisons plots are placed in Appendix E, figures E.1 to E.6.

In general the first order forces and moments computed with Wavescat and with the combination of SWASH and Harberth compare very well for the different wave periods, wave directions and wave heights (forces and moments are normalized with the wave amplitude). The similarity of results associated with different regular wave heights confirms the expected linear relation between wave amplitude and first-order forces. Since SWASH is a non-linear wave model, non-linearities could be incorporated in the input data imposed to Harberth simulations, especially for the wave condition with 1m wave height. However these effects are not significant in this case. The linearity in results supports the comparisons against Wavescat model outcomes, which are based on linear potential theory also for the treatment of the incident waves.

So-called irregular frequencies are known to have detrimental effects on computations with boundary-integral methods (see section 2.2.1). In the simulations with the frequency-domain panel model Wavescat a lid was applied in the surface of the non-physical domain inside the ship. This measure reduces considerably the influence of irregular frequencies. However, the same measure is not applied in Harberth model because it operates in time-domain and such an implementation is much more complicated in this case. Therefore effects of irregular frequencies are expected in Harberth results within their frequency range. The first irregular frequency can be approximated with the following relation:

$$\omega_{irr} \approx \sqrt{\frac{\pi g}{B} \tanh \frac{\pi d}{B}} \tag{3.4}$$

where B the breadth and d the draft of the ship. This gives $\omega_{irr} \approx 0.7 rad/s$ (or $T_{irr} \approx 8.8s$). Despite two of the simulated wave conditions are within the irregular frequency range, Harberth outcomes are still compatible with Wavescat results, suggesting that the effect of this numerical aspect is not so significant in this case. Furthermore, mooring issues are mostly related to low frequency oscillations, so the effects of irregular frequencies at a relatively high frequency range (say >0.1Hz) is usually not critical.

Similarly, computations of forces and moments are performed based on SWASH results considering 3 and 2 vertical layers. To reduce the number of Harberth simulations only the regular waves with $H_{wave} = 0.01m$ and wave direction of 225° are considered (normalized results associated to the other wave heights are nearly the same and all forces and moments modes are excited with this direction).

Although considerably less wave information is available along the water column, the first order forces and moments resulting from these computations are in good agreement with the results associated to the 20 layer SWASH simulations. The comparisons plots are provided in Appendix E, figures E.10 and E.11. More pronounced differences occur for the shorter wave periods (i.e. larger kd, more curved vertical profiles). Because the transfer functions are relatively small for these frequencies, they are normalized with the results based on the 20 layer SWASH simulations. The comparisons are given in Figures 3.9 and 3.10.

For the lower kd values results are generally consistent, however for $kd = 5$ deviations on the predicted first-order forces can be in the order of 50%, especially when only 2 vertical layers are applied (Figures 3.9 and 3.10). This inaccuracy is expected since under those condition the vertical profile of pressure and velocity is more curved, requiring more vertical layers for a proper representation at the collocation points. Although the sloping vertical profiles are apparently more accurate (Figures 3.6 and 3.7), the advantage of considering this interpolation method is not evident on the results.

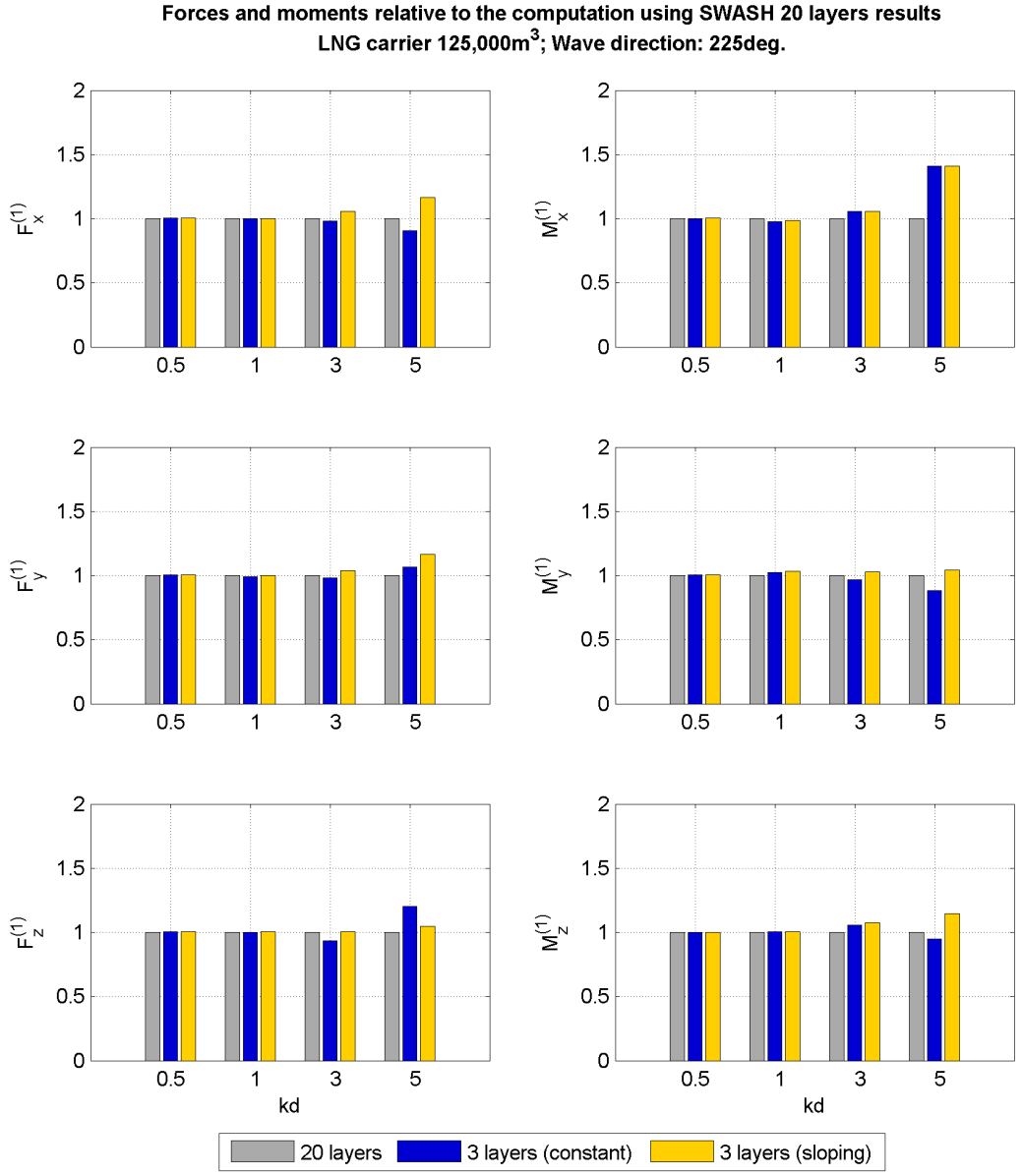

FIGURE 3.9: First-order forces and moments relative to the results associated to SWASH simulations with 20 layers.

The absolute first-order response of the $125,000m^3$ LNG carrier moored in 20m water depth is mainly associated to the lower *kd*. So provided that two or more vertical layers are used in SWASH, the two methods proposed for the vertical interpolation of horizontal velocities give satisfactory predictions of the first-order forces and moments acting on the LNG carrier. This could not be the case for a ship considerably excited by waves with large *kd* values (e.g. a ship is moored on relatively deep waters - large *depth/draft* ratio). Although, the main benefit of the hybrid approach with a non-linear wave model and Harberth is in shallow waters, where waves are usually non-linear and complex harbour geometries may be involved. In deeper waters the linear wave theory often suffices for the computation of incident waves, so the wave exciting

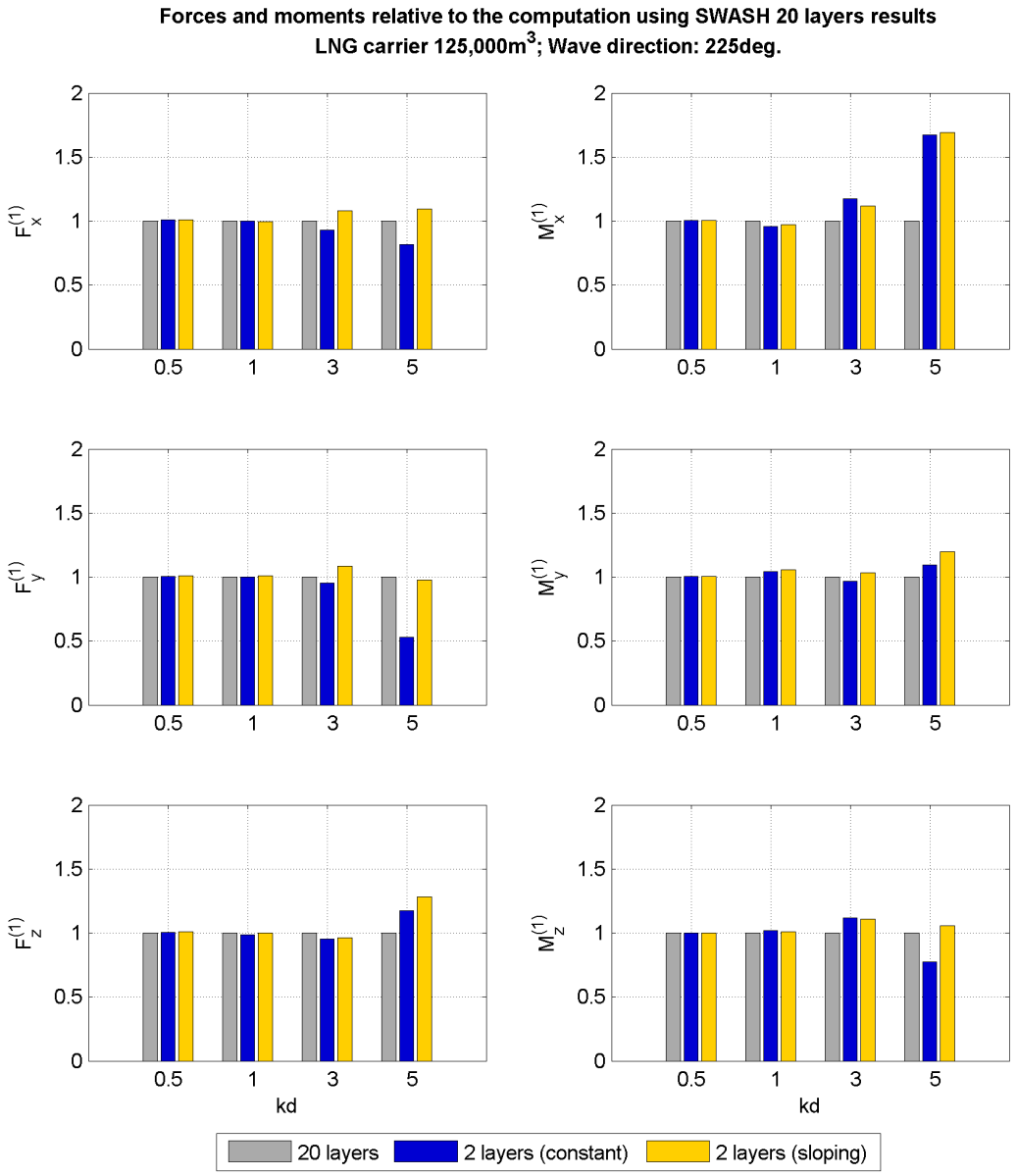

FIGURE 3.10: First-order forces and moments relative to the results associated to SWASH simulations with 20 layers.

forces can be determined with simpler tools.

Second-order forces and moments on regular waves

First-order wave forces acting on a ship are oscillatory quantities with the same frequencies as the primary waves. Second-order forces on irregular waves are generally composed of low frequency oscillations and high frequencies components, with frequency the order of two times the wave frequency. The high frequency oscillating forces are of no consequence to the dynamic

behaviour of the moored ship, so attention is given only to the mean and slow varying drift force due to second-order effects.

The direct contribution of second-order forces is generally small compared to the first-order forces, but the oscillating period is much longer - associated to the wave grouping. On mooring studies those forces will be relevant due to the excitation of the system (ship and mooring lines) at resonant frequencies, potentially amplifying the resulting loads and motions. In this sense, second-order forces on the x-direction (F_x) are of more relevance, although sway and yaw motions are also related to low-frequency forcing.

The second-order forces are computed considering ship motions induced by the first-order forces. However, only free floating heave, roll and pitch motions are considered by Harberth in the computation of second-order forces. This choice is made to prevent the ship to slowly drift away. In frequency-domain models the ship moves in six degrees of freedom, making oscillations around an equilibrium position. This difference in movements may justify deviations in the computed drift forces.

The four individual contributions to the total second-order forces and moments are listed below (a detailed description is provided in Section 2.2.1.3):

I) Relative wave elevation;
II) Pressure drop due to first order velocity;
III) Product of 1^{st} order pressure gradient and 1^{st} order motion;
IV) Products of 1^{st} order angular motions and 1^{st} order inertia forces.

The two main components of the second-order forces (I and II) are only partially influenced by the simplified motions, i.e. component I: roll motions are disregarded to determine $X_3^{(1)}$, and component II: the contribution of the radiated potentials to the total potential is incomplete. The third and fourth contributions are directly related to the first order motions of the body, so a larger influence is expected. This is the case especially for the third term, since the fourth term is generally very small compared to the others.

Initially the second order-forces computed with Harberth based on SWASH simulations with 20 layers are presented. The same Harberth simulations described in the comparisons of first-order forces are considered here (Table 3.1), including the additional verification of the coupling procedure using the linear wave theory. After a general description of these results, the influence of the vertical resolution considered in SWASH simulations in the computations of total second-order forces is verified.

The first order ship motions predicted with Harberth model and with the frequency-domain Wavescat model are compared in Appendix E, Figures E.12 to E.15. Notice that in Wavescat the ship is allowed to move in six degrees of freedom.

The amplitude of heave, roll and pitch motions predicted with SWASH+Harberth based on the different wave input compare well with Wavescat predictions. The largest disagreement occur for the near-resonance roll motion on beam waves (270°). This is mainly due to the absence of viscous damping of motions, which is by definition not taken into account with the linear potential model. Roll damping could be increased to compensate viscous effects, however the reported deviation is not critical for this project so no additional action is taken. The phase shift between the motion modes and the wave at the position of the center of gravity of the vessel are also in agreement when motions are not negligible. The determination of the phase shift is difficult for very small ship motions, so in this case the deviations may be also related to the analysis.

In general the simplification of the motions in Harberth is not expected to introduce considerable errors in the computation of second-order forces for the tested wave conditions. On regular waves with direction of 180° (head waves) heave and pitch motions dominate over the other modes, so the overall motions are fairly predicted by Harberth in comparison with Wavescat model. The same applies for the wave direction 225°, except for the lower frequency yaw motions that are considerable in the Wavescat model results while in Harberth this mode is not taken into account. On beam waves (270°) the neglected motions have only a marginal influence, though a more pronounced disagreement between the results of the two models is reported for the predicted roll motions around the resonance period.

Figures 3.11, 3.12 and 3.13 give the total second-order mean drift forces computed with Harberth and Wavescat, for wave directions 180°, 225° and 270°, respectively. Figures showing the contribution of the individual second-order components associated to the wave direction 225° are given in Appendix E, subsection E.2.2. This wave direction excites all force and motion modes, and these results are qualitatively comparable to the other simulated directions.

The total second-order forces computed with Harberth for the different wave inputs are in agreement with each other, implying the consistency of the coupling procedure and Harberth computations.

The second-order forces resulted from Harberth simulations and the Wavescat model compare generally well. Deviations associated to the longer wave period (18s) and wave direction 225° are likely related to the disagreements in yaw motions. The larger differences for the wave direction 270° are partially related to the overprediction of near-resonance roll motions.

The influence of the number of layers considered in SWASH computations on the second-order forces computed with Harberth, using the developed coupling tool to combine both models, is illustrated in Figure 3.14. Results are provided for wave direction 225°, in which all force and motion modes are excited. Qualitatively these results can be extend to other directions.

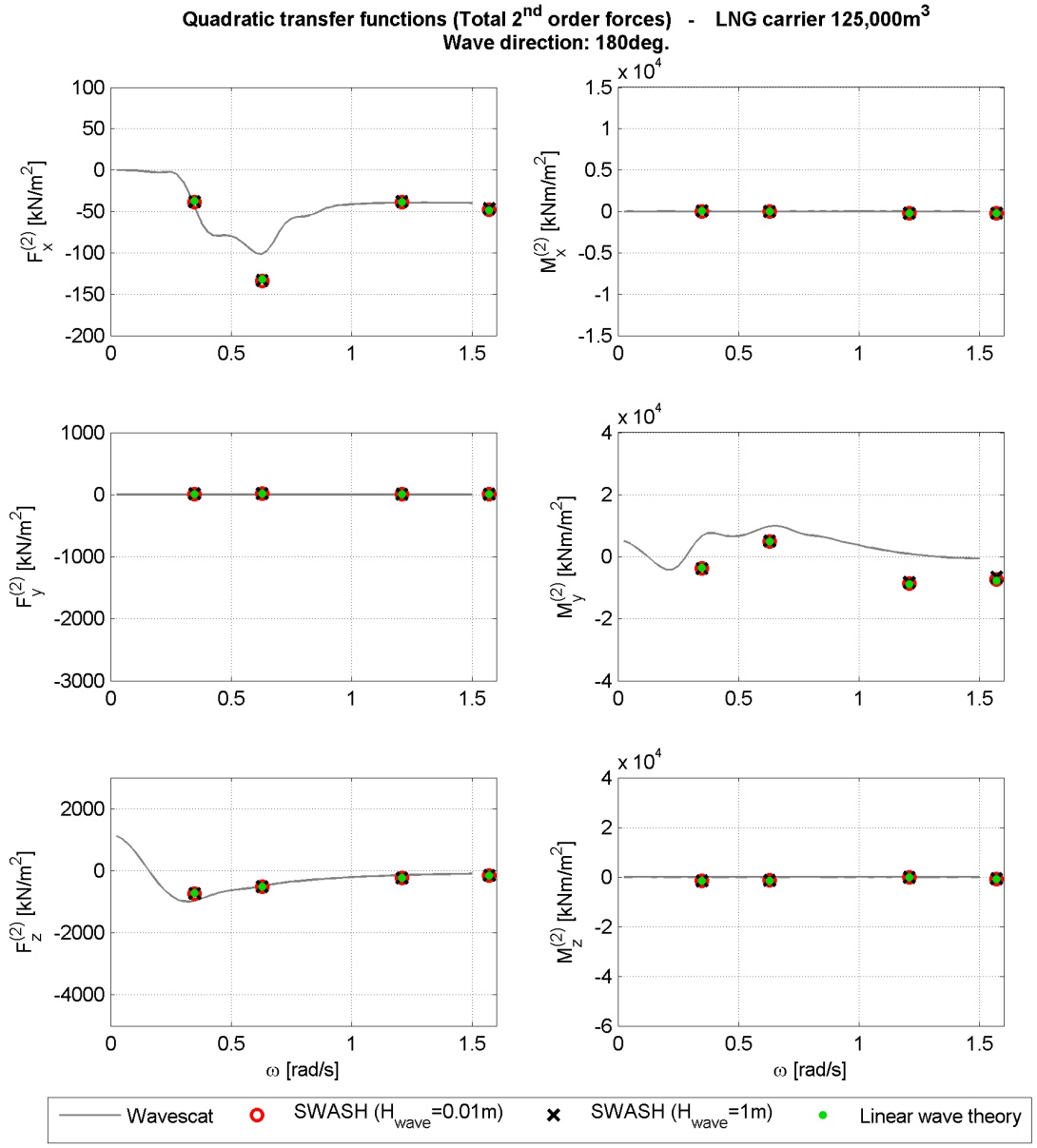

FIGURE 3.11: Total second order mean drift forces computed with Harberth and Wavescat (Regular wave direction = 180°).

As already expected based on the comparisons of velocity profiles (Figures 3.6 and 3.7) and the similar analysis performed for the first-order forces (Figures 3.9 and 3.10), the greater deviations are associated to the larger kd values (say $kd \geq 3$). In this case the vertical profile of velocity and pressure is more curved, requiring the use of more vertical layers in the wave model for a proper representation of the wave quantities along the water depth. Further, the different approaches used to interpolate the horizontal velocity along the vertical are not clearly associated to the relative accuracy of the results.

The absolute deviations on the second-order forces introduced by the use of limited number of

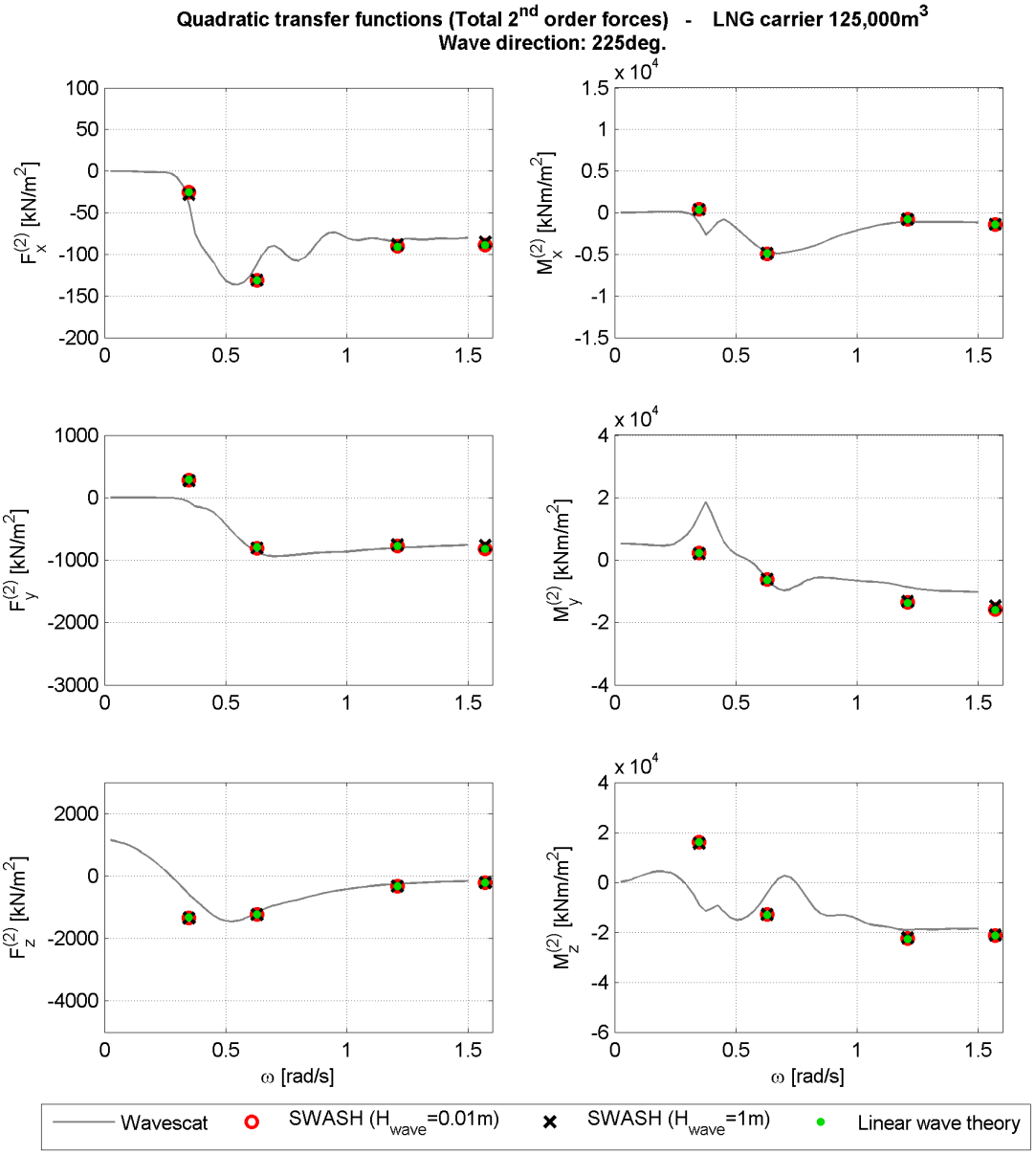

FIGURE 3.12: Total second order mean drift forces computed with Harberth and Wavescat (Regular wave direction = 225°).

layers in SWASH are generally small compared to the differences relative to Wavescat model. Therefore, provided that the bulk wave parameters are well resolved by SWASH, neither the number of layers in the wave model nor the coupling tool are expected to introduce considerable errors to the second-order forces computed with Harberth model.

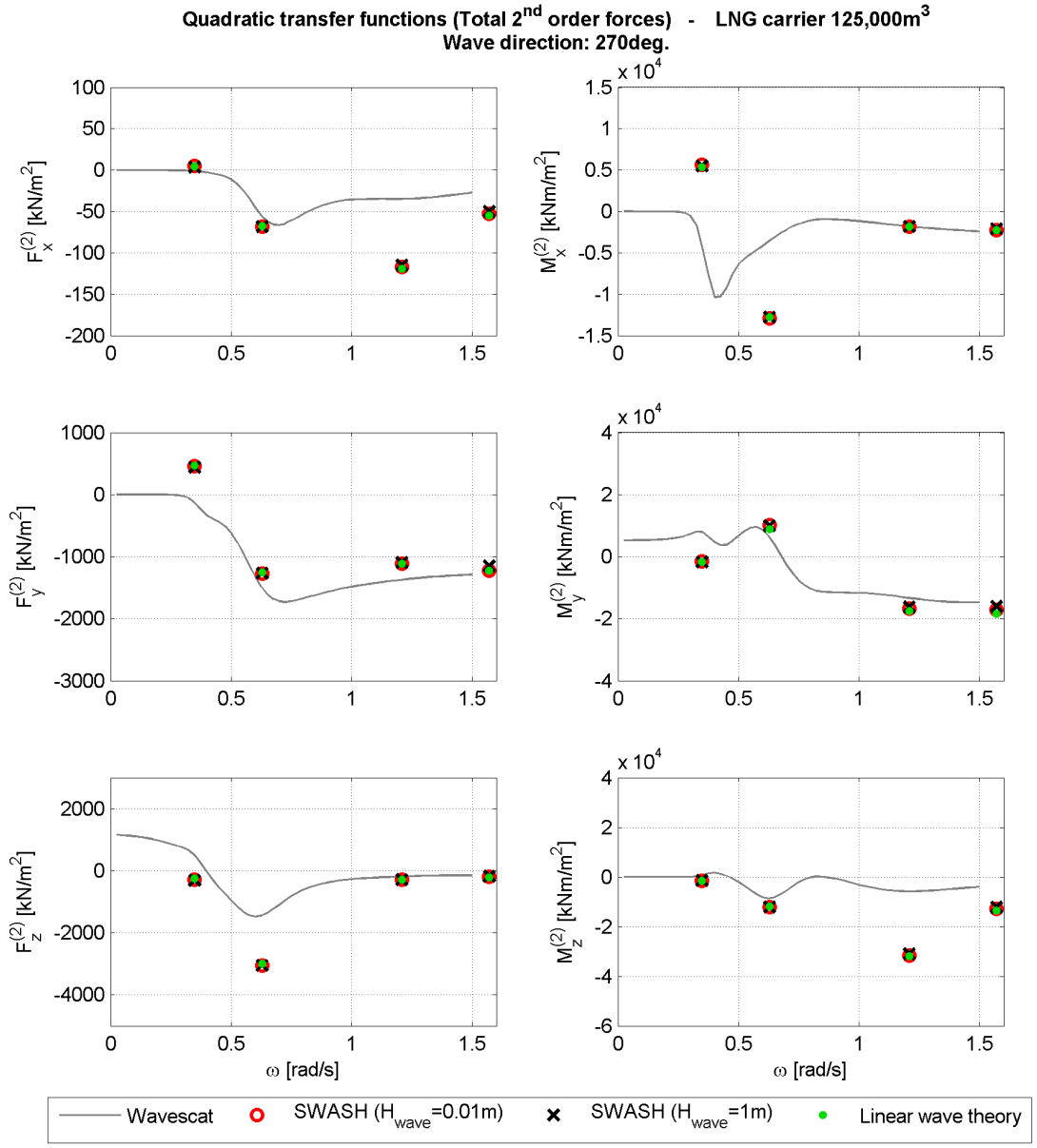

FIGURE 3.13: Total second order mean drift forces computed with Harberth and Wavescat (Regular wave direction = 270°).

3.2 Bichromatic waves

Bichromatic wave conditions result from the superposition of two primary components with different wave periods and wavelengths. Due to spatial and temporal variations of the phase shift between the two components, the interaction of the individual waves vary on space and time. Where the primary waves are in phase the amplitudes are summed resulting in a group of relatively bigger waves (i.e. wave groups). Accordingly, where the phase difference is (nearly) π, the two components are out of phase and tend to cancel each other, resulting in relatively smaller waves. This interaction leads to a modulation of wave height, commonly referred as

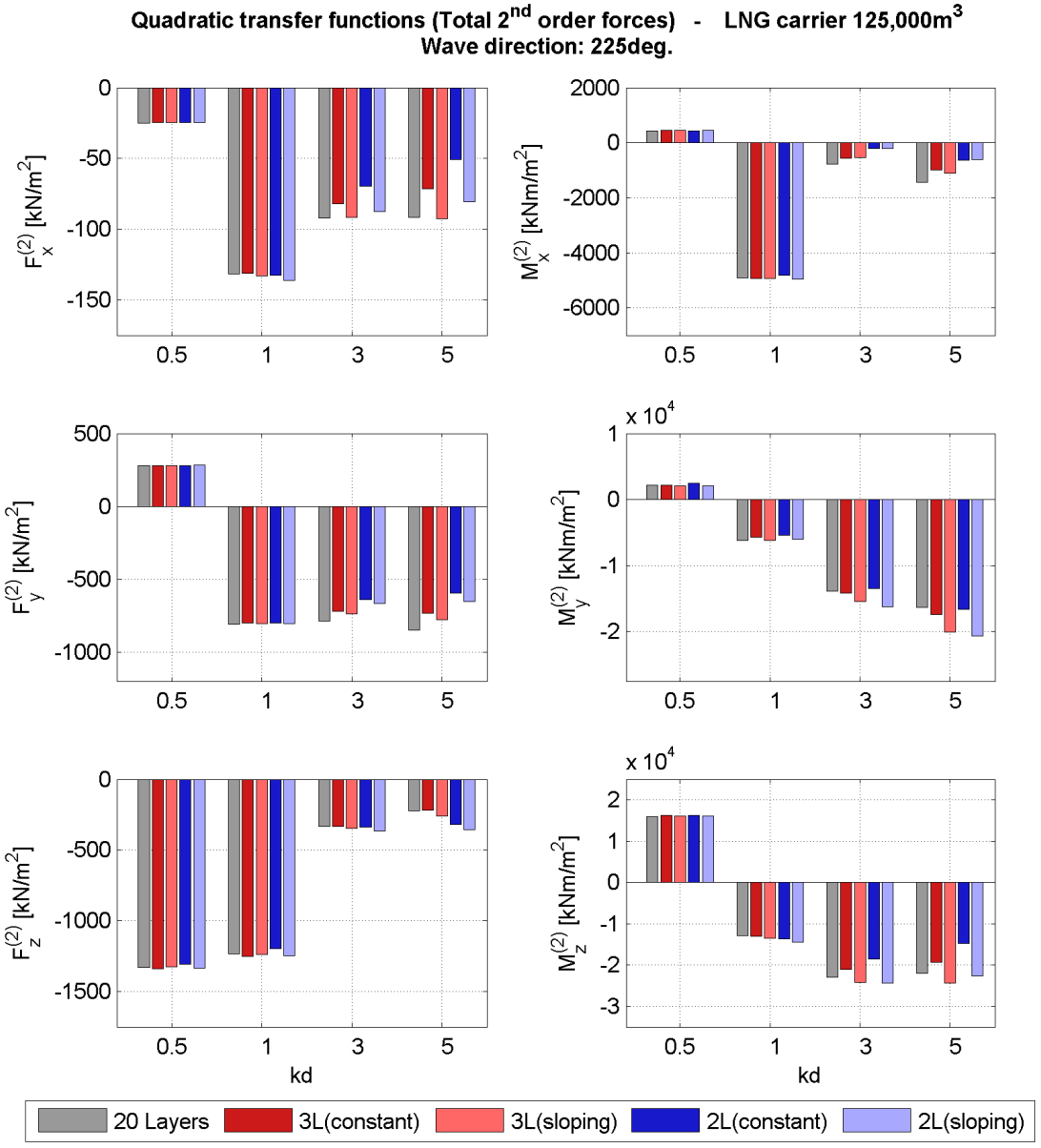

FIGURE 3.14: Total second order mean drift forces computed with Harberth based on SWASH simulations with different number of vertical layers (Regular wave direction = 225°).

wave envelope. The group frequency and group wave number ($k = 2\pi/\lambda$) are respectively the differences between the frequencies and the wave numbers of the primary components.

Wave induced radiation stress tensors S_{xx} and S_{yy} are maximum under high waves and minimum under low waves, so the radiation stresses are also modulated on bichromatic wave conditions. The gradients in radiation stresses due to alternating groups act as resulting forces within the water volume, and are compensated by water level set-downs and set-ups. These wave-like water level variations have the length and period of wave groups, but are out-of-phase with respect to the envelope amplitude. They travel with the propagation velocity of the envelope (i.e. *bound long waves*), instead of the velocity of free waves which conform to the dispersion relation. The

amplitude of the bound wave due to a couple of unidirectional primary waves at frequencies f_m and f_n can be estimated following Hasselmann (1962):

$$a_{nm} \;=\; D_{nm}\, a_m\, a_n \tag{3.5}$$

where a_{nm} is the amplitude of a bound wave component, a_n and a_m denote the amplitudes of the associated primary waves, and D_{nm} is the interaction coefficient expressed as:

$$D_{nm} = -\frac{gk_nk_m}{2\omega_n\omega_m} + \frac{\omega_n^2 - \omega_n\omega_m + \omega_m^2}{2g} - C\frac{g(\omega_n - \omega_m)}{\omega_n\omega_m\left[gk_{nm}\tanh(k_{nm}d) - (\omega_n - \omega_m)^2\right]} \tag{3.6}$$

where $\omega(= 2\pi f)$ is the radial frequency and the coefficient C is defined as:

$$C = (\omega_n - \omega_m)\left(\frac{(\omega_n\omega_m)^2}{g^2} + k_nk_m\right) - \frac{1}{2}\left(\frac{\omega_nk_m^2}{\cosh^2(k_md)} - \frac{\omega_mk_n^2}{\cosh^2(k_nd)}\right) \tag{3.7}$$

Realistic irregular wave fields can be seen as the superposition of numerous wave components with different wave heights, frequencies and directions. Similarly to the bichromatic conditions, the alternation of groups of higher waves and of lower waves induce bound long waves. However, the directionality of the carrier waves plays an important role on the resulting infragravity energy. Especially in shallow water, the long-wave amplitude in natural wave fields is smaller than in plane wave trains, even for small difference angles between the short-wave components (Sand, 1982).

The periods of the bound long waves may overlap the natural periods of a moored ship. Because damping of motions is rather low for those periods, large amplitude of motions and mooring forces may result from infragravity waves (which include free and bound long waves). Therefore, a proper representation of these waves is specially relevant when studying the behaviour of moored vessels.

In this section results of SWASH simulations considering bichromatic wave conditions are presented. These simulations include different wave conditions and model settings. The coupling tool described on section 3.1.2 is applied so that wave forces acting on a moored ship are evaluated based on the SWASH results and Harberth model.

3.2.1 Wave modelling

The tests with bichromatic waves in SWASH consider a flat bottom 15 meters below the still water level. Similarly to the tests with regular waves, the computational domain is a *2DV* domain, with grid points along one dimension in the horizontal plane and sigma layers through

the vertical. However, the sponge layer considered on the bichromatic wave simulations is longer (4000m) in order to minimize reflection of low frequency waves.

The incoming boundary condition in SWASH is defined as the superposition of two harmonic components using the second-order correction implemented in the model, which correspond to the sub-harmonics induced by the waves grouping (i.e., bound long waves). The second-order correction is implemented to prevent the introduction of spurious free waves at the boundary (Rijnsdorp et al., 2012).

A total of 8 tests considering different bichromatic waves and model settings were simulated in SWASH model. The variations considered in the tests are summarized below:

- Wave conditions (2): kd of short waves $\approx$ 1.5 and 0.5
- Horizontal resolution (2): 40 and 20 grid points/λ
- Vertical resolution (2): 3 and 2 vertical layers

The 'Adapted set' of numerical schemes is applied for the advective terms of the momentum balance equation to prevent excessive numerical dissipation (schemes are given in Table 3.2). The characteristics of the simulated bichromatic wave conditions are listed in Table 3.2. The wave periods of the primary components are defined so that the bound long wave period (T_{blw}) is approximately 10 times the mean primary wave period ($T_{m,n}$). Therefore the wave groups are composed of approximately 10 waves and $\Delta f_{m,n}/f_{m,n} \approx 0.1$.

Table 3.7: Bichromatic wave conditions #1 and #2. Indices m and n refer to the individual primary components of each condition; m,n refers to a characteristic values of the short wave field.

Parameter	**#1**	**#2**
Depth (m)	15	15
$a_{m,n}$ (m)	0.5	0.5
T_m (s)	16.95	6.94
T_n (s)	15.38	6.29
$\lambda_{m,n}$ (m)	186	62
$kd_{m,n}$	0.5	1.5
$ka_{m,n}$	0.03	0.1
Stokes ratio$_{m,n}$	0.23	0.07
a_{blw} (m)	0.108	0.018
T_{blw} (s)	166	66
λ_{blw} (m)	1791	405

The bound long wave amplitude induced by bichromatic waves with $a_m = a_n$ and $\Delta f/f = 0.1$, made relative to the amplitude of the (short) wave envelope, is given in Figure 3.15, as a function

of the amplitude of the short wave envelope and to the (primary) wave length, both normalized with the local water depth (d). The figure indicates that the bound long waves are generally much smaller than the primary waves, but become more relevant on shallow water conditions (lower kd) and under more energetic primary components.

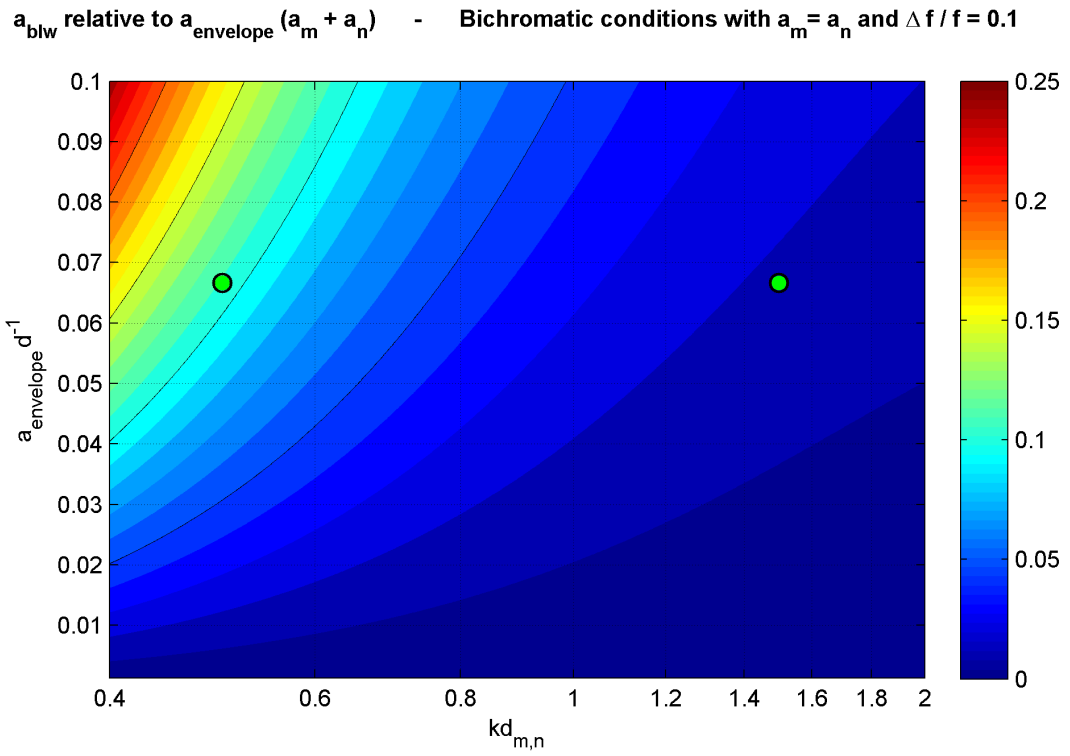

FIGURE 3.15: Bound long wave amplitude relative to the amplitude of the short wave envelope, as a function of kd and short wave amplitude (relative to water depth). The green dots indicate the conditions simulated with SWASH.

Figure 3.16 gives the water level time series and amplitude spectrum for the two bichromatic conditions. The water level time series are calculated using a Matlab routine provided by Pieter Smit (TU Delft), which applies Hasselmann theory for non-linear wave interactions. Besides the primary components, the amplitude spectra indicate the presence of second-order components at lower frequencies (bound long wave) with frequency equal to the difference of the primary waves frequency ($f_m - f_n$), and higher frequency components (higher harmonics) with frequencies of $2f_m$, $2f_n$ and $f_m + f_n$. The bound long wave amplitude is larger for the wave condition #1 because the kd value associated to the primary components is smaller (see Figure 3.15).

The results of the simulations are analysed along the first 2km of the numerical domain from the forcing boundary. This is a typical length scale on practical applications of wave penetration in harbours. For the wave conditions #1 this distance is approximately the length of the bound long wave (λ_{blw}), or 10 primary wave lengths ($\lambda_{m,n}$). For wave condition #2, 2km corresponds to approximately 5 bound wave lengths, or 32 primary wave lengths.

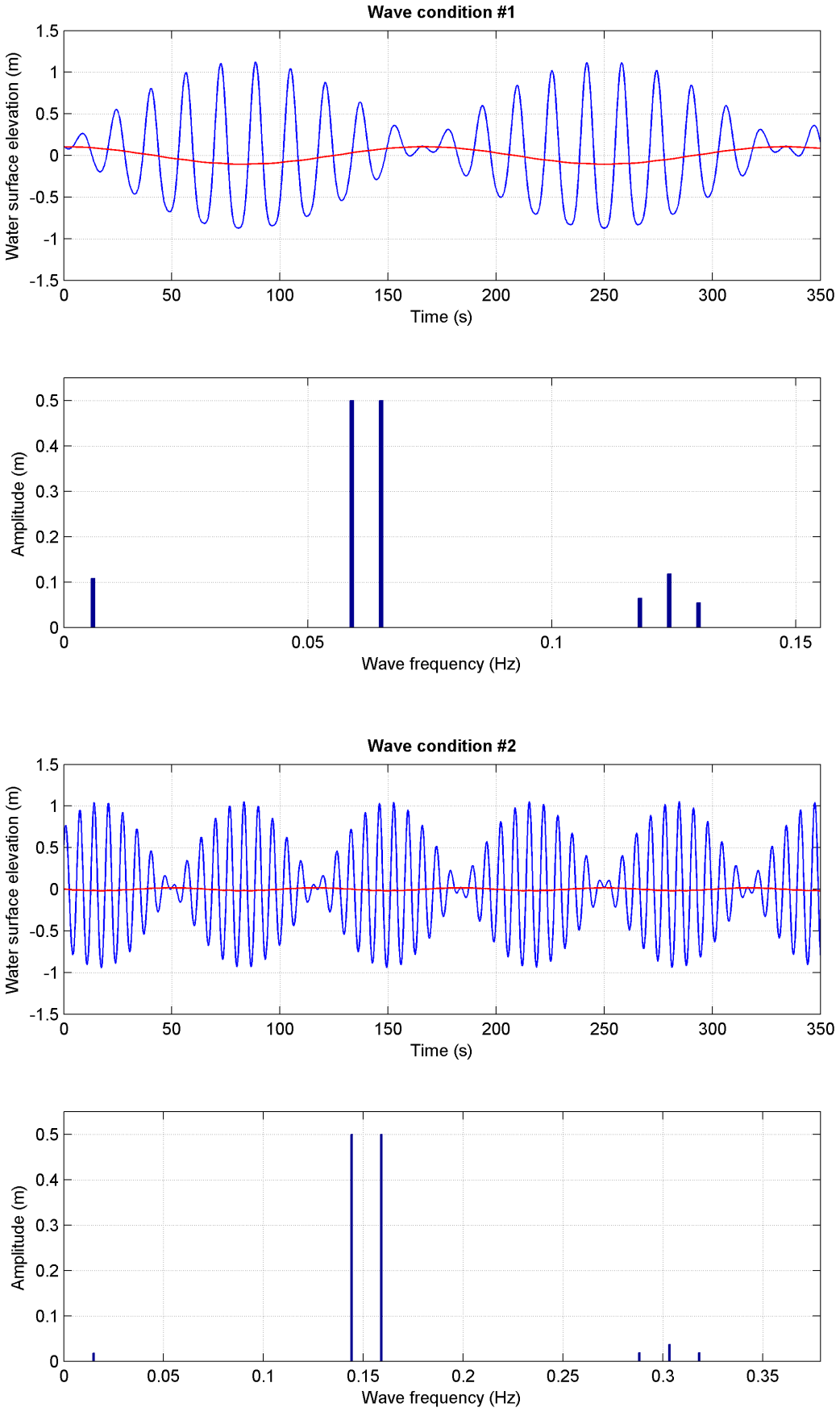

FIGURE 3.16: Water surface elevation time series and amplitude spectrum associated to bichromatic wave conditions #1 and #2. Blue line: total water level signal; red line: low frequency water level signal.

Numerical dissipation and generation of spurious waves at the boundary can induce changes on the amplitude of the wave envelope along the domain. Though, changes on the wave envelope can also be induced by non-linear interactions between the primary components. On relatively shallow waters these interactions may lead to a demodulation of the wave groups, decreasing the maximum wave height (Shemer et al., 1998). This effects become more pronounced as the distance from the incoming boundary increases.

Figure 3.17 gives the amplitude of the wave envelope at three different locations along the domain of simulation: in the vicinity of the incoming boundary (x=0m), at 500m away from the incoming boundary (x=500m), and at x=2000m. Results relate to the two bichromatic conditions and the different horizontal and vertical resolution.

The short wave behaviour along the domain follows from the findings obtained from the tests with regular waves. In agreement with those tests, the number of vertical layers does not influence significantly the short wave amplitude along the domain of simulation. The differences on Figure 3.17 are mainly due to the different forcing conditions (kd of short waves) and horizontal resolution of the computational domain.

For the bichromatic wave condition #1, a slight increase of the envelope amplitude takes place between x=0m and x=500m. This is likely related to the spurious higher harmonics introduced at the boundary due to first order forcing (Stokes ratio in this case is approx. 0.23). Between x=500m and x=2000m there is a small decay on the wave envelope amplitude. This effect is more pronounced on the simulation with lower horizontal resolution, so it is attributed to numerical dissipation.

A decay on the wave envelope amplitude along the numerical domain is also observed for the bichromatic condition #2. A drop on the envelope amplitude occur between x=0m and x=500m for all grid configurations, which is related to the determination of the boundary condition in SWASH. As for the tests with regular waves, this effect increases with the kd value of the waves. From x=500m to x=2000m a gradual decay on the envelope amplitude is noticed. As on the results of bichromatic condition #1, the decay is more pronounced when the horizontal resolution of 20 grid points per wave length is considered, so it is attributed to numerical dissipation. The resulting wave envelope amplitude at x=2000m is smaller for the wave condition #2.

The infragravity wave amplitude along the domain associated with the different bichromatic conditions and computational grid definitions is given on Figure 3.18.

At the incoming boundary (x=0m) the infragravity wave amplitude is determined by the second order boundary condition implemented in SWASH, which is generally in agreement with the analytical solution for the considered bichromatic conditions. Variations on infragravity wave amplitude along the domain can be attributed to the interaction with spurious free long waves

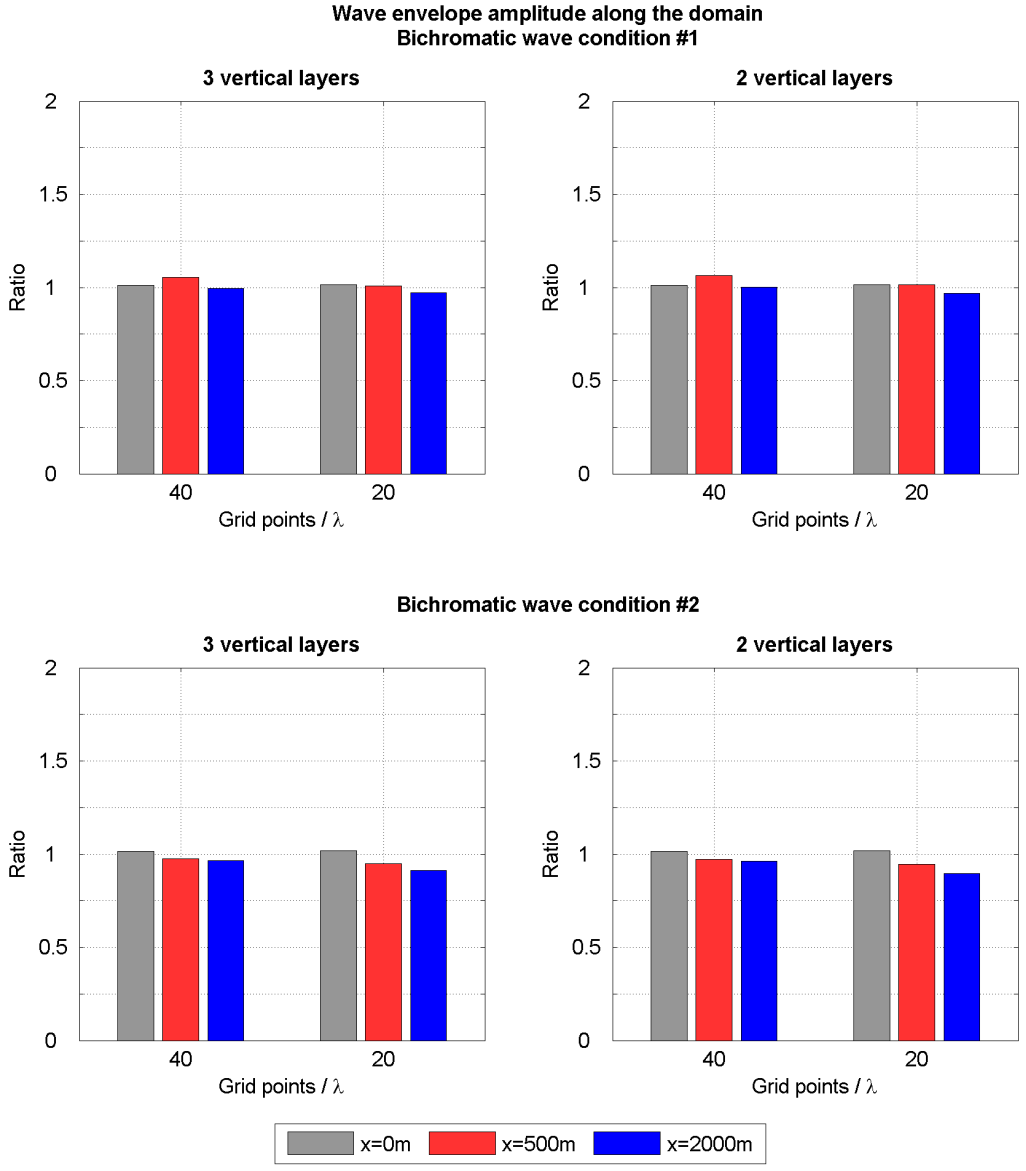

FIGURE 3.17: Modelled wave envelope amplitude along the domain of simulation relative to the wave envelope amplitude at the incoming boundary - bichromatic wave conditions #1 and #2.

generated at the boundary, and to changes on the short wave pattern due to numerical dissipation and non-linear effects (i.e., demodulation of the wave groups, SHEMER ET AL., 1998). Free and bound infragravity waves are not separated on the analysis because the non-linear interactions between short waves cause a demodulation of wave groups and therefore the wave field is not homogeneous on space (although these effects are considered to be small in the first 2km of the domain). Nevertheless, because the second order bound long wave is included on the boundary condition, the generation of spurious free long waves is expected to be limited (RIJNSDORP ET AL., 2012, 2014).

All simulations show a reduced infragravity wave at x=2000m. The bound long wave amplitude

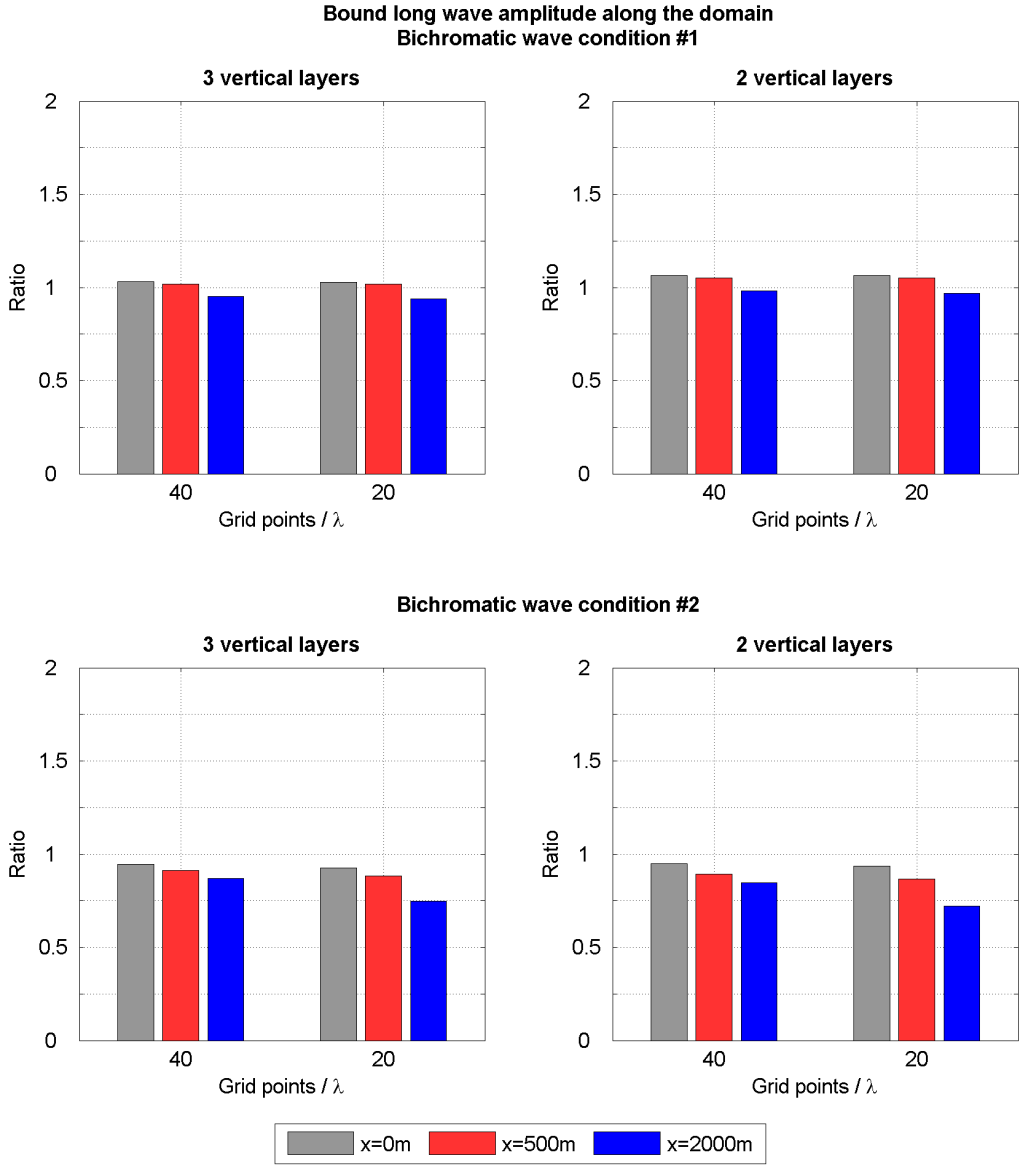

FIGURE 3.18: Modelled low frequency wave amplitude along the domain of simulation relative to the equilibrium bound long wave amplitude at the incoming boundary - bichromatic wave conditions #1 and #2.

is proportional to the amplitude of the short wave envelope squared, therefore larger errors are expected for the infragravity waves in comparisons to the deviations in the short waves (Figure 3.17). The decay on the infragravity wave amplitude are mostly explained by the changes reported for the short waves.

SWASH model is able to accurately reproduce the analytical bound long energy for the different wave and grid configurations considered on the tests. However, as expected, amplitude errors on the short waves lead to increased deviations on the predicted bound long waves.

3.2.2 Computation of forces acting on a ship: Bichromatic waves

The results of SWASH for the bichromatic wave conditions (#1 and #2) were converted into Harberth model input files using the coupling tool developed for the tests with regular waves. A description of the tool is given in Section 3.1.2. The vertical interpolation of the horizontal velocity components considered uniform velocity through each vertical layer of the wave model (see Figure 3.7 for an impression of the vertical distribution of horizontal velocities). The waves are considered to propagate towards the direction 225° on the body coordinate system. The specific ship considered in Harberth computations is the same applied on the calculations with regular waves: a 125,000m^3 LNG carrier (L×B×T: 273×42×11.5m). The mesh representing the hull of the vessel contains 1134 panels and 126 water line segments. Additional information about the ship is given on Table 3.5 and Figure 3.8.

As in the wave simulations with SWASH, in Harberth computations the bottom is considered to be 15m below the mean water surface level. The Green functions and retardation periods are both 3 minutes and the duration of the simulations is 20 minutes.

Harberth results consist of time series of total forces and moments on the six degrees of freedom. Further, Harberth results include separated time series containing the different contributions considered in the computation of forces:

- **First order forces and moments**
  - Froude-Krylov forces and moments
  - Diffraction forces and moments
- **Second order forces**
  - (I) Relative wave elevation
  - (II) Pressure drop due to first order velocity
  - (III) Product of 1st order pressure gradient and 1st order motion
  - (IV) Products of 1st order angular motions and 1st order inertia forces

The combination of all forcing terms provide the total forces and moments acting on the ship. The low frequency oscillations, with frequencies in the range of the wave groups, are subsequently separated from the higher frequency oscillations by means of a low-pass filter. Parameters derived from the time series of forces and moments associated to the bichromatic wave conditions #1 and #2 are given in Table 3.8 and 3.9, respectively.

The mean first-order forces and moments are generally very small, except for the moment around the y-axis. This is attributed to the asymmetry on the hull along the x-axis. The second-order

TABLE 3.8: Forces and moments acting on the ship associated to bichromatic wave conditions #1 and direction 225°. The short amplitude corresponds to the upper limit of the higher frequency oscillations; Phase indicates the lag between low frequency waves and force components; 1st and 2nd refer to first- and second-order forces.

Component		**Mean**	**Ampl. (short)**	**T_m (short)**	**Ampl. (long)**	**T (long)**	**Phase (long)**
Incident wave		0.0m	1.05m	15.8s	0.11m	166.1s	0°
Fx [MN]	**1st**	0.00	4.92	16.9s	0.30	165.8s	-92°
	2nd	-0.12	0.80	8.3s	0.12	166.8s	-1°
	Total	-0.13	4.95	16.9s	0.33	165.8s	-69°
Fy [MN]	**1st**	0.00	5.10	16.9s	0.77	165.8s	-92°
	2nd	-0.13	1.68	8.2s	0.15	167.3s	28°
	Total	-0.13	5.56	16.9s	0.71	165.8s	-81°
Fz [MN]	**1st**	-0.30	16.63	16.9	9.67	166.7	2°
	2nd	-1.61	1.49	8.4s	1.51	166.7s	0°
	Total	-1.91	16.86	16.9s	11.17	166.7s	2°
Mx [MNm]	**1st**	0.01	67.05	16.9s	2.97	167.5s	83°
	2nd	-0.30	7.47	9.5s	0.66	168.0s	55°
	Total	-0.29	67.71	16.9s	3.57	167.7s	79°
My [MNm]	**1st**	-3.07	2857.29	16.8s	128.80	165.8s	-72°
	2nd	-16.61	144.27	8.8s	24.58	165.8s	-49°
	Total	-19.68	2860.76	16.9s	152.28	165.8s	-67°
Mz [MNm]	**1st**	-0.02	1544.82	16.9s	6.47	165.7s	-17°
	2nd	-57.73	65.82	7.4s	56.42	166.7s	-1°
	Total	-57.75	1595.87	16.9s	62.62	166.5s	-3°

contribution have a mean component (i.e. mean drift force), which accordingly corresponds to the major part of the mean total forces and moments.

The oscillating wave loads at the frequency of the short waves are the greatest contribution to the total forces and moments signal. These are dominated by the first-order components (Froude-Krylov forces + Diffraction forces), with oscillating period similar to the (short) waves. The second-order components are considerably smaller and correspond to products of the first-order quantities at the incident wave frequency. So besides a mean or slow-varying contribution due to wave grouping, the second-order forces have high frequency oscillations at approximately twice the frequency of the incident waves. This contribution changes the shape of the total signal but not alters considerably the amplitude of the total forces. Further, the horizontal motions of floating bodies in response to these high-frequency forces is generally small and they are often disregarded in dynamic analyses.

The low frequency variations on the wave loads take place on the time scales of the wave groups. These components are of prime importance on dynamic mooring studies because they overlap

TABLE 3.9: Forces and moments acting on the ship associated to bichromatic wave conditions #2 and direction 225°. The short amplitude corresponds to the upper limit of the higher frequency oscillations; Phase indicates the lag between low frequency waves and force components; 1st and 2nd refer to first- and second-order forces.

Component		**Mean**	**Ampl. (short)**	**T_m (short)**	**Ampl. (long)**	**T (long)**	**Phase (long)**
Incident wave		0.0m	0.96m	6.4s	0.017m	66.6s	0°
Fx [MN]	**1st**	0.00	1.78	6.9s	0.21	66.6s	-94°
	2nd	-0.04	0.07	3.3s	0.05	66.7s	-291°
	Total	-0.04	1.79	6.9s	0.16	66.6s	-89°
Fy [MN]	**1st**	0.00	2.68	6.3s	0.45	66.6s	-98°
	2nd	-0.42	0.20	3.3s	0.32	66.6s	-337°
	Total	-0.42	2.71	6.3s	0.40	66.5s	-55°
Fz [MN]	**1st**	-0.16	3.71	7.0s	0.94	66.6s	-340°
	2nd	-0.29	0.03	3.6s	0.19	66.6s	-3°
	Total	-0.45	3.71	7.0s	1.12	66.6s	-344°
Mx [MNm]	**1st**	0.00	22.39	6.3s	1.55	66.7s	-291°
	2nd	-1.31	0.68	3.8s	0.85	66.6s	-10°
	Total	-1.31	22.33	6.3s	1.90	66.6s	-318°
My [MNm]	**1st**	-6.22	515.48	6.3s	67.92	66.6s	-90°
	2nd	-4.07	1.82	4.3s	14.75	66.6s	-85°
	Total	-10.29	516.06	6.3s	82.61	66.6s	-89°
Mz [MNm]	**1st**	-0.01	358.93	6.9s	17.48	66.6s	-10°
	2nd	-10.19	20.76	3.3s	20.83	66.7s	-276°
	Total	-10.20	356.87	6.9s	26.77	66.7s	-317°

the resonant frequency range of the moored ship and motions with these frequencies are barely damped. The first-order low frequency forces are due to the second-order waves (i.e. bound long waves), and the second-order contribution is the slow varying drift force due to wave grouping.

Although the bound long wave amplitude associated to the bichromatic wave condition #2 is almost one order of magnitude smaller than condition #1, the first-order slow varying loads are of the same order for the two conditions (except for Fz that is directly related to the long wave amplitude). The other modes are related to the bound long wave steepness, which is similar to the two conditions ($\lambda_{blw,\#1} = 1791m$ and $\lambda_{blw,\#2} = 405m$, giving a wave steepness of $6.1 \cdot 10^{-5}$ and $4.2 \cdot 10^{-5}$, respectively). The low frequency second-order loads due to the slow varying drift force are proportional to the short wave amplitude squared and dependent on the short wave frequency and direction. These second-order loads are of the same order of magnitude for the two bichromatic wave conditions.

The horizontal low-frequency first-order forces (Fx and Fy) and moments (Mx and My) tend to be 90° out of phase with the bound long wave, which corresponds to the maximum water level

gradients on the bound long wave. The first-order slow-varying vertical force (Fz) is generally in phase with the wave groups. There is no clear relation between the phases of the first- and second-order low-frequency loads, so the resulting total low frequency forces and moments can be larger or smaller than the main individual component.

Fixed mooring structures are usually located on areas protected from direct short wave incidence. On these situations, the second-order waves (i.e. bound long waves) and second-order loads are expected to be considerably small relative to the first-order quantities. The free/released infragravity waves are likely the major contributor to the slow-varying total wave loads, being part of the first-order load signals.

3.3 Conclusions

The main findings from this chapter are listed below:

- The required computation time in SWASH simulations is strictly related to the horizontal resolution of the model. In practical applications a trade-off should be made between the representation of the higher frequencies in the spectra and the computation time. Based on the results of the tests with regular waves, a resolution of 20 grid points/wave length can give sufficiently accurate results for general engineering applications;

- The tests with regular waves indicate that dispersion errors in SWASH are larger for non-linear waves[3] and low horizontal grid resolution (say ≈10 grid points per wave length). Nevertheless, these errors are generally small enough to be neglected on studies of wave penetration in harbours;

- For waves with high kd value (say $kd \geq 3$), a drop in wave energy near the boundary can lead to considerable wave amplitude errors in SWASH. These errors can be partially reduced by increasing the number of vertical layers. Although, waves with large kd values in coastal areas have usually only little energy and therefore are not of prime relevance in wave penetration studies. For example, in 25m water depth, which is a representative water depth at the incoming boundary of detailed coastal wave models, kd values larger than 3 correspond to wave periods shorter than 5.8 seconds. These periods are generally away from the peak of the wave spectra for energetic conditions.

- A gradual decay of wave energy along the domain due to numerical dissipation may cause amplitude errors in SWASH, specially for bigger waves and low horizontal resolution.

[3]The degree of non-linearity relates to the wave steepness and relative water depth, and can be determined with the ratio between the amplitude of the second-order Stokes correction and the primary wave amplitude (e.g., Stokes ratio - description available in Section 3.1.1)

These errors are minimized by applying higher order numerical schemes to the advection terms in the momentum equation and/or by increasing horizontal resolution on cost of longer computation times;

- The boundary conditions implemented in SWASH do not include second-order higher harmonics. When the wave conditions are non-linear[3] at the model boundary, spurious free higher harmonics are introduced at the boundary point in order to match the imposed symmetrical signal. The spurious short waves can propagate through the domain, specially if the associated frequency and *kd* number are not too large for the given computational grid resolution. Nonetheless, the spurious waves are by definition shorter and smaller than the most energetic waves (e.g., waves associated to the peak of the spectra), so the associated effects are expected to be relatively small in studies of wave penetration in harbours.

- The bound long wave amplitude is dependent on the amplitude and *kd* value of the short waves. SWASH can accurately reproduce the bound long waves induced by bichromatic conditions, provided that the short waves are well represented in the model (i.e., the selected model settings ensure small amplitude errors).

- The agreement between Harberth model results for the different wave information (i.e., defined from SWASH simulations and determined based on linear wave theory) indicate that the coupling procedure is consistently implemented in the developed tool.

- Regarding the Harberth computations based on SWASH simulations of regular waves with H=0.01m and H=1m, the first- and second-order forces are indeed linearly and quadratically related to the wave height. This coherence implies that the effects of non-linearities in the incident waves are not relevant for those conditions, so comparisons with results of the Wavescat model, which is purely based on the linear potential theory, are consistent.

- The first-order forces and moments acting on a ship computed with 'SWASH model, the developed coupling tool, and Harberth model' are in satisfactory agreement with Wavescat model results for the tested conditions.

- The second-order forces and moments computed with 'SWASH model, the developed coupling tool, and Harberth model' are in reasonable agreement with Wavescat model results for the tested conditions. The reported differences are mainly related to the simplification in the Harberth model, where the ship is allowed only to heave, roll and pitch (in Wavescat model the ship can move in 6 degrees of freedom). Further, if relevant viscous roll damping should be taken into account to better represent the near resonance roll motions. The influence of the simplified motions might be relevant in applications where the

first-order waves and the associated surge, sway and yaw motions are significant. Otherwise and especially in coastal waters, the low-frequency loads will be likely dominated by the low-frequency waves, which are taken into account in the computations of first-order forces. An example can be a coastal harbour partially sheltered from the short waves and surrounded by relatively shallow and exposed areas.

- The computed forces and moments for the bichromatic wave conditions indicate that the first-order loads oscillating on the same frequencies as the short waves are generally dominant. The higher frequency second-order loads are a relatively small contribution to the total 'high-frequency' forces and moments. The low-frequency forces and moments, with the frequency of the wave groups, are about one order of magnitude smaller than the 'high-frequency' loads. For the simulated conditions, the contribution of the slow-varying second-order drift forces is usually smaller than of the low-frequency wave. Therefore, especially when the low-frequency waves are relevant (i.e., shallow waters, low kd's), possible inaccuracies in the computation second-order forces due to the incorporated assumptions in Harberth have only limited impact on the total low-frequency forces.

- For general applications on wave penetration in coastal harbours (typically $kd < 3$) the developed coupling tool does not influence the accuracy of the overall procedure, neither introduces stricter requirements. Therefore, in most applications the coupling process will not be critical.

- When 3 and 2 vertical layers are considered in SWASH, deviations on the computed forces/moments may occur especially for large kd values (say $kd \gtrsim 5$). In such conditions the vertical profiles of particle velocity and pressure are more curved, requiring more layers to properly prescribe the wave quantities along the hull of the ship. Thus, more vertical layers should be considered in the SWASH simulations when the forces associated to waves with large kd values are expected to be relevant.

- Assuming that Harberth model is accurate within its range of application, the wave modelling is the most critical process on the overall approach potentially influencing the accuracy of the results. Amplitude errors in the wave model result in a proportional deviances on the prediction of first-order wave forces and moments. Slow-varying forces and moments are associated to second-order terms (i.e. second-order waves and second-order forces), so inaccuracies on the short wave predictions result in larger deviances of low-frequency forces and moments. Since these loads are of prime importance for dynamic mooring studies, a precise representation of the short waves in the SWASH model is required to obtain consistent estimates of the wave loads.

Chapter 4

Validation of the tool

4.1 Description of the validation model

In this chapter the results obtained with the combination of SWASH, the developed coupling tool, and Harberth are compared with data from physical scale model. The model tests were conducted at WL|Delft Hydraulics (actual Deltares), in the directional wave basin Vinjé with a modelled uniform water depth of 20m (WL|Delft Hydraulics report, 2004). Figures 4.1 and 4.2 give an impression of the basin setup during the experiments.

The measured datasets include waves at different locations in the basin and forces and moments acting on a restrained ship. The natural frequencies of the mounted ship forces frame were also determined. The ship used in the tests is a Panamax container vessel (L×W×D = 255 × 32.26 × 12.00m) at a model scale of 1:100 (Table 4.1). The scales are provided on prototype scale using Froude scaling. The equality in Froude number (F_n = *inertia force/gravity force* = $U/\sqrt{gd}$) between the model and full scale ensure that gravity forces and therefore surface waves are correctly scaled.

Table 4.1: Dimensions of the Panamax container vessel.

Designation	Symbol	Unit	Magnitude
Length between perpendiculars	L_{pp}	m	255.00
Breadth	B	m	32.26
Draft	d	m	12.00
Displacement volume	Δ	m^3	58,660
Centre of gravity above keel	$\overline{KG}$	m	13.5
Transverse radius of gyration	k_{xx}	m	12.4
Longitudinal radius of gyration	k_{yy}	m	69.25
Longitudinal radius of gyration	k_{zz}	m	70.35

A large steel frame is used to hold the ship on its positions and to provide support for six force transducers to measure the forces on the ship in the six degrees of freedom. The purpose of the experiment is to model the wave forces only, so the ship is restrained and the mooring lines did not have to be represented in the physical model. The simulation of ship motions excited by the wave forces is rather straightforward, although the representation of the low-frequency wave forces is critical for the correct modelling of the horizontal ship motions (Van der Molen, 2006).

The tests consisted of series of regular waves, irregular long-crested waves and irregular short-crested waves. In each case several tests were performed with different (significant) wave heights, (peak) wave periods and (mean) wave directions. Measurements of waves and forces are done for two basin situations:

1. the ship in open water: ship is in the center of the basin (position GRSM in Figure 4.2), and the x-axis on the ship coordinate system makes an angle of 120° with the Cartesian coordinate system given on Figure 4.2.

2. the ship in a schematic harbour basin: the position of the ship in the basin is the same as in the open water tests. The internal dimensions of the harbour basin are 1200 x 400m (prototype scale), with the ship located in the middle of the longest wall (i.e. 600m to each side from the center of the ship). The ship's mid line is 20m away from the quay wall, resulting in a gap of approximately 4m between the ship and the wall. The outer part of the wall is filled with gravel in order to minimize reflection back to the wavemaker.

To specify the wave directions, a global coordinate system is used with the origin at the wavemaker, the x-axis directed into the basin and perpendicular to the wavemaker. The harbour basin and the ship are placed under an angle of 120° with respect to the global coordinate system. Figure 4.2 shows the layout of the tests, with the wave maker on the left side and gravel slopes on the opposing side to minimize wave reflection. The wave gauges GHM01, GHM02 and GHM03 are located at 300m from the wavemaker and 660m apart. The gauge GRSM is situated at the position of the midpoint of the ship.

The wavemaker in the basin consists of a large number of independent piston type paddles, enabling wave generation in all directions including directional spreading. The second order long waves are included in the waveboard control signals to produce the correct wave motions in the basin up to second order and avoid otherwise generated spurious long waves. The waveboard is equipped with active reflection compensation to absorb waves reflected from the basin, thus reducing the development of unwanted oscillations (Van Dongeren et al., 2001).

The physical modelling of low-frequency waves is rather difficult because the active reflection compensation method cannot eliminate all spurious effects, especially if the reflected waves are

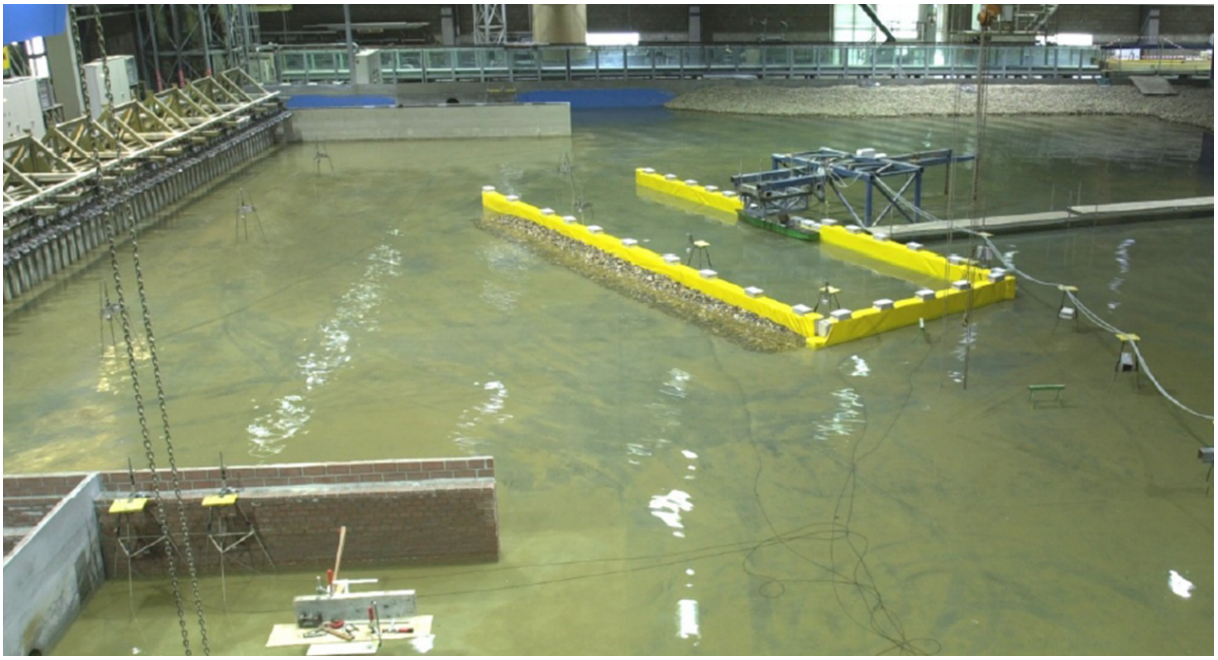

FIGURE 4.1: Model test set-up.

obliquely incident on the wavemaker. The reflected short waves, on the other hand, are much lower than the incident waves due to breaking of short waves against the slopes.

Regarding the measurements of forces on the ship connected to the force frame, problems occur especially in the correct measurement of the roll moments (Mx). This is because Mx is mainly measured as (relatively small) differences between two vertical forces.

The wave conditions considered on the validation are listed on Table 4.2. Tests A correspond to uni-directional regular waves. For the spectral forcing a JONSWAP spectra with peak enhancement factor of $\gamma = 3.3$ is used (Tests B and C).

TABLE 4.2: Wave conditions considered in the validation of the approach (wave directions on the global coordinate system). On Tests A and B the ship is in open water; on Tests C the ship is in the harbour basin. The numbers in brackets are the original naming from WL|DELFT HYDRAULICS REPORT (2004) and VAN DER MOLEN (2006).

Test	$\mathbf{H_s}$ **(m)**	$\mathbf{T_p}$ **(s)**	**Dir (°)**	**Spreading**	**Jonswap** γ
A1 (2.1.2)	2	10	0	Uni-directional	(Regular)
A2 (2.1.5)	2	10	30	Uni-directional	(Regular)
B1 (2.3.1.2)	1.5	10	0	$\cos^2$	3.3
B2 (2.3.1.4)	1.5	15	0	$\cos^4$	3.3
C1 (4.3.1.2)	3	15	0	$\cos^2$	3.3
C2 (4.3.2.1)	6	10	30	$\cos^2$	3.3
C3 (4.3.3.2)	6	15	30	$\cos^4$	3.3

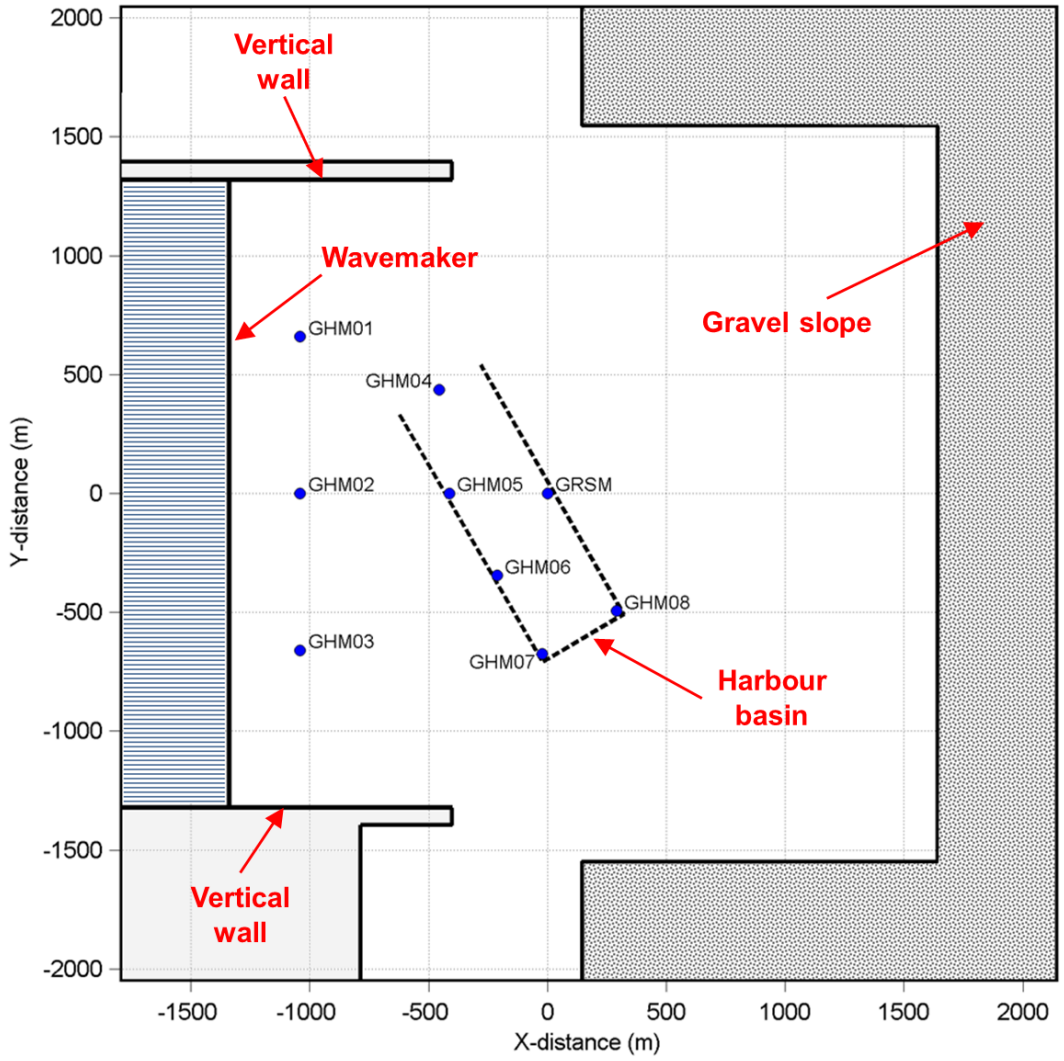

FIGURE 4.2: Layout of the test basin. The wave maker is indicated on the left side of the figure (X $\approx$ -1400m ; -1400m $\leq$ Y $\leq$ 1400m). A gravel sloping edge is taken on the opposite margins in order to reduce wave reflection. When present, the midpoint of the ship is positioned at the origin of the coordinate system (X=0m, Y=0m).

4.2 Wave modelling and computation of wave forces acting on a ship

The SWASH wave model was configured to represent the testing basin. The computational grid has maximum resolution of approximately $4\times4m^2$ in the areas of primary interest, and grid cells of $11\times11m^2$ at the opposite corners of the domain (Figure 4.3). Following from the linear wave theory, a wave with T=10s is 121m long on 20m water depth. Therefore, the finer grid resolution corresponds to approximately 30 grid points per wave length for this condition.

When the model is forced with a wave spectrum, higher frequency components are present in

the simulation, which might be not so well represented by the numerical grid. For instance, a wave with 5s period in 20m water depth is 39m long. In this case the finer grid resolution corresponds to approximately 10 grid points per wave length, which may lead to inaccuracies especially if the height of the short waves is relatively large (see Section 3.1.1). It is considered, however, that only a limited ammount of energy is associated with the high-frequency bands of the spectra and the corresponding forces and moments acting on a ship are relatively small, also because those waves are short relative to the ship's size. Therefore, the drawbacks related to the grid spacing are expected to be marginal.

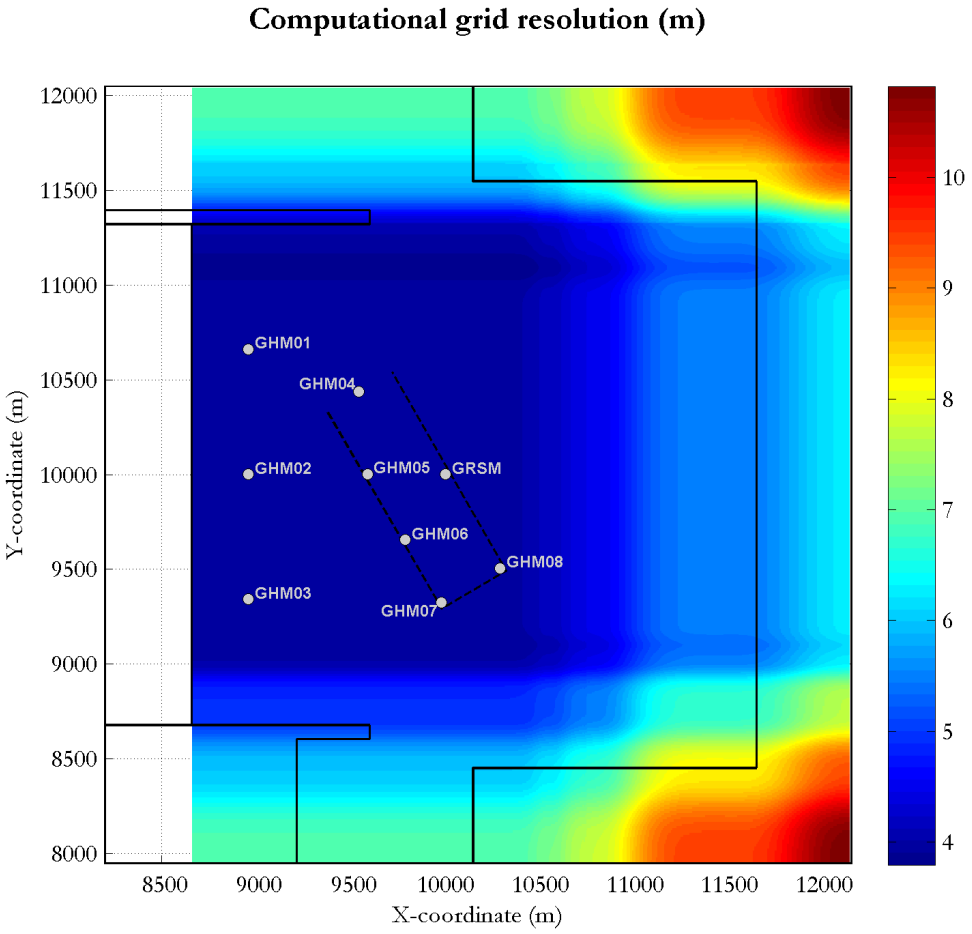

FIGURE 4.3: Horizontal resolution of the computational grid ($\sqrt{\Delta x \cdot \Delta y}$).

The bottom level is 20m below the mean water level. The vertical side walls near the wave maker (left part of the domain) and the gravel slopes are included in the simulations as structures (numerical instabilities occurred when including the vertical walls as excluded computational cells or in the bottom level definition). The vertical side walls are 40m high from the bottom. The side slopes have steepness of 1:5. Reflection, dissipation and transmission through the structures are determined by SWASH based on its porosity and d_{50}. The porosity of the side walls is defined as zero (though the minimum value of 0.1 is adopted by SWASH), which mean

that this structure is impermeable. The porosity considered for the side slopes is 0.45. The d_{50} of both structures is 2m. The representation of the harbour basin is described in Section 4.2.3, in which the Tests C are treated.

Similarly to the active reflection compensation used in the model tests, the incoming boundary condition in SWASH is weakly reflective, which means that up to a certain extent reflection can be minimized by compensating the signal for the outgoing waves. It is known, however, that both the mechanical and numerical wavemaker have limitations to compensate for short waves and waves approaching in a large angle (say more than 30° with the wavemaker normal). Because their individual characteristics may differ, it may cause differenced between the wave fields in the physical tests and numerical simulations.

The time steps considered in SWASH computations are associated to Courant numbers in the order of 0.6. The first 12 minutes of the measured and simulated datasets are neglected to prevent the influence of the still initial conditions on the different analysis. This is approximately the time required for a wave with T=5.4s to cross the domain, reflect against the gravel slope, and get back at the wavemaker (considering wave propagation along the x-axis of the basin, see Figure 4.2). The celerity of longer waves is larger and therefore the same distance is covered in a shorter time.

The 12 minutes spin up time proved to be sufficient for the Tests A with regular waves of T=10s. For Tests B and C with spectral conditions, the main components of the spectra are assumed to be stabilized along the basin after the considered spin up time. Nevertheless, the duration of the simulations with spectral wave forcing (Tests B and C) is 3 hours, so possible small effects of the initial conditions remaining after the first 12 minutes are likely minimized in the overall analyses.

The bottom friction coefficient is calculated using the Manning formula with a coefficient of $0.019 m^{1/3} s$, which gives a friction coefficient of $c_f = 0.0013$ in 20m water depth. The 'Adapted set' of numerical schemes for the advective terms in the momentum equation is applied in these simulations: the second order Central Differences scheme is applied for the vertical advection of horizontal moment, the second order BDF scheme is applied to the horizontal advection of vertical moment, and the vertical advection of vertical moment is treated using the first order upwind scheme (see Table 3.2). As identified on the tests with regular waves (Section 3.1), with these numerical schemes the amount of numerical dissipation is considerably reduced relative to the 'Default set' of schemes. This is specially the case under non-linear wave conditions.

For waves propagating over intermediate distances (say $\mathcal{O}(10)$ wave lengths) in the absence of strongly sheared currents, turbulence has only marginal effects on the wave motion and can – to a good approximation – be neglected (Rijnsdorp et. al, 2014). This is the case for tests A and B, in which relatively small wave heights are considered. On tests C the significant wave

heights exceed 6 m, so relatively large bed shear stresses are expected to take place. To allow the influence of bottom friction to extend over the vertical, some vertical mixing is introduced by means of the vertical exchange of momentum due to turbulent stresses (background eddy viscosity of $10^{-3}m^2/s$).

Depth induced wave breaking is not a dominant process in these tests, still the *Breaking* option in SWASH was activated in the initial tests. This option might be included to better reproduce the development of bore-like flows in the surf zone when poor vertical grid resolutions are applied. A general description of this option is given in Appendix A; for a detailed description one is referred to Smit et. al (2013).

Numerical issues occurred near the fully reflective vertical walls during simulations of extreme wave conditions (Hs $\gtrsim 6m$) when the *Breaking* option was activated. It occurred because the critical vertical velocities were occasionally exceeded and the non-hydrostatic pressures were locally neglected. This shows to be a good approximation in the surf zone (Smit et. al, 2013; Rijnsdorp et. al, 2014), but not at 20 m water depth with highly non-hydrostatic waves ($T < 10s$). By neglecting the non-hydrostatic pressures, pressure gradients integrated over the water depth became too large leading to unrealistic fluxes. The issue reinforces itself as the extreme fluxes cause high vertical velocities on the adjacent cells and consequent negligence of non-hydrostatic pressures at those nearby locations, causing the model to stop due to unacceptable results. This was resolved by not considering the *Breaking* option in the simulations of extreme waves. It is highlighted however that independently of the *Breaking* option, energy dissipation due to wave breaking process is intrinsically included in SWASH formulation while balancing mass and momentum in regions where the wave height is comparable to the local water depth.

The computation of forces acting on the ship using Harberth model involves less parameter and configuration choices in comparison to the wave model SWASH. The basic settings considered in Harberth computations are similar to ones used in Chapter 3 (Table 3.6), but the simulation time is longer and a different mesh is employed. The mesh of the Panamax ship representing the modelled vessel is given in Figure 4.4.

In the Tests C, with the ship in the harbour basin, a quay wall at 20m to starboard side from the ship centre line is considered in the computation of the scattered and radiated potentials with the linear potential model. The coefficient ϵ_t determines the transmission of wave energy through the quay wall in Harberth, and is a numerical solution to artificially include friction and viscous effects between the quay wall and the ship. As recommended in Van der Molen (2006) and Mike21-Harberth User Manual (2007), the transmission coefficient $\epsilon_t = 0.02$ is used in the simulations. It represents a smooth quay wall close to the ship. In case of rough structures such as rubble-mound breakwaters the value could be much larger.

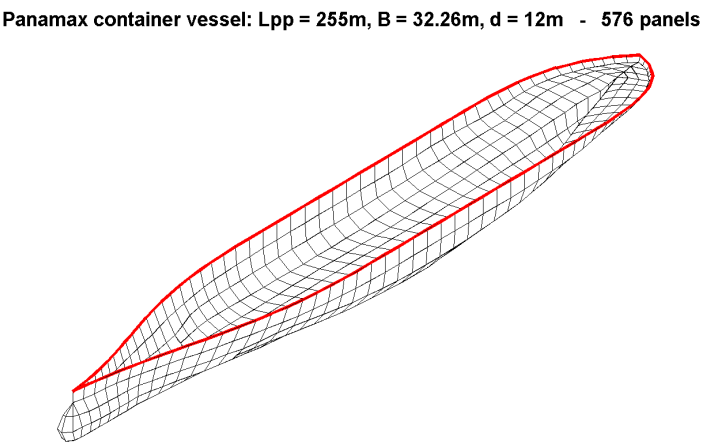

FIGURE 4.4: Panel description of the Panamax container vessel (576 panels and 104 water line segments).

The coupling tool developed in Chapter 3 to combine SWASH model and Harberth was extended to cope with 3D wave results recorded during the SWASH simulations (in this case every 0.8 s) for a volume surrounding the ship. The size of such output file can easily exceed 1GB, and the number of calculations to define the wave quantities at the collocations points along the hull of the ship ($\approx$ 500 points) and every time step during approximately 3 hours is rather large. The coupling Matlab routine used to create Harberth input files from SWASH outputs had to be optimized to prevent lack of RAM memory and speed up the calculations to feasible times ($\approx$ 15 minutes).

4.2.1 Tests A1 and A2: Regular waves with the ship in open water

Regular waves with H=2m and T=10s are considered in these tests. The propagation direction relative to the perpendicular of the wavemaker are 0° (A1) and 30° (A2). In the model tests the mechanical wavemaker was set differently for the oblique wave conditions: a number of wave paddles in the 'upper' side of the wavemaker (see Figure 4.2) was de-activated to prevent excessive reflection against the vertical wall. In the other end of the wavemaker waves were generated towards the side wall to form a wider homogeneous wave field. These settings were not implemented in the numerical simulations, therefore the characteristics of the wavemaker are uniform for both wave conditions A1 and A2.

The wave conditions were simulated in the SWASH model considering 2 and 3 vertical layers. Figure 4.5 gives an overview of the model results along the entire domain, including the dissipation of short wave energy along the porous side slopes (indicated by the dashed lines).

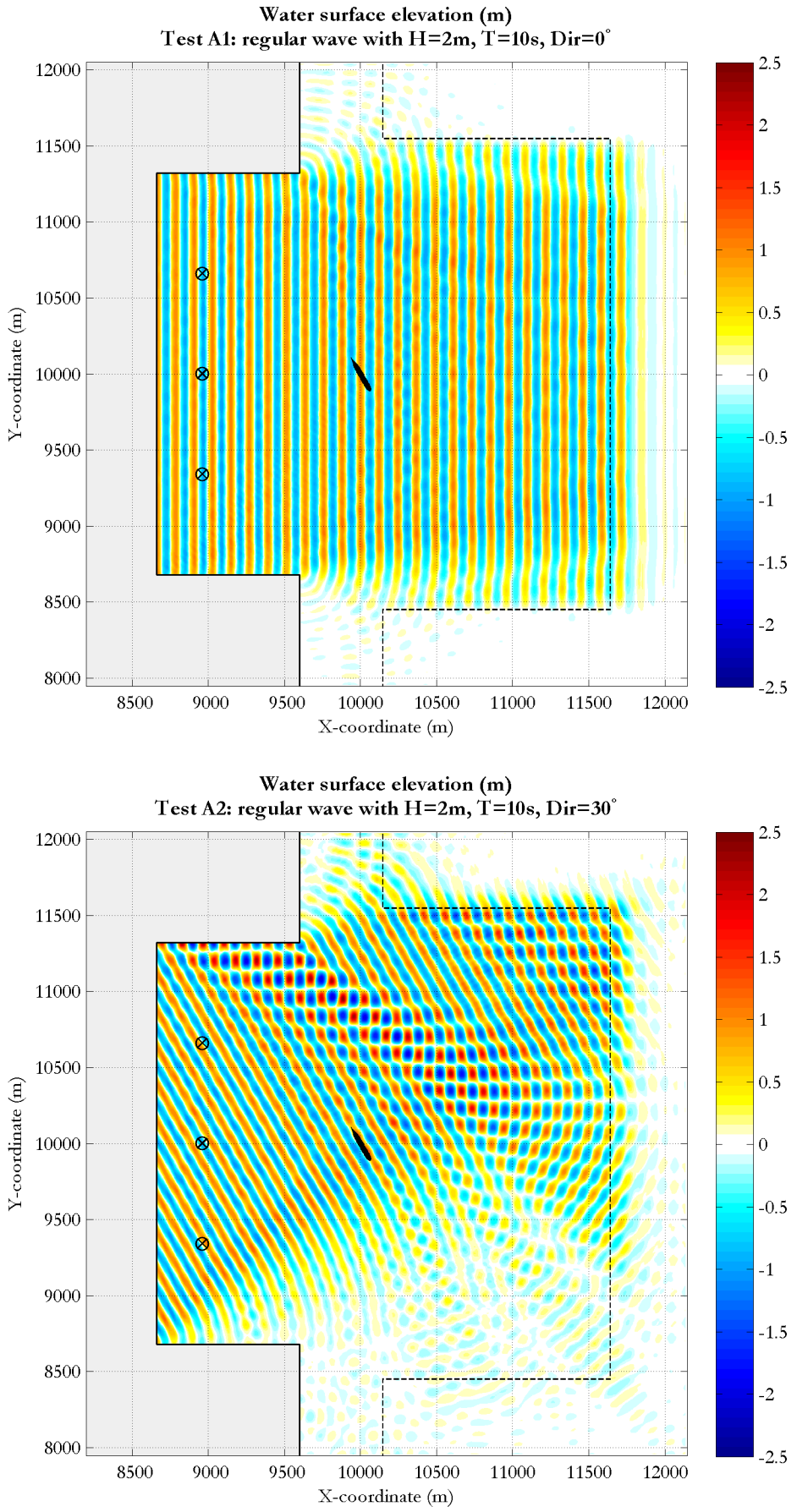

FIGURE 4.5: Simulated instantaneous water surface elevation along the computational domain. Test A1 and A2. The markers indicate the location of wave measurements for these tests.

Wave reflection against the vertical wall can be noticed on the upper left corner of Figure 4.5 (bottom plot), causing the so-called diamond pattern resulted from the interaction of two wave trains with different directions of propagation. On the bottom left corner wave diffraction takes place, spreading the wave energy towards the sheltered area adjacent to the vertical wall. The region where the ship is located is not significantly affected by those disturbances and the wave condition is nearly regular. For the Test A2 the wave direction and ship orientation have 90° difference (i.e. beam waves).

The mean wave amplitudes measured and simulated for the wave gauges GHM01, GHM02 and GHM03 are given in Table 4.3. These are computed from the recorded time series of water surface elevation, excluding the first 12 minutes of simulation to prevent the influence of the still initial condition.

TABLE 4.3: Measured and simulated wave amplitudes in meters. The three wave gauges are located along the wave maker (see Figure 4.2). The imposed regular wave amplitude for the simulations is 1m.

	Wave gauge	**Measured**	**Simulated (2 layers)**	**Simulated (3 layers)**
Test A1	GHM01	1.05	0.98	0.99
	GHM02	0.80	1.02	1.04
	GHM03	0.71	0.94	0.97
Test A2	GHM01	1.16	0.94	0.99
	GHM02	0.90	0.91	0.92
	GHM03	1.48	1.01	1.01

The results given in Table 4.3 indicate a variation of regular wave height along the wave maker, which is more pronounced on the measured data set. Although, the waves signals at the different locations are indeed regular with 10s period. The wave height variations can be attributed to the superposition of the waves imposed by the wave maker and reflected along the limits of the basin/computational domain. Regarding the measurements they can also be due to inaccuracies on data sampling and/or on the wavemaker (i.e. different settings of the wavemaker near the side walls during Test A2, deviations on the imposed wave height, and introduction of spurious directional components). Wave reflection against the restrained ship, which is present only in the physical scale tests, is not expected to explain the large variations of wave height measured along the wave gauges because of the relatively small dimensions of the ship relative to:

- the wave length: waves are expected to diffract around the body;
- the water depth: at most partial reflection would occur;
- the basin: the reflected wave energy would spread out being not significant away from the body.

Alternatively, different porosities and grain diameters along the side slopes could be tested on SWASH model, enhancing wave reflection and possibly increasing the spatial variation of wave height along the domain of simulation. However, the above mentioned additional tests were not made since short wave reflection is generally unwanted on scale model tests (and for this reason the gravel slopes were built on the basin). Further, the variation on wave height may be associated to the other argued reasons.

SWASH model results around the hull of the ship were converted into Harberth input files using the coupling tool described on Section 3.1.2 and extended to handle 3D model results. The constant and linear (sloping) vertical profiles through each model layer were considered for the vertical interpolation of horizontal velocities. Further, SWASH simulations with 2 and 3 vertical layers of Tests A1 and A2 were included in the verification, resulting in 8 Harberth simulations for the validation tests with regular waves. The results of these simulations are compared with the measured forces and moments on Figure 4.6. Since the ship is restrained to a fixed position on the scale model tests, only the first two second order load components are taken into account in the comparisons (components III and IV are second order corrections due to the moving body).

In general the comparisons of the measured and simulated waves loads acting on the ship are satisfactory, specially for the three force components and the moment around the y-axis. The comparison of moments around the x-axis indicate good agreement for Test A1, whereas for A2 the simulations underestimate this moment component. This mismatch may be related to the difficulties in determining the 'roll moment' (Mx) from the forces measured by the transducers, since the roll moment is measured as a (small) difference between two large components (Van der Molen, 2006). For both tests A1 and A2 the simulated moments around the z-axis are smaller than the measured moments.

Van der Molen (2006) used data from the same experiment in the validation of Harberth model. In a test with passing ship waves similar differences between measured and simulated roll and yaw moments were found. The comparisons also included the results of computations using the frequency-domain panel model DELFRAC, which is widely validated and can be considered a reliable tool. The results of DELFRAC were nearly identical to the ones associate to Harberth for all force and moment modes. This suggests that the observed differences are likely associated to factors not directly related to the numerical tools applied, such as inaccuracies on measurements and on the representation of the hull of the ship in the mesh. Nevertheless, possible differences between the wave fields in the vicinity of the ship may also explain the observed differences in the associated wave loads.

Results associated to SWASH simulations with different vertical resolution (i.e. 2 and 3 layers) and using the different methods for vertical interpolation of horizontal velocity are similar. These results are consistent with the findings from Chapter 3, which indicates that for relatively small

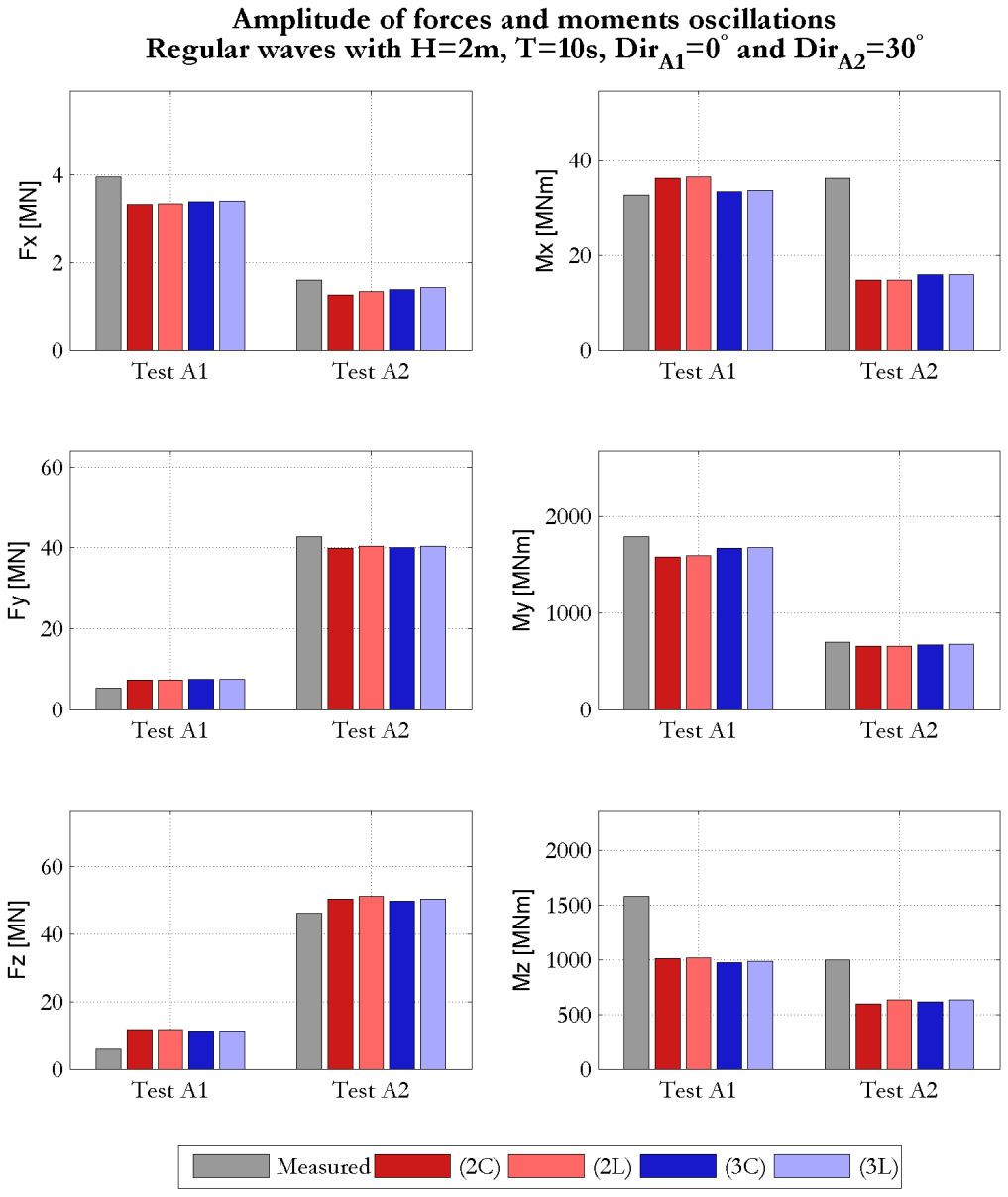

FIGURE 4.6: Measured and simulated forces acting on the Panamax vessel exposed to regular waves: Tests A1 and A2, SWASH model with 3 and 2 vertical layers, and constant (C) and linear (L) vertical profiles of horizontal velocity.

kd values (say $kd < 3$) the methods of vertical interpolation and the number of vertical layers (provided that at least 2 layers are taken) have small influence on the computed loads.

4.2.2 Tests B1 and B2: Spectral waves with the ship in open water

In Tests B1 and B2 the wave conditions are represented by JONSWAP spectra with significant wave height of 1.5m, propagation direction normal to the wave maker (0° Cartesian), and peak wave period of 10s and 15s, respectively. The duration of these simulations must be sufficiently long to minimize the influence of the still initial conditions and ensure a consistent estimation of the wave spectra and wave parameters at different locations.

The required duration of the simulations is determined based on the measured wave dataset for test B1 and B2, which have a duration of 5 hours in prototype scale. Wave parameters were determined varying gradually the length of the analysed time series, starting the calculations at 12 minutes after the beginning of the test (the duration of the spin up time is discussed in Section 4.2). Spectral parameters are derived from the total spectral and the low-frequency bands ($\leq 0.03Hz$). The results considering different realization times are made relative to the wave parameters associated to the complete time series (only excluding the initial 12 minutes). It implies that the relative results after 5 hours are necessarily '1' even if they are not sufficiently converged, because the final parameters are the reference for calculating the relative deviations. This verification is presented on Figure 4.7.

After 3 hours of the experiment, the total wave heights are only slightly affected by increasing the length of the analysed time series. Differently, the bottom plot in Figure 4.7 indicates that the determined long wave heights are considerably influenced by the length of the time series. These large relative deviations are associated to the small low-frequency wave heights (in the order of 0.03m), which makes the relative results rather sensitive to small absolute errors.

The absolute low-frequency wave heights for Tests B1 and B2 as a function of the duration of the analysed time series are given in Figure 4.8. In this case the convergence of the absolute results is more clear, evidencing the limitation of analysing relative deviations for such small quantities.

Based on the upper plot in Figure 4.7 and Figure 4.8, it is justifiable to consider a simulation time in SWASH of three hours, so that the computation effort is reduced without affecting the total wave parameters. It should be kept in mind that especially the relative comparisons of low-frequency parameters might be influenced by the duration of the simulation and the relatively small absolute quantities.

Instantaneous maps of simulated water surface elevation at the ending times of Test B1 and B2 are given on Figure 4.9. The differences in wave frequency and directional spreading are clearly

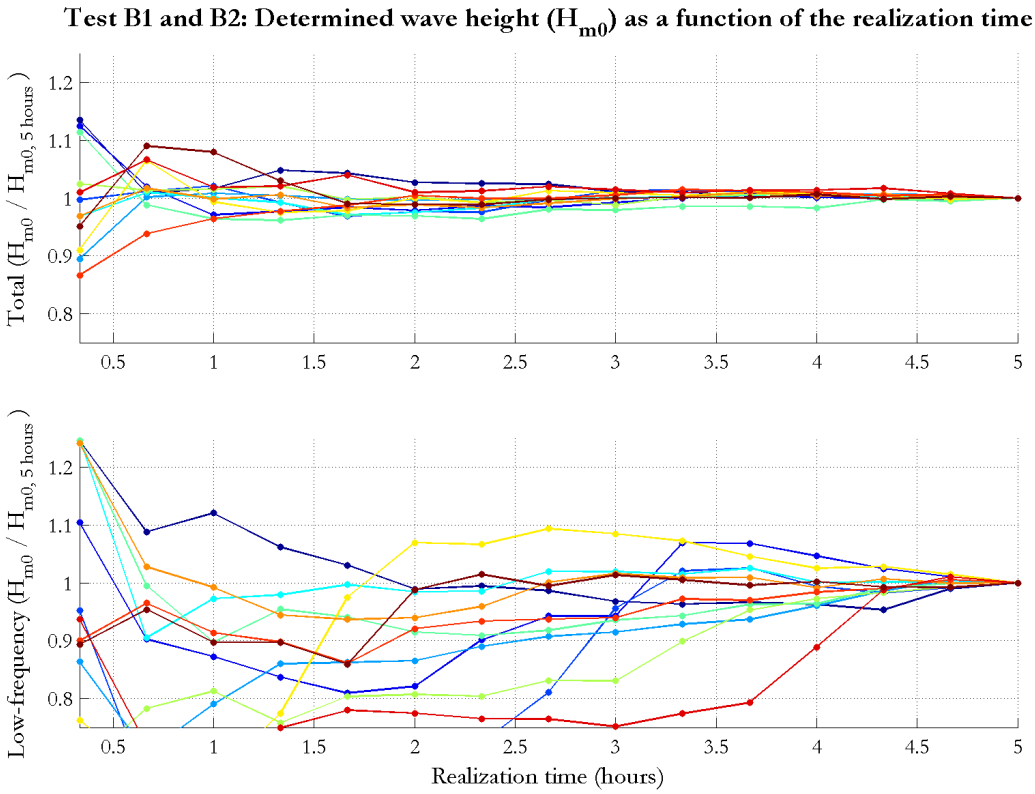

FIGURE 4.7: Influence of the realization time on the determination of relative wave parameters: Tests B1 and B2. The colours relate to the different time series (locations and tests), which are not treated individually in this verification.

visible in the plots. Further, in both tests it is evident the wave damping along the porous slopes on the opposite side of the wave maker.

The calculated wave height at the different measuring locations available for these tests are given on Table 4.4 and 4.5. Only three measuring gauges are available for the comparisons in Test B2.

For Test B1, both measurements and simulations indicate that the maximum wave heights occur near the wave maker (GHM01, GHM02 and GHM03). At GHM07 and GHM08 waves are smaller due to wave diffraction transferring wave energy towards the side slopes. The differences between measured and simulated total significant wave heights are in the order of 2%, which can be considered accurate and within the accepted error margin due to the realization effects.

The amount of energy is considerably smaller in the low frequency bands ($T \geq 33s$). The wave amplitudes are likely beyond the accuracy limits of the wave gauges (0.02 m in prototype = 0.2 mm in the tests). The simulated low frequency energy is similarly small, although large relative errors are observed because very small numbers are compared.

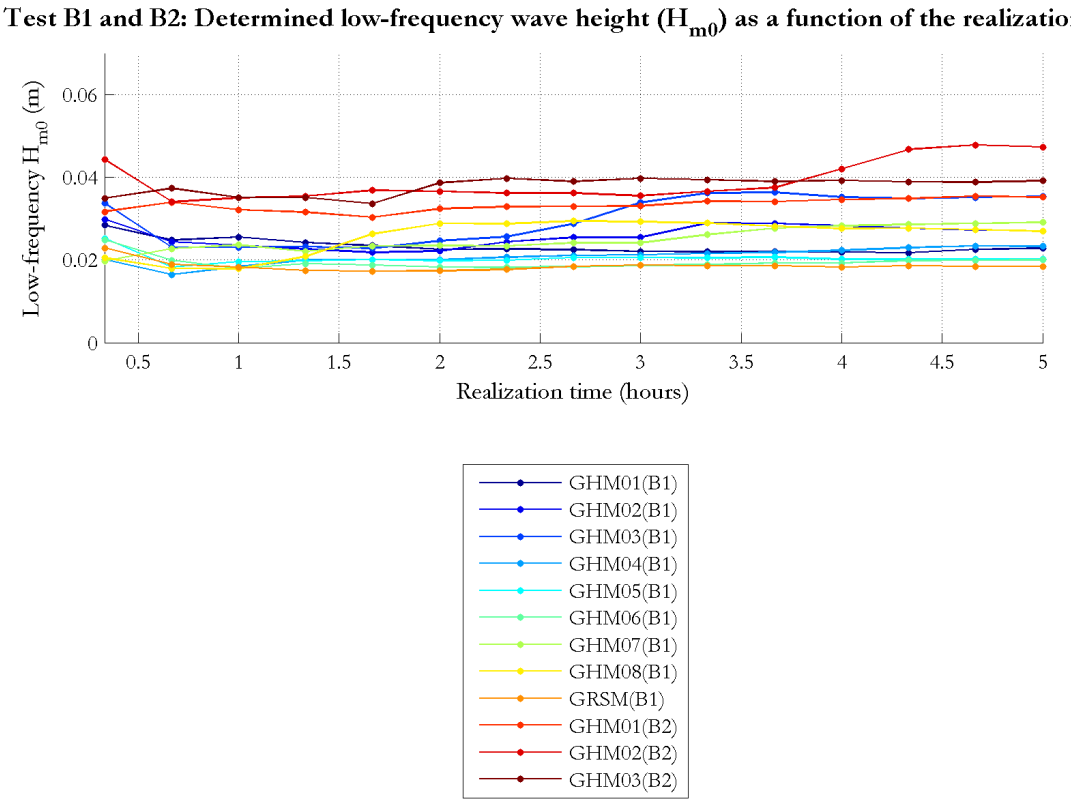

FIGURE 4.8: Influence of the realization time on the determination of low-frequency wave parameters: Tests B1 and B2. The colours relate to the different measured time series (locations and tests).

Only the three wave gauges along the wavemaker are available for Test B2. The measured and simulated total significant wave height are agreeing on these locations, with small relative errors in the order of 2%. As for the Test B1, the amplitude of long waves is very small both in the measurements and simulations, so even though the absolute errors are small, they result in large relative deviations. The compared low-frequency wave heights are influenced by the resolution of the measuring gauges and the length of the realization.

Measured and simulated wave spectra for simulations B1 and B2 are given in Figures 4.10 and 4.11, respectively. For these tests the wave field is relatively homogeneous across the measuring gauges, so the comparisons of spectra are made only for few locations on the central axis of the basin.

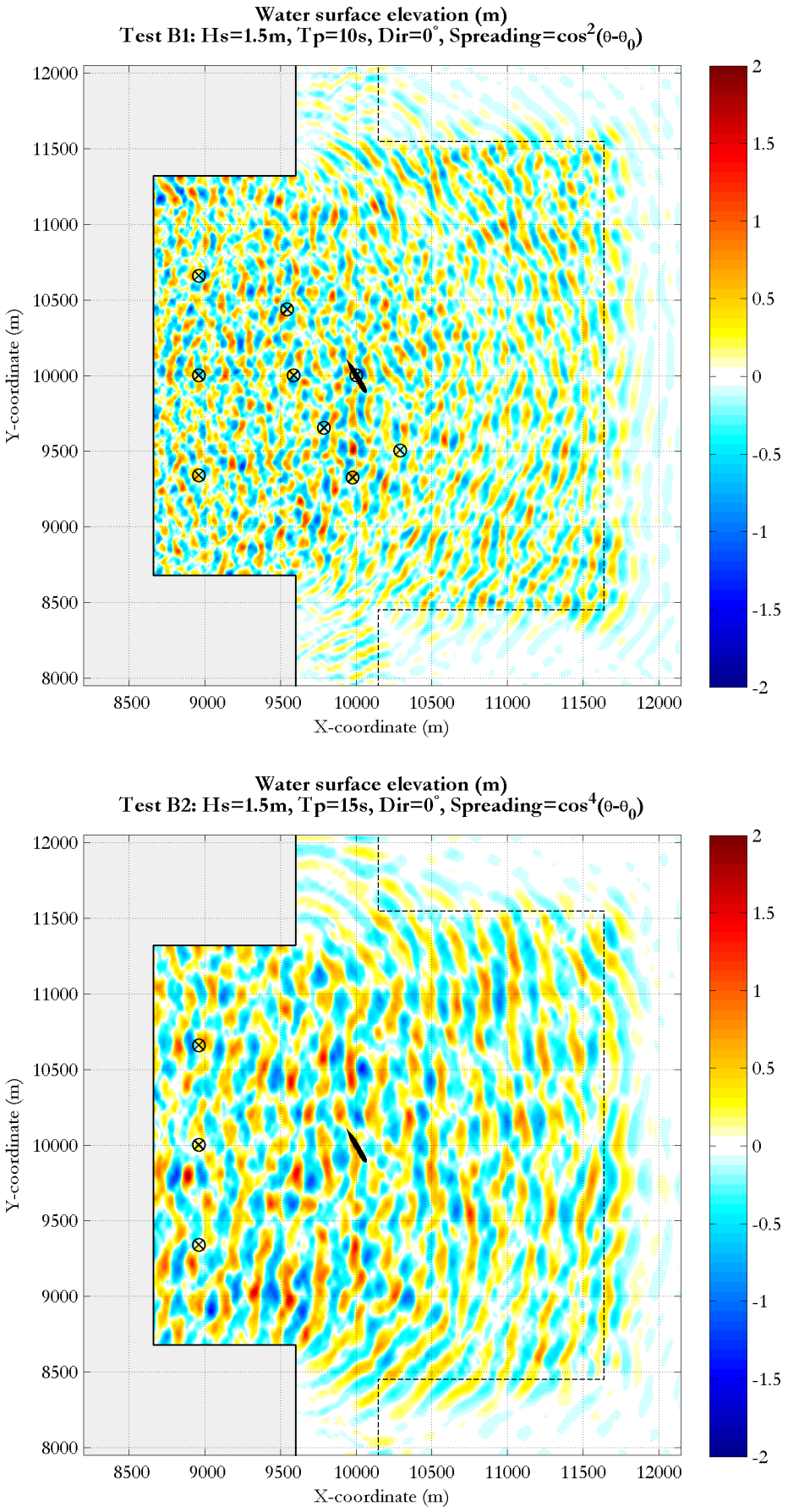

FIGURE 4.9: Water level elevation along the domain at the ending time of Test B1 and B2 simulation. The markers indicate the position of the wave measuring gauges.

TABLE 4.4: Measured and simulated wave heights in meters: Test B1 (open water). The location of the wave gauges is given in Figure 4.2).

Wave gauge	**Hm_0 (total) [m]**			**Hm_0 (low frequency) [m]**		
	Measured	Simulated	Difference	Measured	Simulated	Difference
GHM01	1.50	1.53	0.03 (2.0%)	0.022	0.018	-0.004 (-18.1%)
GHM02	1.48	1.50	0.02 (1.4%)	0.025	0.019	-0.006 (-24.3%)
GHM03	1.53	1.50	-0.03 (-2.1%)	0.034	0.017	-0.017 (-48.9%)
GHM04	1.44	1.47	0.02 (1.7%)	0.021	0.019	-0.002 (-11.1%)
GHM05	1.45	1.47	0.02 (1.6%)	0.021	0.020	-0.001 (-4.3%)
GHM06	1.42	1.44	0.02 (1.7%)	0.019	0.018	-0.001 (-6.4%)
GHM07	1.36	1.35	-0.01 (-0.9%)	0.024	0.018	-0.006 (-25.1%)
GHM08	1.38	1.35	-0.03 (-1.8%)	0.029	0.017	-0.012 (-41.5%)
GRSM	1.41	1.41	0.00 (-0.1%)	0.019	0.017	-0.001 (-7.5%)

TABLE 4.5: Measured and simulated wave heights in meters: Test B2 (open water). The location of the wave gauges is given in Figure 4.2).

Wave gauge	**Hm_0 (total) [m]**			**Hm_0 (low frequency) [m]**		
	Measured	Simulated	Difference	Measured	Simulated	Difference
GHM01	1.47	1.51	0.04 (2.8%)	0.033	0.039	0.006 (16.8%)
GHM02	1.52	1.51	-0.01 (-0.6%)	0.036	0.041	0.006 (16.0%)
GHM03	1.54	1.50	-0.03 (-2.1%)	0.040	0.041	0.001 (2.2%)

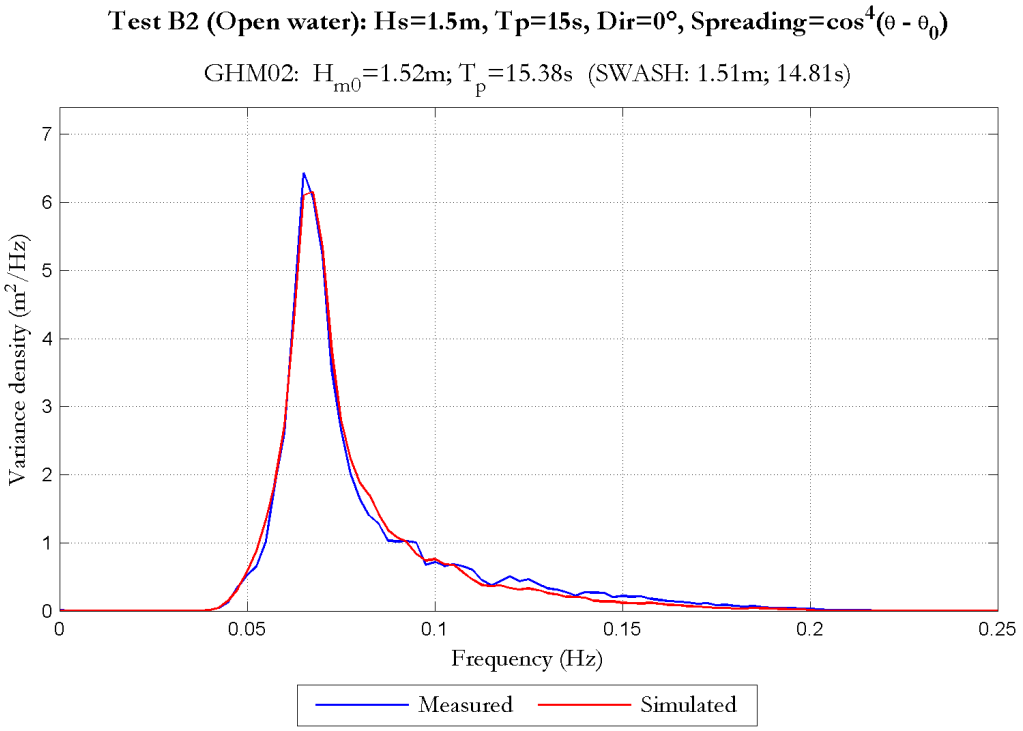

FIGURE 4.11: Comparison of measured and simulated wave spectra for test B2.

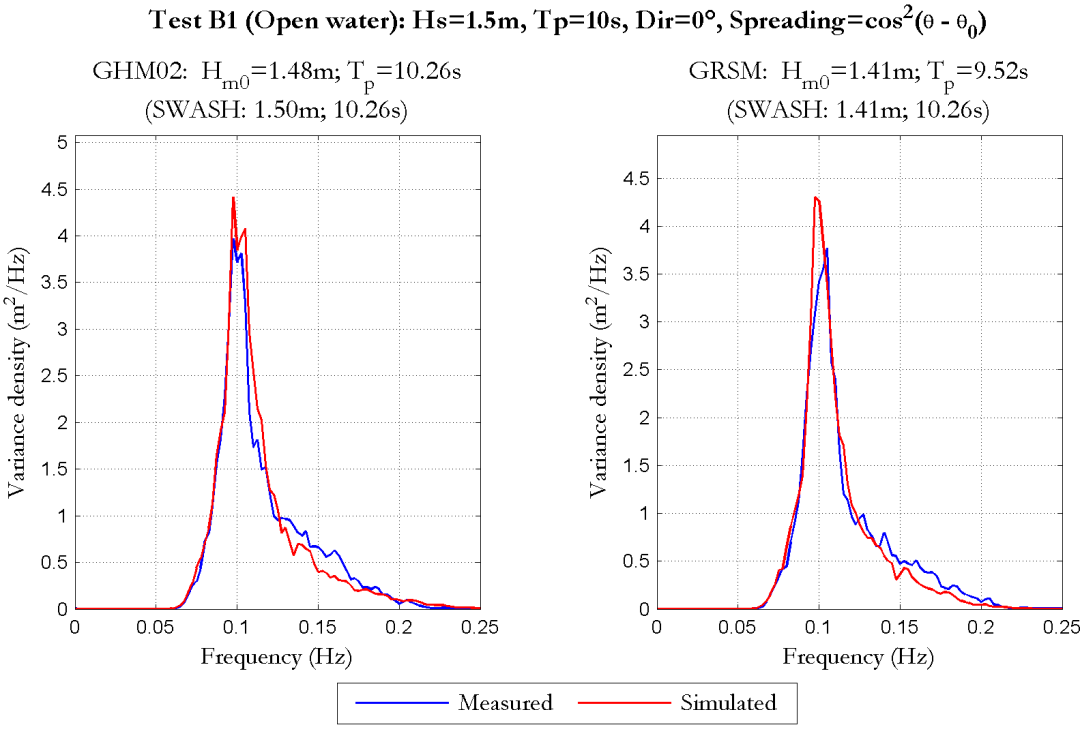

FIGURE 4.10: Comparison of measured and simulated wave spectra for test B1.

For both Test B1 and B2 the measured and simulated wave spectra are corresponding well. Following from the tests with regular waves, an under estimation of energy in the high frequency tail of the spectra was expected due to the relatively scarce grid resolution for those (short) waves. However, the reported differences are local and very small. This might be related to the fact that those wave components have small amplitude, and numerical dissipation for linear wave is negligible.

The results of SWASH simulations were converted into Harberth model input files using the developed coupling tool. The records of first and second-order forces and moments were combined since these are measured simultaneously in the tests. The third and fourth components of second-order forces were not taken into account because the ship is retrained so corrections due to the moving ship are not applicable. The measured and computed forces and moments acting on the ship during Test B1 are compared in Table 4.6 and Figure 4.12. Results for Test B2 are given on Table 4.7 and Figure 4.13.

TABLE 4.6: Measured and simulated significant force amplitudes: Test B1. $Fm_0 = 2\sqrt{m_0}$; Low-frequency band: $f \leq 0.03Hz$.

Mode	Fm_0 (total)			Fm_0 (low frequency)		
	Measured	Simulated	%	Measured	Simulated	%
Fx [MN]	1.76	1.60	-9.2	0.06	0.08	35.1
Fy [MN]	11.73	11.96	2.0	0.22	0.30	38.6
Fz [MN]	13.94	16.43	17.9	0.47	0.46	-1.7
Mx [MNm]	24.01	23.83	-0.8	3.14	0.69	-77.9
My [MNm]	788.71	749.38	-5.0	12.82	19.60	52.9
Mz [MNm]	707.83	513.09	-27.5	10.51	20.84	98.2

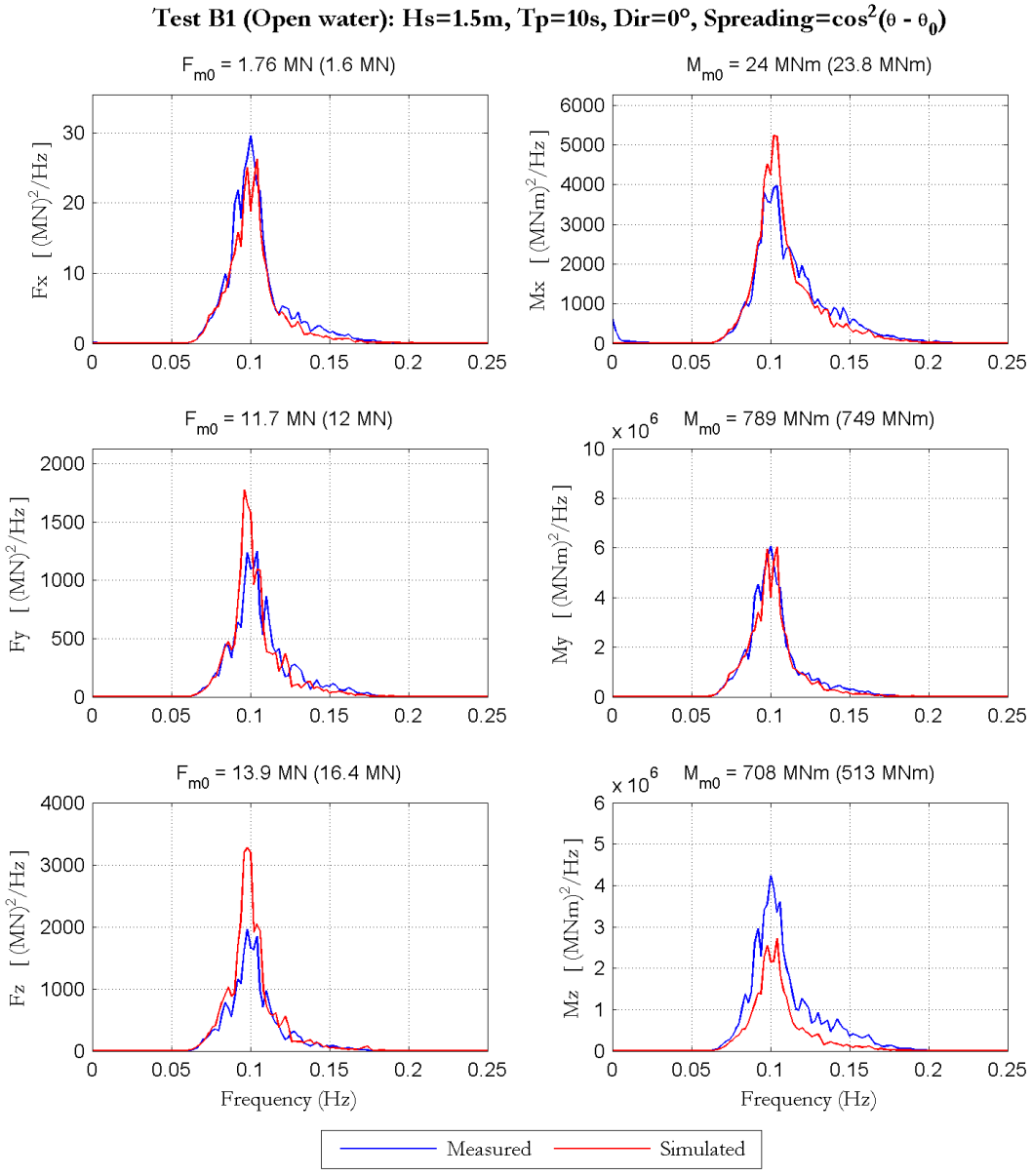

FIGURE 4.12: Comparison of measured and simulated spectra of forces and moments: Test B1. $Fm_0 = 2\sqrt{m_0}$.

TABLE 4.7: Measured and simulated significant force amplitudes: Test B2. $Fm_0 = 2\sqrt{m_0}$; Low-frequency band: $f \leq 0.03Hz$.

Mode	Fm_0 (total)			Fm_0 (low frequency)		
	Measured	Simulated	%	Measured	Simulated	%
Fx [MN]	2.57	2.36	-8.3	0.06	0.08	39.6
Fy [MN]	14.08	15.42	9.5	0.27	0.26	-3.5
Fz [MN]	21.65	25.63	18.4	1.21	1.40	16.4
Mx [MNm]	22.96	23.79	3.6	1.69	0.49	-71.3
My [MNm]	1165.35	1079.86	-7.3	27.32	33.43	22.4
Mz [MNm]	707.46	556.95	-21.3	10.30	14.53	41.1

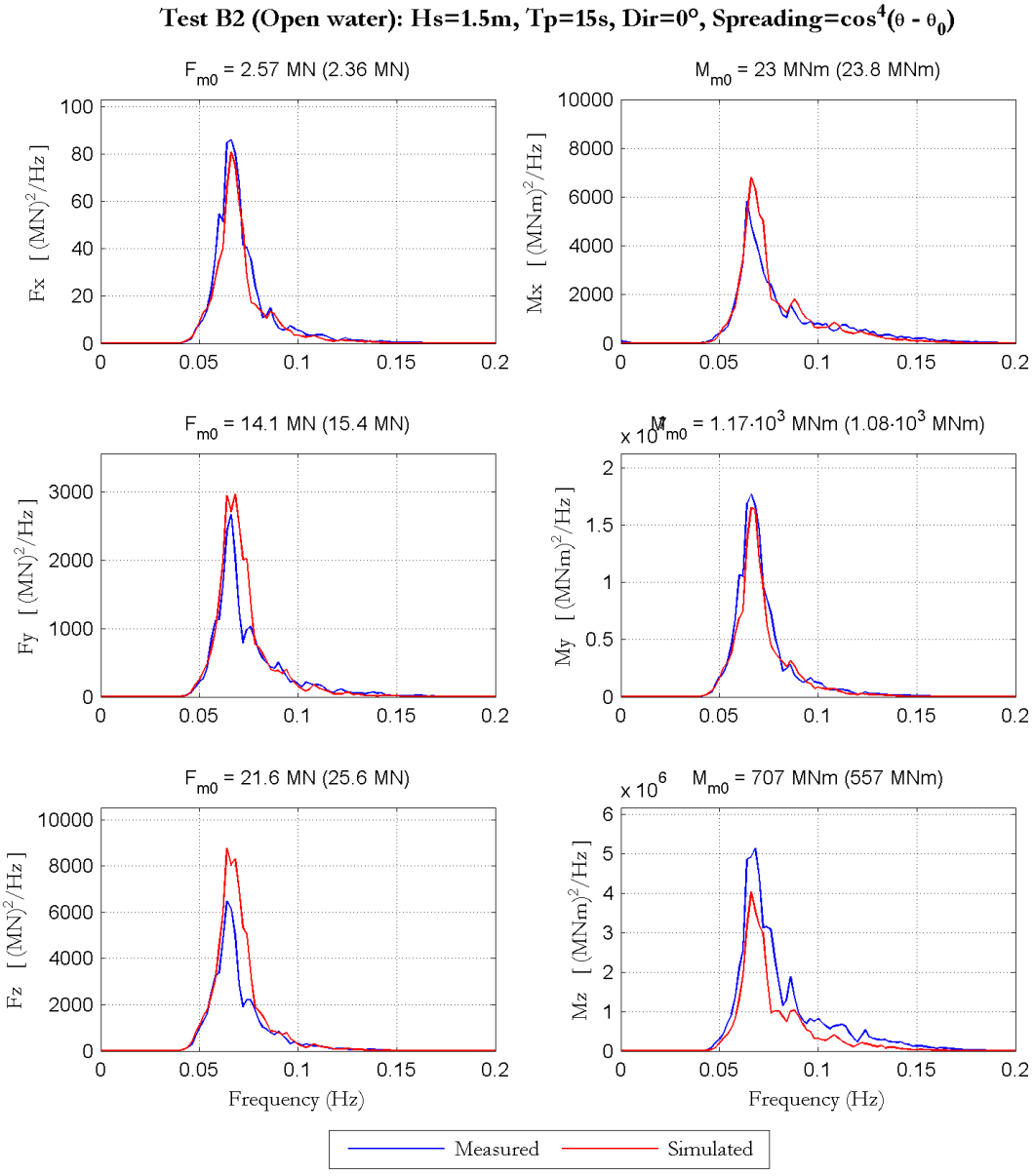

FIGURE 4.13: Comparison of measured and simulated spectra of forces and moments: Test B2. $Fm_0 = 2\sqrt{m_0}$.

Deviations in the measured and computed spectra of forces and moments can be attributed to different sources of inaccuracies, i.e. the wave modelling, the coupling tool, the computations of Harberth, and limitations on the measurements. In view of that, the results of both tests B1 and B2 are considered satisfactory. The relative errors associated to the low frequency forces are larger, however these correspond to small absolute errors that may be also influenced to the accuracy of the force transducers.

The comparisons of measured and simulated wave heights and 1D-spectra are in good agreement, so the differences between measured and computed forces are not likely related to the modelled wave energy and periods. The same applies for the coupling tool, which has shown to be accurate for the range of kd considered in the tests ($kd < 1.5$). Therefore, differences in forces/moments can be attributed to the directional character of the simulated and measured waves, to Harberth computations (particularly errors in the scattered potentials), and to the measurement of forces and moments.

The under estimation of the Z-moment in both tests B1 and B2 was also reported for Tests A1 and A2 with regular waves. As argued for the results of Tests A, these differences are probably related to an external factor, i.e. errors in the measurements or on the mesh representing the hull of the modelled ship.

4.2.3 Tests C1, C2 and C3: Spectral waves with the ship in the harbour basin

Tests C1, C2 and C3 consider a harbour situated in the middle of the testing basin. The harbour layout is composed by vertical impermeable walls (i.e. quay walls) and a porous slope in the outer side of the wall, between the harbour and the wavemaker. These structures were included in SWASH simulations by imposing their horizontal/vertical dimensions, porosity and D_{n50}. The import grid used to specify the space varying characteristics of the structures is made finer than the computational grid, so only small interpolation errors are expected.

The vertical walls surrounding the harbour are $15m$ wide, $50m$ high (from the bottom level), and have a porosity set as 0 (though the minimum value of 0.1 is used by SWASH in the computations). The porous slope is placed in the outer side of the vertical wall in order to reduce wave reflection back towards the wavemaker. In the numerical model it was implemented as a porous structure (p=0.45) with slope of 1:3, starting at $85m$ from the wall. The top of the sloping structure is approximately $28m$ high measuring from the bottom of the basin ($8m$ above the mean water level).

According to Van der Molen (2006), who was involved on the model test set-up and also used the measured datasets, in order to prevent too much reflection against the vertical side wall,

the wave paddles close to the wall are not used in the tests with oblique wave direction (30°). The active reflection compensation method was also applied on this section of the wavemaker. However, the length of the wavemaker section switched-off is not available.

In SWASH the wavemaker length was reduced in 680 m from the side wall. As in the model tests, active reflection compensation was considered along the unused section of the wavemaker. Although, it is known that both in the testing basin and in the numerical model only partial compensation for the outgoing waves is possible, especially when waves approach obliquely the wave maker (say wave direction $> 30°$ with the wavemaker normal). Further, the (in)ability to compensate reflection may vary between the mechanical and numerical wavemaker, leading to differences between the wave fields.

Near the opposite end of the wavemaker waves were generated towards the side wall during the tests with oblique wave direction (30°). The reflected waves from the wall line up with the other waves to form a wider homogeneous wave field (Dalrymple, 1989). The same is not applied in the numerical simulations. The influence of this simplification is assumed to be away from the entrance of the harbour basin, affecting only marginally the wave field around the moored ship and the resulting wave exciting forces and moments.

Standing waves or seiches are expected to occur in the rectangular shaped basin on both longitudinal and transversal directions. On the longitudinal direction the basin is semi-enclosed, so the standing waves have a node of water level at the open end of the basin and an anti-node at the closed end. On the transversal direction both sides are closed, so the standing wave occur with anti-nodes in both sides. An infinite number of seiching modes is possible, in which the period of oscillation decreases with mode number. However, in practice the lower modes are dominant, as frictional damping affects the higher modes preferentially.

The periods associated to the first seiching modes of the modelled basin can be calculated taking the dimensions of the basin (1200m long $\times$ 400m wide), the location of the nodes/anti-nodes as given in the previous paragraph, and the wave celerity ($c = \sqrt{gd}$ for such long waves in 20m water depth). Results are given in Table 4.8. A combination of longitudinal and transversal waves with an oblique propagation into basin is also possible. SWASH can take those waves into account but the associated periods cannot be easily estimated beforehand.

The measured wave datasets are complete for the three different wave conditions (Tests C1, C2 and C3), with data measured at all the 9 locations indicated on Figure 4.2. The influence of the length of the analysed time series on the calculated wave spectra parameters is shown in Figure 4.14. This analysis is similar to the one performed for tests 'B'. For the tests 'C', however, there is a stronger convergence of the low-frequency wave height to its final value because those waves are more significant, so the influence of small absolute deviations is reduced. It is highlighted that the relative results associated to the whole time series (7.5 hours) are necessarily '1' even

TABLE 4.8: Standing wave periods for the longitudinal and transversal directions of the basin.

Mode	Longitudinal		Transversal	
	T [s]	f [Hz]	T [s]	f [Hz]
1	342.7	0.0029	57.1	0.0175
2	114.2	0.0088	28.6	0.0350
3	68.5	0.0146	19.0	0.0525
4	49.0	0.0204	14.3	0.0700
5	38.1	0.0263	11.4	0.0875

if they are not sufficiently converged. It occurs because the final parameters are the reference for calculating the relative deviations.

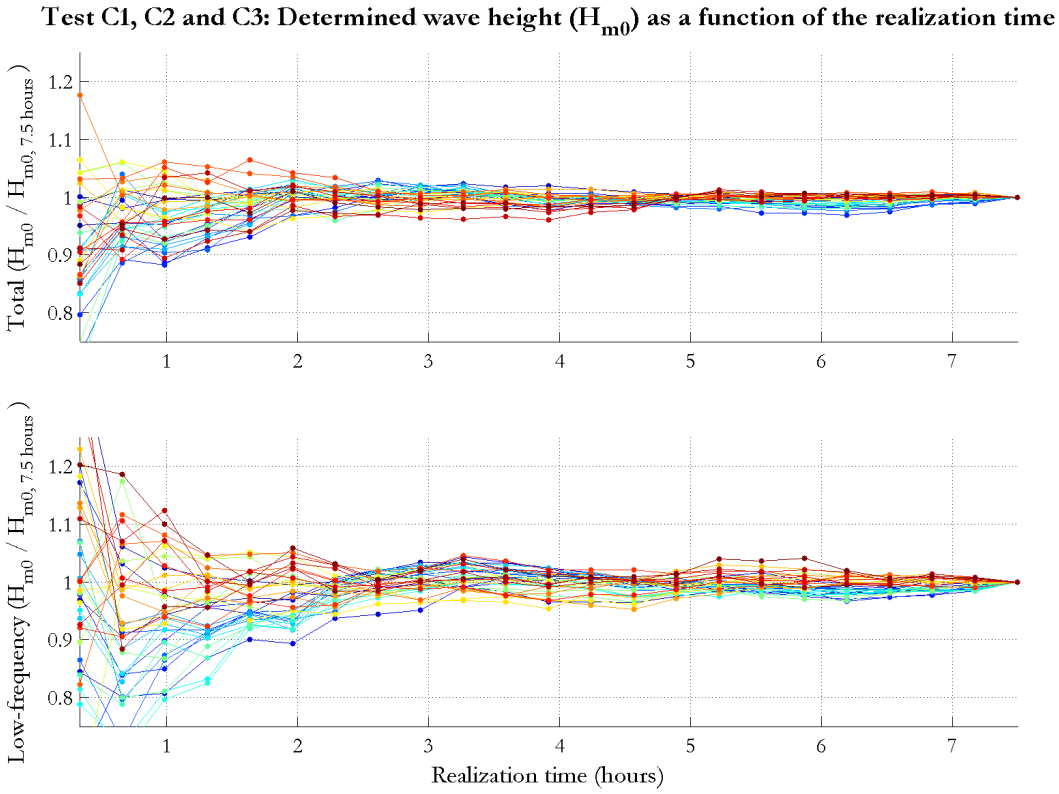

FIGURE 4.14: Influence of the realization time on the determination of wave parameters: Tests C1, C2 and C3. The colours relate to the different time series (locations and tests), which are not treated individually in this verification.

Spectral parameters derived from time series shorter than 2 hours are not consistent. With 3 hours time series the convergence is considered sufficient. Therefore the duration of the numerical simulations is set as 3 hours, so that the required computation times are reduced while ensuring reliable outcomes. Accordingly, only the first 3 hours or measurements are used for the verifications. The first 12 minutes are excluded from both the measured and numerically

simulated time series to prevent the influence of the initial conditions on the analysis (the duration of the spin up time is discussed in Section 4.2).

Energy dissipation due to bottom friction is important for the seiching modes of the harbour basin. Because the scaling used in the physical model tests is based on the Froude number and the fluid viscosity is not properly handled, the Reynolds number is incorrectly represented in the tests implying that *scale effects* can take place on the viscous effects. As the Reynolds number is much lower in the tests than in prototype, the boundary layer in small-scale models can have laminar characteristics leading to a higher boundary roughness coefficient. Consequently, viscous bottom friction in the model tests can be significantly greater than in prototype (HUGHES, 1993). Sensitivity tests with different quadratic bottom friction coefficients were carried and the value $c_f = 0.03$ gave satisfactory results for both short and long waves in the harbour basin. This value was adopted in the numerical simulations of Tests C.

Different wave results for tests C1, C2 and C3 are given in sequence. Snapshots of instantaneous water level surface elevation give an overview of the waves simulated with SWASH along the basin (Figures 4.15 and 4.16). Tables 4.9, 4.10 and 4.11 provide a comparison of measured and simulated total and low frequency ($T \geq 33s$) wave heights at the different measuring locations. Computed maps of significant wave height and comparisons of measured and simulated wave spectra are given in Appendix F.

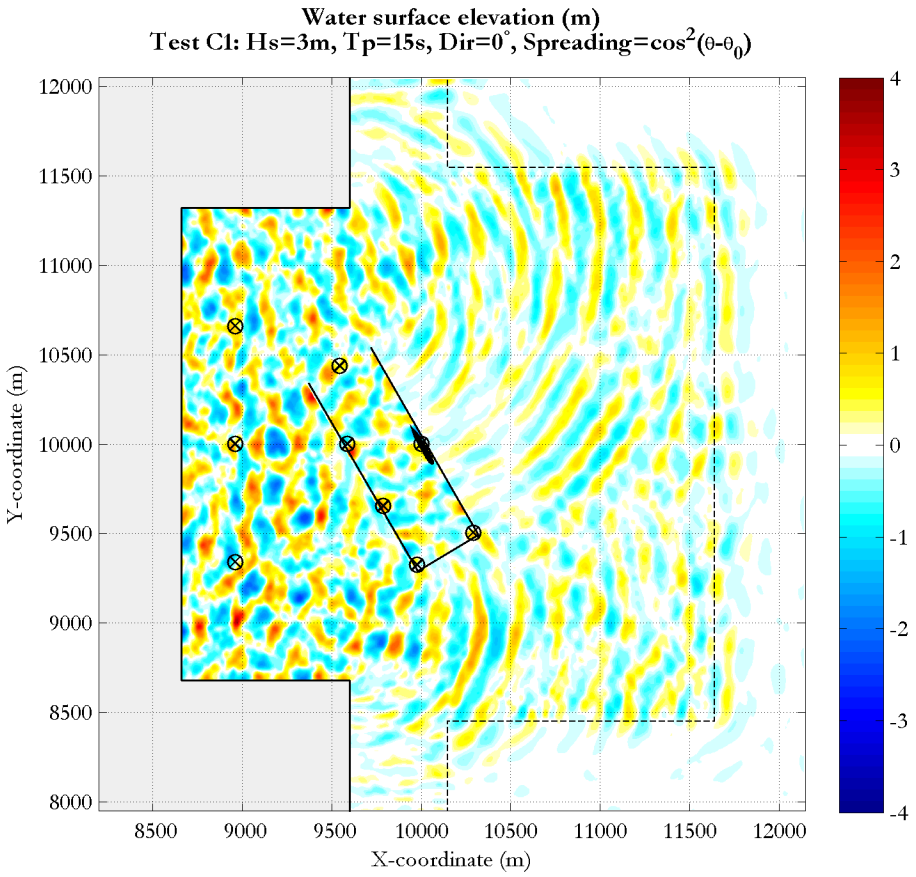

FIGURE 4.15: Water level elevation along the domain at the ending time of Test C1 simulation. The markers indicate the position of the wave measuring gauges.

Given the complexity of the simulations, the comparisons between measured and simulated waves is satisfactory. For the Test C1, in which the mean wave direction is normal to the wavemaker and no additional settings are applied to deal with the wave reflection on the vertical side walls. Regarding Tests C2 and C3, the fact that SWASH could properly handle the simulation of such energetic waves is remarkable.

The effects of the increased bottom friction coefficient to compensate the *scale effects* are more pronounced on short waves away from the wavemaker and on the low-frequency modes of the harbour basin. Although the overall wave results are considered sufficiently accurate for the Tests C, additional sensitivity tests varying the bottom friction coefficient could potentially lead to a better agreement with measurements.

Differences between measured and predicted wave parameters can be partially attributed to the following issues:

- The length of the inactive wavemaker section near the left-side wall (looking from the wave maker) considered in the numerical simulations is uncertain and likely different than

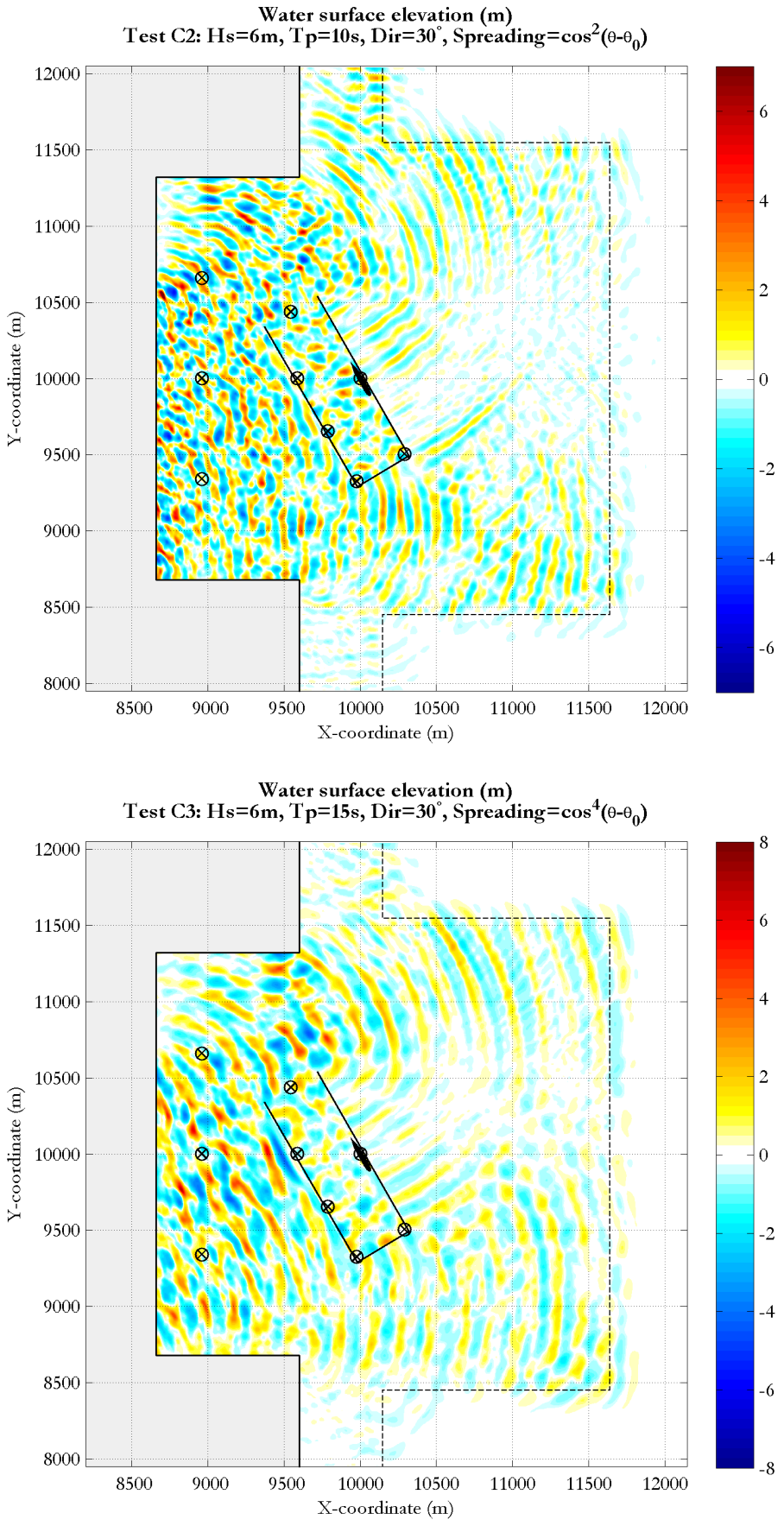

FIGURE 4.16: Water level elevation along the domain at the ending time of Test C2 and C3. The markers indicate the position of the wave measuring gauges.

TABLE 4.9: Measured and simulated wave heights in meters: Test C1 (Hs=3m, Tp=15s, Dir=0°). The location of the wave gauges is given in Figure 4.2.

Wave	**Hm_0 (total) [m]**			**Hm_0 (low frequency) [m]**		
gauge	Measured	Simulated	Difference	Measured	Simulated	Difference
GHM01	2.89	3.03	0.15 (5.1 %)	0.107	0.127	0.020 (19.1 %)
GHM02	3.03	2.99	-0.04 (-1.2 %)	0.122	0.134	0.012 (9.7 %)
GHM03	3.00	2.93	-0.07 (-2.2 %)	0.116	0.150	0.033 (28.5 %)
GHM04	3.11	2.75	-0.35 (-11.3 %)	0.137	0.145	0.008 (6.0 %)
GHM05	3.00	2.78	-0.22 (-7.2 %)	0.159	0.154	-0.005 (-3.1 %)
GHM06	3.31	3.02	-0.29 (-8.8 %)	0.175	0.178	0.003 (1.8 %)
GHM07	3.57	3.43	-0.14 (-3.8 %)	0.228	0.242	0.014 (6.2 %)
GHM08	3.82	4.03	0.21 (5.5 %)	0.206	0.235	0.029 (14.0 %)
GRSM	3.20	3.12	-0.08 (-2.4 %)	0.170	0.183	0.013 (7.6 %)

TABLE 4.10: Measured and simulated wave heights in meters: Test C2 (Hs=6m, Tp=10s, Dir=30°). The location of the wave gauges is given in Figure 4.2.

Wave	**Hm_0 (total) [m]**			**Hm_0 (low frequency) [m]**		
gauge	Measured	Simulated	Difference	Measured	Simulated	Difference
GHM01	5.81	6.05	0.24 (4.2 %)	0.284	0.362	0.078 (27.3 %)
GHM02	6.17	6.58	0.42 (6.7 %)	0.347	0.429	0.082 (23.6 %)
GHM03	6.36	6.14	-0.22 (-3.5 %)	0.328	0.398	0.070 (21.2 %)
GHM04	5.41	4.85	-0.56 (-10.3 %)	0.313	0.277	-0.036 (-11.5 %)
GHM05	4.10	4.54	0.44 (10.8 %)	0.315	0.318	0.004 (1.2 %)
GHM06	4.04	5.00	0.95 (23.5 %)	0.282	0.332	0.051 (18.0 %)
GHM07	3.88	4.18	0.30 (7.8 %)	0.405	0.480	0.075 (18.6 %)
GHM08	3.97	3.75	-0.22 (-5.6 %)	0.386	0.412	0.027 (6.9 %)
GRSM	4.19	3.56	-0.63 (-15.0 %)	0.299	0.307	0.007 (2.4 %)

TABLE 4.11: Measured and simulated wave heights in meters: Test C3 (Hs=6m, Tp=15s, Dir=30°). The location of the wave gauges is given in Figure 4.2.

Wave	**Hm_0 (total) [m]**			**Hm_0 (low frequency) [m]**		
gauge	Measured	Simulated	Difference	Measured	Simulated	Difference
GHM01	5.86	5.75	-0.11 (-1.8 %)	0.431	0.451	0.020 (4.6 %)
GHM02	6.17	6.25	0.07 (1.2 %)	0.537	0.606	0.069 (12.9 %)
GHM03	6.18	5.89	-0.28 (-4.6 %)	0.503	0.683	0.180 (35.8 %)
GHM04	5.25	4.54	-0.70 (-13.4 %)	0.485	0.446	-0.038 (-7.9 %)
GHM05	4.94	4.79	-0.15 (-3.1 %)	0.606	0.551	-0.055 (-9.0 %)
GHM06	4.97	4.66	-0.31 (-6.3 %)	0.625	0.578	-0.047 (-7.5 %)
GHM07	5.54	5.31	-0.24 (-4.3 %)	0.858	0.762	-0.096 (-11.2 %)
GHM08	5.87	5.51	-0.36 (-6.1 %)	0.812	0.731	-0.081 (-10.0 %)
GRSM	4.47	4.00	-0.47 (-10.5 %)	0.622	0.577	-0.045 (-7.2 %)

the length used in the tests. These paddles were switched-off in the tests with oblique waves in order to prevent too much reflection against the vertical side wall, however the exact distance is not available. The reflected waves propagate directly into the harbour, so the results are sensitive to this definition.

- Differences in the reflection characteristics of the gravel slopes and wavemaker in the physical model tests and in the numerical simulations. It can affect the long waves out of the harbour basin, especially between the wavemaker and the harbour wall.

- In Test C2 the mean direction is oblique to the wavemaker and a large directional spreading is considered, so a considerable amount of wave energy is associated to directions nearly parallel to the wavemaker. It is known that both the numerical and mechanical wavemaker are unable to generate very oblique waves. Because their (in)ability in this sense probably differ, it may explain differences between measured and simulated wave heights inside the harbour.

- The maps of simulated significant wave height given in Appendix F show large gradients of wave height near the vertical walls of the harbour, caused by full wave reflection and development of standing waves. In this case, small discrepancies in the directional wave spectrum outside the harbour (possibly affected by the issues mentioned in the previous items), in the location of the gauges near the walls, and in the position of the walls, may cause relative large differences between measured and simulated waves.

The total wave spectra given in Appendix F show that in general the predicted wave energy is correctly distributed along the wave frequencies, indicating that the physical processes are well reproduced in the numerical simulations.

For the low-frequency spectra a perfect match was not necessarily expected since those waves are associated to second-order processes and thus more sensitive to inaccuracies. Nonetheless, the general distribution of the energy along the low-frequency components is reasonably reproduced by the model, including energy peaks around the seiching modes of the harbour basin. Energy peaks are not clear in the low-frequency spectra measured/simulated outside the harbour, inferring that only little energy is attributed to standing waves through the entire testing basin.

The wave results in the vicinity of the ship were converted into Harberth input files using the coupling tool. The computed forces and moments are compared with the measurements in Tables 4.12, 4.13 and 4.14. Figures 4.17, 4.18 and 4.19 give the spectra of forces and moments for the different tests. As for the Tests A and B presented previously, the components of the second-order forces directly related to the ship motions (components III and IV) are disregarded in the comparisons because the tested ship is restrained to a fixed position.

TABLE 4.12: Measured and simulated significant force amplitudes: Test C1. $Fm_0 = 2\sqrt{m_0}$; Low-frequency band: $f \leq 0.03Hz$. Deviations in the simulated wave height at the location of the ship: ΔHs_{total}=-2.4%; ΔHs_{LF}=+7.6%.

Mode	Fm_0 (total)			Fm_0 (low frequency)		
	Measured	Simulated	%	Measured	Simulated	%
Fx [MN]	6.63	5.86	-11.6	0.35	0.39	10.4
Fy [MN]	21.50	18.79	-12.6	0.84	0.69	-18.4
Fz [MN]	53.64	52.27	-2.5	4.66	4.99	7.2
Mx [MNm]	47.85	37.03	-22.6	5.21	1.41	-72.9
My [MNm]	2880.53	2680.53	-6.9	139.87	144.01	3.0
Mz [MNm]	1280.84	893.85	-30.2	49.58	35.90	-27.6

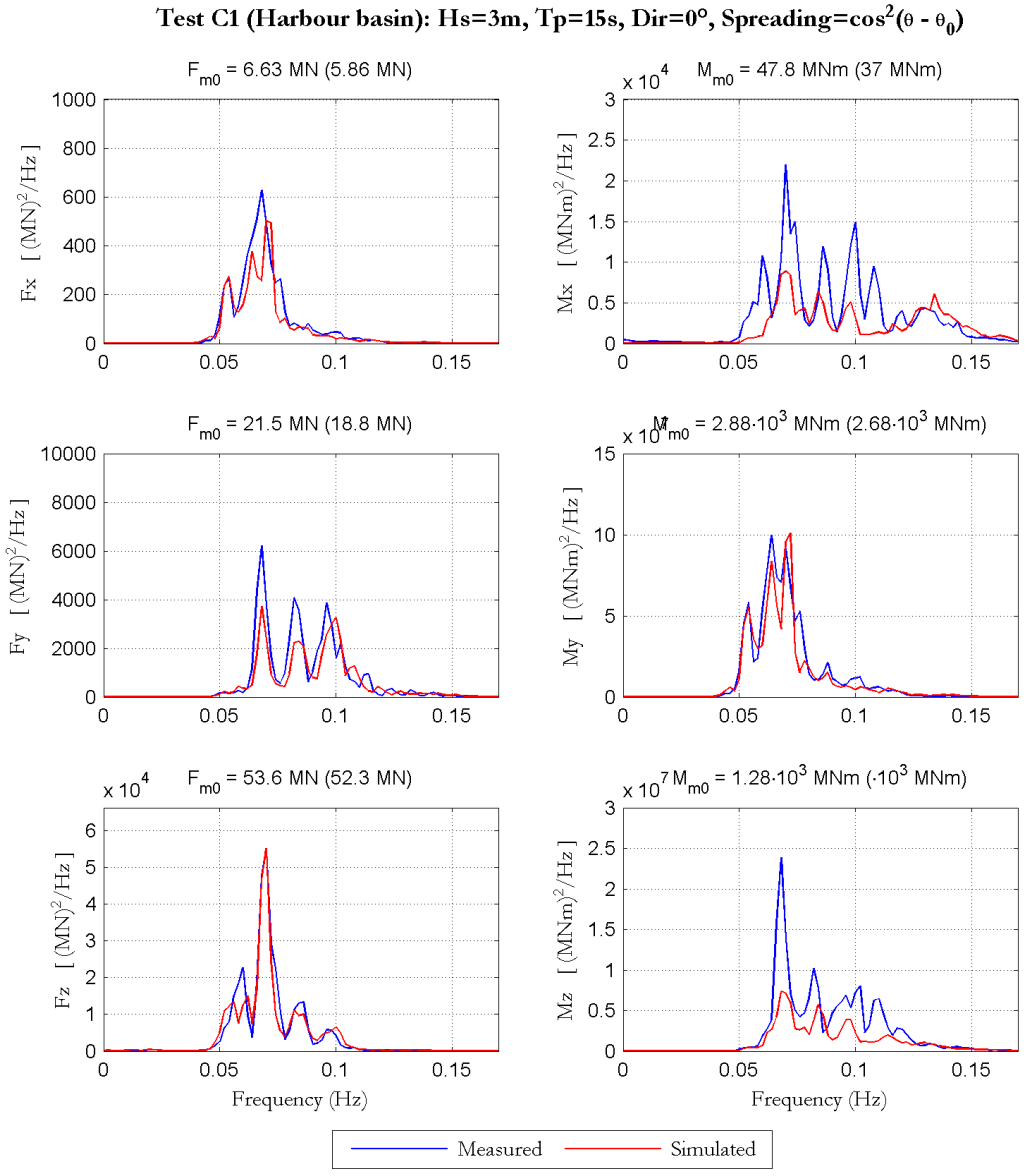

FIGURE 4.17: Comparison of measured and simulated spectra of forces and moments: Test C1. $Fm_0 = 2\sqrt{m_0}$.

TABLE 4.13: Measured and simulated significant force amplitudes: Test C2. $Fm_0 = 2\sqrt{m_0}$; Low-frequency band: $f \leq 0.03Hz$. Deviations in the simulated wave height at the location of the ship: ΔHs_{total}=-15%; ΔHs_{LF}=+2.4%.

Mode	Fm_0 (total)			Fm_0 (low frequency)		
	Measured	Simulated	%	Measured	Simulated	%
Fx [MN]	7.91	5.97	-24.5	0.55	0.62	12.4
Fy [MN]	58.32	55.37	-5.1	4.56	1.88	-58.7
Fz [MN]	76.52	79.41	3.8	8.77	8.87	1.1
Mx [MNm]	173.58	68.19	-60.7	30.97	3.06	-90.1
My [MNm]	3938.17	2993.95	-24.0	264.50	239.43	-9.5
Mz [MNm]	3286.20	1845.49	-43.8	161.56	102.95	-36.3

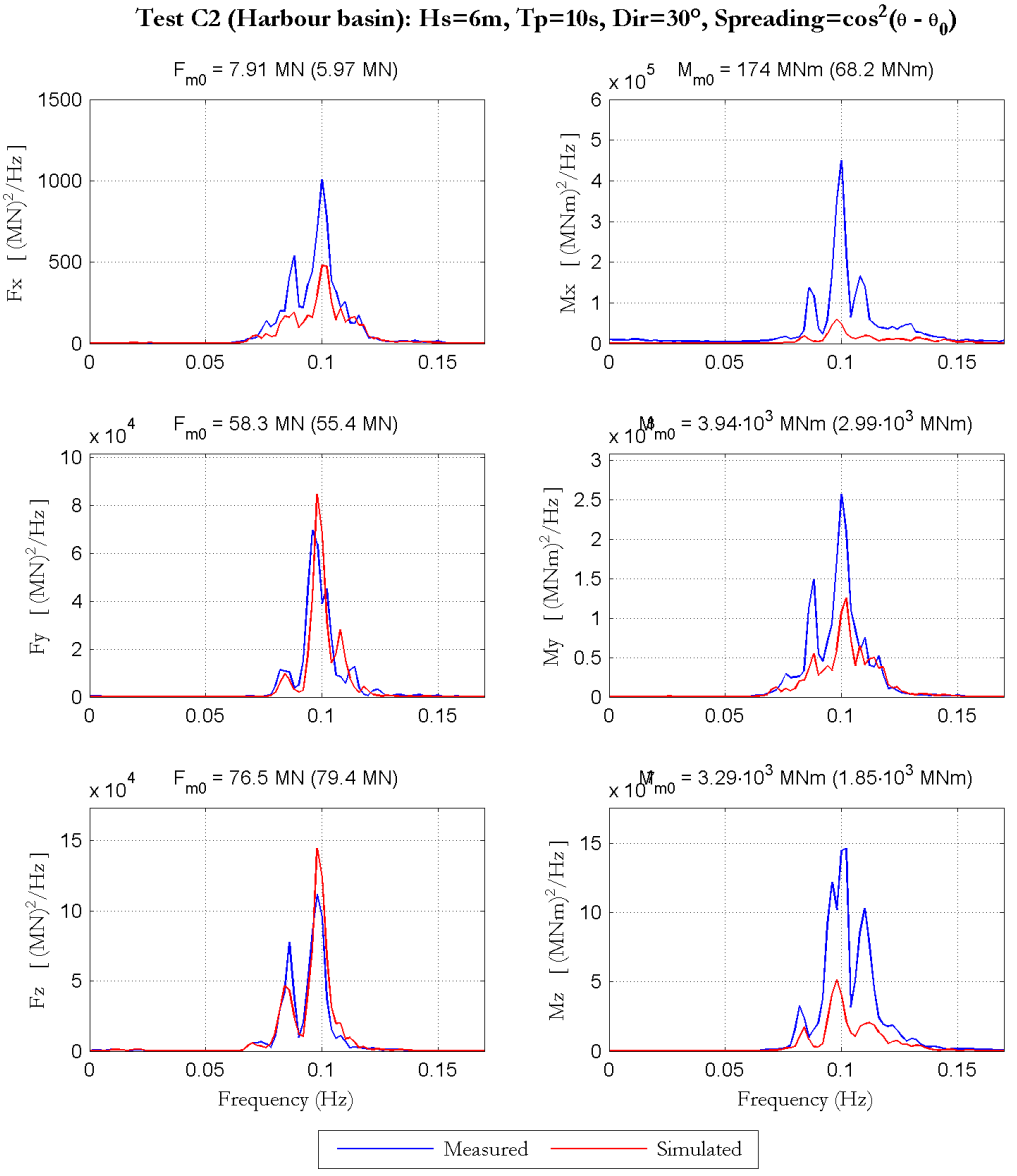

FIGURE 4.18: Comparison of measured and simulated spectra of forces and moments: Test C2. $Fm_0 = 2\sqrt{m_0}$.

TABLE 4.14: Measured and simulated significant force amplitudes: Test C3. $Fm_0 = 2\sqrt{m_0}$; Low-frequency band: $f \leq 0.03Hz$. Deviations in the simulated wave height at the location of the ship: ΔHs_{total}=-10.5%; ΔHs_{LF}=-7.2%.

Mode	Fm_0 (total)			Fm_0 (low frequency)		
	Measured	Simulated	%	Measured	Simulated	%
Fx [MN]	9.63	8.03	-16.6	1.20	1.05	-12.4
Fy [MN]	35.94	31.43	-12.6	2.13	1.78	-16.3
Fz [MN]	92.43	86.72	-6.2	17.66	16.79	-4.9
Mx [MNm]	119.49	52.43	-56.1	25.45	3.35	-86.9
My [MNm]	4178.86	3588.40	-14.1	492.63	423.40	-14.1
Mz [MNm]	2141.08	1350.01	-36.9	121.45	82.72	-31.9

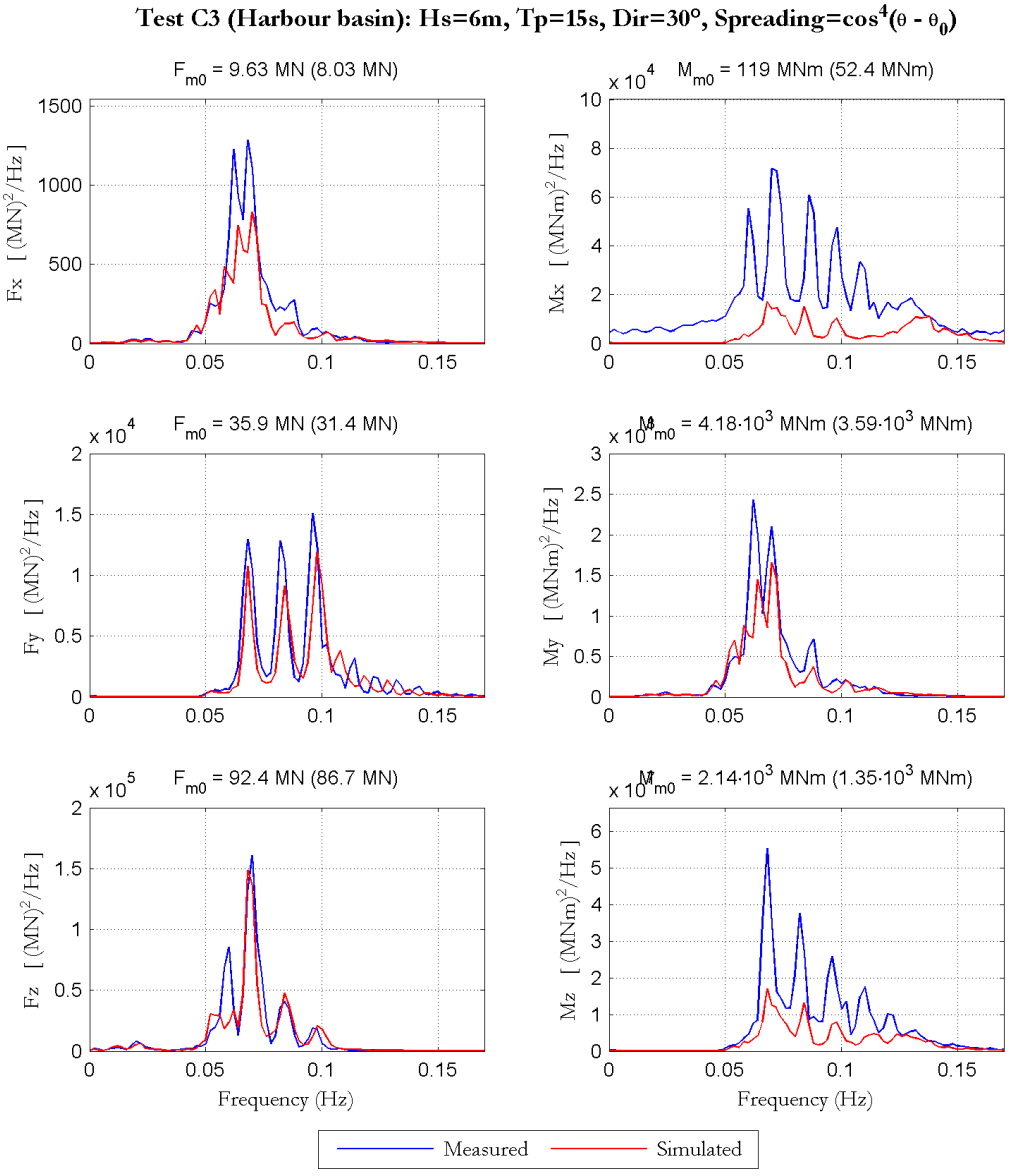

FIGURE 4.19: Comparison of measured and simulated spectra of forces and moments: Test C3. $Fm_0 = 2\sqrt{m_0}$.

Except for the roll and yaw moments, and considering the limitations in the wave simulations discussed previously in this section, the comparisons between measured and simulated loads acting on the ship are in good agreement regarding both the bulk parameters and the spectra. The under and overestimation of the simulated wave height at the location of the ship quoted on the caption of Tables 4.12, 4.13 and 4.14 partially explain the deviations on total and low-frequency forces. The reproduction of the peaks in the forces/moments spectra indicate that the complex wave field is properly represented by SWASH and dealt in Harberth computations.

General differences between measured and simulated forces and moments are attributed to disagreements in the wave fields, inaccuracies in Harberth model (especially in the computation of the scattered waves), and limitations in the measuring transducers (mainly for the measured moments). 'Roll moments' are known to be difficult to measure accurately, so the differences are likely associated to measurement errors. The computations of 'yaw moments' are similarly smaller than the measurements in the Tests A and B. These differences can also be noticed on results of Van der Molen (2006) and Van der Molen & Wenneker (2008), who used measurements from the same experiment. So it may be associated to external factors such as a misrepresentation of the hull of the vessel by the mesh and specific problems in the measurement of moments.

Harberth uses a linear potential model to compute the scattering of the undisturbed incident waves around the hull of the ship. The linear model is expected to be inaccurate under non-linear conditions, although a clear measure of these effects cannot be clearly estimated beforehand. Although the incident waves are rather extreme on Tests C, the effects of the linear assumption for the scattered and radiated waves appear to be only marginal. These results imply that the limits of application of Harberth with this respect are likely far beyond practical limits for large vessels (i.e., critical loads on the fixed mooring structures and excessive motions of the moored ship).

Harberth assumes that the second-order forces are small corrections to the first-order quantities. The measured forces and moments cannot be split into first- and second-order loads, so only indirect conclusions can be drawn in this case. In practice the main influence of the second-order forces is related to the slow varying drift forces acting on moored vessels, so possible inaccuracies on the computed second-order forces could be seen in the low-frequency forces. Nonetheless, disagreements on these frequencies might be also related to the observed deviations in the low-frequency waves. Although the low-frequency forces are generally much smaller than first-order forces, they become relevant when the dynamic behaviour of the ship and mooring system is taken into consideration (i.e. resonance and amplification of loads). In this sense, (not excessive) errors on the absolute low-frequency wave loads are not so critical, provided that energy is present in the correct frequency range.

Only heave, roll and pitch motions are taken into account by Harberth for the computation of second-order forces. The influence of this simplification cannot be derived directly from the measurements because the ship is restrained to a fixed position. Nevertheless, the second-order terms directly related to the ship motions have limited contribution to the (low-frequency) second-order forces, which in turn is only part of the total low-frequency forces (i.e. these are also related to low-frequency waves included in the computation of first-order forces). Therefore, the influence of the motions simplification is expected to be small, especially on relatively sheltered harbours in coastal areas where the contribution of low-frequency waves will likely dominate the low-frequency forces.

4.3 Conclusions

The main conclusions from this chapter are listed below:

- The SWASH model proved to be capable to reproduce complex wave propagation, in this case involving considerable wave reflection, wave diffraction, non-linearities and extreme wave heights. Therefore the model is a potential candidate for practical applications involving wave penetration in harbours. This is especially the case when extreme waves are involved, since widely used operational Boussinesq wave models are renown to become numerically unstable under those situations.

- Detailed information about the setup of the model test is of prime importance when setting up numerical models aiming to reproduce the experiments. The lack of information limits the capacity of drawing conclusions and understanding possible disagreements between measured and modelled results.

- The modelling approach (SWASH + coupling tool + Harberth) proved to be robust and accurate for the validation tests. Besides the influence of the realization time and limitations inherent to the numerical tools and the physical scale tests, differences reported in the validation are likely related to inaccuracies in the representation of the basin in the SWASH model (i and ii), inaccuracies in the measurements (iii), the singularities of the numerical and mechanical wavemakers (iv):

  i) the characteristics of the porous slopes;

  ii) viscous bottom friction in the scale model can be significantly greater than in prototype due to *scaling effects*. Bottom friction is specially relevant for the damping of the low-frequency wave motions associated to the seiching modes in the harbour basin. A more extensive calibration of the bottom friction coefficient used in the numerical simulations could lead to a better representation of the measured waves;

iii) the very small low-frequency waves in Tests B, and the 'Roll' and 'Yaw-moments' in general;

iv) effectiveness of the active reflection compensation, length of the de-activated section near the vertical side wall in Tests C2 and C3, and the treatment of waves generated nearly parallel to the wavemaker (mainly in Test C2).

- The computed forces and moments are in agreement with measurements even for the highly non-linear wave conditions, indicating that the use of the linear potential model by Harberth for the computation of the scattered waves is still valid in such cases. These results suggest that the limits of application of the Harberth model with this respect are likely far beyond practical limits for large vessels (i.e. critical loads on the fixed mooring structures and excessive motions of the moored ship). The influence of the linear potential model for the radiated waves and the assumption of relatively small ship motions could not be addressed based on the validation results because in the model tests the ship is restrained to a fixed position.

- The reported errors on the simulated low-frequency forces and moments might be related to inaccuracies on the computations of second-order forces and on the simulated incident short and long waves. Although both the measured and predicted low-frequency forces are about one order of magnitude smaller than the first-order forces in the short wave frequencies, they are relevant when the dynamic behaviour of the ship and mooring system is taken into consideration (i.e. resonance and amplification of loads). In this sense, not excessive absolute errors on the low-frequency wave loads are generally not so critical, provided that the energy is distributed in the correct frequency range.

- The developed coupling tool to combine SWASH and Harberth models in order to predict wave forces acting on a moored ship is consistent and can be considered available for future applications.

- The wave modelling is the main potential source of inaccuracies to the overall approach. This is not due to limitations in SWASH model, which has shown to be physically consistent and also a robust numerical tool, but to the wrong choices that can be incorporated in the model setup. If the computed wave information provided to the coupling tool and Harberth model is wrong, it will likely result in the correct forces but for the wrong waves, making the overall approach inaccurate.

Chapter 5

Final considerations

The main conclusions of this project are provided in Section 5.1. For more detailed remarks, one is referred to the partial conclusions given at the end of each chapter. Recommendations for future research and possible improvements to the numerical tools used in this project are listed in Section 5.2.

5.1 Conclusions

The main objectives of this study, as proposed in Chapter 1, are:

- Analyse the overall approach identifying the contribution of the different steps and associated assumptions/simplifications to the accuracy of the calculations;
- Develop a coupling tool to combine the wave model SWASH and the 3D diffraction model Harberth in order to compute wave forces acting on floating bodies;
- Investigate the influence of SWASH model definitions in the predictions of forces acting on moored ships;
- Validate the combination SWASH/Harberth for the computation of the wave fields and resulting forces acting on a moored ship.

The SWASH model is able to handle in a robust way the relevant physical processes involved in non-linear wave propagation through intermediate and shallow waters, possibly taking into consideration complex port geometries. The tests described in Chapter 3 indicate that the SWASH model results are consistent provided that: i) the number of vertical layers is sufficient (especially in relatively deep waters); ii) the horizontal resolution of the computational grid

is sufficient; iii) important terms of the momentum equation are modelled with higher-order numerical schemes (especially for non-linear waves in relatively deep waters). Possible inaccuracies in this sense refer to amplitude errors, while dispersion errors have shown to be a minor issue for the tested conditions. The SWASH model computations times are very sensitive to the horizontal grid resolution, so usually a trade-off has to be made between the required accuracy of the results and the acceptable computation time.

The wave simulations of the validation tests show that generally the SWASH model results compare well with the measured datasets, albeit that the numerical model setup may differ from the scale tests in a number of characteristics, e.g. representation of the porous slopes and bottom friction, unknown definition of the wavemaker in oblique waves, proprieties of the wavemakers to absorb reflected waves and generate oblique waves. Further, the SWASH model was able to handle the extreme wave conditions considered in the validation. This is remarkable since one of the motivations for this project is related to the occasional impossibility of simulating extreme waves with the operational Boussinesq model due to numerical instabilities. The absence of a clear restriction in this sense makes SWASH a potential candidate for practical applications involving extreme wave penetration in harbours.

A computational tool was developed to make the coupling between the SWASH model outputs and Harberth model inputs, enabling the combination of the two models to calculate wave forces on moored ships. The tool proved to be accurate for the simplified tested conditions in Chapter 3 and the validation tests in Chapter 4. The performance of the tool is optimal in shallower waters (say $kd < 3$), where the coupling procedure does not add any additional requirement to the wave simulations. For relatively short waves the vertical distribution of wave quantities is more curved and additional vertical layers should be considered in the SWASH modelling in order to accurately prescribe the wave velocities and pressures along the hull of the ship. Nonetheless, waves with these characteristics are generally less relevant in coastal regions.

Linear potential theory is applied in the Harberth model for the computations of the wave-body interactions, so the non-linearities in the scattered and radiated waves are assumed to be sufficiently small. The wave height and the first-order body motions are also assumed sufficiently small compared to the body dimensions so that the first-order forces acting on the restrained body dominate the second-order corrective loads. Further, the Harberth model considers only heave, roll and pitch for the computations of second-order forces.

A series of systematic tests were performed with the Harberth model using as input the undisturbed incident wave information calculated with the SWASH model and processed with the developed coupling tool. The computed first-order forces and first-order heave, roll and pitch motions are generally consistent with the Wavescat model, used as a baseline for comparisons. Larger deviations can occur for the second-order forces, which are partially related to the simplifications of ship motions in Harberth and to disagreements in the predicted body motions.

The result of the studied approach (SWASH + coupling tool + Harberth) for the testing cases considered in the validation indicate that measured and computed forces and moments acting on a restrained ship are generally in good agreement. More pronounced differences occurred for 'roll' and 'yaw' moments, but these can be associated to inaccuracies on the measurements. Overall disagreements might also be related to deviations in the simulated wave fields and in the Harberth computations of forces.

Harberth model results for the extreme wave conditions considered in the validation (incident waves on the hull exceeding 4m significant wave height) are generally consistent with the measurements. It implies that the linear potential model applied by Harberth for the computation of the scattered waves is still valid in such extreme cases. So the limits of application of the model with this respect are likely beyond practical limits for large vessels moored on fixed structures (i.e., safe mooring issues and ship motions exceeding operational limits).

The practical considerations given in the previous paragraphs yield the answer to the research question of the study:

To which extent can the SWASH wave model and the Harberth model be combined in order to accurately compute wave forces acting on moored ships?

Each computational tool considered in the proposed approach (the wave model SWASH, the developed coupling tool, and the diffraction model Harberth) can contribute to the (in)accuracy of the computed wave forces acting on a moored ship.

Although the SWASH model has shown to be physically consistent and a robust numerical tool, the wave modelling is the main potential source of inaccuracies to the overall approach. Possible inaccuracies on the computed short and long waves impact linearly the first-order forces and quadratically the second-order forces. Errors in the wave model can be related to insufficient computational grid resolution and the use of first-order schemes for relatively important terms, but also due to a misrepresentation of the simulated area, e.g. on the bathymetry definition, bottom friction coefficients, implementation of structures and boundary conditions, etc.

The coupling tool is generally sufficiently accurate without introducing additional requirements to the wave simulations. An exception are situations where the mooring location is relatively deep compared to the length of the dominant waves ($kd \gtrsim 5$). In such cases the coupling procedure requires additional vertical layers to be considered in the SWASH simulations.

The computations of first-order forces with the Harberth model will likely be reliable provided that the general model setting are consistent and the hull of the ship and wave information are properly defined. Relatively larger deviations can occur for the second-order forces computed with Harberth, which are partially related to the simplified body motions (i.e. motions other

than heave, roll and pitch are not considered). In practical applications this simplifications will impact the computed slow-varying drift forces, although the relative errors are expected to be reduced when the incident short waves are small and the low-frequency loads are dominated by the low-frequency waves.

Finally, the study shows that the performance of the proposed approach (SWASH + coupling tool + Harberth) is optimal in the situations where it provides an added-value: extreme wave conditions propagating in intermediate/shallow waters and influenced by the port geometry, where complex and non-linear shallow water processes are relevant to define the wave field at mooring location. Under those conditions the potentiality of the proposed approach is remarkable relative to concurrent methods. In deeper and more exposed areas, widely available tools may be applied to compute the wave loads acting on a floating body.

5.2 Recommendations

The items listed below include possible improvements to the numerical tools used in this study and potential subjects for future research.

1. A drop in wave energy in the vicinity of the incoming boundary was reported in the tests with SWASH considering waves with large kd numbers (say $kd > 3$). It is highlighted that this amplitude error is not directly linked to the non-linearity in the imposed wave, instead it is likely attributed to the definition of the imposed discharge signal along the water depth. A further verification and a possible minimization of these effects is recommended.

2. Extend the second-order boundary condition implemented in SWASH to compensate also for bound super harmonics, reducing the generation of spurious short waves when non-linear conditions are imposed.

3. In the validation tests with extreme waves the option *Breaking* had to be de-activated in SWASH because the criteria was met in intermediate waters, near vertical fully reflective walls, leading to numerical instabilities. Notice that dissipation due to wave breaking is intrinsic to the equations solved by SWASH, independently of the *Breaking* functionality. This option is applied to improve the representation of wave breaking and generation of free infragravity waves in the surfzone when limited vertical layers are considered (a general description is given in Appendix A, for detailed information see Smit et al., 2013). The *Breaking* option may by un-available for applications where surfzone processes are relevant and steep reflective boundaries are present, restricting the proven capabilities of SWASH. Therefore, it is recommended to include an additional criteria in the *Breaking* option in order to prevent the non-hydrostatic pressure to be disregarded in intermediate waters.

4. Further verify the computation of second-order forces in the Harberth model, exploring the disagreements, limitations and if possible making improvements in the computation methods.

5. Investigate *scale effects* on viscous bottom friction in physical scale model tests. Understand its occurrence and consequences to short wave propagation over relatively large distances and damping of seiching modes in semi-enclosed basins. Perform sensitivity tests with a numerical wave model, varying the bottom friction formulation and coefficient in order to comprehend the wave damping in scale model tests and its relation to wave damping in prototype scales.

6. Perform additional systematic tests with the proposed modelling chain (SWASH model + coupling tool + Harberth model) considering non-linear waves and variable bottom topography. Compare results with measurements and/or other numerical tools, identifying disagreements and possible limits of application. A verification against typical frequency-domain diffraction models based on linear potential theory could give insight on the applicability of those tools in shallow waters, where non-linearities in the incident waves are not negligible.

7. Develop guidelines for representing coastal and port structures in SWASH model simulations (e.g., breakwaters, quay walls, access channel). Investigate the model robustness, accuracy, wave reflection, transmission and dissipation.

8. Verify the applicability of proposed modelling approach with the SWASH and Harberth models in an existing practical case.

Appendix A

SWASH model

SWASH models water waves by solving the non-hydrostatic Reynolds-averaged Navier–Stokes equations for an incompressible fluid with a constant density and a free surface. The free-surface motion is tracked by applying the non-linear shallow water (NLSW) equations with the addition of a vertical momentum equation and non-hydrostatic pressure in horizontal momentum equations. The numerical approach adopted in SWASH requires much fewer grid cells in the vertical direction than other alternative methods. Additionally, with appropriate conservation properties, the NLSW equations are able to deal accurately with gradients or discontinuities in the flow and the combined effects of wave–wave and wave–current interaction in shallow water without need of any additional modelling.

In a two-dimensional (2DV) framework that is bounded by the free surface $z = \zeta(x,t)$ and the bottom $z = -d(x)$, where t is time and x and z are Cartesian co-ordinates ($z = 0$ is located at the still water level), the governing equations read (Rijnsdorp et al., 2014):

$$\frac{\partial u}{\partial x} + \frac{\partial w}{\partial z} = 0 \tag{A.1}$$

$$\frac{\partial u}{\partial t} + \frac{\partial uu}{\partial x} + \frac{\partial wu}{\partial z} = -\frac{1}{\rho}\frac{\partial (p_h + p_{nh})}{\partial x} + \frac{\partial}{\partial x}\left(\nu^h \frac{\partial u}{\partial x}\right) + \frac{\partial}{\partial z}\left(\nu^v \frac{\partial u}{\partial z}\right) \tag{A.2}$$

$$\underbrace{\frac{\partial w}{\partial t}}_{\substack{Local\\ accel.}} + \underbrace{\frac{\partial uw}{\partial x} + \frac{\partial ww}{\partial z}}_{\substack{Advective\\ accel.}} = \underbrace{-\frac{1}{\rho}\frac{\partial (p_h + p_{nh})}{\partial z}}_{\substack{Pressure\\ gradient}} + \underbrace{\frac{\partial}{\partial x}\left(\nu^h \frac{\partial w}{\partial x}\right) + \frac{\partial}{\partial z}\left(\nu^v \frac{\partial w}{\partial z}\right)}_{\substack{Turbulent\\ stresses}} - g \tag{A.3}$$

Equation A.1 holds the conservation of mass and equations A.2 and A.3 the conservation of x- and z-momentum. Equations are solved in time t and along directions x and z. $u(x,z,t)$ is the horizontal velocity, $w(x,z,t)$ is the vertical velocity, ν^h and ν^v are the horizontal and

vertical kinematic eddy viscosities, respectively, g is the gravitational acceleration, and p_h and p_{nh} are the hydrostatic and non-hydrostatic pressures, respectively. The hydrostatic pressure is expressed in terms of the free surface elevation $\zeta(x, y, t)$ measured from the still water level:

$$\begin{gathered} p_h = \rho g(\zeta - z) \\ \text{such that:} \quad \frac{\partial p_h}{\partial z} = -\rho g \quad \text{and} \quad \frac{\partial p_h}{\partial x} = \rho g \frac{\partial \zeta}{\partial x} \end{gathered} \tag{A.4}$$

An expression for the free surface is obtained by considering the (global) mass balance for the entire water column ($d(x, y)$ is the still water depth):

$$\frac{\partial \zeta}{\partial t} + \frac{\partial}{\partial x} \int_{-d}^{\zeta} u dz = 0 \tag{A.5}$$

The bottom friction term can be included in the horizontal momentum balance equations. The coefficient that can be specified on different ways, including a constant value, the well-know Manning and Chezy roughness coefficients, and the logaritmic wall-law for either smooth or rough beds.

Incident regular or irregular waves are introduced at open boundaries of the computational domain by specifying normal horizontal velocities based on second-order wave theory. Though, in the current version of SWASH (2.00A) only the difference interactions (i.e. bound ig-waves) are incorporated. The sum interactions (i.e. bound super harmonics) are not included for efficiency reasons.

The vertically varying velocity amplitude of the primary wave components is related to the short-wave amplitude an determined by linear wave theory. In coastal waters the bound infragravity wave component are essentially shallow-water waves, for which the vertical variation is negligible. The velocity amplitude associated to the bound infragravity waves is assumed to be vertically constant and is computed based on the free wave components following Hasselmann (1962).

To simulate waves entering the domain without reflections at this boundary, a weakly reflective condition allowing outgoing waves is adopted. The total velocity signal is determined as the superposition of the incident velocity signal and a velocity signal of the reflected waves. To estimate the velocity of the reflected wave signal, the reflected waves are assumed to be shallow water waves, progressive, of constant form and propagating perpendicular to the boundary. The depth averaged horizontal velocity can be calculated from mass conservation using surface elevation of the outgoing waves (i.e. the difference between the target surface elevation and the instantaneous surface elevation computed by SWASH). This type of radiation conditions

has been shown to lead to good results with nearshore wave conditions, especially for waves approaching the boundary on small angles ($< 30^{\circ}$).

Two options are available to approximate the onshore boundary condition: the moving shoreline used in inundation or runup computations; and an absorbing condition (e.g. Sommerfeld's radiation condition) which allows the (long) waves to cross the outflow boundary without reflections. The radiation condition may be combined with a sponge layer technique.

Space discretization of the governing equations is carried out in a staggered grid arrangement, in which the velocity components are located at the center of the cell faces and the water level is located at cell center. With this choice non-physical oscillations related to de-coupling of the unknowns are prevented. The non-hydrostatic pressure along the vertical terrain-following grid can be given either at the cell center (standard layout) or at the layer interface (box layout).

For the time integration of the continuity and momentum equations an explicit leapfrog scheme in conjunction with a second order explicit time step for advection, a first order explicit time step for the viscosity term and a first order implicit time step for the non-hydrostatic part is used. This variant of the leapfrog is second order accurate in time and does not introduce wave damping. To achieve second order accuracy in space for the approximation of the water depth a higher order interpolation is added, augmented with a flux limiter to avoid unwanted oscillations near sharp gradients. A special treatment of the advection term is required for momentum conservation. This is covered with detail in Zijlema et al., 2011.

The non-hydrostatic pressure is governed indirectly by the local continuity equation. This equation is linked to the momentum equations by means of a second order correction pressure technique. The discretized forms of the equations are combined to give a Poisson equation linking the non-hydrostatic pressure correction at a grid point to its neighbours. As a result, local mass conservation is enforced (Zijlema and Stelling, 2005).

Because mass and momentum are strictly conserved at discrete level, the adopted scheme is able to deal with flows with a wide range of Froude numbers. Once the wave height over depth ratio becomes relatively large, a discontinuity develops as a wave steepens up and develops a vertical face. In such a situation, the model conserves momentum over the discontinuity and energy is dissipated at a rate analogous with that of a bore. Therefore, energy dissipation of a breaking wave is intrinsically considered by SWASH.

However, a high vertical resolution is required to reproduce the observed locations of incipient wave breaking (≈ 10 layers), whereas at low vertical resolutions wave breaking is delayed (Smit et al., 2013). To capture wave breaking with only a few vertical layers (say 2 layers) and make the simulations more efficient, the non-hydrostatic pressure can be neglected in the vicinity of a breaking wave, ensuring that a wave develops a vertical face. This approach is initiated once the rate of change of the free surface exceeds a predefined threshold (Smit et al., 2013).

Because the time stepping is of explicit type, the stability criteria should be met for a stable solution (i.e. conditional stability). The well-known CFL condition for 2D problem is given by:

$$Cr = \Delta t \left(\sqrt{gd} + \sqrt{u^2 + v^2}\right) \sqrt{\frac{1}{\Delta x^2} + \frac{1}{\Delta y^2}} \leq 1 \tag{A.6}$$

with Δx and Δy the mesh width, Δt the time step, u and v the flow velocity components, and Cr the Courant number.

The time step is dynamically adjusted by SWASH in order to keep the Courant number within a user prescribed range. Usually, the minimum Courant number (Cr) is set to 0.2, while the maximum Cr is specified in the range of 0.5 to 0.8. For high, nonlinear waves, or wave interaction with structures with steep slopes (e.g. jetties, quays), a maximum Courant number of 0.5 is advised by the SWASH User Manual (2014).

The explicit treatment of the viscosity term leads to an additional stability condition, which is verified during the computations in order to prevent occasional too high eddy viscosity.

The accuracy of the model to the linear dispersion depends on the discretization of the vertical pressure gradient in the momentum equation. The required number of layers is determined by the dimensionless water depth kd (k and d are the wave number and still water depth, respectively): the higher the value of kd, the more vertical layers needed (Zijlema et al., 2011).

When a large number of vertical layers are taken into account, the standard layout using explicit central differences for the approximation of vertical non-hydrostatic pressure gradients is sufficiently accurate and preferable due to its robustness. The box layout applying the implicit Keller-box scheme or compact scheme to determine the gradients is recommended at low vertical resolution, say 5 layers or less, because it gives relative low numerical dispersion and dissipation.

Regarding the computational domain in the horizontal plane, it is recommended to keep the area of interest at least two wave lengths away from the boundaries. Additionally, it is wise to choose the grid axes being aligned as much as possible with the dominant wave direction. One should ensure that the spatial resolution is sufficiently high so that the most energetic wave components are resolved accurately on the grid. According to the User Manual, for low waves (i.e. $H/d \ll 1$) it is sufficient to take 50 grid cells (or 51 grid points) per peak wave length. For relatively high waves, however, it is recommended to take at least 100 grid cells per peak wave length [SWASH User Manual, 2014].

Numerical settings related to the discretization of advection terms in the momentum equation must be taken into account according to the simulated conditions. The default and recommended settings under non-linear and non-hydrostatic conditions are given in Table A.1. It is

highlighted that some of the recommended schemes are automatically considered by SWASH depending on other model settings. Additional explanation is given on Section 5.4.5 of the SWASH User Manual (2014).

Table A.1: Discretization of advection terms in the momentum equations. BDF: 2^{nd} order Backward Difference Scheme; CDS: 2^{nd} order Central Differences Scheme; UPW: 1^{st} order Upwind Scheme. The highlighted schemes are recommended by the model developer (Marcel Zijlema, personal communication 2014).

Term	**Default**	**Adapted**
$u\frac{\delta u}{\delta x}$ (H. Adv. of H-momentum)	BDF	**BDF** or CDS
$w\frac{\delta u}{\delta z}$ (V. Adv. of H-momentum)	UPW	BDF or **CDS**
$u\frac{\delta w}{\delta x}$ (H. Adv. of V-momentum)	Usually ignored	**BDF** or CDS
$w\frac{\delta w}{\delta z}$ (V. Adv. of V-momentum)	Usually ignored	UPW

When the model is forced with wave spectra, the maximum frequency that should be accurately represented by the model is ideally about 1.5 to 2 times the peak frequency. One must be aware that some so-called evanescent modes might be also included in the input spectra. These modes are a general property of the underlying model equations and show exponential decay with distance from the boundary at which the spectrum is imposed. The frequencies at which the evanescent modes are generated is above the cut-off frequency, which is determined by the dispersive properties of the model equations. Accordingly, the cut-off frequency (f_{cf}) is given by:

$$f_{cf} = \frac{\omega_{cf}}{2\pi} = \frac{2K}{2\pi}\sqrt{\frac{g}{d}} \tag{A.7}$$

with K the number of layers used in the model. Hence, the lowest wave period to be considered in the model simulation equals $1/f_{cf}$ (waves shorter than that will be removed by SWASH).

SWASH was recently extended to cover porous flow and predict partial reflection and transmission through breakwater, for instance. The Forchheimer relation is included in the porous momentum equations by means of two extra friction terms f_l (laminar) and f_t (turbulent), in which the grid cells have a porosity ranging from n=0 (wall) to n=1 (pure water). The friction terms in the momentum equation are (Mellink, 2012):

$$\begin{aligned} f_l &= \alpha_0 \frac{(1-n)^2}{n^3}\frac{\nu}{D_{n50}^2}\cdot u \\ f_t &= \beta_0 \frac{(1-n)}{n^3}\cdot\frac{1}{D_{n50}}\cdot u|u| \end{aligned} \tag{A.8}$$

where:

n = pore volume / total volume = porosity

u = horizontal flow velocity
ν = kinematic viscosity
D_{n50} = nominal stone diameter
α_0 = particle-form constant for laminar friction loss (default: 1000)
β_0 = particle-form constant for turbulent friction loss (default: 2.8)

In order to implement a porous structure in a SWASH simulation, the structure height above the bottom level, the characteristic grain size, and porosity should be specified along the domain. SWASH computes an average porosity for a given grid cell based on the porosity and height of the structure relative to the water depth (or vertical dimension of the layer). Therefore, the effect of a porous slope, for example, is approximated as a gradual variation on the average porosity, instead of a physical boundary (the bottom level remains below the structure). Further, the porosity is only taken into account in the horizontal component of the momentum conservation equations, so vertical velocities are not damped by the porous structure (Pés, 2013).

Space-varying input quantities are imposed to SWASH by means of input grids. The spatial resolution of the input grid is not necessarily the same as that of the computational grid. Structures can be represented in the model in different ways: 1) included in the bathymetry definition (impermeable); 2) by means of porous structures; 3) specifying permanently dry points in the computational grid by means of exception values (impermeable); or 4) combinations of the previous options.

From a stability point of view, the second option is preferred. The first choice may be better when detailed results are required in the vicinity of the (impermeable) structure. In this case the modeller is advised to use a larger threshold of water depth to prevent instabilities. The use of exception values on the computational grid may be problematic when the computations involve parallel processing (SWASH User Manual, 2014).

Appendix B

Importing SWASH results into Matlab

Below it is listed the pre-processing procedure to read $2DV$ results of SWASH into Matlab:

1. Spatial coordinates of computational grid are imported (Xp, Yp). In this case Yp is zero in all points since the domain is 1D in space. The size of Xp and Yp is ($N \times 1$);

2. The spatial coordinates at the centre of the grid cells (hereafter called Xc, Yc) are calculated from (Xp, Yp). The size of Xc and Yc is ($N \times 1$);

3. Computed water levels are imported ($WATL$). The last row is deleted since it is 'out of the domain'. The length of the variables becomes *N-1* and it is associated to the coordinates (Xc, Yc);

4. the output variable with the time-dependent thickness of the computational layers (HK) is imported. This variable is associated to the centre of the cells (Xc, Yc), so the last row is deleted and its spatial dimension is *N-1*. The vertical dimension is L (number of vertical layers considered in the simulation);

5. the time-dependent vertical coordinate system is built using the water levels (top of upper layer) and the thickness of the vertical layers. This variable is called Zp, correspond to the level of the vertical faces at the spatial centre of the cell. Its dimension is $L+1$;

6. the level of the vertical centre of the cells at the 2D-position of the computational grids (cell faces) is calculated based on Zp. The vertical dimension of this variable is L and it is called Zc hereafter;

7. the variable VZ containing the velocity in z-direction is imported. The data is associated to the spatial centre of the cells and vertical faces, so the last row is of the matrix is

deleted because it is "out of the domain". The spatial dimensions of the variable are *N-1* and *L+1*, and it is associated the positions (*Xc, Yc, Zp*).

8. by selecting the output quantity *VELK* the x and y-components of the velocity vector (U and V) are exported. Following from the definitions of the staggered grid, the first and the second row of U are deleted. The coordinates (*Xu, Yu*) are created by deleting the first and last row of (*Xp, Yp*), so U is located in the internal cell faces. Since the model is 1D, the variable V is considered to be in the same locations of U, but its value is zero. U and V have the dimensions *N-2* and L, being associated to the coordinates (*Xu, Yu, Zc*);

9. the variable *NHPRSK* containing the distribution of the non-hydrostatic pressure is imported. The variable is associated to the positions (*Xc, Yc*), the last row is deleted. Its vertical dimension is L, with the data located at the centre of the bottom face of the grid cells, so data in the surface is originally absent. The vertical dimension is increased to *L+1* by imposing that the non-hydrostatic pressure is zero at the surface. The horizontal dimension of the variable is *N-1* and it is associated to the coordinates (*Xc, Yc, Zp*);

10. the wave pressure is calculated by summing the piezometric head (calculated using the water levels) and the non-hydrostatic pressure in each grid point. Its final dimensions and associated coordinates are the same as for the non-hydrostatic pressure (previous item).

Appendix C

General SWASH model results

A total of 192 regular wave conditions were simulated in SWASH, as described in Section 3.1. Results associated to the wave conditions listed in Table C.1 and to the finer wave grids (20 vertical layers and 100 grid points per wave length) are presented here. The wave conditions were simulated considering a flat bottom 20m below the still water level.

TABLE C.1: Regular wave conditions simulated in SWASH. Water depth (d) = 20m.

H [m]	**T [s]**	**L_{wave} [m]**	**kd**
0.01	18	242	0.5
0.01	10	121	1
0.01	5.2	42	3
0.01	4	25	5

Besides an illustrative view of the simulated wave profile, a comparison between SWASH results and linear wave theory are also provided.

- **H=0.01m, T=18s, L_{wave}=242m, kd=0.5**

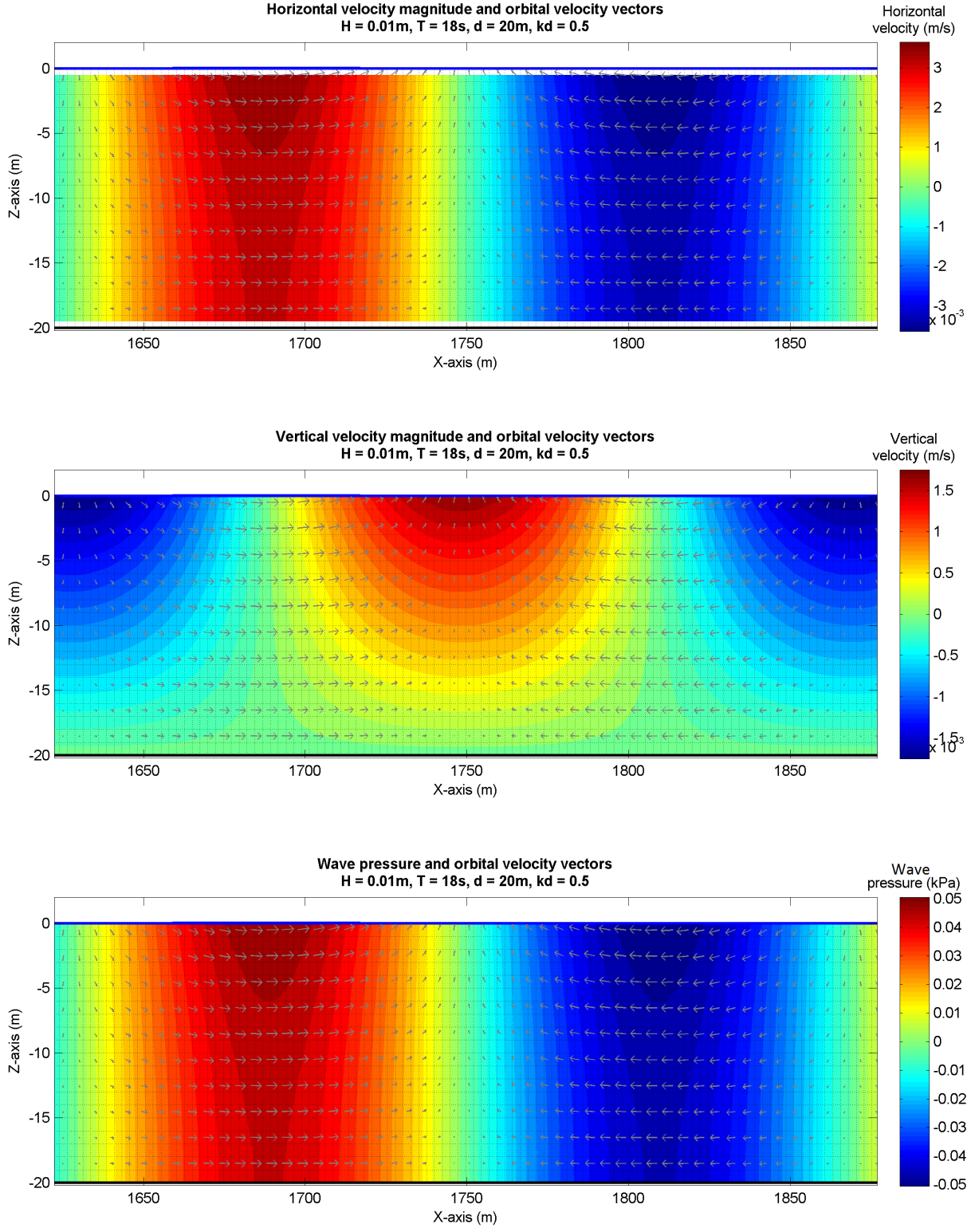

FIGURE C.1: Horizontal velocity, vertical velocity and wave pressure distribution along the wave length and water depth.

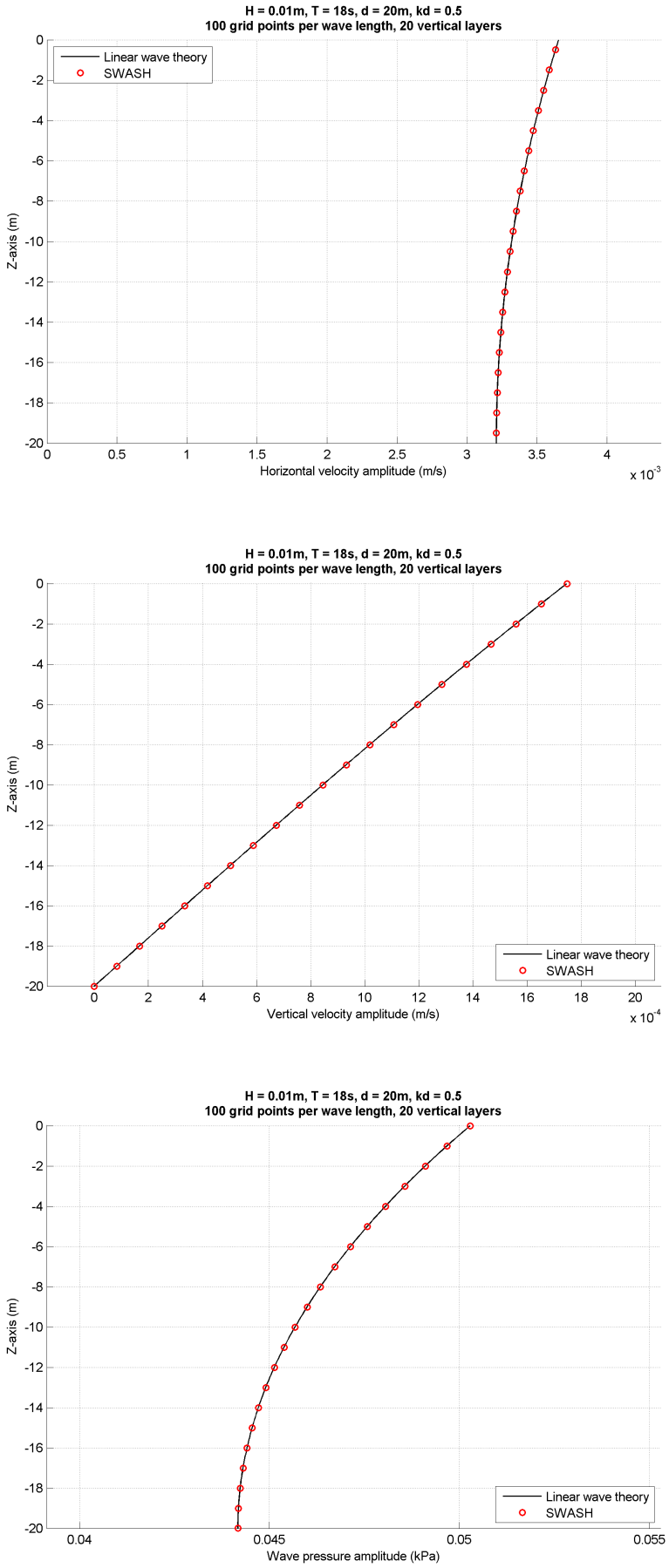

FIGURE C.2: Horizontal velocity, vertical velocity and wave pressure simulated in SWASH and calculated with linear wave theory.

- **H=0.01m, T=10s, L_{wave}=121m, kd=1**

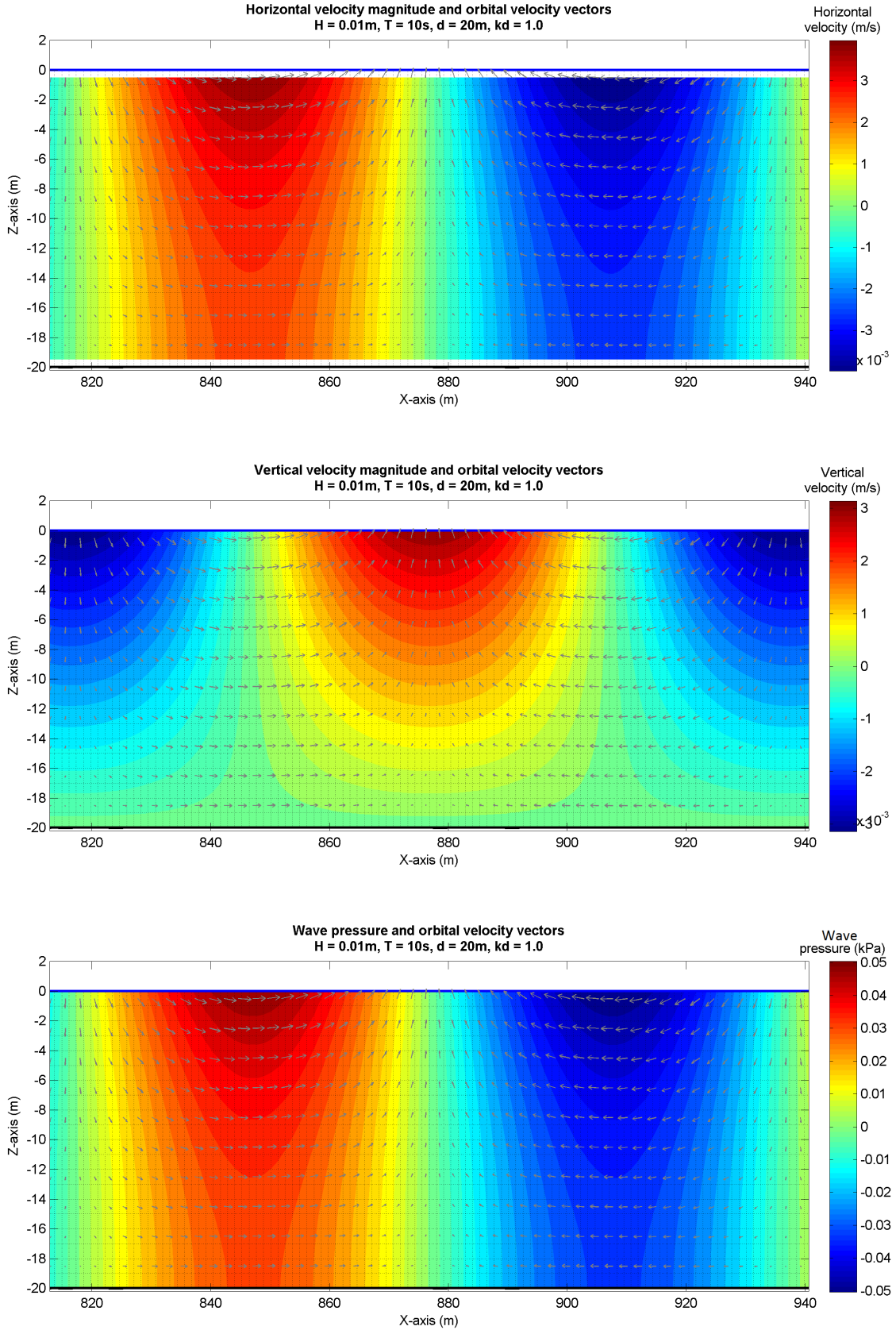

FIGURE C.3: Horizontal velocity, vertical velocity and wave pressure distribution along the wave length and water depth.

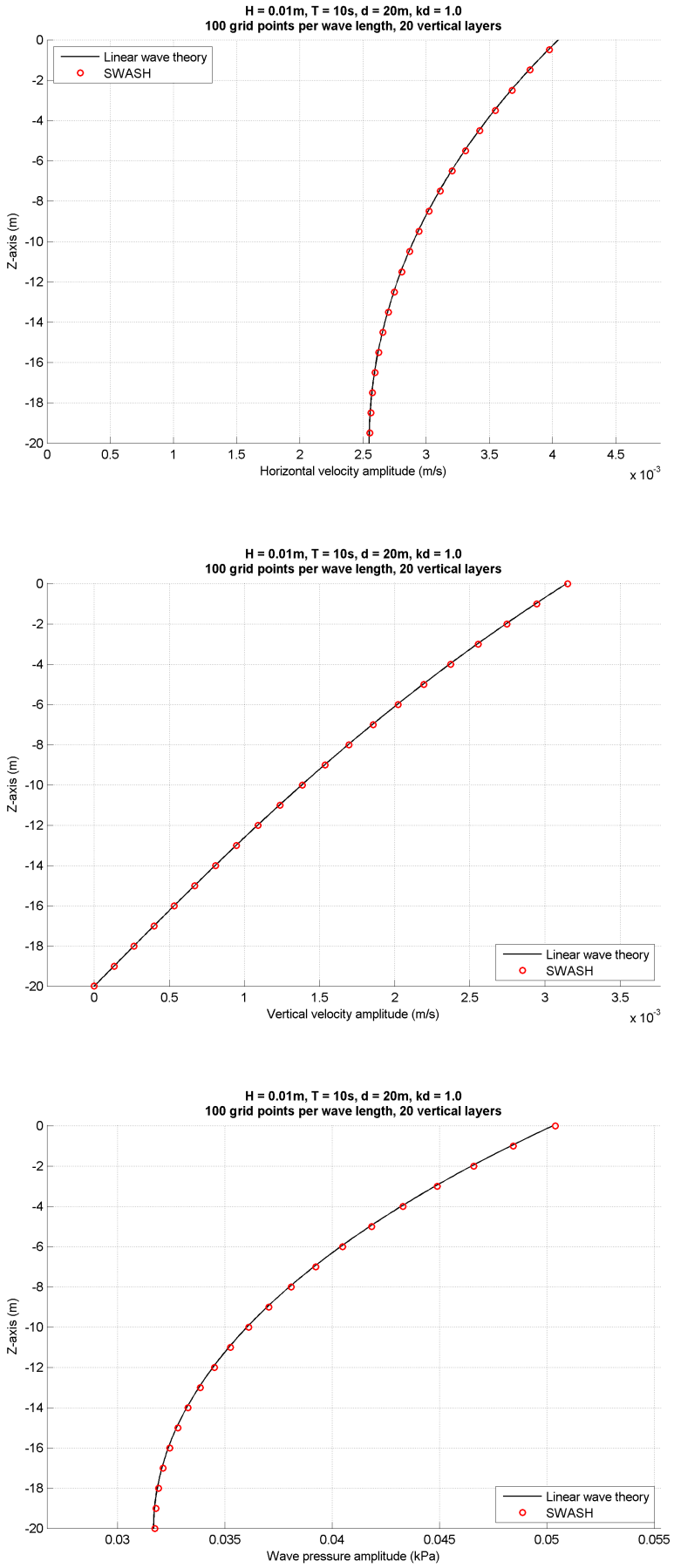

FIGURE C.4: Horizontal velocity, vertical velocity and wave pressure simulated in SWASH and calculated with linear wave theory.

- **H=0.01m, T=5.2s, L_{wave}=42m, kd=3**

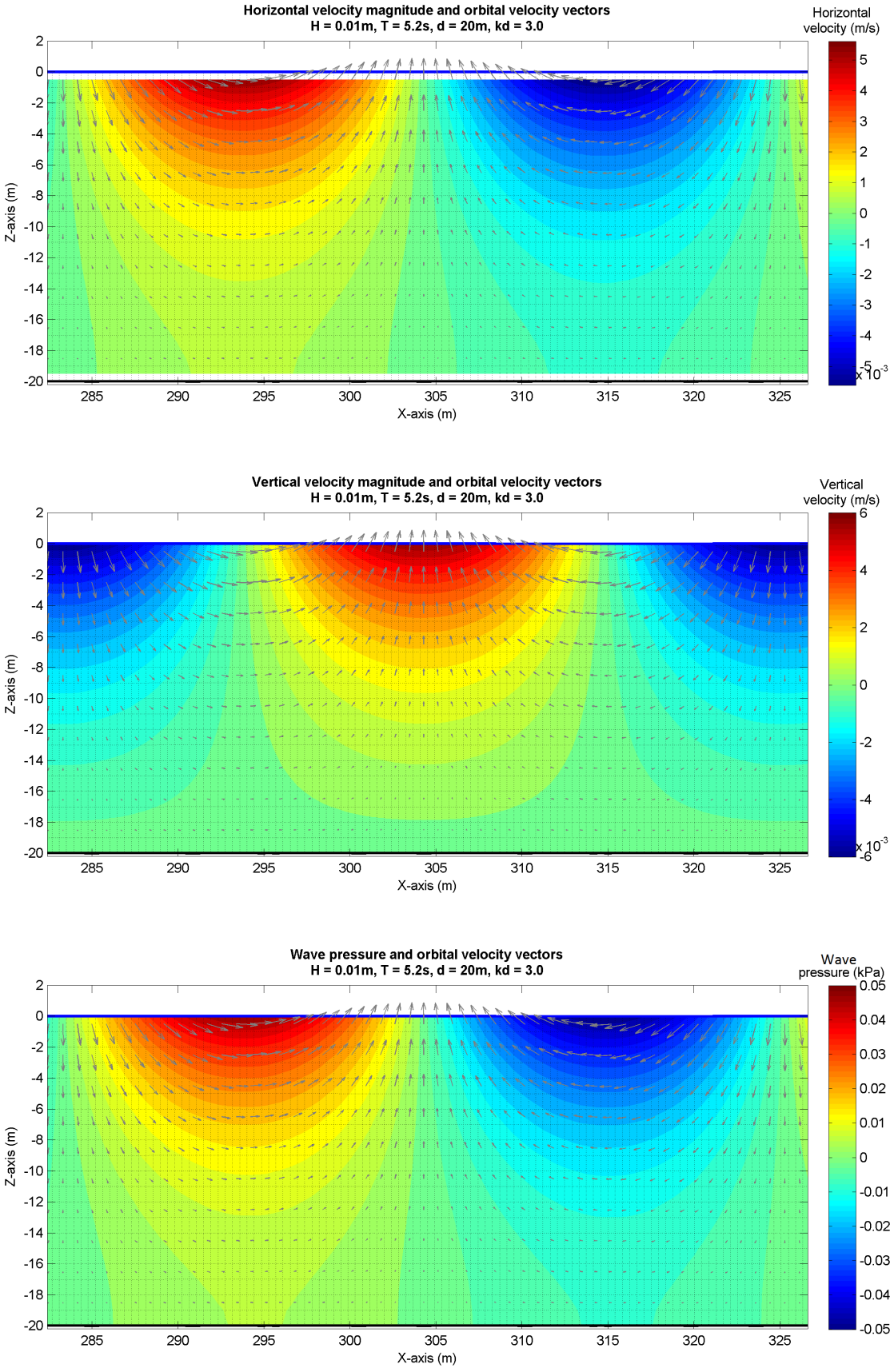

FIGURE C.5: Horizontal velocity, vertical velocity and wave pressure distribution along the wave length and water depth.

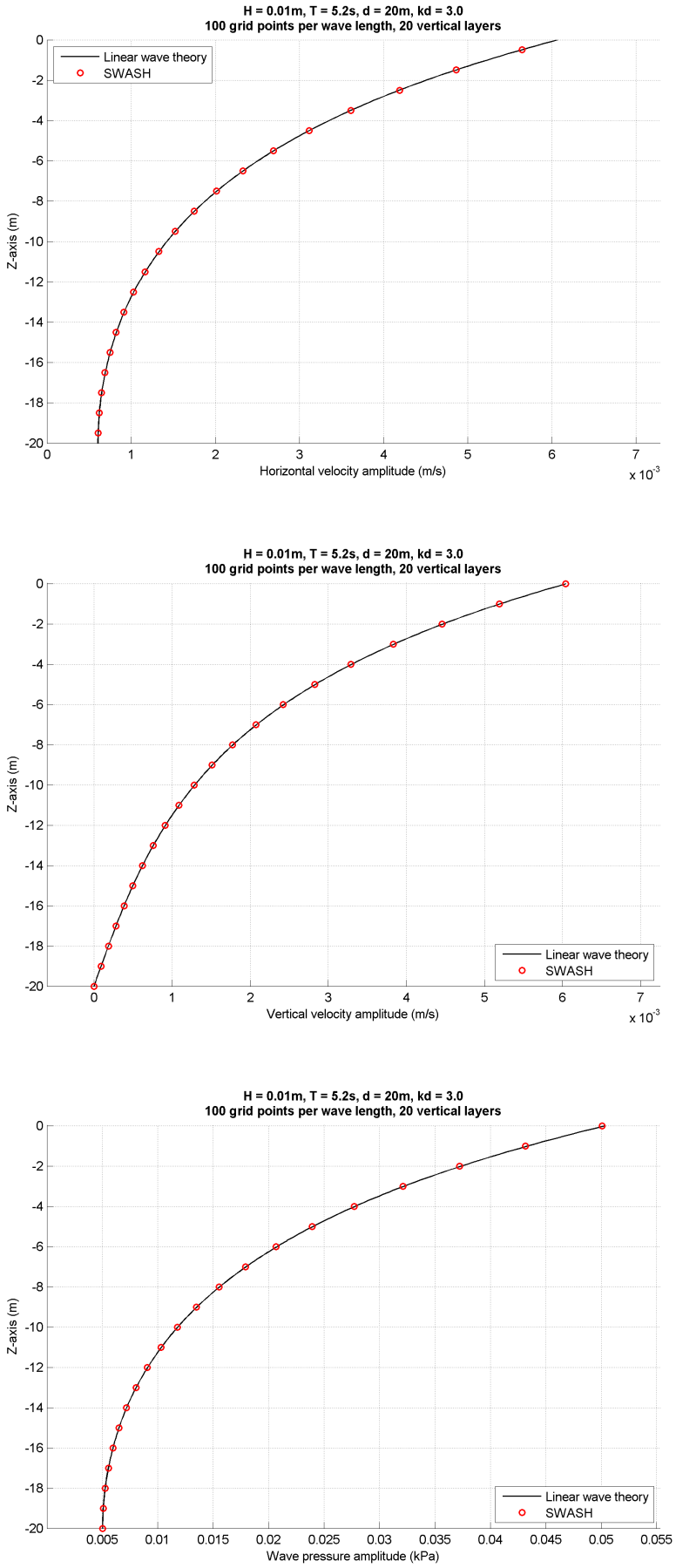

FIGURE C.6: Horizontal velocity, vertical velocity and wave pressure simulated in SWASH and calculated with linear wave theory.

- **H=0.01m, T=4s, L_{wave}=25m, kd=5**

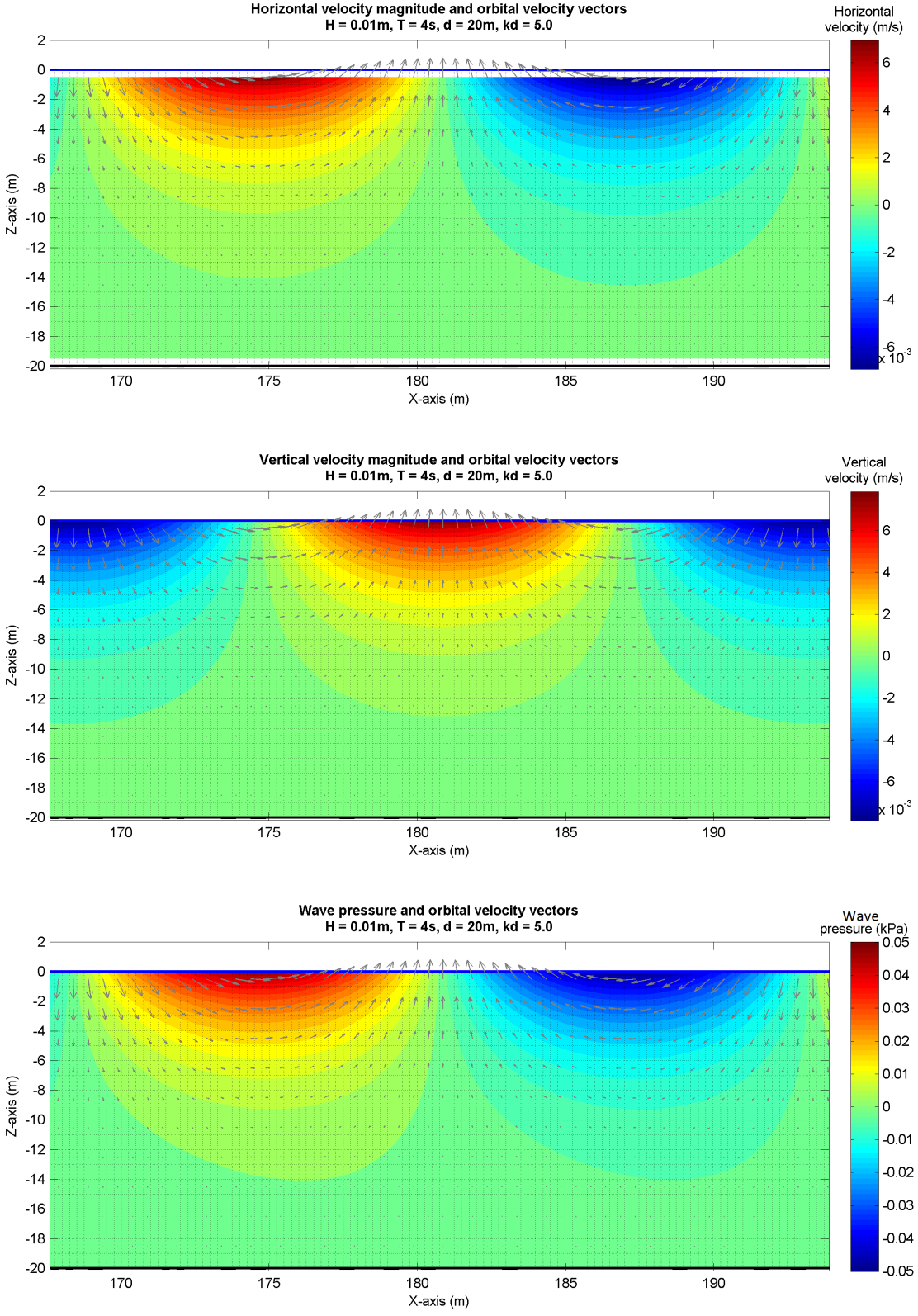

FIGURE C.7: Horizontal velocity, vertical velocity and wave pressure distribution along the wave length and water depth.

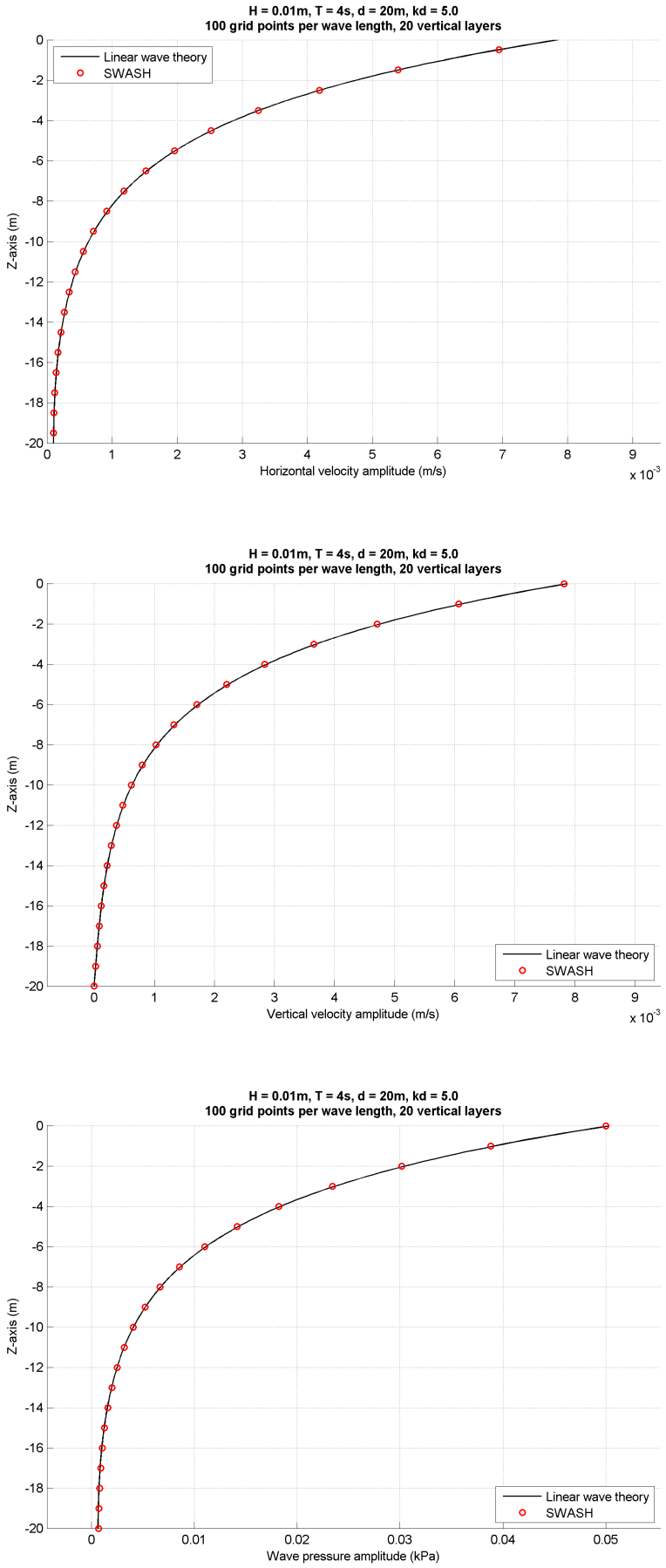

FIGURE C.8: Horizontal velocity, vertical velocity and wave pressure simulated in SWASH and calculated with linear wave theory.

Appendix D

SWASH model results: regular wave simulations

D.1 Dispersion errors

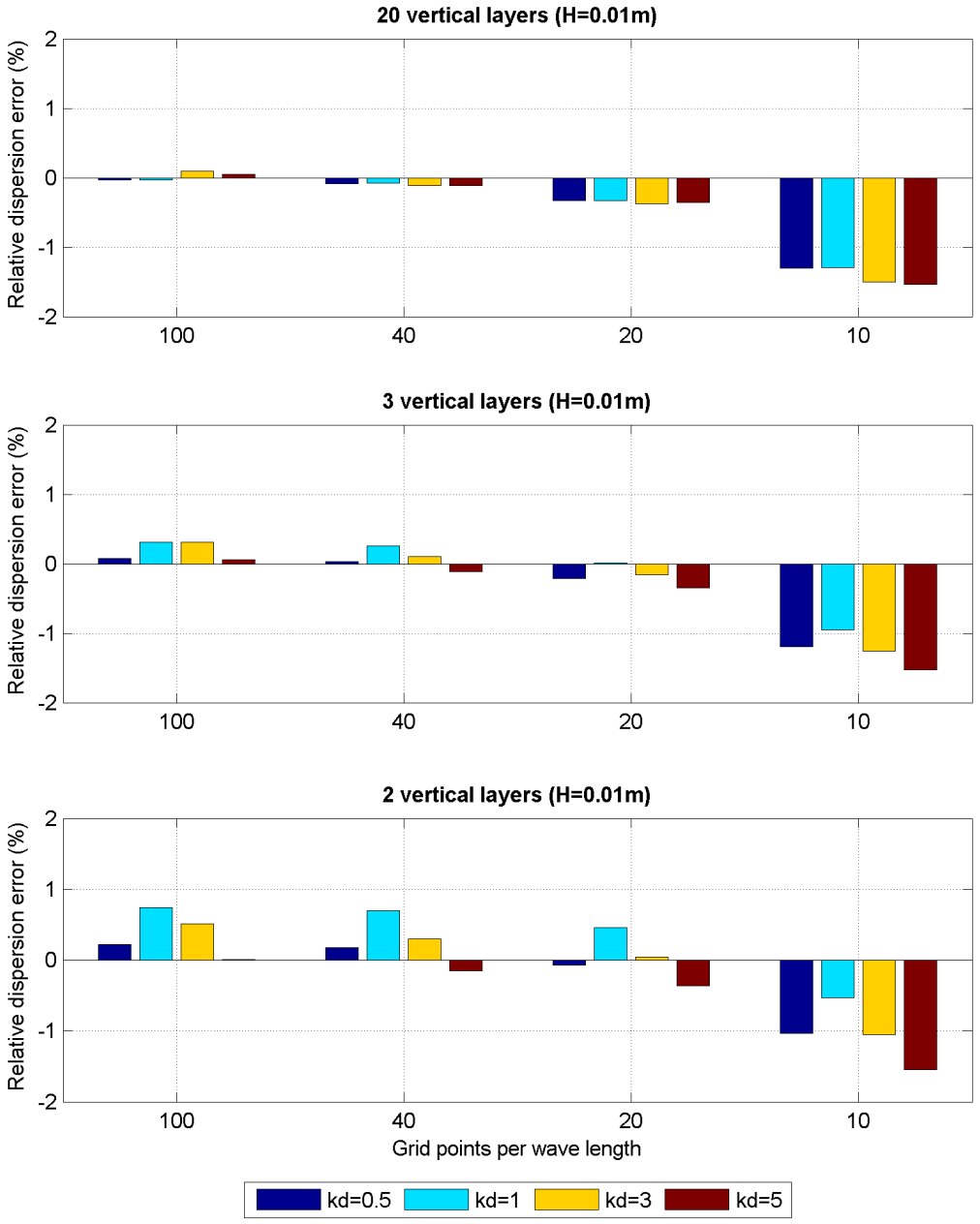

FIGURE D.1: Dispersion errors relative to linear wave theory dispersion relation (wave height=0.01m, 'Default set' of numerical schemes applied to the advection terms of momentum balance equations).

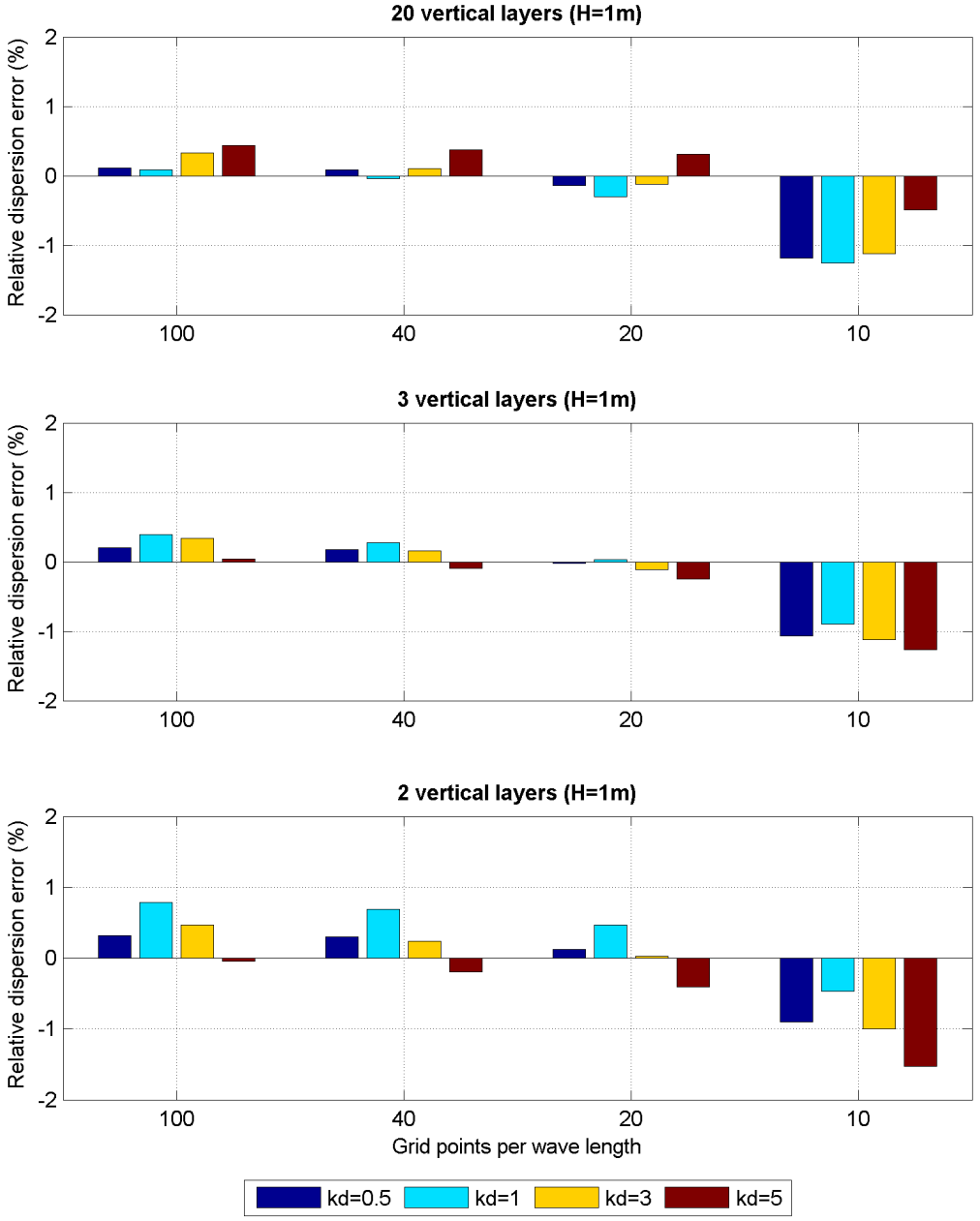

FIGURE D.2: Dispersion errors relative to linear wave theory dispersion relation (wave height=1m, 'Default set' of numerical schemes applied to the advection terms of momentum balance equations).

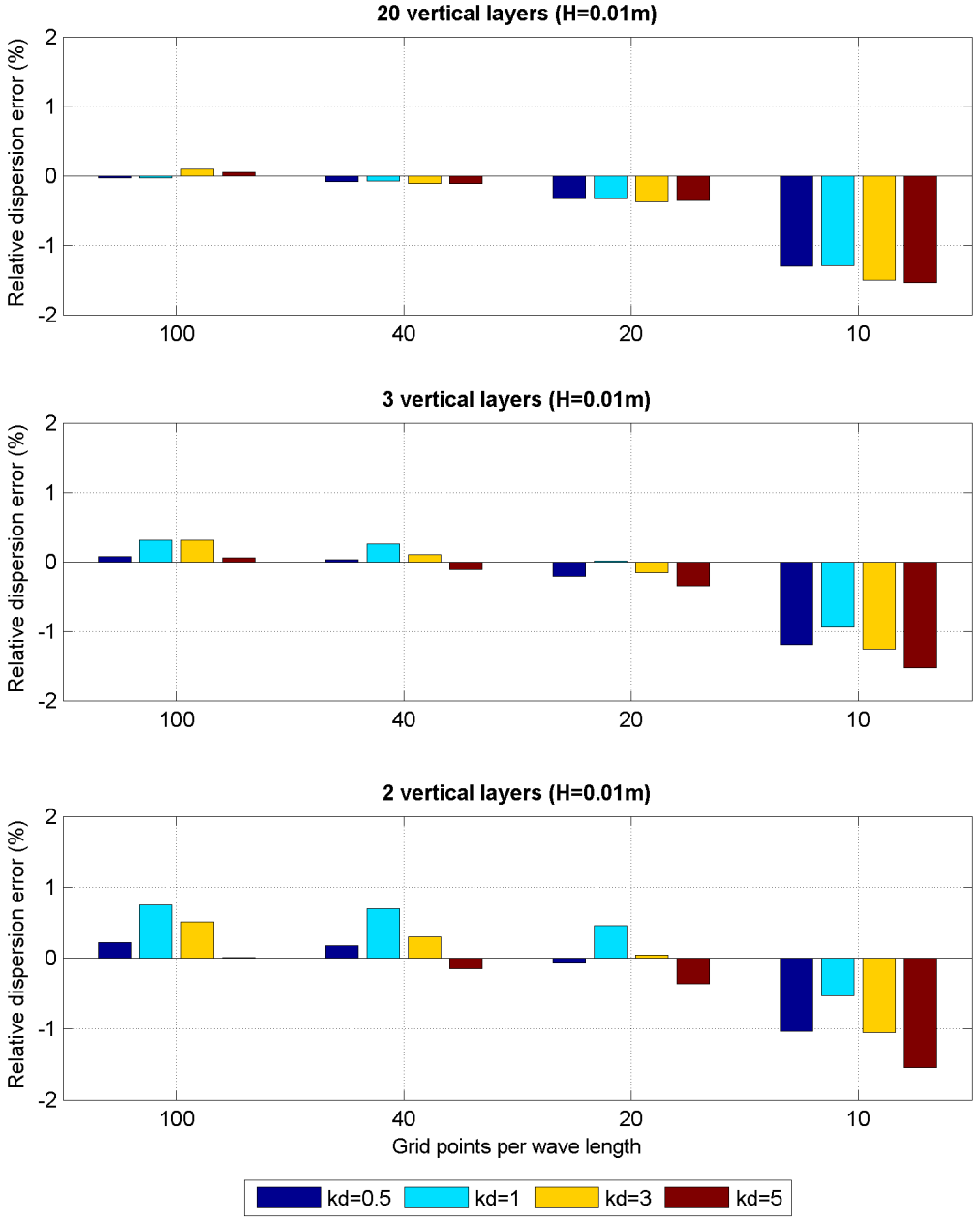

FIGURE D.3: Dispersion errors relative to linear wave theory dispersion relation (wave height=0.01m, 'Adapted set' of numerical schemes applied to the advection terms of momentum balance equations).

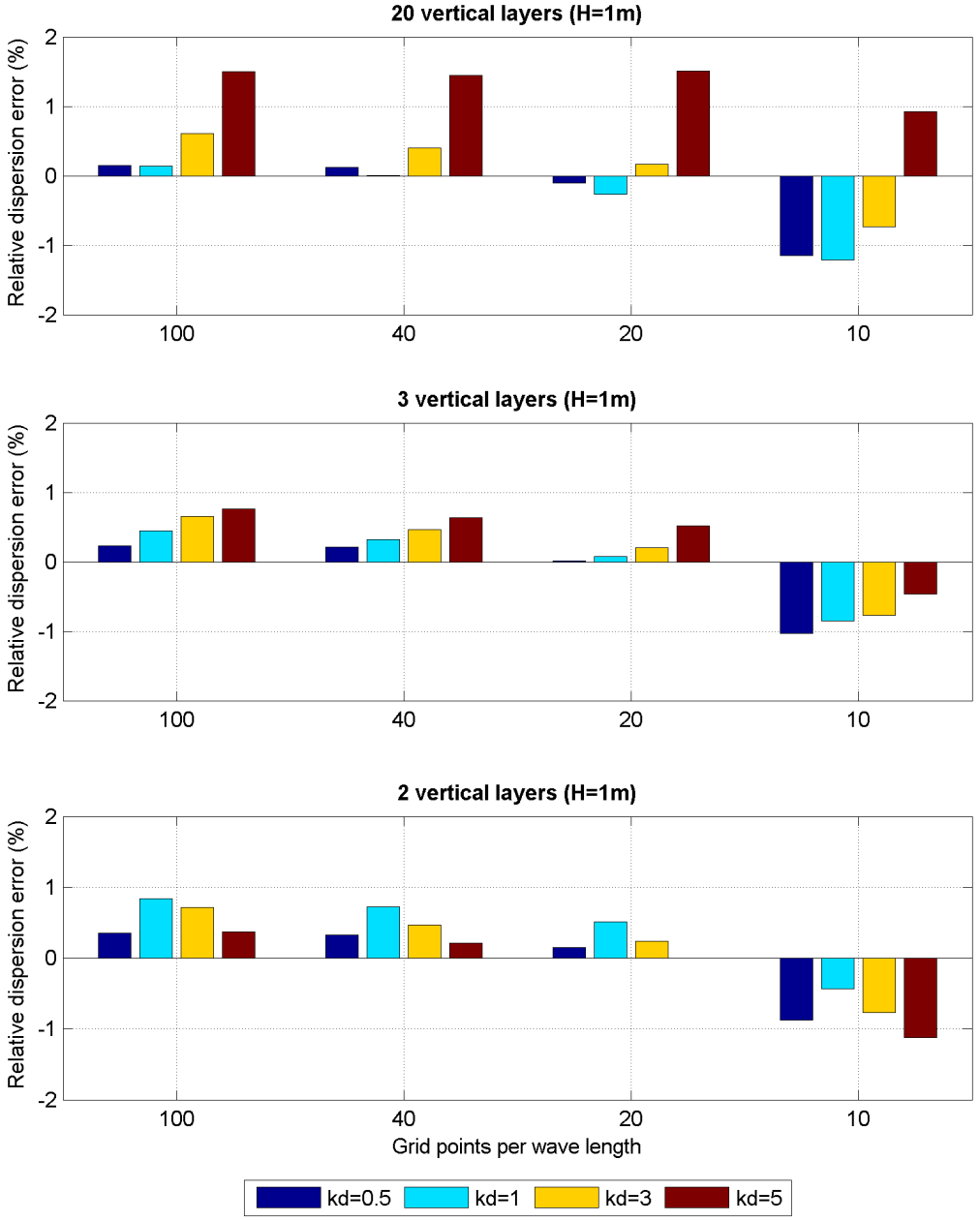

FIGURE D.4: Dispersion errors relative to linear wave theory dispersion relation (wave height=1m, 'Adapted set' of numerical schemes applied to the advection terms of momentum balance equations).

D.2 Amplitude errors near the incomming boundary

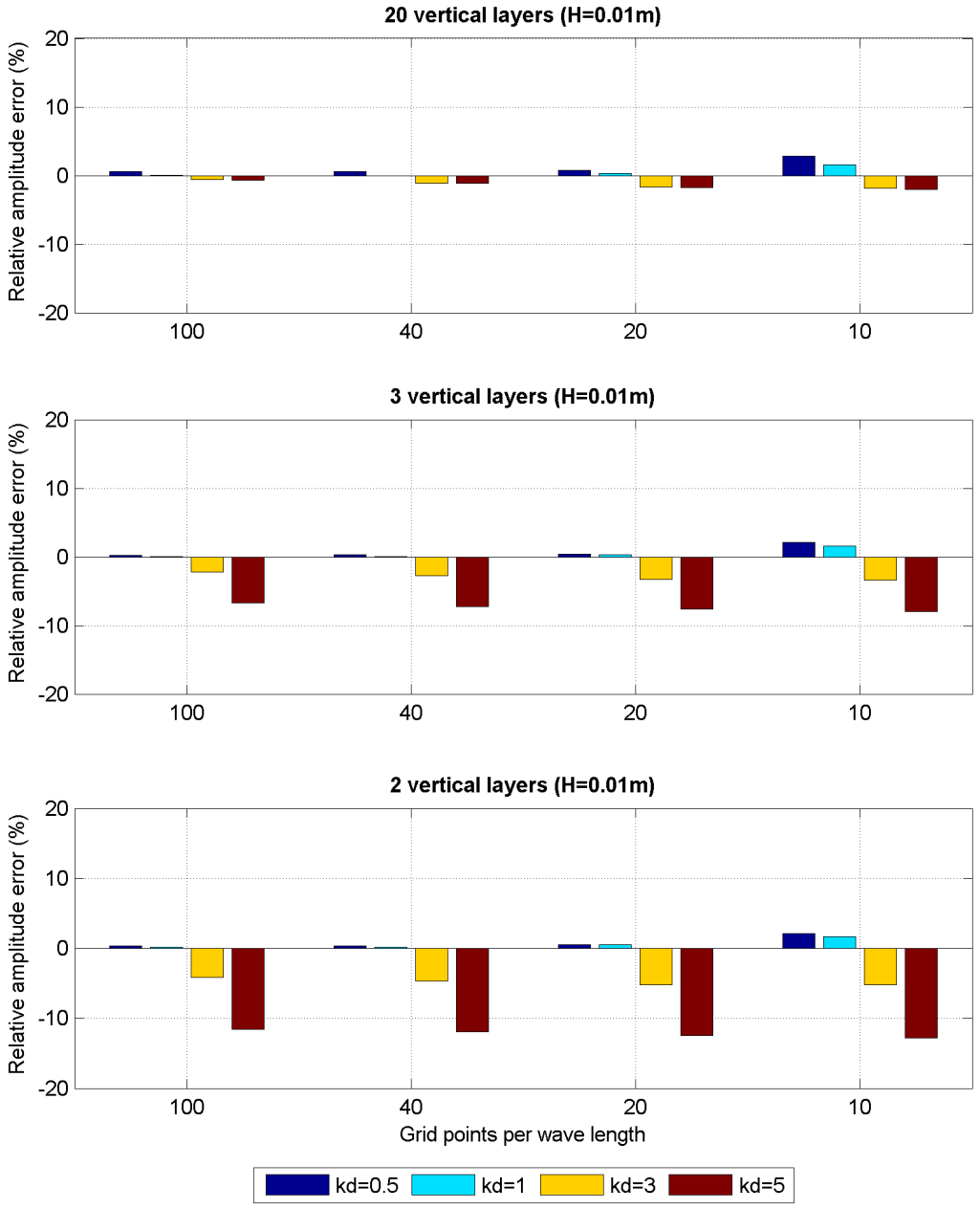

FIGURE D.5: Amplitude error after one wave length from the forcing boundary relative to the forced wave amplitude (0.005m). 'Default set' of numerical schemes applied to the advection terms of momentum balance equations.

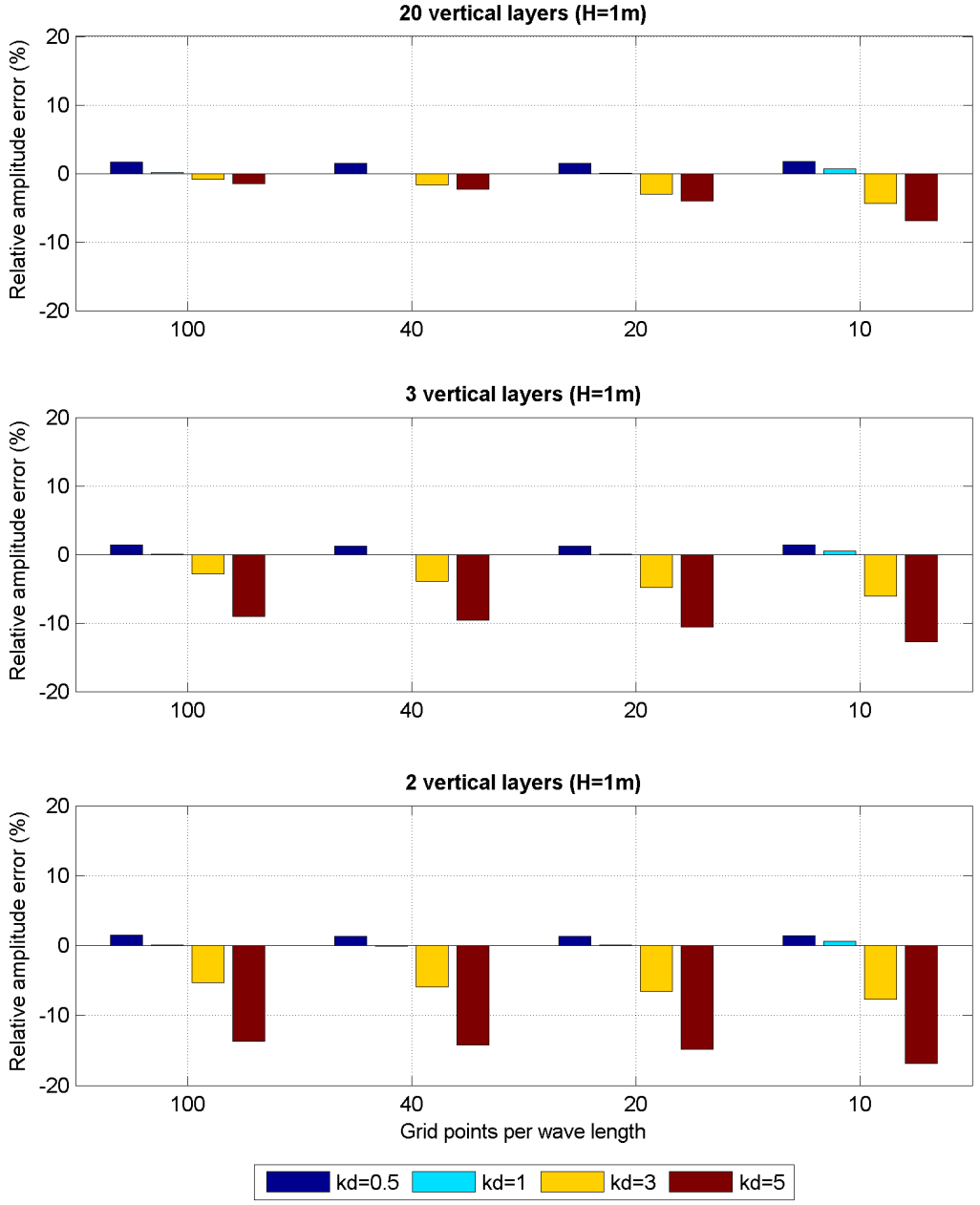

FIGURE D.6: Amplitude error after one wave length from the forcing boundary relative to the forced wave amplitude (0.5m).'Default set' of numerical schemes applied to the advection terms of momentum balance equations.

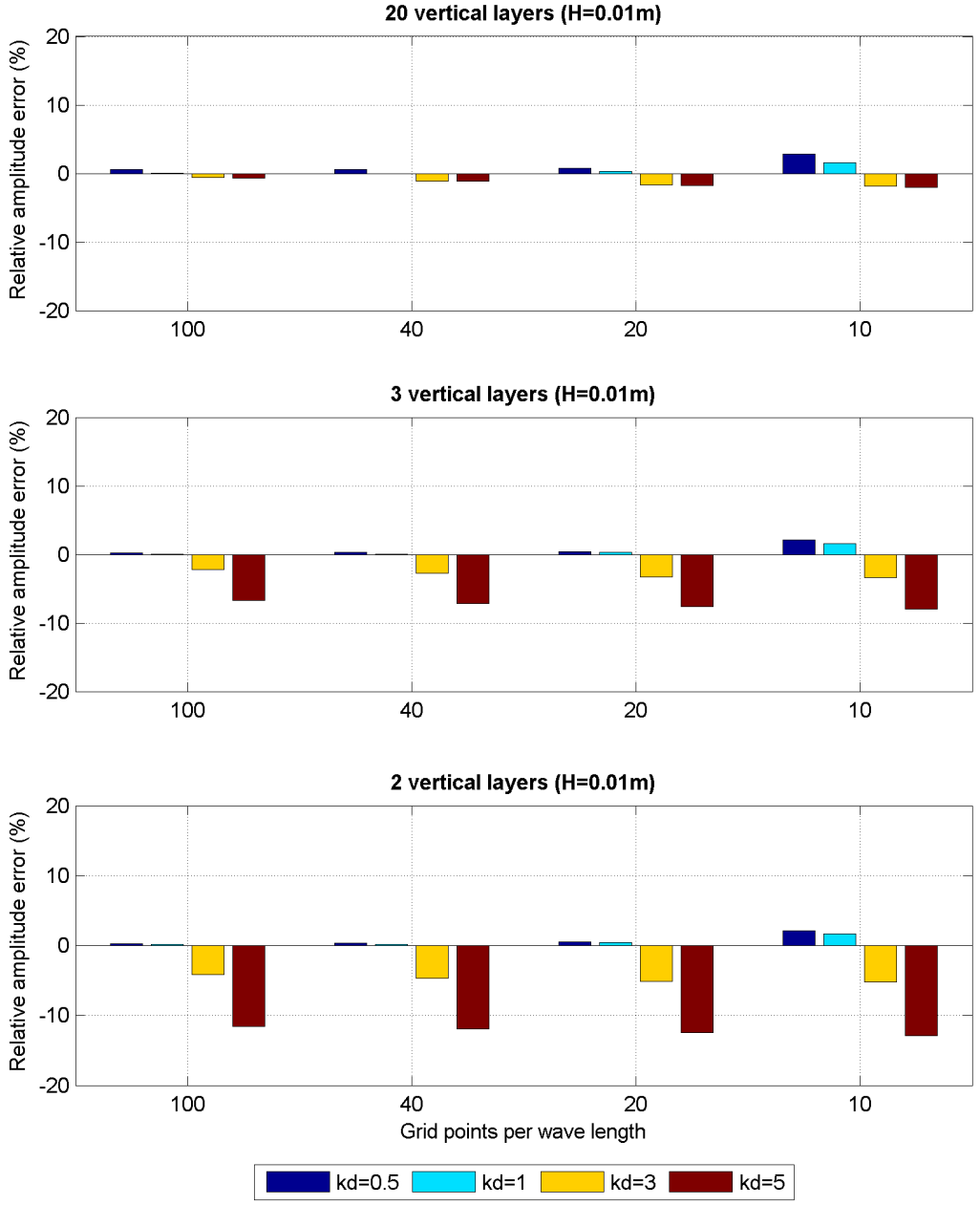

FIGURE D.7: Amplitude error after one wave length from the forcing boundary relative to the forced wave amplitude (0.005m). 'Adapted set' of numerical schemes applied to the advection terms of momentum balance equations.

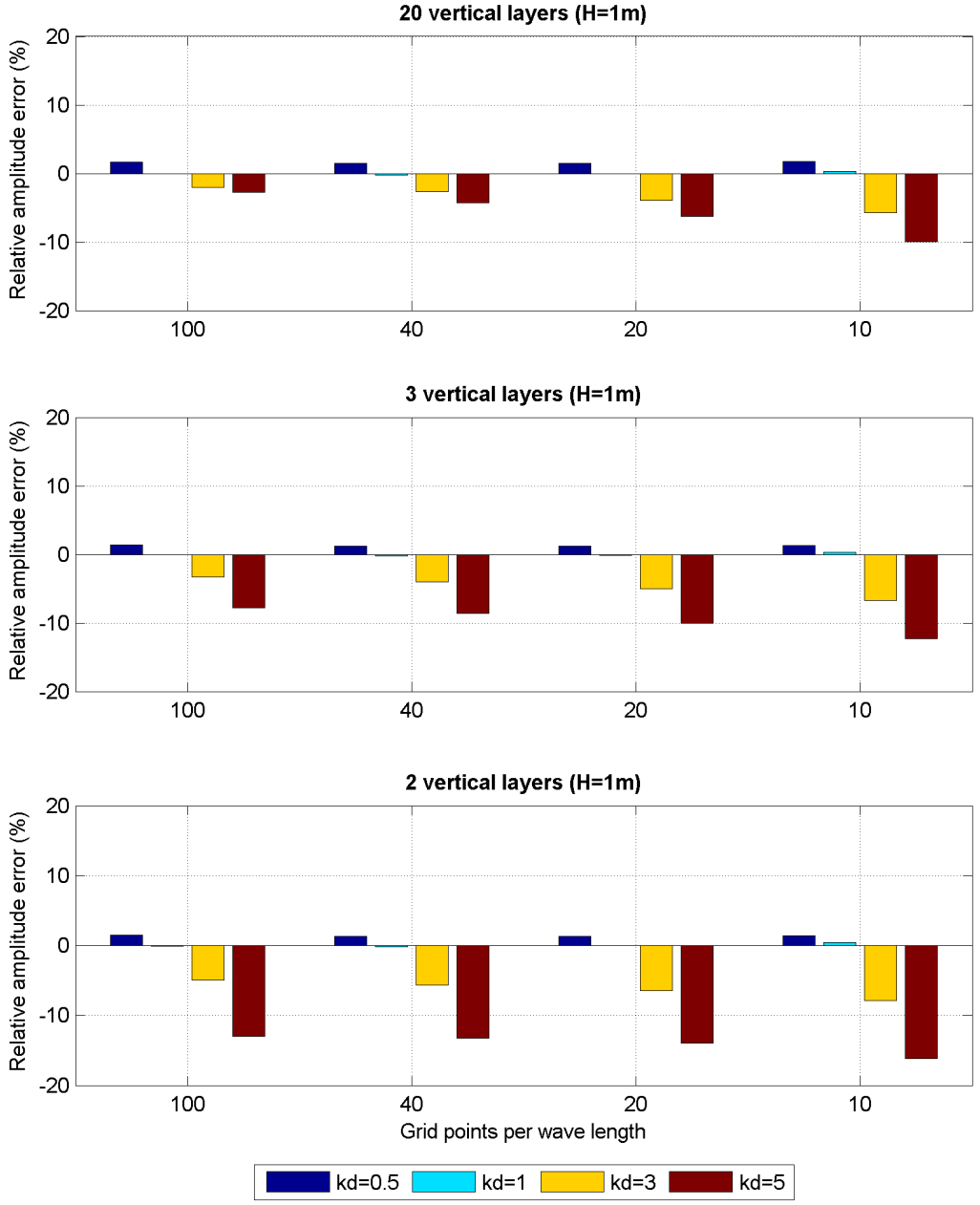

FIGURE D.8: Amplitude error after one wave length from the forcing boundary relative to the forced wave amplitude (0.5m). 'Adapted set' of numerical schemes applied to the advection terms of momentum balance equations.

D.3 Amplitude errors per wave length along the domain

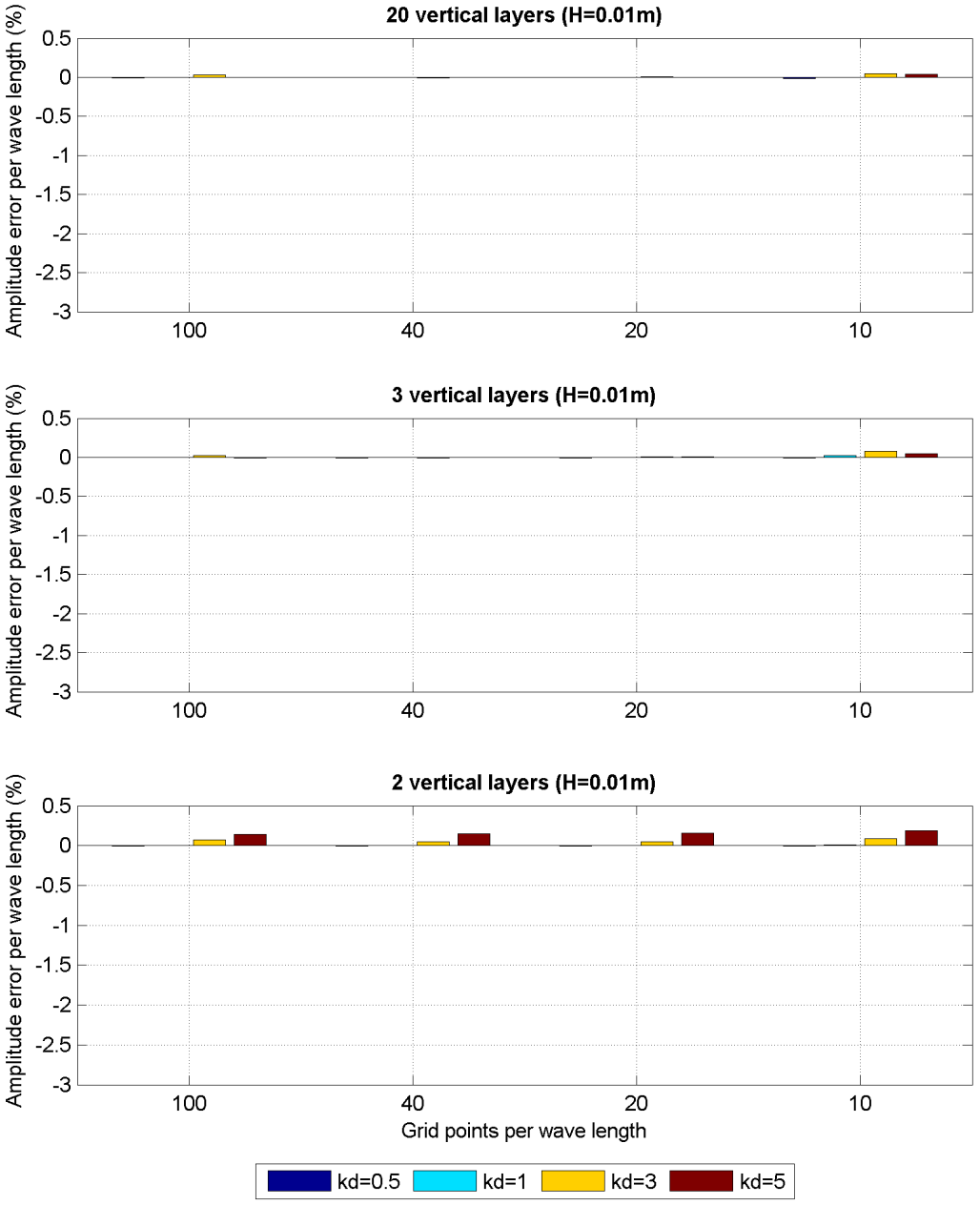

FIGURE D.9: Amplitude error per wave length relative to the forced wave amplitude (0.005m). Calculated from model results within $\lambda \leq x \leq 10\lambda$. 'Default set' of numerical schemes applied to the advection terms of momentum balance equations.

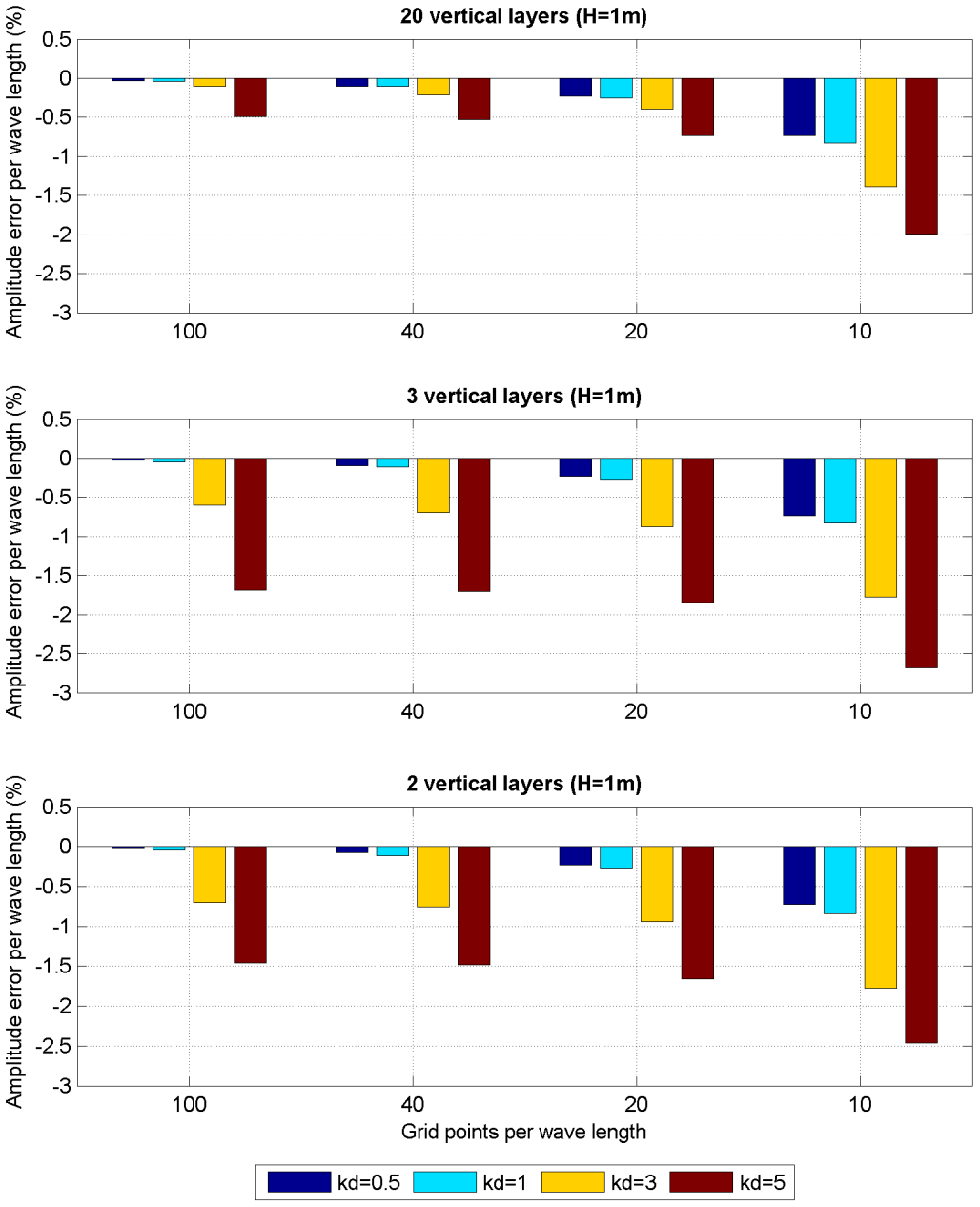

FIGURE D.10: Amplitude error per wave length relative to the forced wave amplitude (0.5m). Calculated from model results within $\lambda \leq x \leq 10\lambda$. 'Default set' of numerical schemes applied to the advection terms of momentum balance equations.

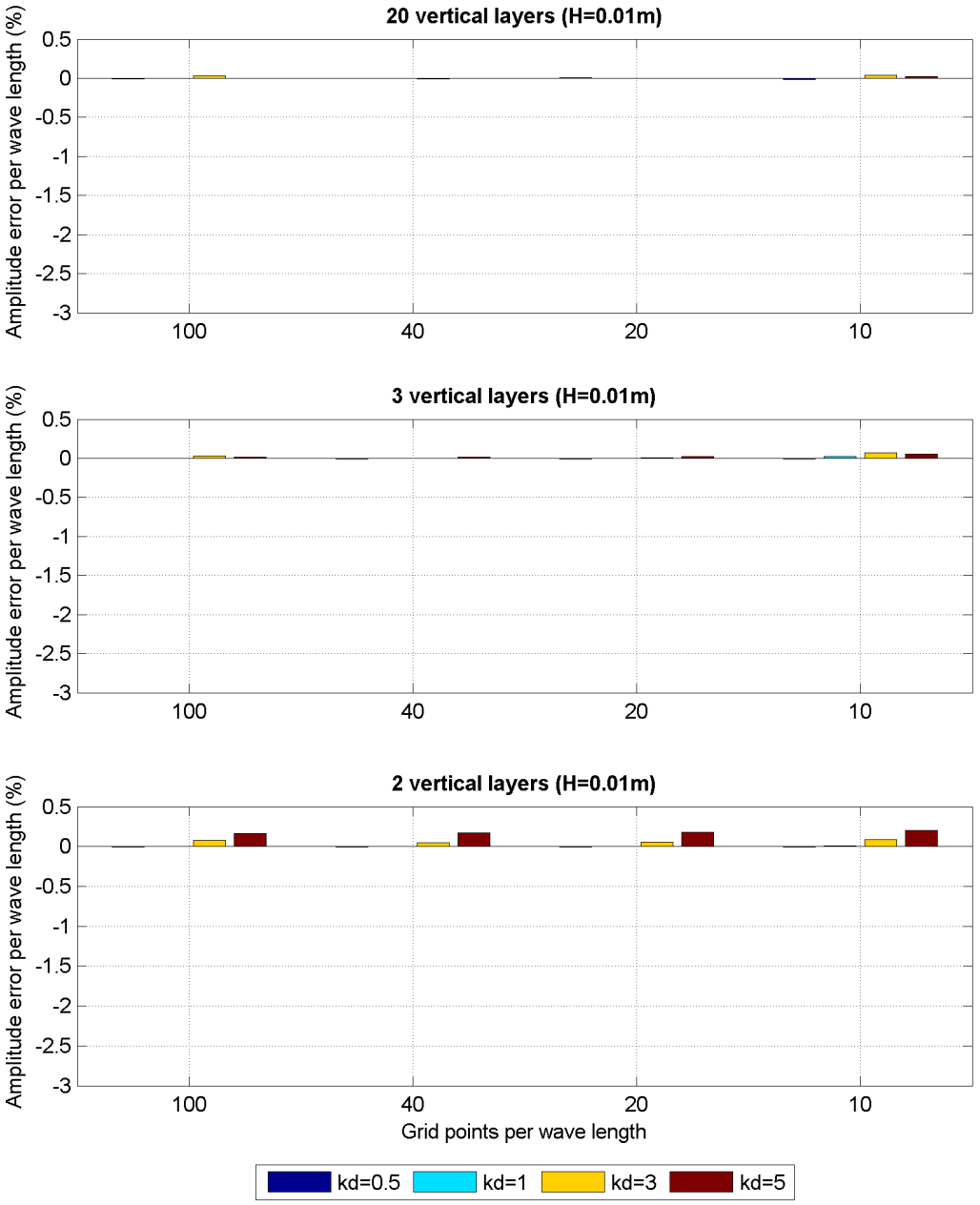

FIGURE D.11: Amplitude error per wave length relative to the forced wave amplitude (0.005m). Calculated from model results within $\lambda \leq x \leq 10\lambda$. 'Adapted set' of numerical schemes applied to the advection terms of momentum balance equations.

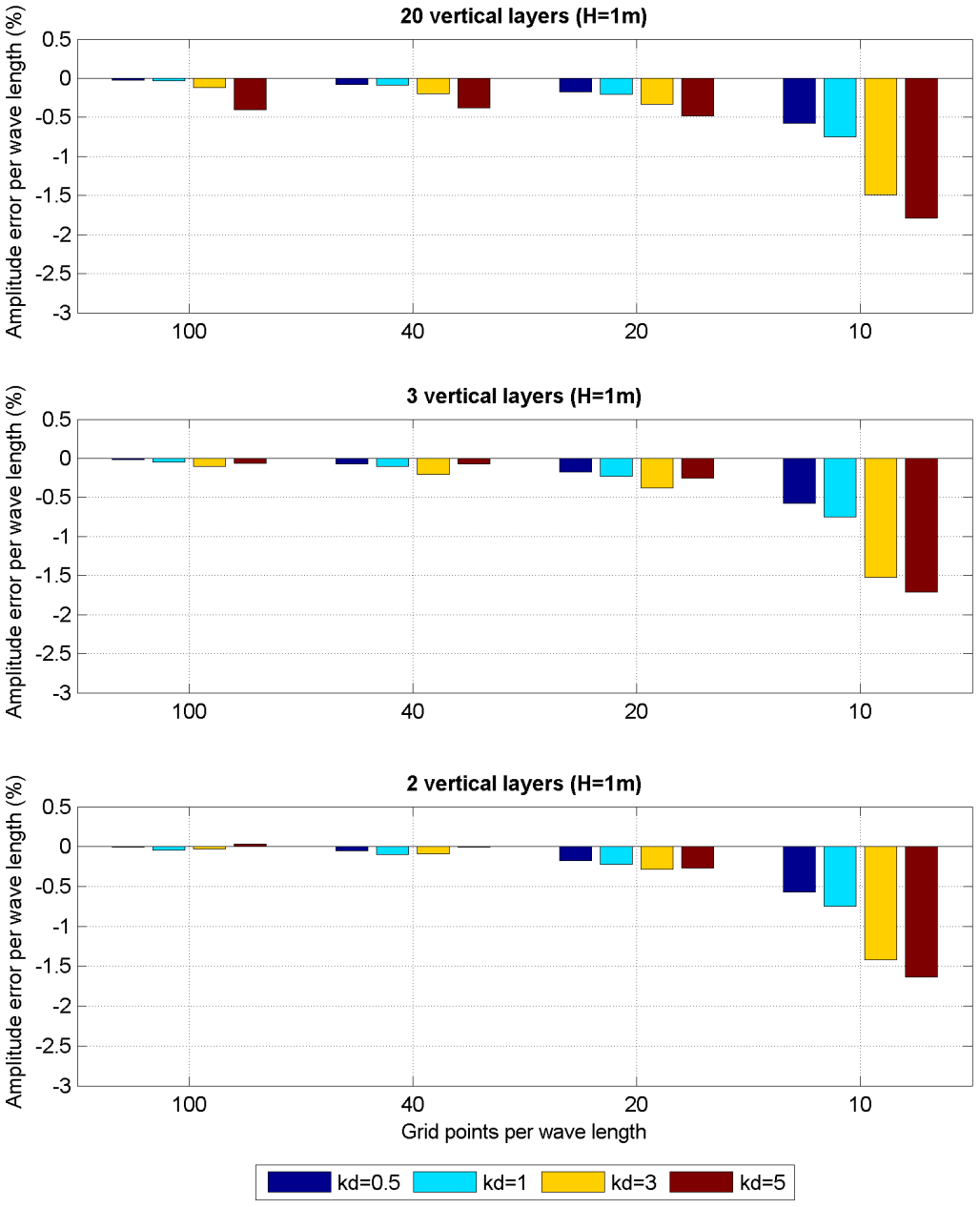

FIGURE D.12: Amplitude error per wave length relative to the forced wave amplitude (0.5m). Calculated from model results within $\lambda \leq x \leq 10\lambda$. 'Adapted set' of numerical schemes applied to the advection terms of momentum balance equations.

Appendix E

Harberth model results

E.1 Regular waves: 1st order forces

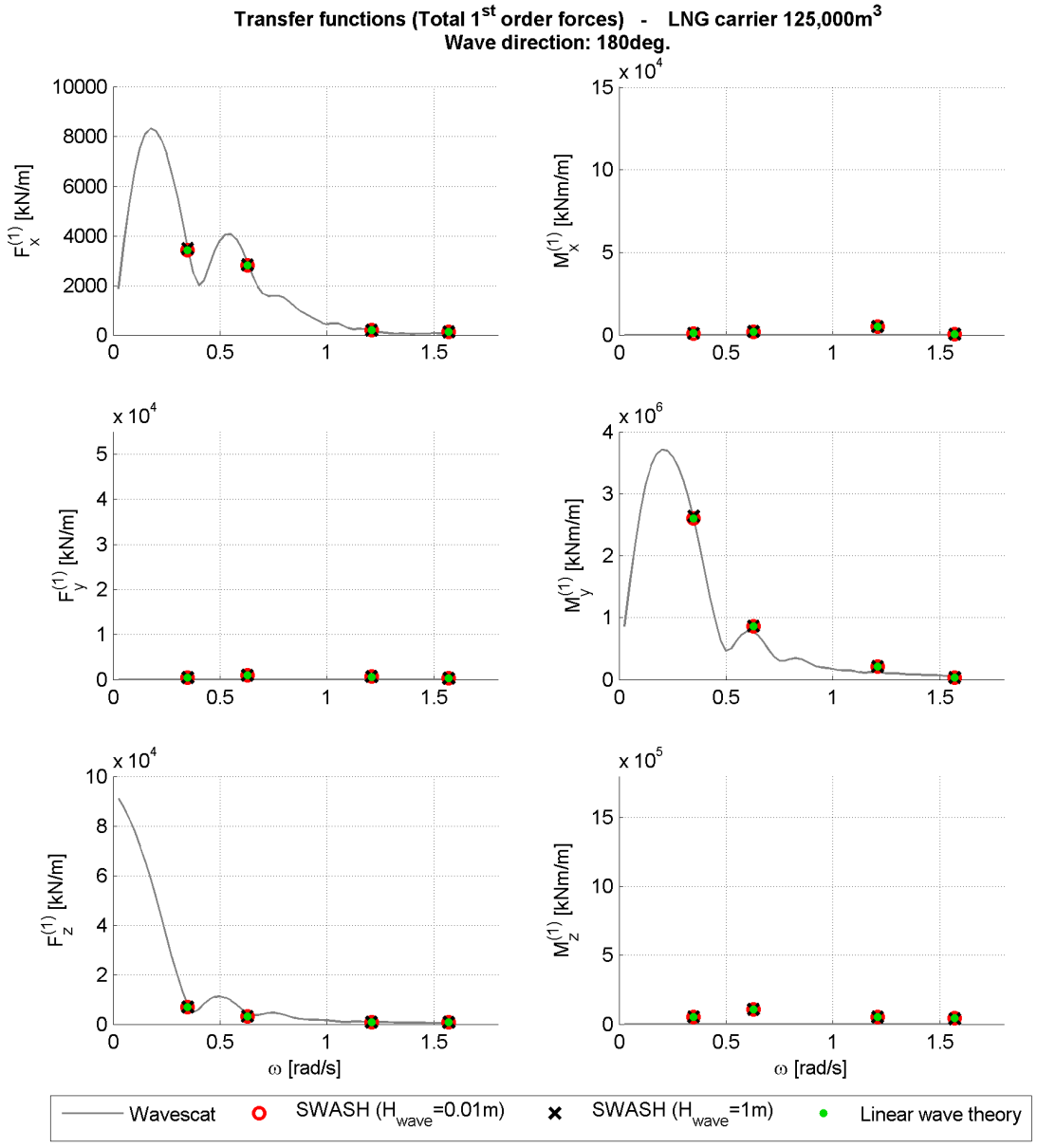

FIGURE E.1: Transfer functions for first order forces computed with Wavescat and Harberth models (wave direction = 180°). SWASH wave model run with 20 vertical layers.

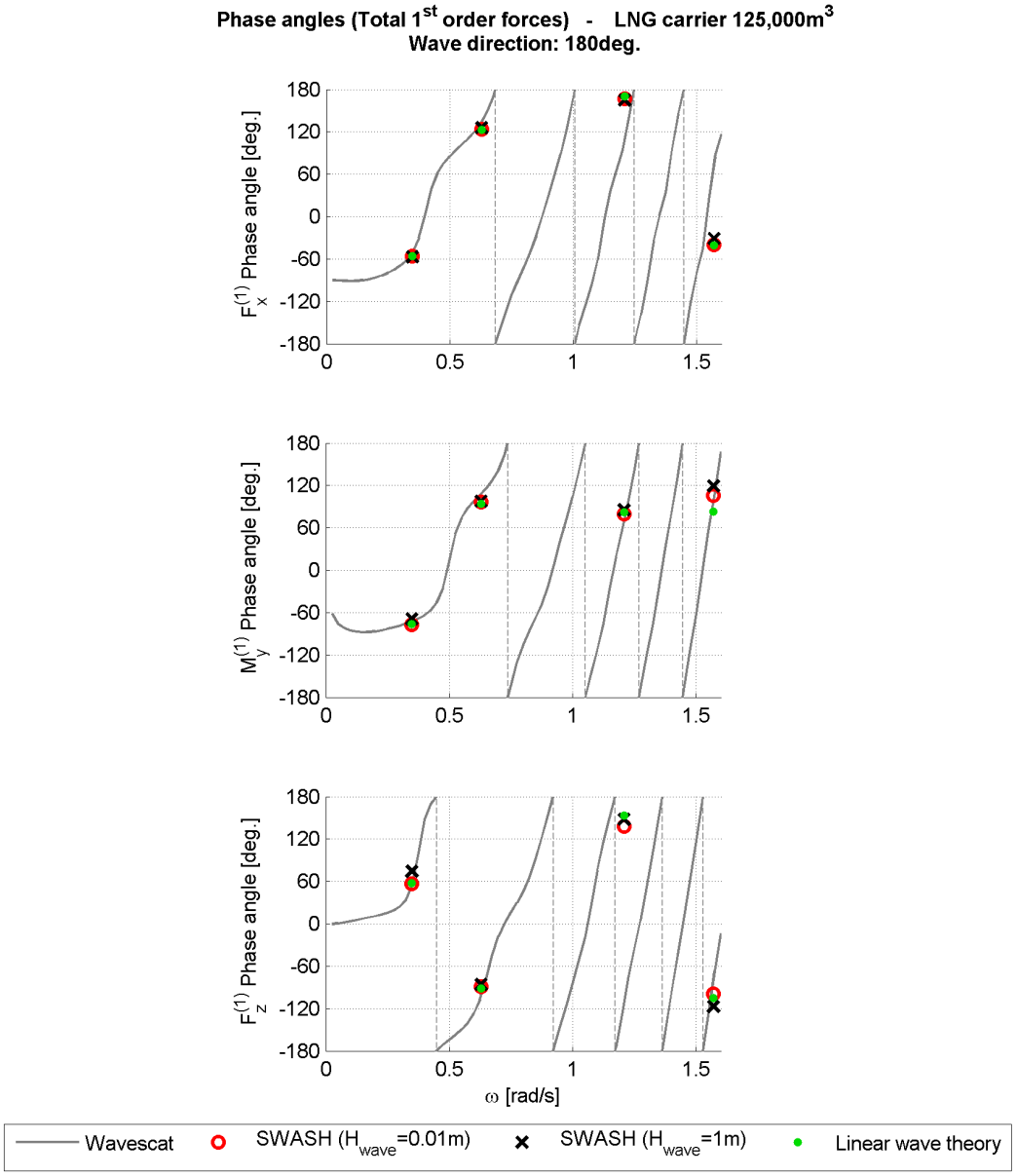

FIGURE E.2: Phase angles for first order forces computed with Wavescat and Harberth models (wave direction = 180°). SWASH wave model run with 20 vertical layers.

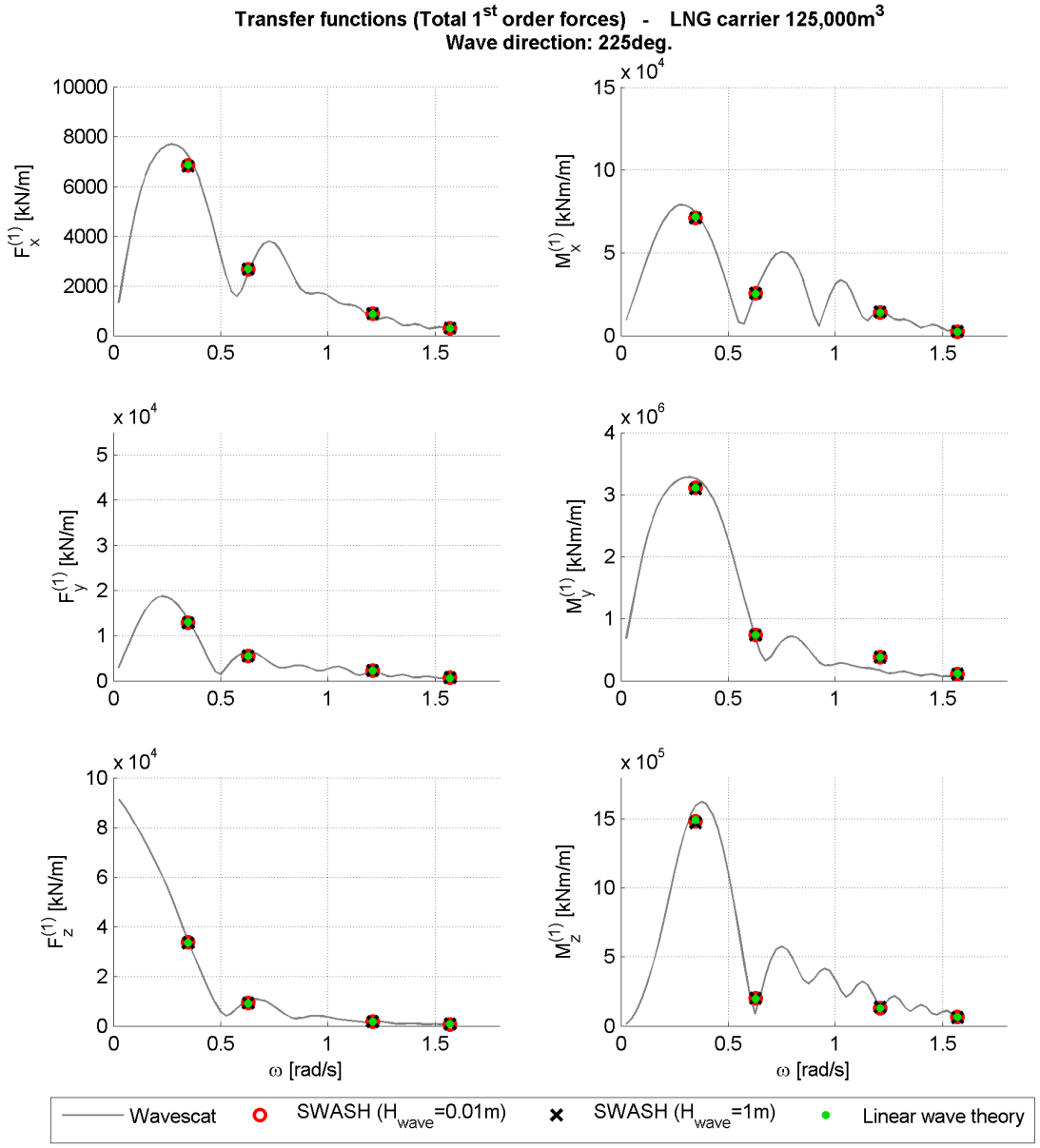

FIGURE E.3: Transfer functions for first order forces computed with Wavescat and Harberth models (wave direction = 225°). SWASH wave model run with 20 vertical layers.

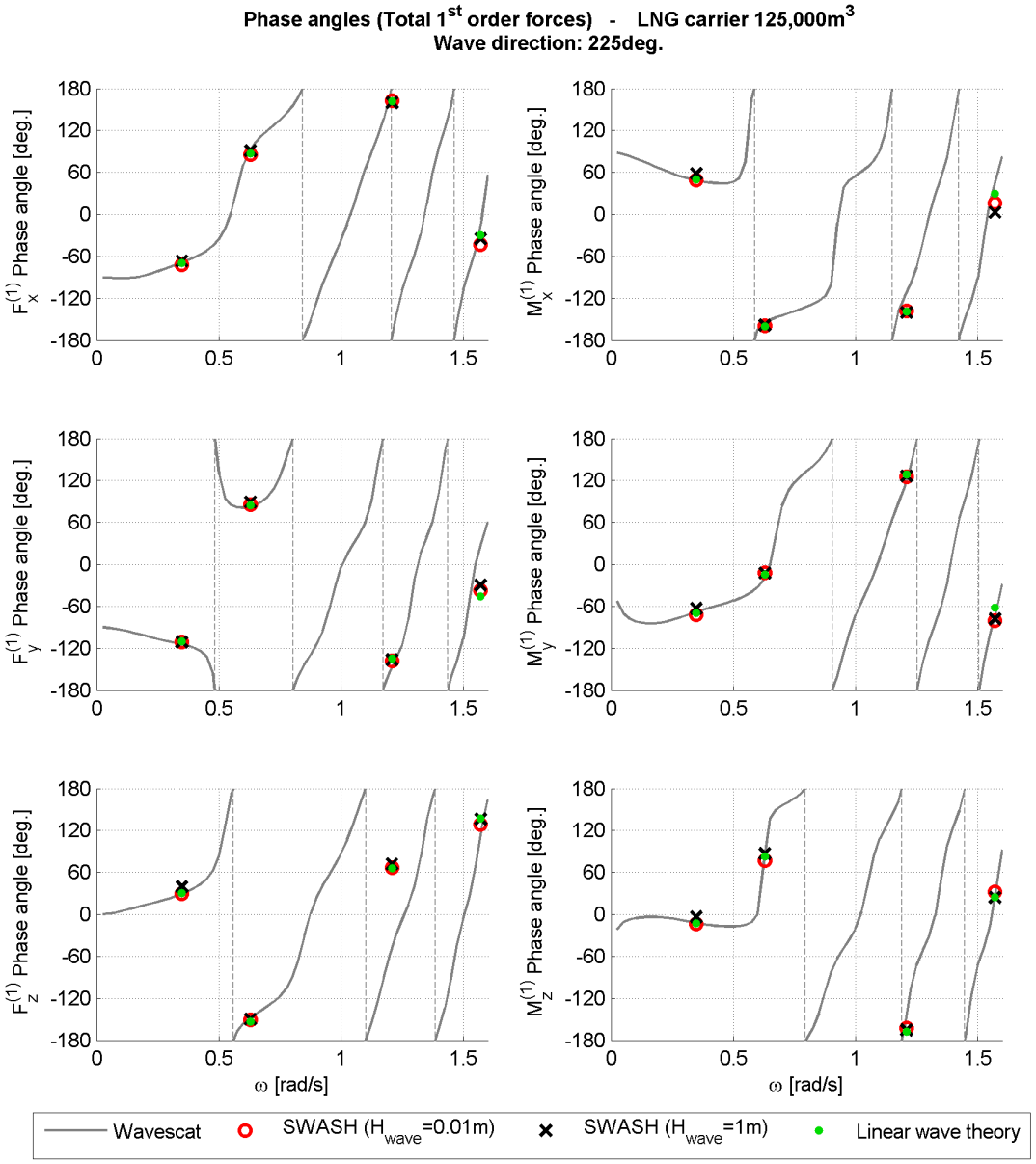

FIGURE E.4: Phase angles for first order forces computed with Wavescat and Harberth models (wave direction = 225°). SWASH wave model run with 20 vertical layers.

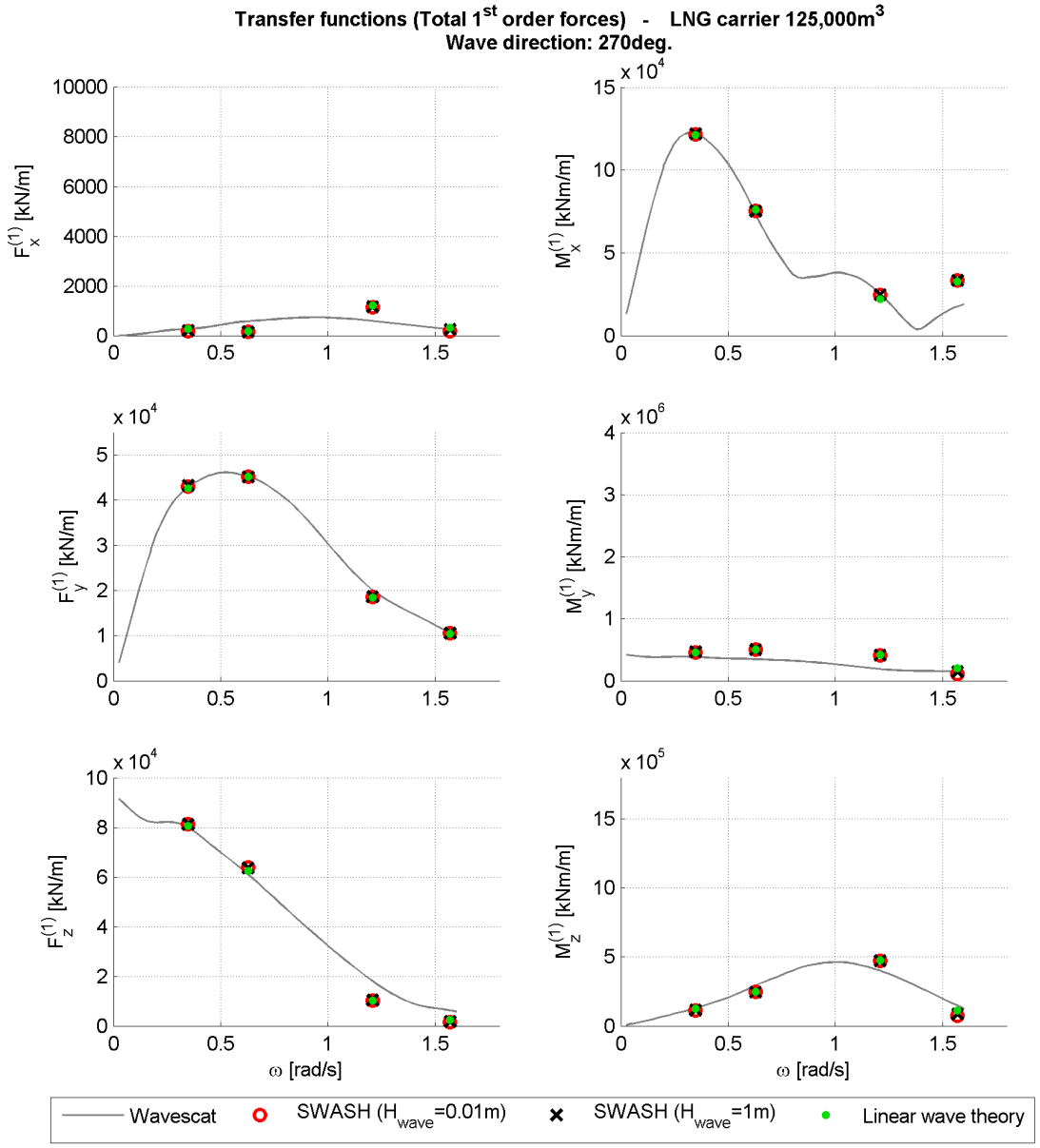

FIGURE E.5: Transfer functions for first order forces computed with Wavescat and Harberth models (wave direction = 270°). SWASH wave model run with 20 vertical layers.

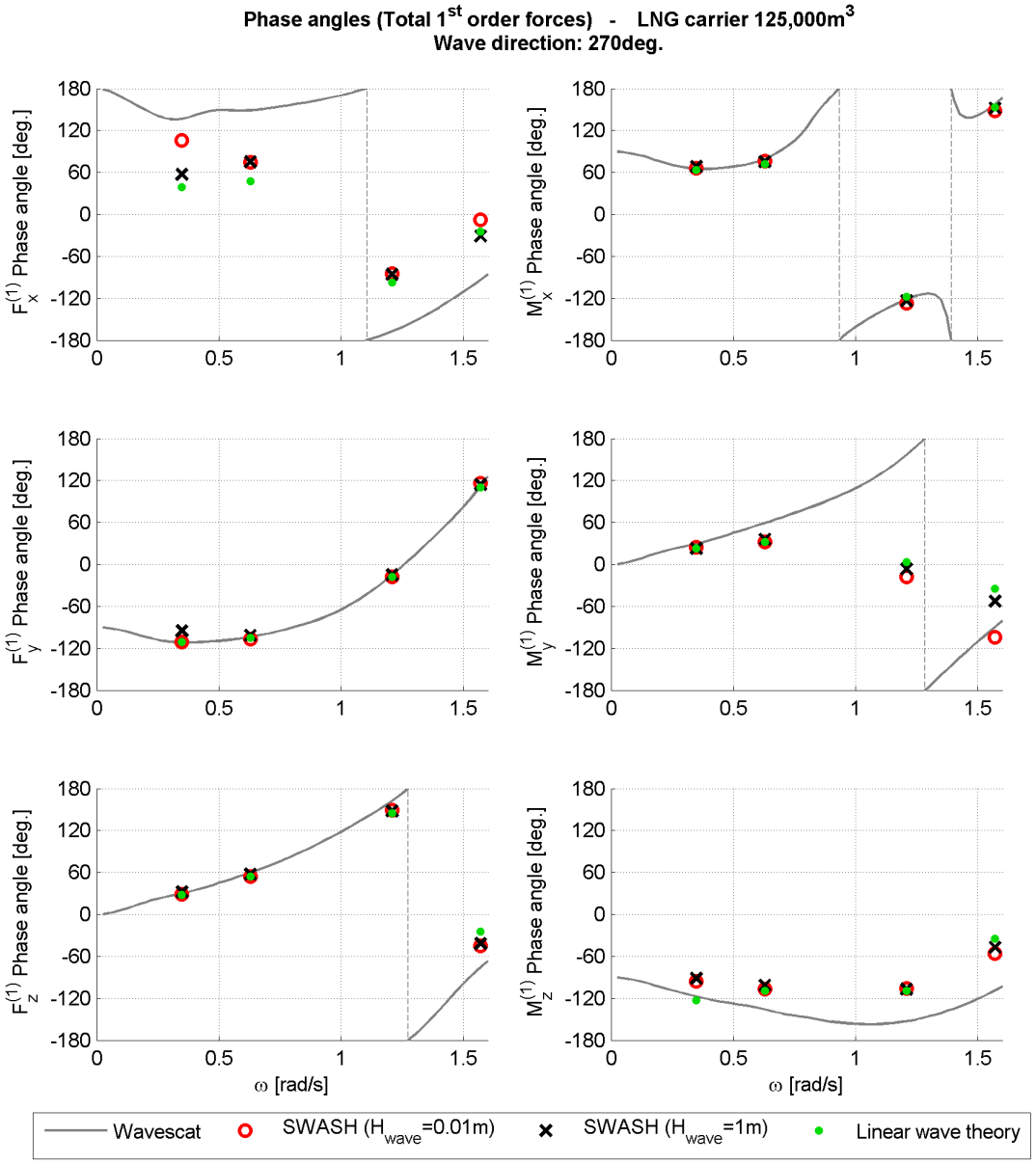

FIGURE E.6: Phase angles for first order forces computed with Wavescat and Harberth models (wave direction = 270°). SWASH wave model run with 20 vertical layers.

E.1.1 Froude-Krylov forces *vs.* Diffraction forces

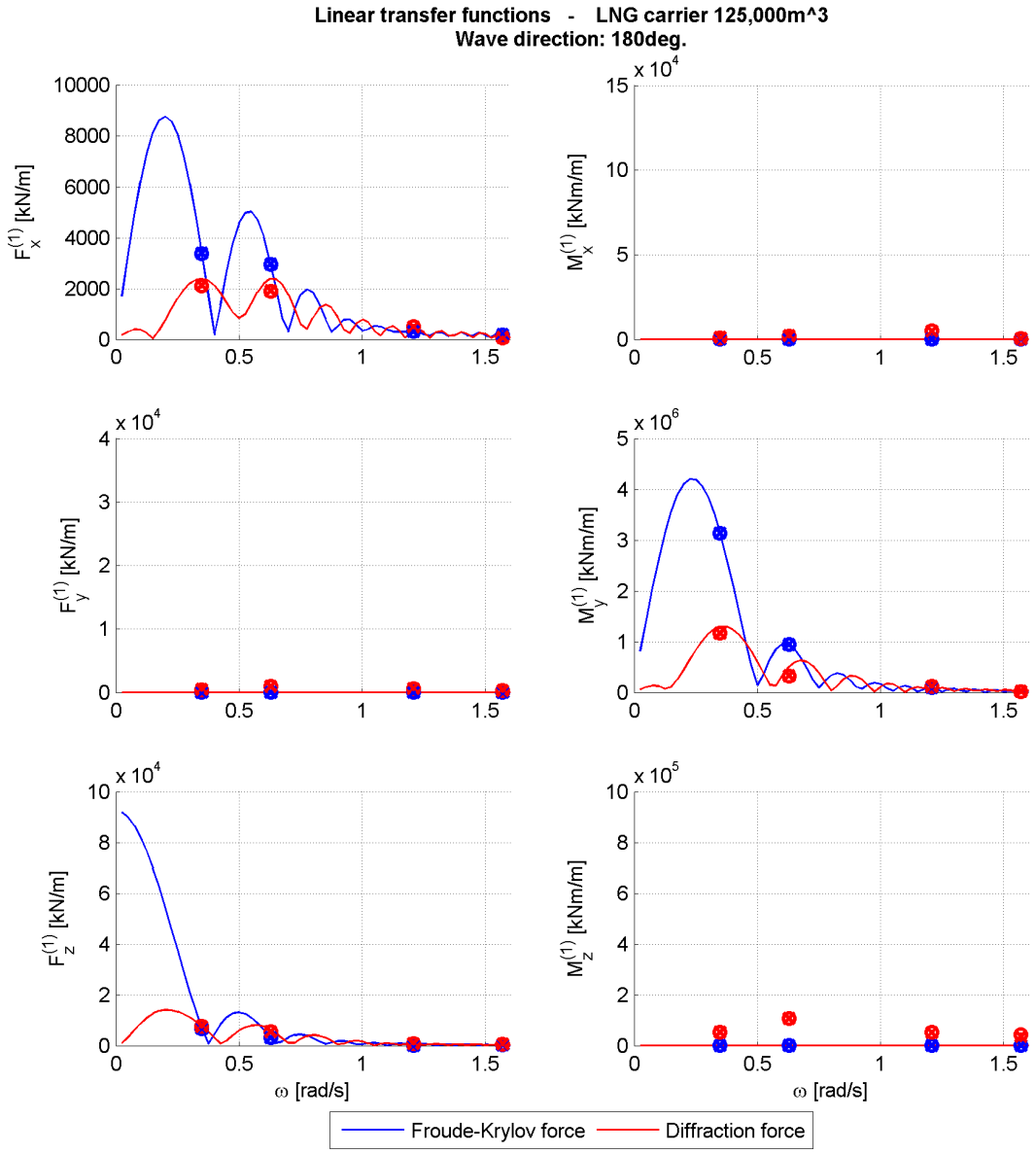

FIGURE E.7: First order forces computed with Wavescat (lines) and Harberth (symbols) models: SWASH wave model run with 20 vertical layers (wave direction = 180°).

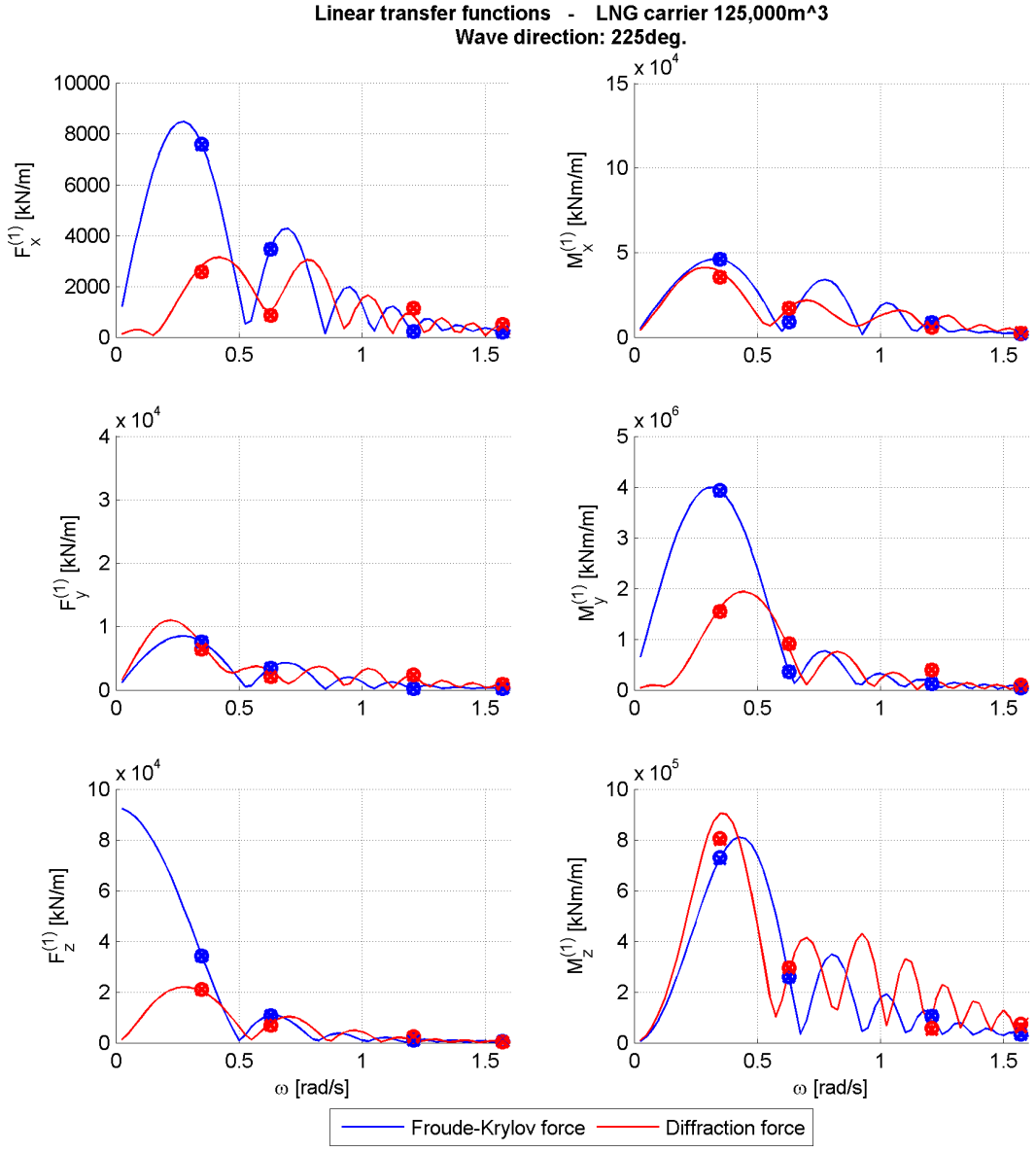

FIGURE E.8: First order forces computed with Wavescat (lines) and Harberth (symbols) models: SWASH wave model run with 20 vertical layers (wave direction = 225°).

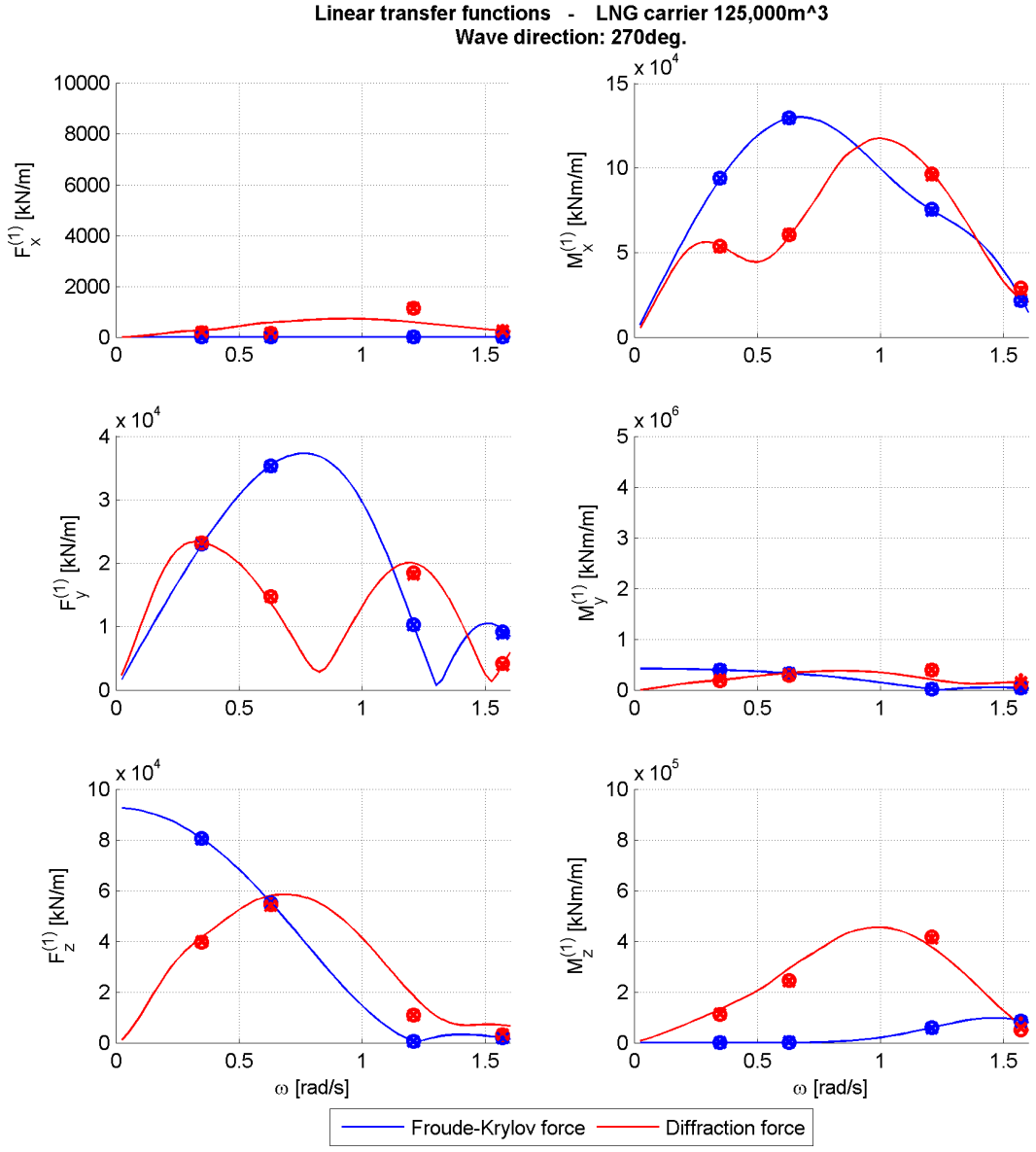

FIGURE E.9: First order forces computed with Wavescat (lines) and Harberth (symbols) models: SWASH wave model run with 20 vertical layers (wave direction = 270°).

E.1.2 1st order forces with 3 and 2 vertical layers in SWASH

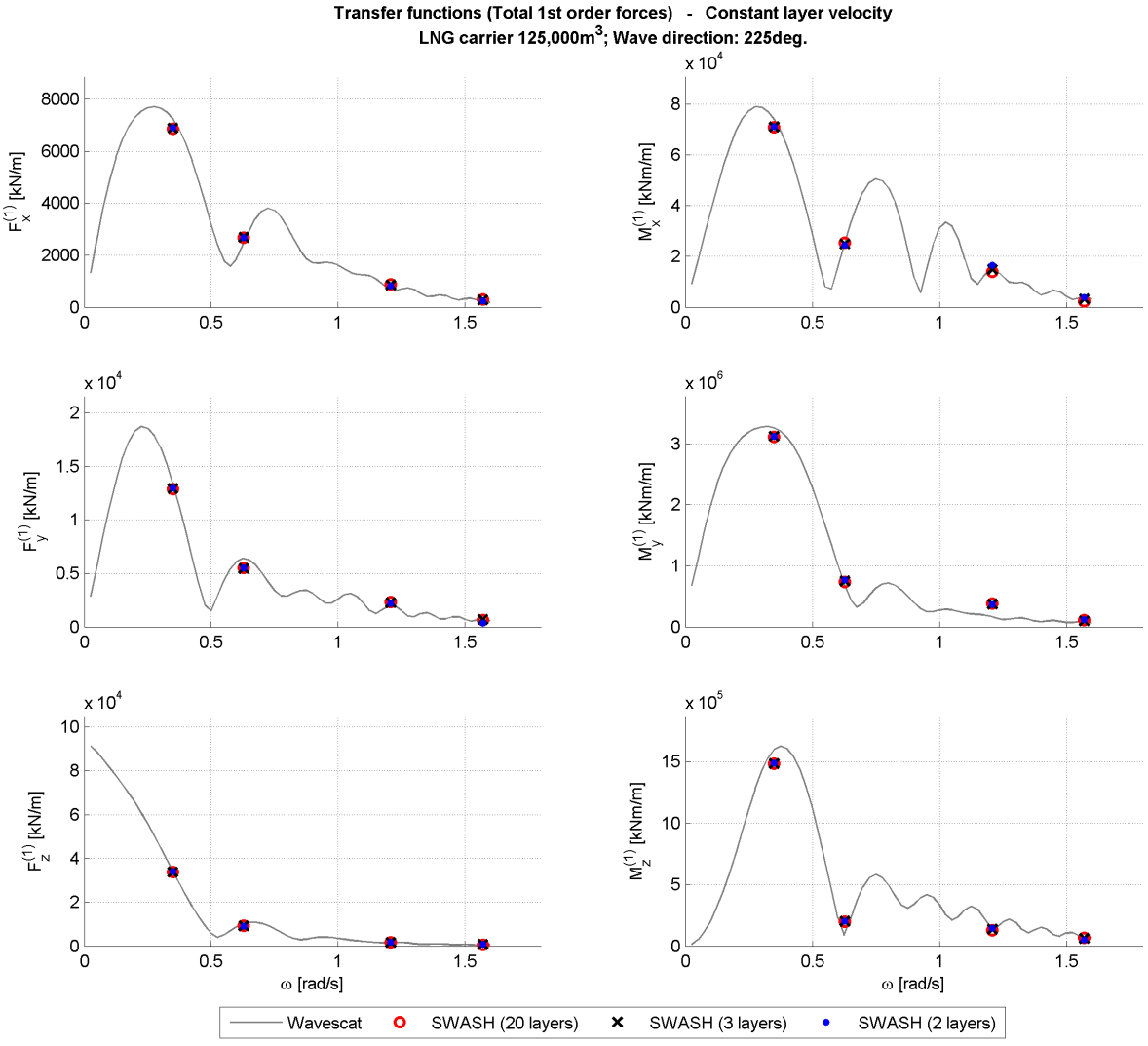

FIGURE E.10: First order forces computed with Wavescat (lines) and Harberth (symbols) models: SWASH wave model run with 3 and 2 vertical layers. Vertical interpolation method I: constant velocity along the layer.

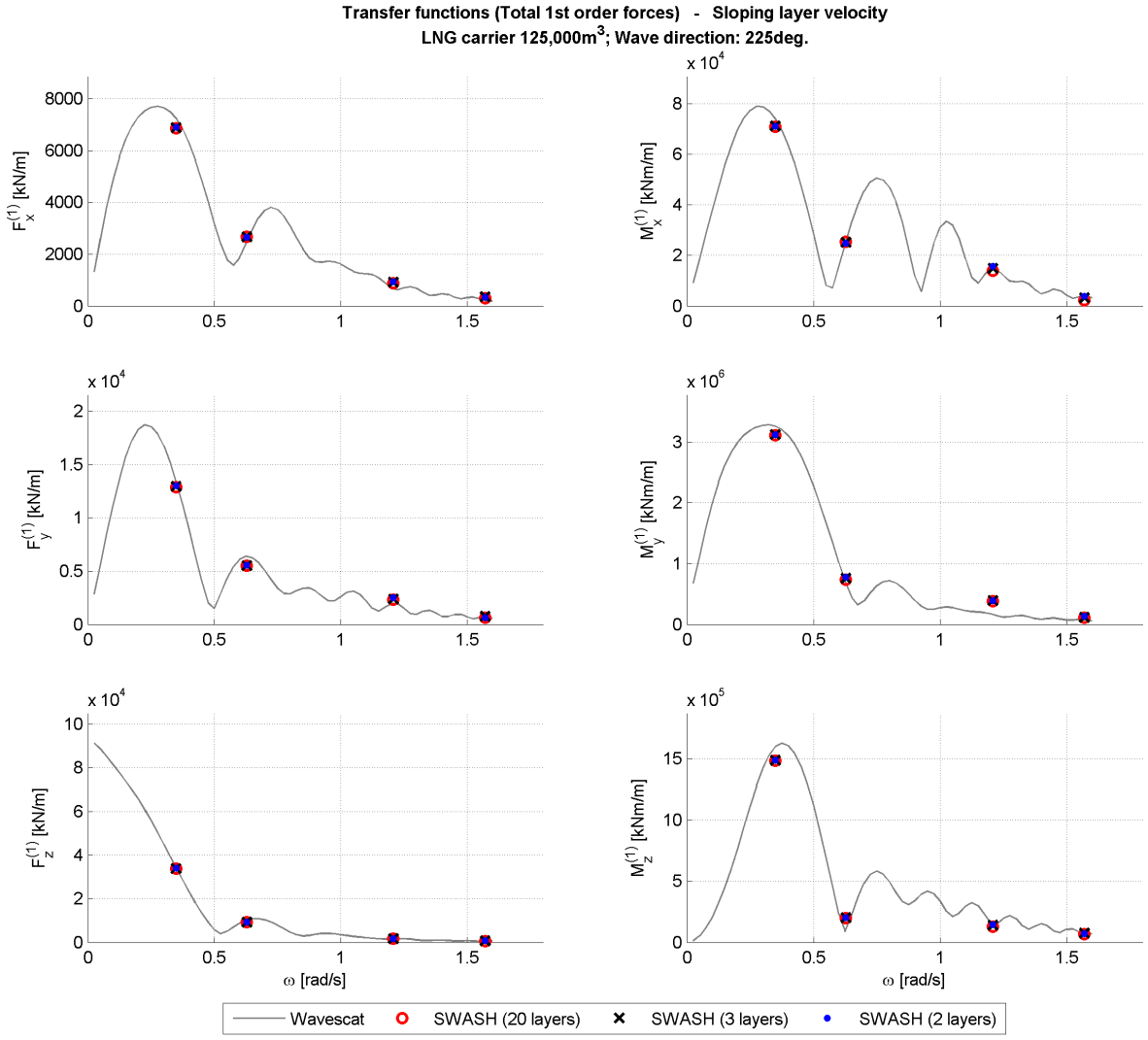

FIGURE E.11: First order forces computed with Wavescat (lines) and Harberth (symbols) models: SWASH wave model run with 3 and 2 vertical layers. Vertical interpolation method II: sloping velocity along the layer.

E.2 Regular waves: 2nd order forces

E.2.1 Ship motions

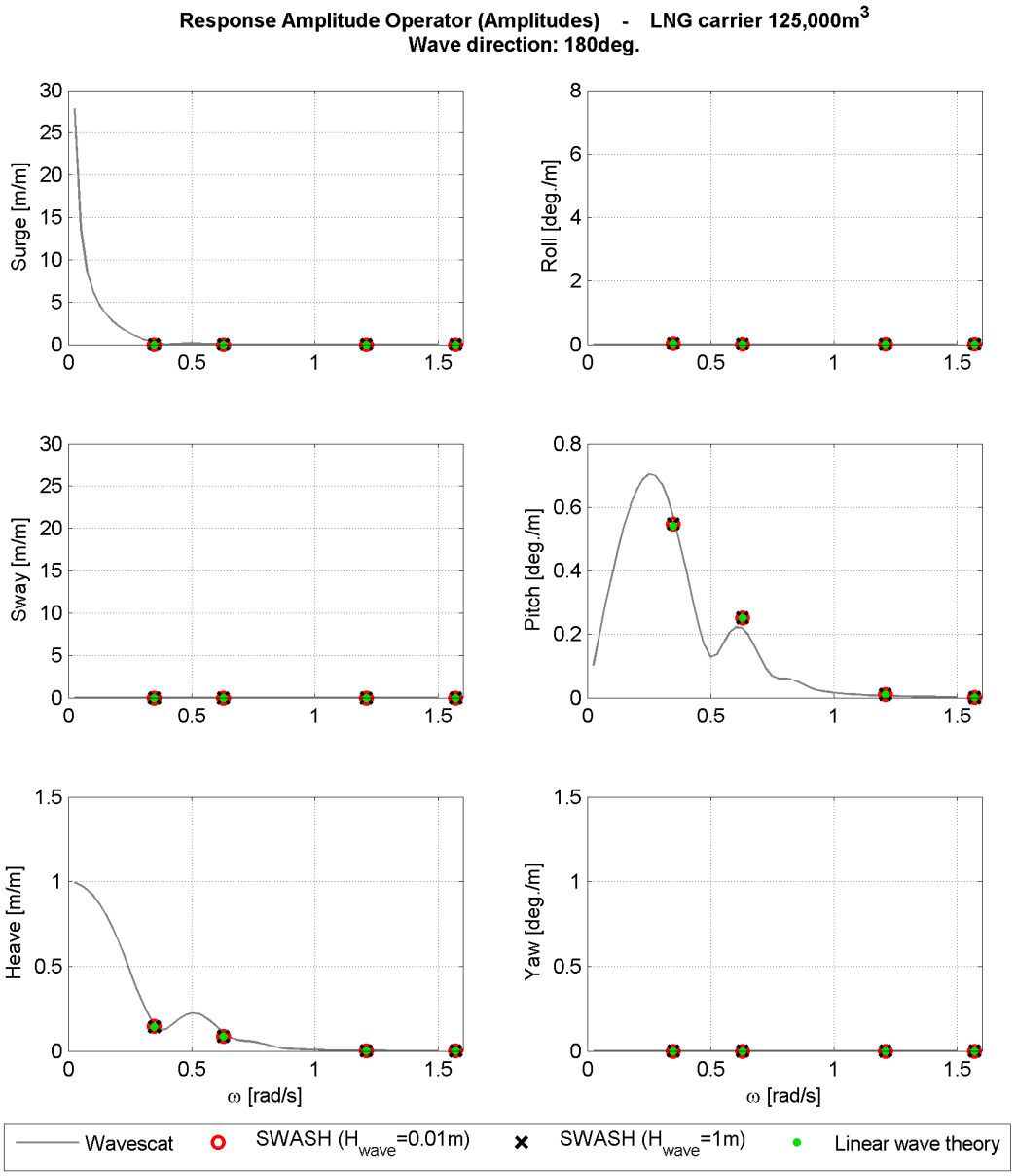

FIGURE E.12: First-order ship motions predicted with Wavescat and Harberth model (Regular wave direction = 180°) applied on the computation of second-order forces. Harberth takes into account only heave, roll and pitch motions, other modes are neglected.

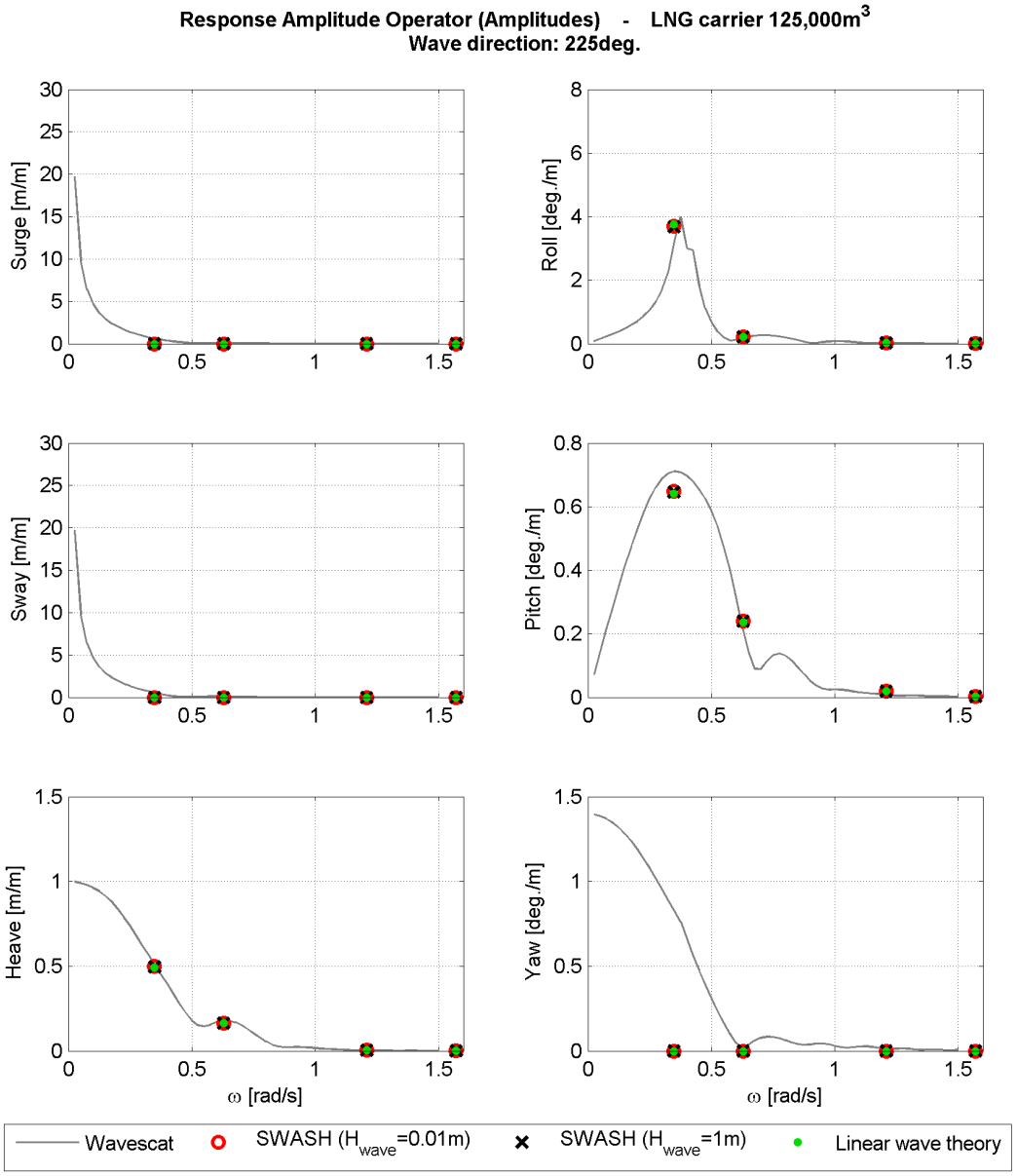

FIGURE E.13: First-order ship motions predicted with Wavescat and Harberth model (Regular wave direction = 225°) applied on the computation of second-order forces. Harberth takes into account only heave, roll and pitch motions, other modes are neglected.

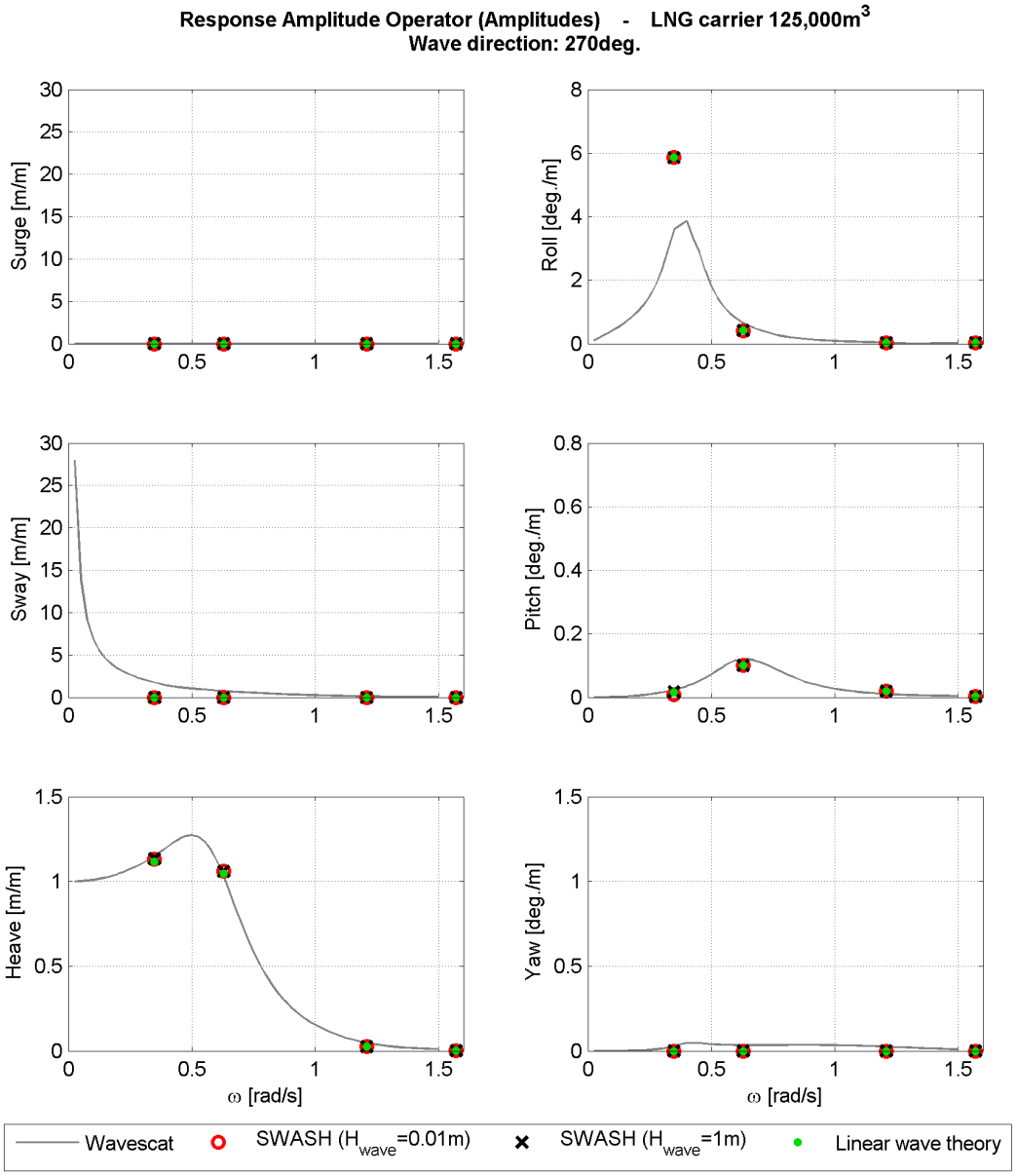

FIGURE E.14: First-order ship motions predicted with Wavescat and Harberth model (Regular wave direction = 270°) applied on the computation of second-order forces. Harberth takes into account only heave, roll and pitch motions, other modes are neglected.

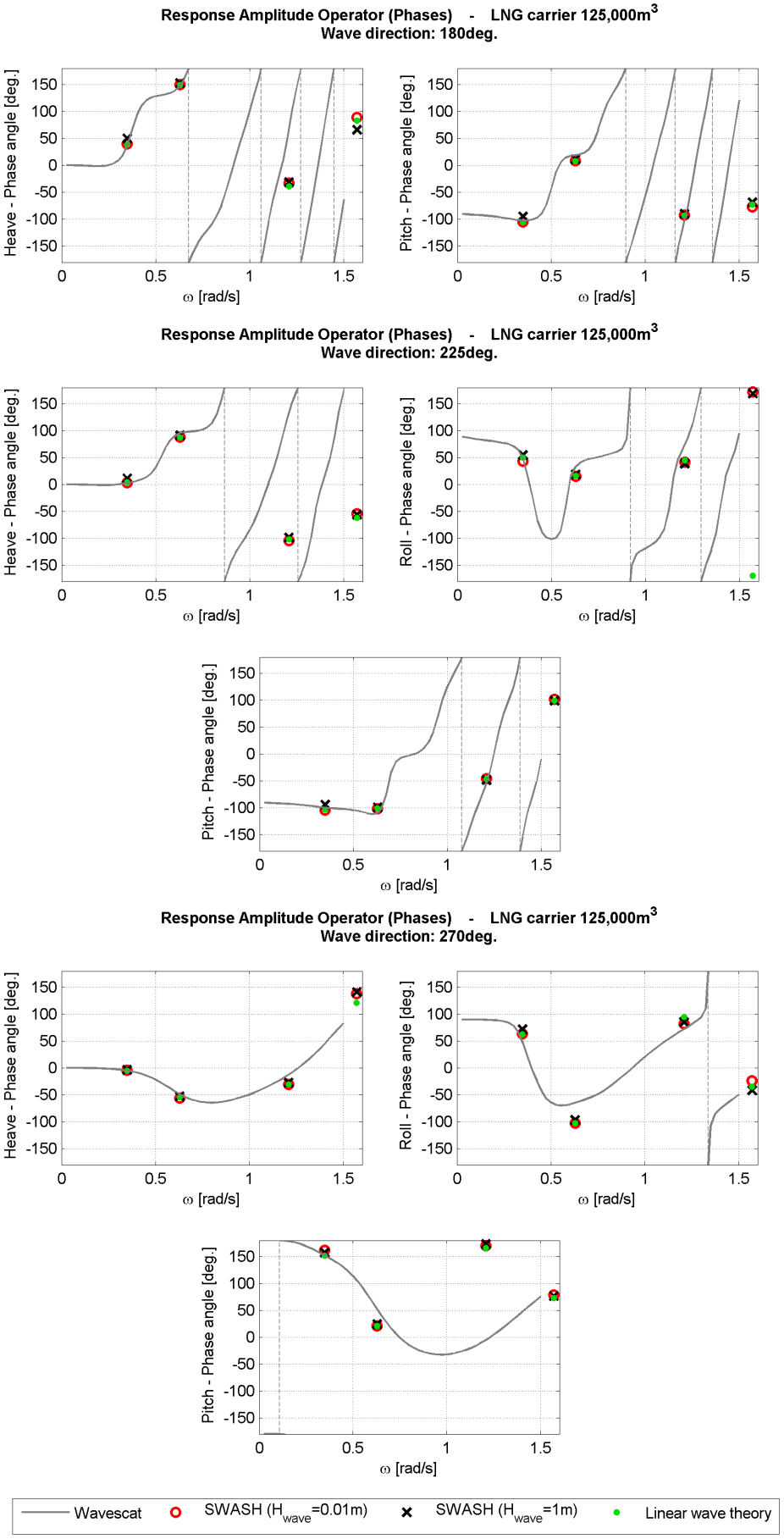

FIGURE E.15: Phase shift of first-order ship motions predicted with Wavescat and Harberth model. Harberth takes into account only heave and pitch motions, other modes are neglected.

E.2.2 Contribution of individual components to the total second-order forces

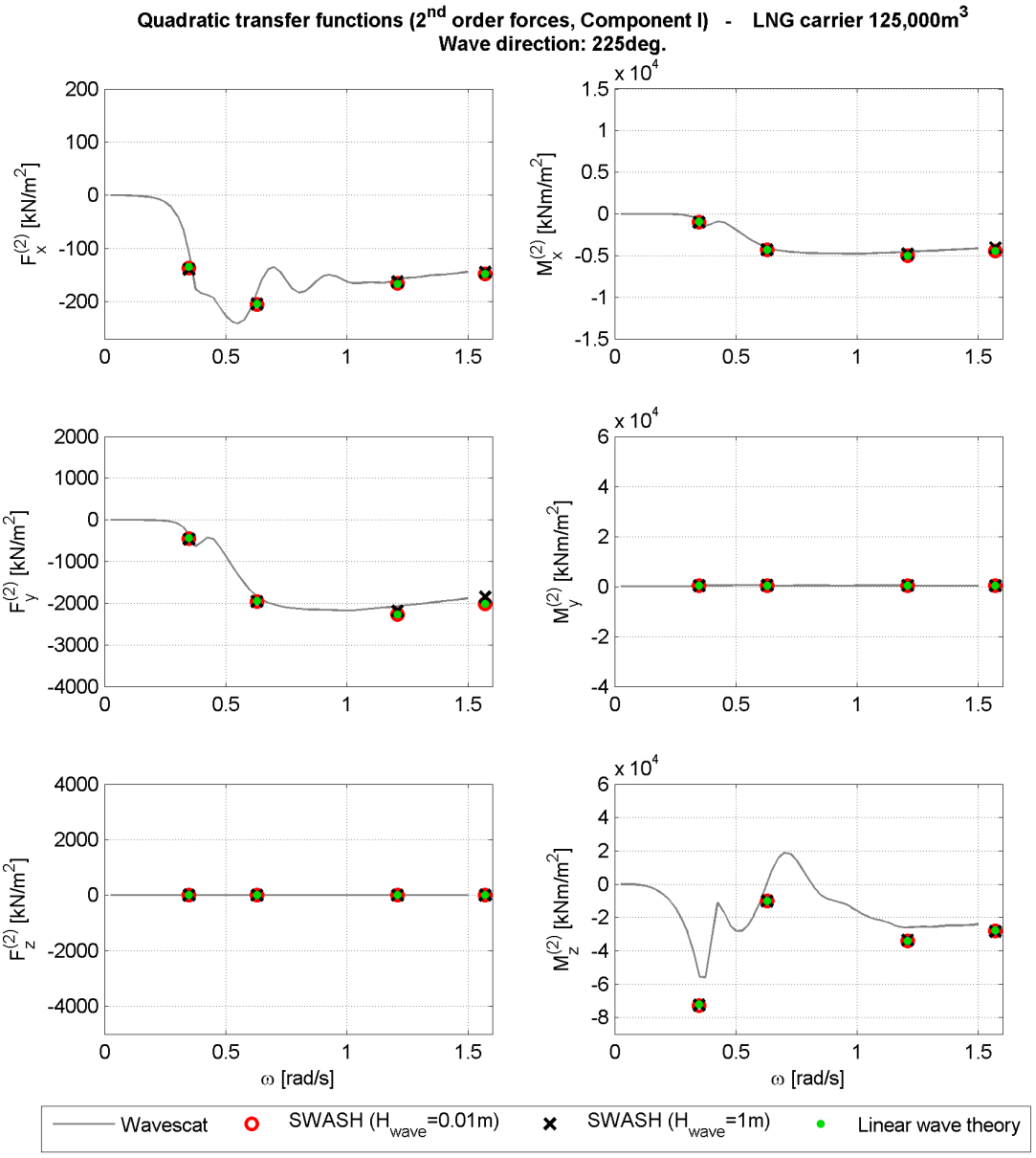

FIGURE E.16: Second-order forces predicted with Wavescat and Harberth model: Component I (Regular wave direction = 225°).

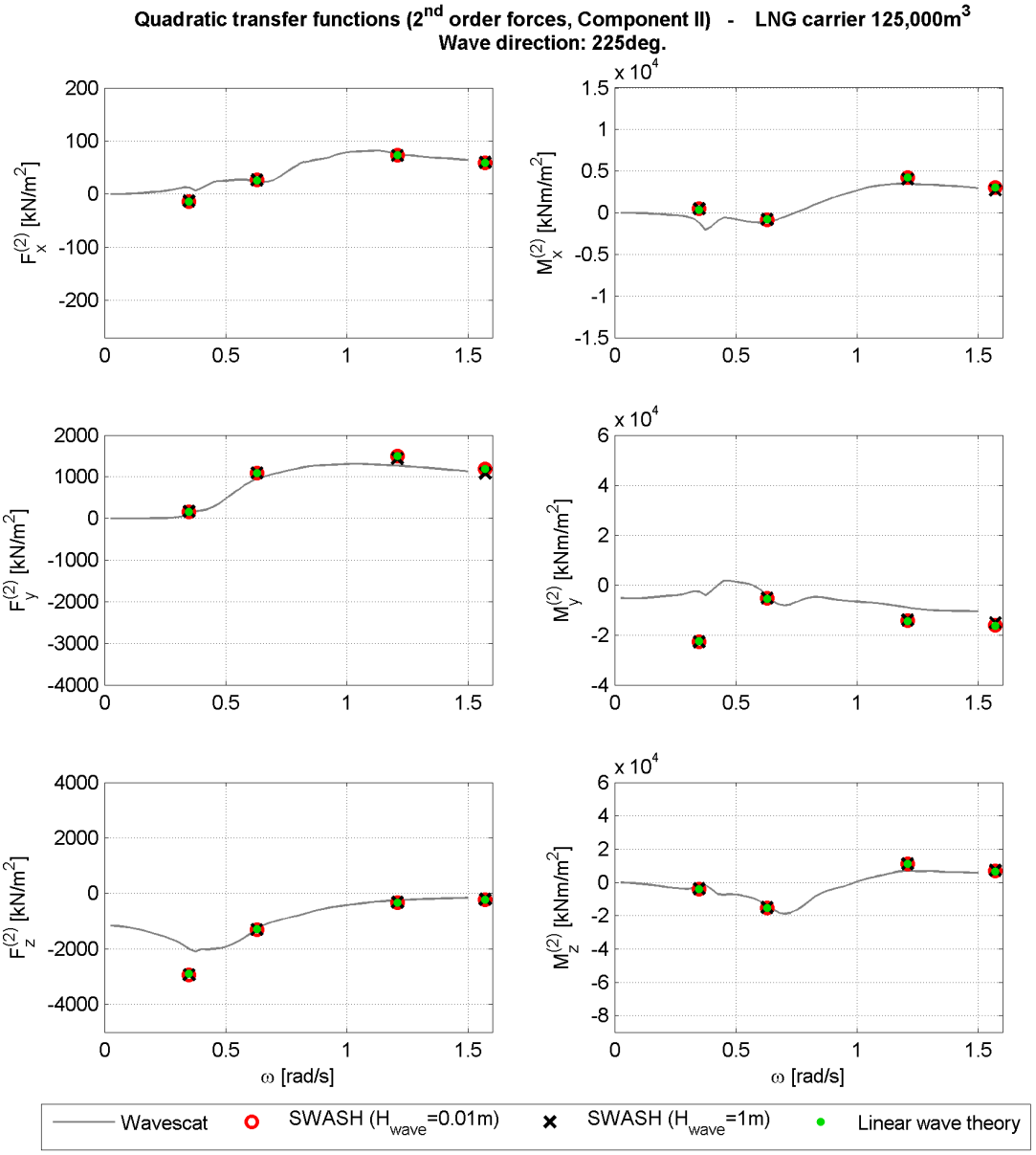

FIGURE E.17: Second-order forces predicted with Wavescat and Harberth model: Component II (Regular wave direction = 225°).

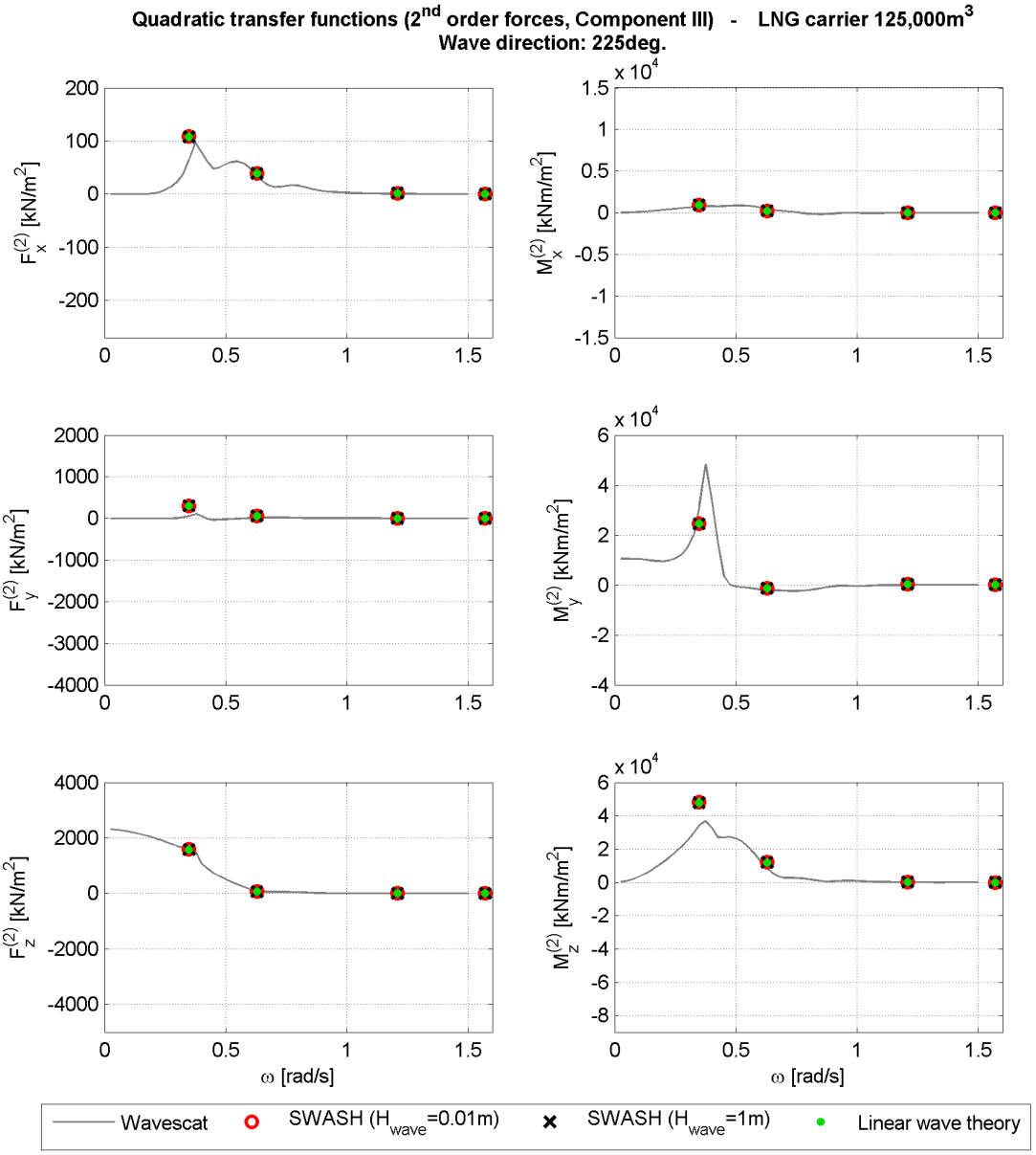

FIGURE E.18: Second-order forces predicted with Wavescat and Harberth model: Component III (Regular wave direction = 225°).

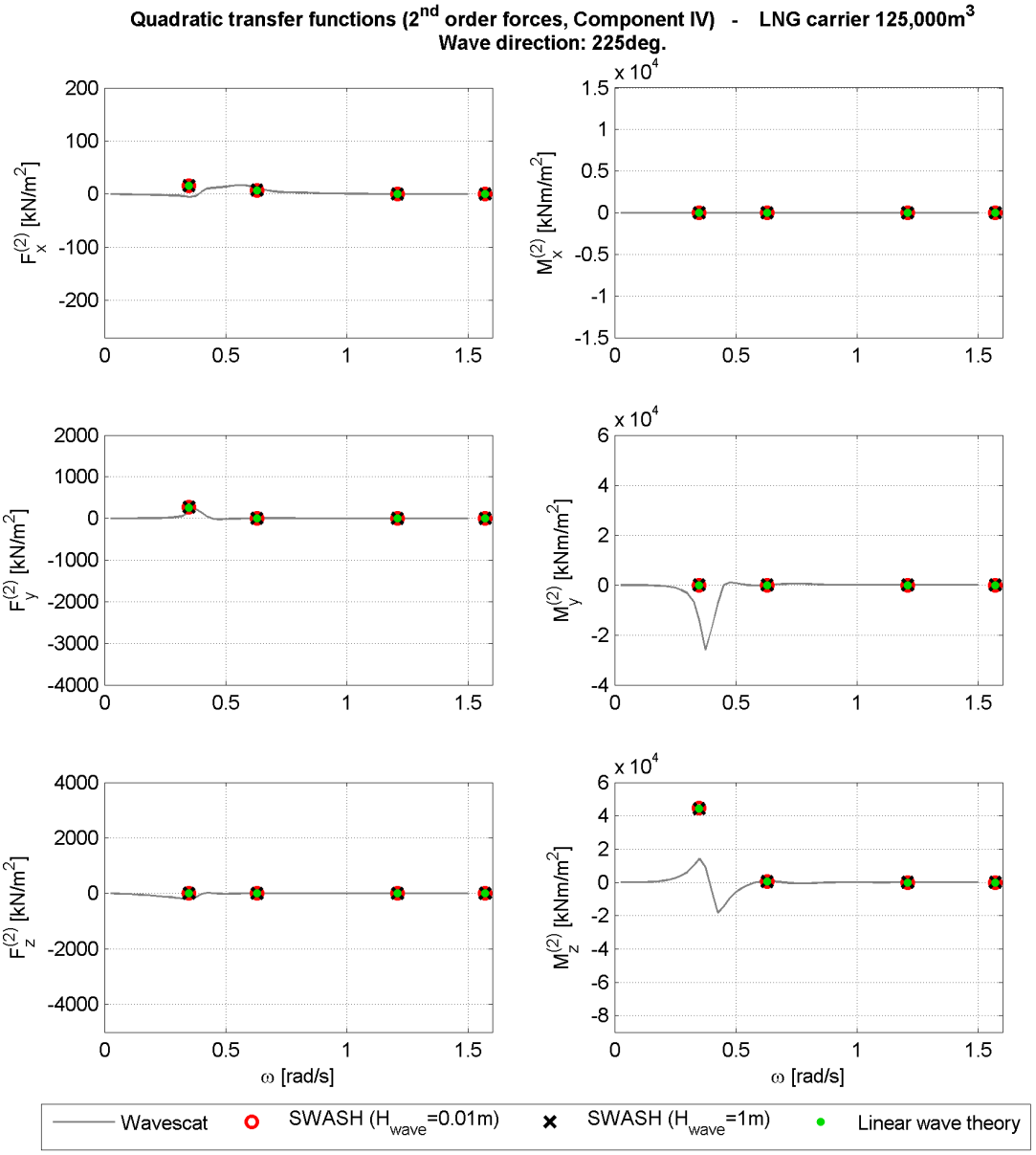

FIGURE E.19: Second-order forces predicted with Wavescat and Harberth model: Component IV (Regular wave direction = 225°).

Appendix F

Validation plots

F.1 Tests C: wave model results

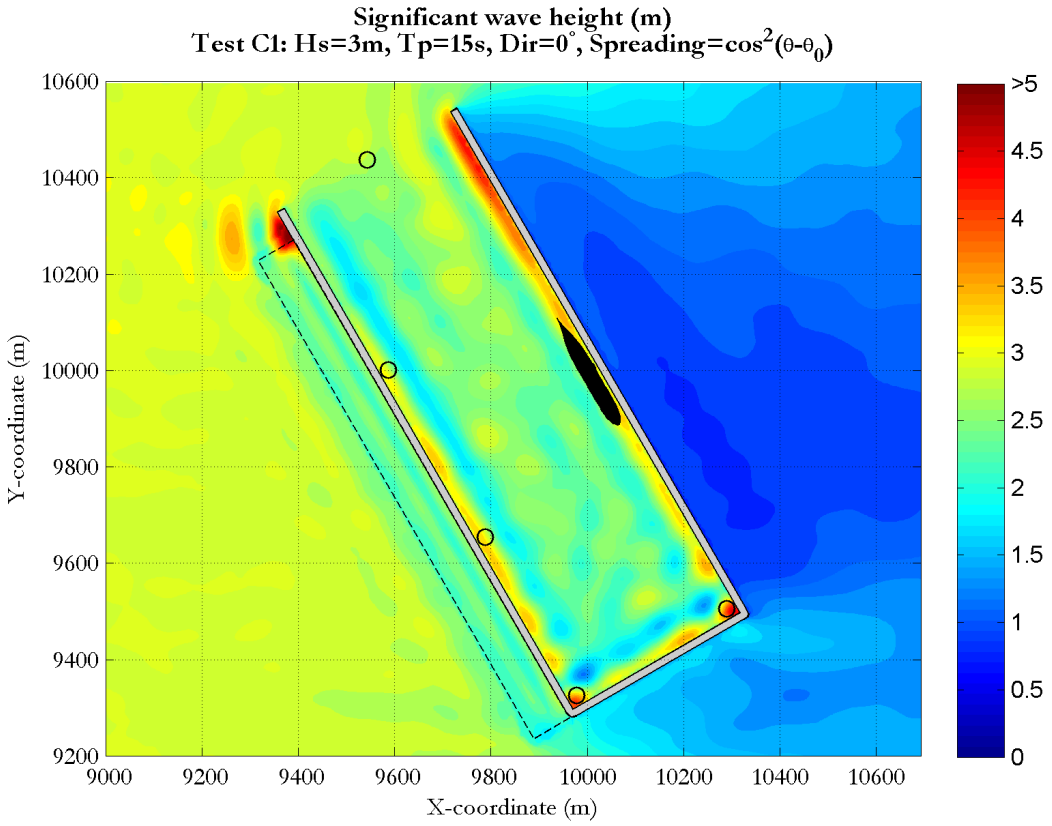

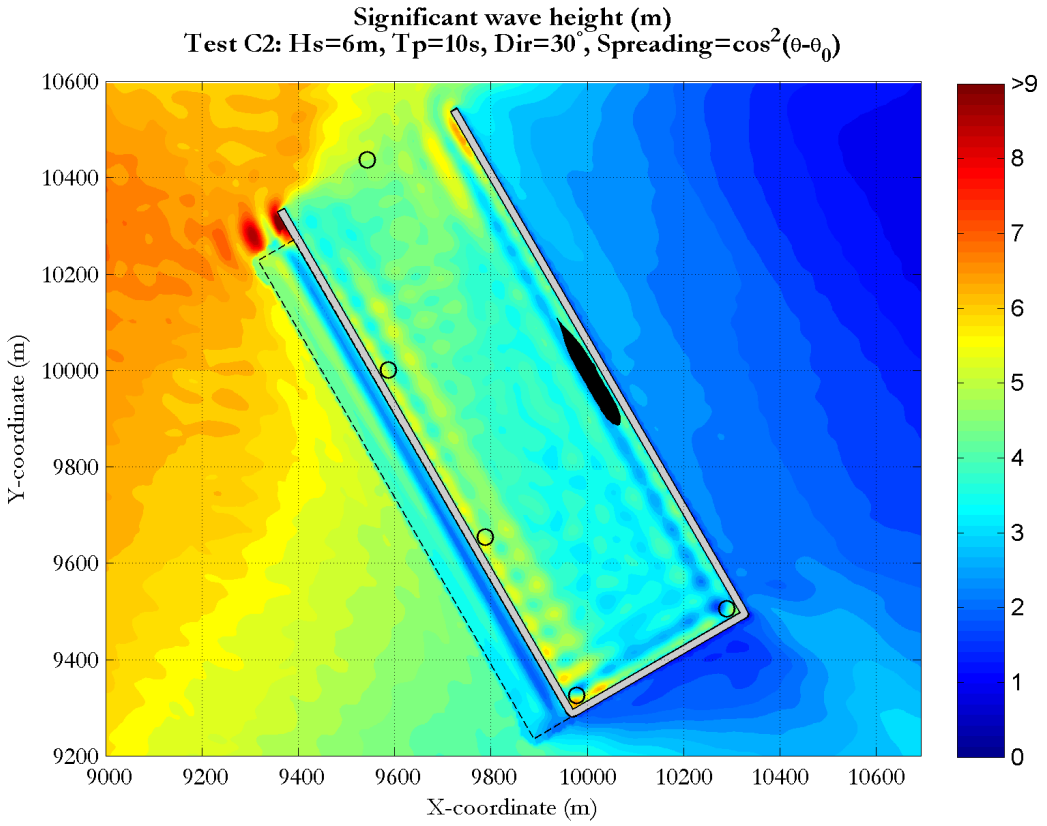
Significant wave height (m)
Test C2: Hs=6m, Tp=10s, Dir=30°, Spreading=cos²(θ-θ0)
Y-coordinate (m)
X-coordinate (m)
10600
10400
10200
10000
9800
9600
9400
9200
9000
9200
9400
9600
9800
10000
10200
10400
10600
>9
8
7
6
5
4
3
2
1
0

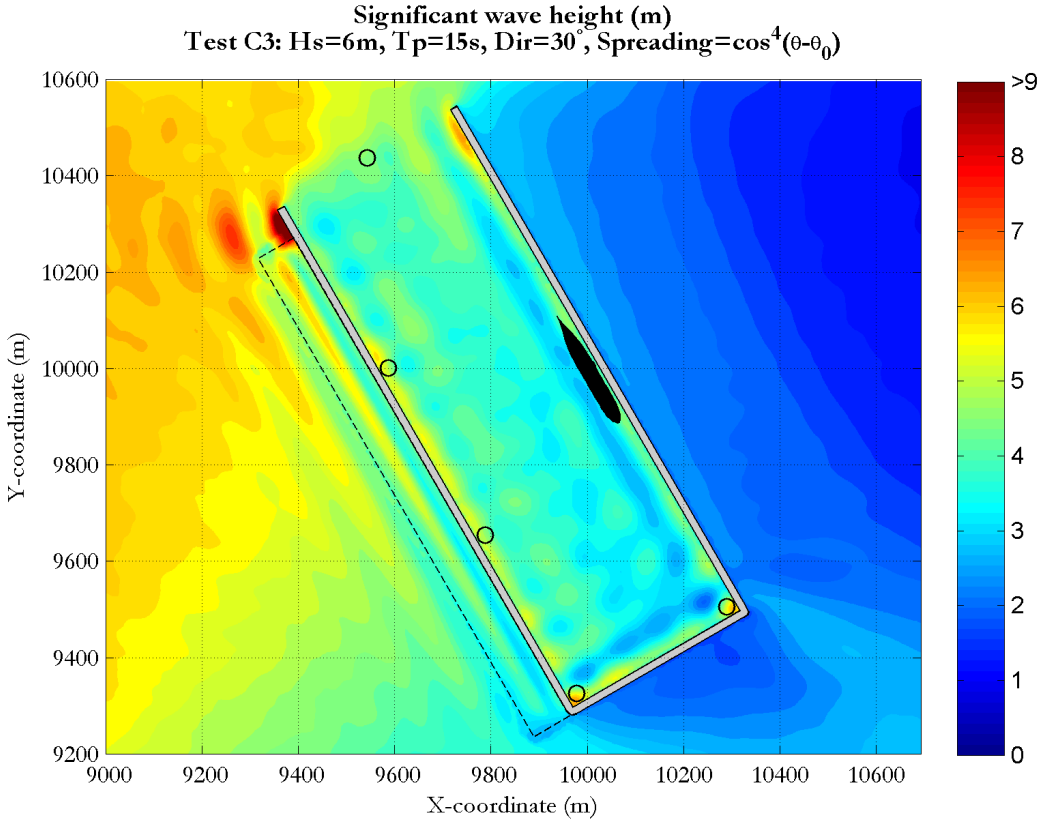
Significant wave height (m)
Test C3: Hs=6m, Tp=15s, Dir=30°, Spreading=cos⁴(θ-θ0)
Y-coordinate (m)
X-coordinate (m)
10600
10400
10200
10000
9800
9600
9400
9200
9000
9200
9400
9600
9800
10000
10200
10400
10600
>9
8
7
6
5
4
3
2
1
0

Test C1 (Harbour basin): Hs=3m, Tp=15s, Dir=0°, Spreading=$\cos^2(\theta - \theta_0)$

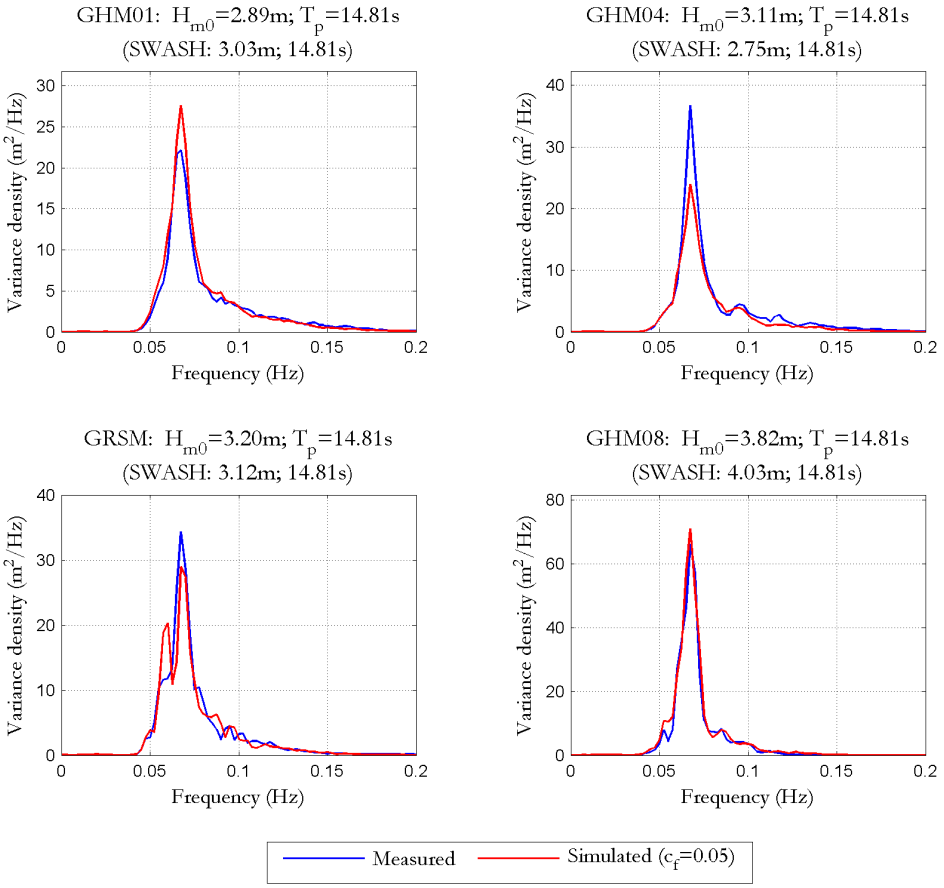

Test C1 (Harbour basin): Hs=3m, Tp=15s, Dir=0°, Spreading=$\cos^2(\theta - \theta_0)$

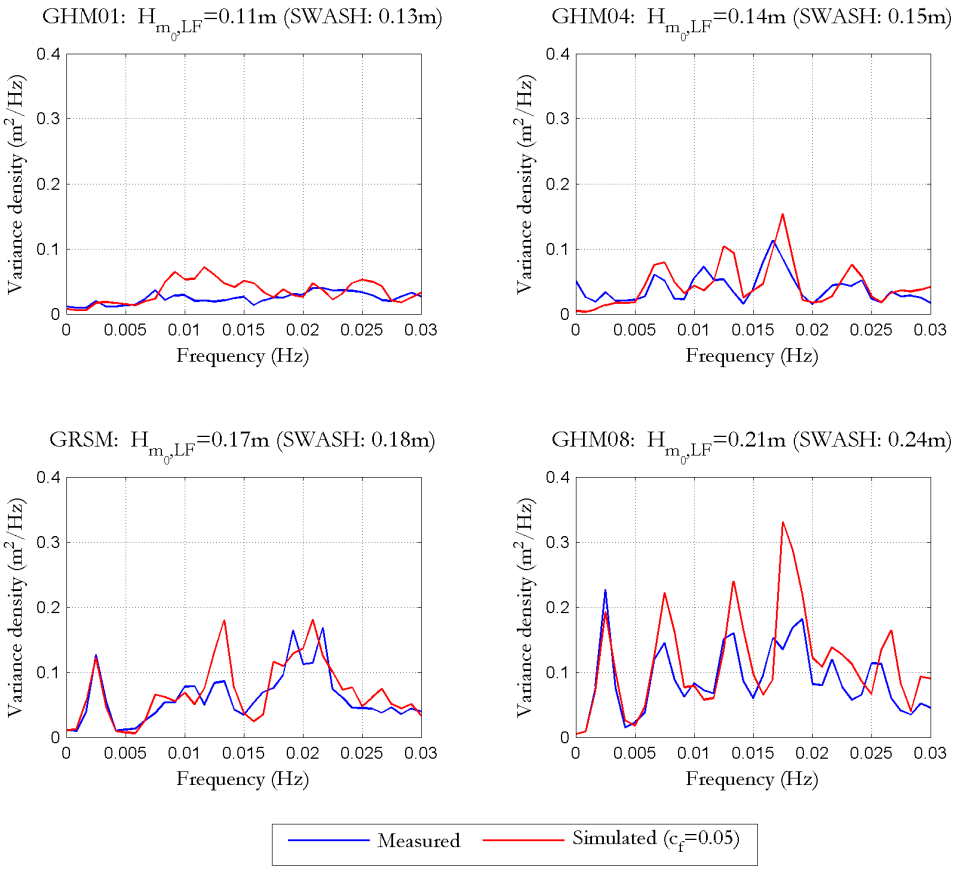

Test C2 (Harbour basin): Hs=6m, Tp=10s, Dir=30°, Spreading=cos^2(θ - θ$_0$)

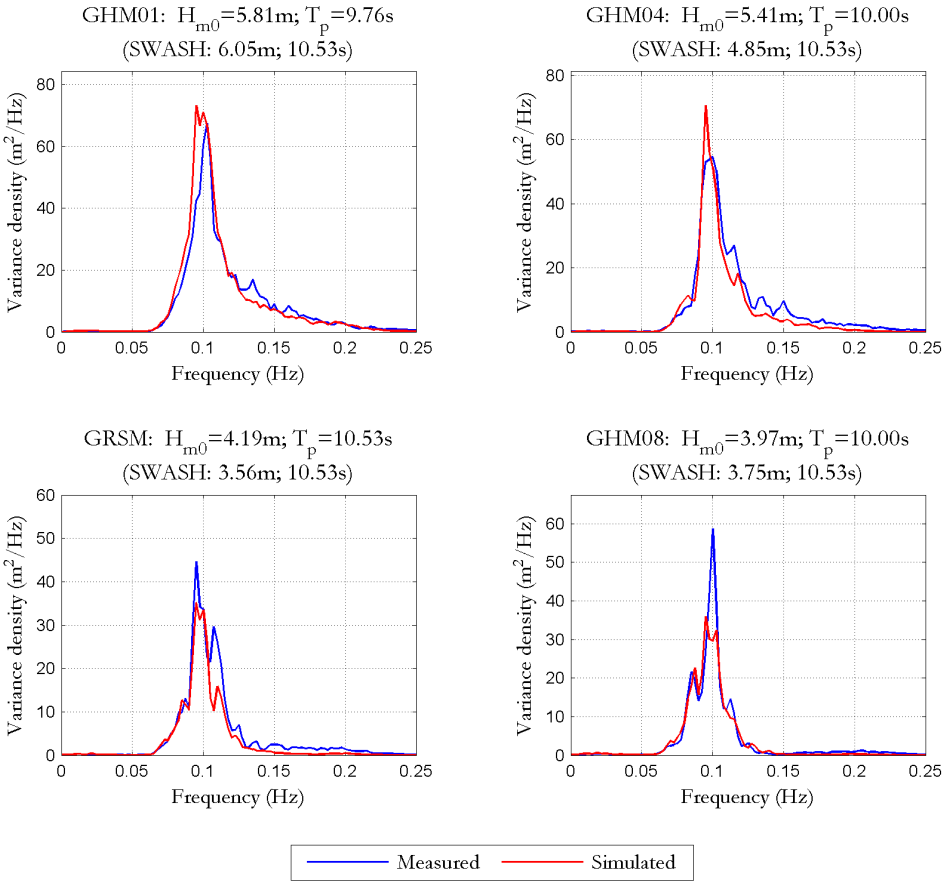

Test C2 (Harbour basin): Hs=6m, Tp=10s, Dir=30°, Spreading=cos^2(θ - θ$_0$)

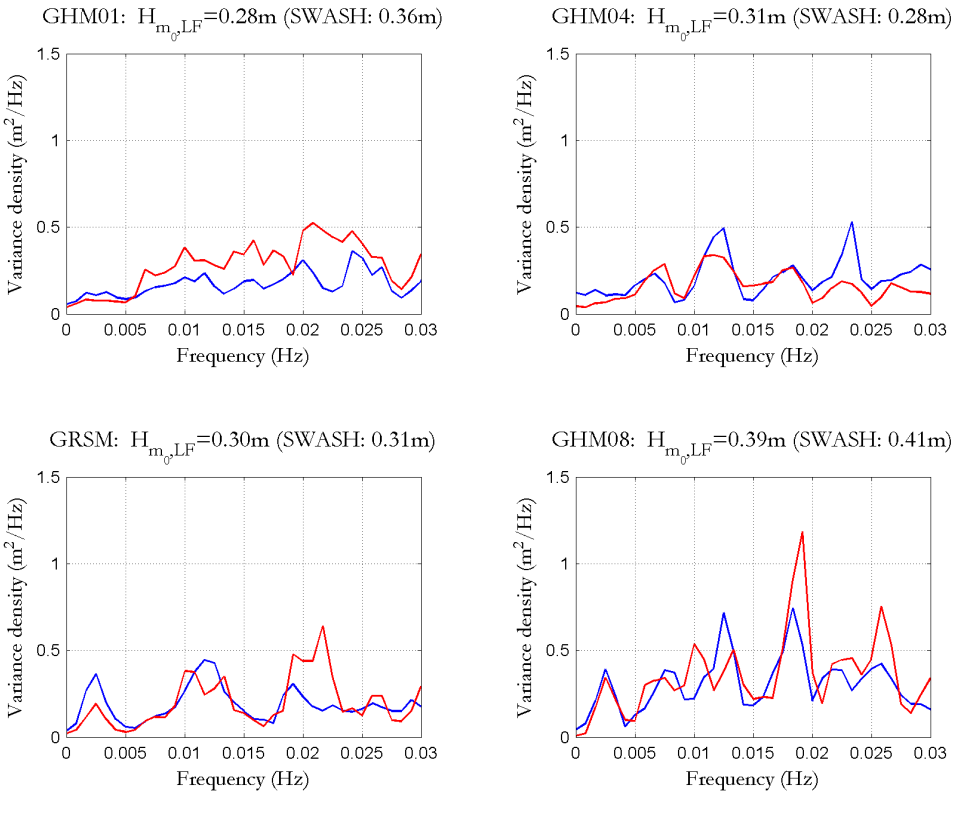

Test C3 (Harbour basin): Hs=6m, Tp=15s, Dir=30°, Spreading=cos^4(θ - θ$_0$)

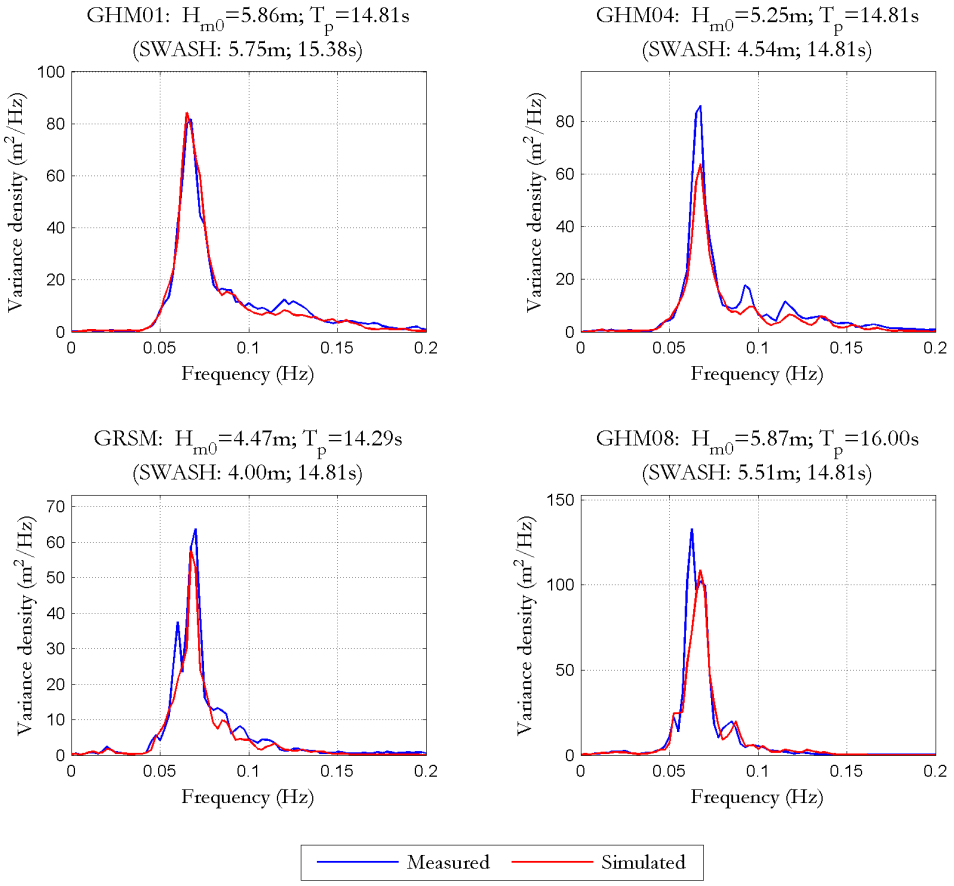

Test C3 (Harbour basin): Hs=6m, Tp=15s, Dir=30°, Spreading=cos^4(θ - θ$_0$)

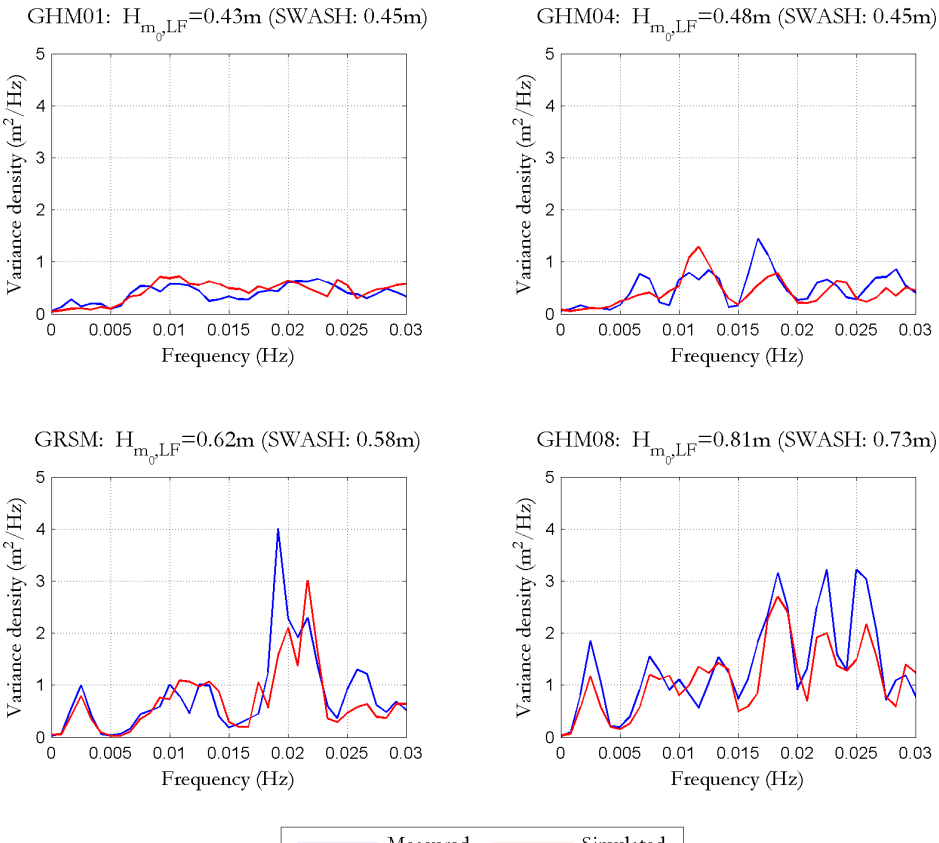

Bibliography

[1] Bingham, H. B. (2000). *A hybrid Boussinesq-panel method for predicting the motion of a moored ship.* Coastal Engineering, 40, 21–38.

[2] CSIR Report, (2011). *Boundary element model Wavescat: description and validation.* (Written by Dr.ir. W. van der Molen).

[3] Dalrymple, R.A., (1989). *Directional wavemaker theory with sidewall reflection.* J. Hydraulic Research; 27, 23–34.

[4] Hasselmann, K. (1962). *On the non-linear energy transfer in a gravity-wave spectrum Part 1. General theory.* J. Fluid Mech. 12, 481–500.

[5] Holthuijsen, L.H. (2007). *Waves in oceanic and coastal waters.* Cambridge University Press, Cambridge, UK.

[6] Hughes, S.A., (1993). *Physical models and laboratory techniques in coastal engineering.* World Scientific, Singapore.

[7] Journée, J.M.J.; Massie, W.W. (2001). *Offshore Hydromechanics.* First edition. Delft University of Technology, Delft, The Netherlands.

[8] Mellink, B., (2012). *Numerical and experimental research of wave interaction with a porous breakwater.* Master thesis, Delft University of Technology, Delft, The Netherlands.

[9] *Mike21-Harberth User Manual* (2007). Delft University of Technology and Royal Haskoning (written by Dr.ir. W. van der Molen).

[10] Pés, V.M. (2013). *Applicability and Limitations of the SWASH model to predict Wave Overtopping.* MSc thesis, Universitat Politècnica de Catalunya, Barcelona, Spain.

[11] Pinkster, J.A. (1980). *Low frequency second order wave exciting forces on floating structures.* Doctoral dissertation, Delft University of Technology, Delft, The Netherlands.

[12] Pinkster, J.A. (1995). *Hydrodynamic Interaction Effects in Waves.* ISOPE'95, The Hague, The Netherlands.

[13] Rijnsdorp, D.P.; Smit, P.B.; Zijlema, M., (2012). Non-hydrostatic modelling of infragravity waves using SWASH. Coastal Engineering.

[14] Rijnsdorp, D.P.; Smit, P.B.; Zijlema, M., (2014). *Non-hydrostatic modelling of infragravity waves under laboratory conditions*. Coastal Eng. 85, 30–42.

[15] Sand, S.E. (1982). *Long waves in directional seas*. Coastal Engineering, 6:195-208.

[16] Shemer, L.; Kit, E.; Haiying Jiao; Eitan, O., (1998). *Experiments on nonlinear wave groups in intermediate water depth.*. J. of waterway, port, coastal and ocean engineering.

[17] Smit, P.B.; Zijlema, M.; Stelling, G.S., (2013). *Depth-induced wave breaking in a nonhydrostatic, near-shore wave model*. Coast. Eng. 76, 1–16.

[18] *User manual SWASH* (2014). Delft University of Technology, Delft, The Netherlands. Retrieved March 21, 2014, from http://swash.sourceforge.net/online_doc/swashuse/.

[19] *User manual SWASH version 2.00* (2014). Delft University of Technology, Delft, The Netherlands.

[20] WL | Delft Hydraulics report, (2004). *Projectbeschrijving R&D Havens EZ-LIP: H3896.40 Validatie golfkrachten op schepen*. Delft, The Netherlands.

[21] van Dongeren, A.R.; Klopman, G.; Reniers, A.J.H.M.; Petit, H.A.H., (2001). *High quality laboratory wave generation for flumes and basins*. In Proc. WAVES (Vol. 2, pp. 1190–1199). San Francisco, CA.

[22] van der Molen, W. (2006). *Behaviour of Moored Ships in Harbours*. Doctoral dissertation, Delft University of Technology, Delft, The Netherlands.

[23] van der Molen, W.; Wenneker, I., (2008). *Time-domain calculation of moored ship motions in nonlinear waves*. Coastal Eng. 55, 409–422. doi: 10.1016/j.coastaleng.2008.01.001.

[24] van der Wel, M., (2011). *The behaviour of a moored oil tanker in the Port of Leixões, Portugal, with use of numerical models*. Master thesis, Delft University of Technology, Delft, The Netherlands.

[25] Zijlema, M.; Stelling, G.S., (2005). *Further experiences with computing non-hydrostatic free-surface flows involving water waves*. Int. J. Numer. Meth. Fluids 48, 169–197.

[26] Zijlema, M.; Stelling, G.; Smit, P., (2011). *SWASH: An operational public domain code for simulating wave fields and rapidly varied flows in coastal waters*. Coastal Eng. 58, 992–1012. doi:10.1016/j.coastaleng.2011.05.015.